Universitat de les Illes Balears

UNIVERSITÉ DE GRENOBLE

DOCTORAL THESIS

2014

EDDIES IN THE WESTERN MEDITERRANEAN SEA: CHARACTERIZATION AND UNDERSTANDING FROM SATELLITE OBSERVATIONS AND MODEL SIMULATIONS

Romain Escudier

Universitat de les Illes Balears

UNIVERSITÉ DE GRENOBLE

DOCTORAL THESIS

2014

Doctoral Programme of *Physics*

EDDIES IN THE WESTERN MEDITERRANEAN SEA: CHARACTERIZATION AND UNDERSTANDING FROM SATELLITE OBSERVATIONS AND MODEL SIMULATIONS

Romain Escudier

Directora: Ananda Pascual Ascaso

Co-director: Pierre Brasseur

Tutor: Damià Gomis Bosch

Doctor by the *Universitat de les Illes Balears* and *Université de Grenoble*

Universitat de les Illes Balears

UNIVERSITÉ DE GRENOBLE

THÈSE

Pour obtenir le grade de

DOCTEUR DE L'UNIVERSITÉ DE GRENOBLE

préparée dans le cadre d'une cotutelle entre l'*Université de Grenoble* et l'*Universitat de les Illes Balears*

Spécialité : **Physique appliquée à l'ocean**

Arrêté ministériel : le 6 janvier 2005 -7 août 2006

Présentée par

Romain Escudier

Thèse dirigée par **Ananda Pascual Ascaso**
codirigée par **Pierre Brasseur**

préparée au sein de l'**Institut Mediterrani d'Estudis Avançats (IMEDEA)** et du **Laboratoire de Glaciologie et Géophysique de l'Environnement (LGGE)**

dans les Écoles Doctorales de **Física de l'UIB** et **Terre-Univers-Environnement de l'UdG**

Tourbillons mésoéchelle dans la Méditerranée occidentale : charactérisation et compréhension à l'aide d'observations altimetriques et de simulations numériques

Thèse qui sera soutenue publiquement le **21 Janvier 2015**,
devant le jury composé de :

Damiá Gomis
Professeur à l'UIB, Président
Dudley Chelton
Professeur émérite à l'OSU, Rapporteur
Jordi Font
Professeur à l'ICM, Rapporteur
Bernard Barnier
Directeur de Recherche CNRS (LGGE), Examinateur
Lionel Renault
Chercheur à UCLA, Examinateur
Ananda Pascual Ascaso
Chercheuse titulaire CSIC (IMEDEA), Directrice de thèse
Pierre Brasseur
Directeur de Recherche CNRS (LGGE), Co-Directeur de thèse

Université Joseph Fourier / Université Pierre Mendès France / Université Stendhal / Université de Savoie / Grenoble INP

Acknowledgements

Mes remerciements vont tout d'abord à Ananda Pascual pour m'avoir donné l'opportunité de réaliser cette thèse et son soutien tout au long de ces quatres années. Toujours à l'écoute, elle su me guider tout en sachant me laisser prendre des initiatives.

Je voudrais ensuite remercier Pierre Brasseur pour avoir accepté de nous accompagner dans cette aventure. Encadrer la thèse à distance n'a pas toujours été facile mais Pierre a été là pour m'aider à prendre du recul voire réorienter mes recherches quand il le fallait.

Je suis reconnaissant au CSIC qui, avec la bourse de thèse JAE, m'a permis de travailler sur ce sujet de thèse. Je remercie également le CNRS pour m'avoir financé mes derniers mois de thèse ainsi que le projet MyOcean2 qui m'a permis d'assister à plusieurs conférences au cours de ma thèse.

Merci à Lionel Renault, qui m'a initié aux mystères de la modélisation. Même après s'être expatrié à l'autre bout du monde, il a continué à s'investir dans mon projet de thèse.

Je souhaite également remercier Dudley Chelton pour son accueil à Corvallis, sa disponibilité et son apport scientifique.

Un grand merci à tous ceux que j'ai rencontré au cours de cette thèse et qui ont fait de ces années une belle histoire. Je pense bien sûr aux collèques de l'IMEDEA (et SOCIB), qui, pour la plupart, sont devenus des amis. J'ai adoré nos discussions interminables, qu'elles aient été lors des séminaires

"imedeicos", sur la terrasse à midi ou le soir autour d'une caña. Je pense aussi à toute l'équipe MEOM à Grenoble qui m'a fait sentir chez moi à chacun de mes séjours là-bas. L'ambiance chaleureuse et l'esprit d'entraide est une des grandes qualités de cette équipe.

Je n'oublie pas les amis, à Palma, en France ou dispersé dans le monde, ainsi que ma famille qui ont souvent été le soutien dont j'avais besoin pour continuer. Merci à plus particulièrement à mes parents pour leurs conseils, leur soutien et leur aide dans la correction de ce manuscrit.

Thank you all.

Abstract

Mesoscale eddies are relatively small structures that dominate the ocean variability and have large impact on large scale circulation, heat fluxes and biological processes. In the western Mediterranean Sea, a high number of eddies has been observed and studied in the past with in-situ observations. Yet, a systematic characterization of these eddies is still lacking due to the small scales involved in these processes in this region where the Rossby deformation radius that characterizes the horizontal scales of the eddies is small (10-15 km).

The objective of this thesis is to perform a characterization of mesoscale eddies in the western Mediterranean. For this purpose, we propose to develop tools to study the fine scales of the basin. First, we develop an eddy resolving simulation of the region for the last 20 years. The performance of the simulation is evaluated with independent observations (drifters, satellites, hydrographic profiles) showing realistic behavior. This simulation shows that existing altimetry maps underestimate the mesoscale signal. Therefore, we attempt to improve existing satellite altimetry products to better resolve mesoscale eddies. We show that this improvement is possible but at the cost of the homogeneity of the fields; the resolution can only be improved at times and locations where altimetric observations are densely distributed.

In a second part, we apply three different eddy detection and

tracking methods to extract eddy characteristics from the outputs of the high-resolution simulation, a coarser simulation and altimetry maps. The results allow the determination of some characteristics of the detected eddies. The size of the eddies can greatly vary but is around 25-30 km. About 30 eddies are detected per day in the region with a very heterogeneous spatial distribution. Unlike other areas of the open ocean, they are mainly advected by currents of the region. Eddies can be separated according to their lifespan. Long-lived eddies are larger in amplitude and scale and have a seasonal cycle with a peak in late summer, while short-lived eddies are smaller and more present in winter. The penetration depth of detected eddies has also a large variance but the mean depth is around 300 meters. Anticyclones extend deeper in the water column and have a more conic shape than cyclones.

Resumen

Los remolinos de mesoescala son estructuras relativamente pequeñas que dominan la variabilidad del océano y tienen un fuerte impacto en la circulación de gran escala, los flujos de calor y los procesos biológicos. En el Mediterráneo occidental, se han estudiado numerosos remolinos a partir de observaciones in-situ. Sin embargo, todavía falta una caracterización sistemática de estos remolinos ya que las escalas implicadas en los procesos de esta región son pequeñas. Se estima que el radio de deformación de Rossby asociado a las escalas horizontales típicas de los remolinos varia entre 10 y 15 km.

El objetivo de esta tesis es realizar una caracterización de los remolinos de mesoescala en el Mediterráneo occidental. Con este fin, se propone el desarrollo de herramientas para el estudio de las estas estructuras. En primer lugar, se implementa una simulación numérica de la región durante los últimos 20 años con una resolución suficiente para resolver remolinos. Usando observaciones independientes (boyas, satélites, perfiles hydrograficos) se demuestra el realismo de la simulación. Además esta simulación muestra que los mapas de altimetría existentes subestiman la señal de la mesoescala. En este contexto, se propone un nuevo método para mejorar la resolución de los productos de altimetría por satélite existentes con el objectivo de estudiar los remolinos de mesoescala. Se demuestra que el nuevo método mejora los mapas altimétricos, sin embargo,

conlleva una pérdida de la homogeneidad de los campos; la resolución sólo puede mejorarse en determinados momentos y lugares en los que las observaciones altimétricas están presentes de forma muy densa.

En la segunda parte de la tesis, se aplican tres métodos diferentes de detección y de seguimiento de remolinos para extraer las características de los remolinos a partir de las salidas tanto de la simulación de alta resolución, como de una simulación más de menor resolución y de los mapas de altimetría. Los resultados permiten determinar algunas propriedades de los remolinos detectados. El radio de los remolinos puede variar mucho pero la mayoría es alrededor de 25-30 km. Aproximadamente se detectan 30 remolinos por día en la región con una distribución espacial muy heterogénea. A diferencia de otras zonas del océano abierto, éstos son principalmente advectados por las corrientes de la región. Podemos separar los remolinos según su tiempo de vida. Los remolinos de vida larga (más de cuatro semanas) tienen mayor amplitud y escala y tienen un ciclo estacional con un pico a finales de verano, mientras que los remolinos de corta duración son más pequeños y más presentes en invierno. La profundidad de penetración de los remolinos detectados tiene también una gran variabilidad con un valor medio de alrededor 300 m. Los remolinos anticiclónicos se extienden más profundamente en la columna de agua y muestran una forma más cónica que los ciclónicos.

Contents

Chapter 1

Motivation and objectives

Motivation

While appearing stable, the ocean is in fact an agitated fluid that never stops moving. These motions cover a wide range of spatial and temporal scales as illustrated in figure 1.1. In this figure, processes with a spatial scale from 1 mm to 10^5 km and temporal scales from 0.1 seconds to 10000 years are identified. In physical oceanography, these scales are usually separated into three categories. Large scales or synoptic scales represent the mean currents and permanent structures as well as very large (more than 500 km) and slow processes (more than 100 days). Mesoscale dynamics which dominate the variability of the ocean (Chelton et al., 2007), cover transient coherent structures that are smaller and faster than large scale structures. Finally, sub-mesoscale processes are smaller than the mesoscale and can be caused by mesoscale dynamics through frontogenesis or created by ageostrophic baroclinic instabilities (*e.g.* Molemaker et al. 2005) as well as forced motions due to atmospheric forcing (Thomas et al., 2008).

The focus of this thesis is the mesoscale structures which are omnipresent at global ocean and play a key role in multiple

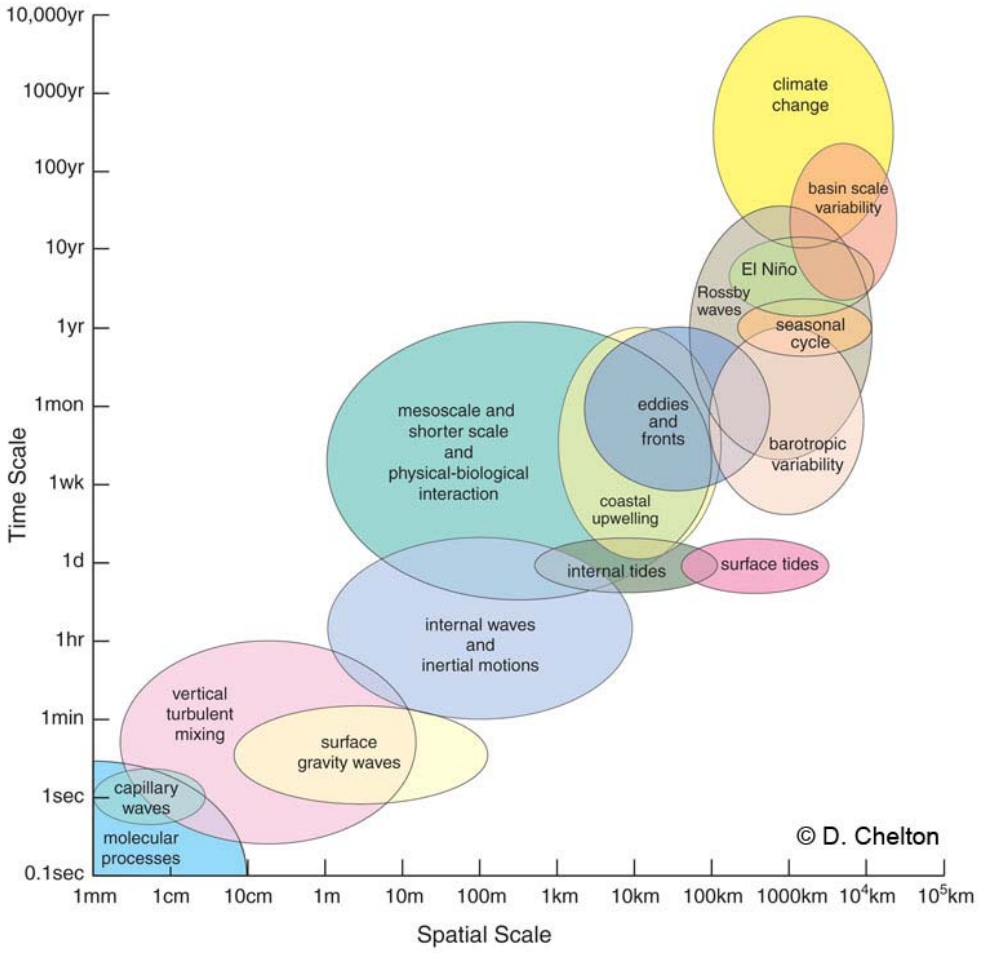

Figure 1.1: Scales of the main processes in the ocean. Courtesy of D. Chelton.

ocean processes but are not yet fully analyzed and monitored in a global scale due to their relatively small size. A useful dimensionless number which enables us to separate the mesoscale from the submesoscale, based on their dynamical properties is the Rossby number (Ro). This number is the ratio between inertial force and the Coriolis acceleration force due to the rotation of the Earth in the Navier-Stokes equations.

$$Ro = \frac{U}{Lf} \tag{1.1}$$

where U is a characteristic velocity, L a characteristic length scale and f is the Coriolis frequency *i.e.* $f = 2\Omega \sin(\Phi)$ with Ω the rotational speed of the Earth and Φ the latitude. If this

number is large (high speed or small size), inertial and centrifugal forces dominate and Coriolis forces can be neglected at the first order. If conversely, it is small, it means that the fluid is significantly affected by rotational effects and these must be included in the computations of the flow. In this case, an equilibrium is found between Coriolis forces and the pressure gradient of the fluid, and this state is called geostrophic balance. Mesoscale processes have small Rossby number ($O(0.1)$) and are sometimes called quasi-geostrophic motions as you can apply the geostrophic balance to them. This means the geostrophic currents (u_g, v_g) can be computed from the pressure (p) gradient as:

$$\begin{aligned} f v_g &= \frac{1}{\rho}\frac{\partial p}{\partial x} \\ f u_g &= -\frac{1}{\rho}\frac{\partial p}{\partial y} \end{aligned} \tag{1.2}$$

Sub-mesoscale processes which have a Rossby number ($O(1)$) cannot be described by quasi-geostrophic theory and therefore have to be separated from mesoscale processes (Thomas et al., 2008).

The Rossby number is associated with the Rossby radius of deformation, the length scale at which Coriolis forces become as important as inertial forces. An estimation of this scale is (Chelton et al., 1998):

$$Rd = \frac{1}{|f|\pi}\int_{-H}^{0} N(z)\,dz \tag{1.3}$$

with $N(z)$ the BruntVaisala frequency and H the scale height. This scale gives us the lower limit for the mesoscale structures in terms of size. The corresponding upper limit cannot be so easily defined and is usually defined to be smaller than the scale of the main currents. In this thesis and in our region of study,

the upper limit will not be defined in term of size but in term of temporal duration. Indeed, we define mesoscale processes as transient processes which separate them from the main circulation. We will see that, with our detection algorithms, it correspond to the size that is generally arbitrarily defined as the definition of mesoscale in the Mediterranean Sea.

Although mesoscale phenomena can take various forms such as vortices, meanders, rings or narrow jets, they are mainly composed of eddies. Ocean mesoscale eddies, which are at the core of the thesis, can be defined as oceanic currents flowing in a closed circulation. Mesoscale eddies are stable due to geostrophic balance such that gravitational forces are compensated by Coriolis forces.

Mesoscale eddies are ubiquitous in the ocean as observed by satellite altimeters in Chelton et al. (2007) with energy levels usually above those of the mean flow by one or more orders of magnitude. These estimations come from current velocities calculated from merchant ships (Wyrtki et al., 1976), surface drifters (Richardson, 1983) or altimetry and numerical models (Thoppil et al., 2011). High levels of Eddy Kinetic Energy (EKE), the transient part of the Kinetic Energy (KE), are found along the main fronts in the ocean (Western boundary currents such as the Gulf Stream and Kuroshio Current or the Brazil-Malvinas Confluence) as shown by Ducet et al. (2000), indicating that the most frequent mechanism for the formation of these structure can be baroclinic instability of the mean currents. This instability occurs in strongly stratified fluids where there is a vertical shear of the horizontal velocity. In these cases, the fluid can be stable (geostrophic equilibrium) but not at the lowest energy level possible and therefore, there is a supply of available potential energy. Under certain conditions, an

instability can form and there is a transfer of this potential energy to the kinetic energy of the disturbance, thereby boosting its growth. Another possible instability is barotropic instability which occurs when there is a strong horizontal shear of the current. In this case, the transfer of energy is between kinetic energy of the mean flow and kinetic energy of the instability. Oceanic mean flows have both vertical and horizontal shears which means that both instabilities can coexist.

In regions where there is no strong mean current, mesoscale eddies can be directly generated by the fluctuating wind (Frankignoul and Müller, 1979). Willett et al. (2006) have also proposed that the coastal eddies in the coastal region between southern Mexico and Panama are created by Ekman pumping associated with the wind stress curl. Finally, interactions of currents with topography can be a potential mechanism for the generation of mesoscale eddies. This is apparent in EKE maps where high energy is found near major topographic obstacles.

Because of their non-linear dynamics, eddies transport water mass with its heat content as well as chemical (e.g. salt) and biological properties (*e.g.* nutrients, biomass) over large distances (McWilliams, 1985). Their crucial role in the transport of heat fluxes has been shown in many studies (Wunsch, 1999; Jayne and Marotzke, 2002; Colas et al., 2012) but the relevance of eddy transport in the Mediterranean is still unknown. Eddy salt transport (Zhurbas et al., 2004) could be significant in the Mediterranean which is a concentration basin. Concerning biology, apart from transporting biomass (Feng et al., 2007; Llinás et al., 2008), mesoscale eddies modify the local Mixed Layer Depth (MLD), significantly enhancing primary production (Oschlies and Garçon, 1998; Levy et al., 1998; Mahadevan et al., 2012). Mesoscale eddies can also feed energy back to

the main flow and drive large scale circulation (Lozier, 1997; Holland, 1978), making them a key component of the ocean dynamics.

In this thesis, the purpose is to study mesoscale dynamics in a challenging region: the Western Mediterranean Sea (WMed). In this semi-enclosed basin, the Rossby deformation radius is relatively small: 10-15 km (Robinson et al., 2001) and therefore mesoscale structures vary in size from 10-15 km to 150 km. As explained above, the upper limit here is the one usually given but was also confirmed by our analysis of mesoscales defined as non permanent structures. Figure 1.2 (extracted from Beuvier et al. 2012) shows the Rossby radius (Ro) that is computed from the MEDATLAS database (MEDAR Group et al., 2003) following the equation 1.3. In the WMed, we see that Ro ranges from 6 km at the south-eastern coast of France to 15 km north of the Algerian shore. Over shallow shelves such as in the Gulf of Lion, it is even smaller at around 3 km.

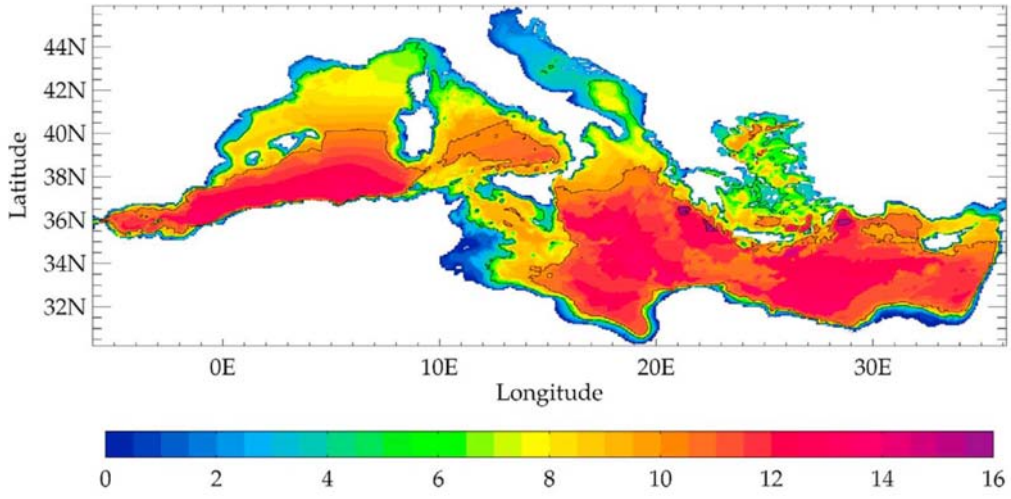

Figure 1.2: First Rossby radius of deformation (km, contours every 5 km), computed from the MEDATLAS database state representative of the end of the 1990s and from the bathymetry of NEMOMED12. Figure extracted from Beuvier et al. (2012).

Objective

This small Rossby radius has prevented a systematic monitoring of mesoscale activity in the WMed region. Indeed, sparse in situ data or crude model simulations have not been enough to obtain a statistical robust and homogeneous picture of mesoscale activity.

Therefore there are still some crucial scientific issues associated with WMed eddies. First, there is the characterization of mesoscale activity in the region. What are its magnitude, its spatial patterns and temporal variability? How are these mesoscale structures in terms of size, intensity and anomalies in density which they provoke? Then questions about the formation of these mesoscale eddies in the WMed are still unanswered and work is still needed to understand the role of wind, topography or instabilities of currents. Finally, we lack an evaluation on the impact of mesoscale activity on large scale processes, heat and salt fluxes, and biological mechanisms. All these question are inter-connected and are critical if we want to predict the evolution of mesoscale processes and their impact on ecosystems.

Some of these questions have been answered in part by the community using the available tools in terms of observation and numerical modelling which we describe in chapter 2. Yet, these tools are not enough to fully understand mesoscale in the Western Mediterranean and to try and begin to answer some of these questions, we will develop new tools to study the mesoscale in the WMed. These new tools will need datasets with resolution high enough to monitor mesoscale eddies in the region. The increasing computing power available for numerical modelling enables the design of continuously higher reso-

lution simulations that can now approach the full resolution of mesoscale dynamics. Therefore, new high resolution, long-term, simulation of the WMed that is eddy-resolving is developed toward this specific goal. Its implementation is described in chapter 3 and its outputs are analyzed and validated in chapter 4, with the objective of representing mesoscale activity in the region of study well. High resolution observational data is an excellent complementary source of information that can be used in combination with the model outputs. In this idea, we attempt to improve existing satellite altimetry gridded maps which now cover a relatively long period of time (1992-2012) with the focus on better resolving mesoscale dynamics in chapter 5. Then, automatic eddy detection and tracking algorithms of eddies helps us to characterize mesoscale eddies in the region. These algorithms are applied on satellite altimetry maps, the high resolution model and a lower resolution model outputs in chapter 6. These tools allow us to shed some light on the characterization of the mesoscale dynamic, the first scientific issue stressed above. The spatial and temporal distribution of mesoscale eddies is determined as well as physical characteristics of the eddies. Some hypotheses on the formation processes and the influence of wind are examined but more study is required and the tools we develop will help in this endeavor. The impact of mesoscale activity is studied with the help of the models but the issue is still a work in progress.

Chapter 2

The Western Mediterranean Sea

Contents

The Mediterranean Sea is a relatively small sea but with huge importance because of several factors. First, it is the birthplace of several major civilizations and thus people started studying it a long time ago. During a very long period of time, the Mediterranean was the main mean of transport for goods and people in the region. It is now suffering strong anthropogenic pressure due to the density of human population living along its coasts and it is crucial to study and understand the impacts of this pressure (Hulme et al., 1999).

What also makes the Mediterranean Sea unique and valuable for scientists is that many fundamental processes that occur in the global ocean happen there at a smaller scale. That is why it is often called a miniature ocean (Bethoux et al., 1999). The dimensions and mid-latitude location of the Mediterranean makes it easier to study and sample. Examples of such processes are deep convection (Herrmann and Somot, 2008), cascading, thermohaline circulation and water mass interactions (Wüst, 1961), baroclinic instabilities (Millot, 1987), transport through small straits and mesoscale activity (Robinson et al., 2001).

Finally, the Mediterranean Sea is a concentration basin, as there is more evaporation than precipitation at the surface. Therefore, there is a formation of salty water called Mediterranean Water (MW) that enters the Atlantic, participates in the circulation of this ocean and consequently impact on the global thermohaline conveyor belt (Broecker et al., 1991). Potter and Lozier (2004) reported the impact of the warmed up MW on the Atlantic heat content and therefore on the climate at mid-latitudes. The MW then propagates far north until the Norwegian-Greenland Sea as described by Arhan (1987) where it can influence the deep water formation (Schmitz Jr, 1996; Iorga and Lozier, 1999) or directly impacts them on their re-

turn circulation as proposed by Keeling and Peng (1995).

2.1 Geography

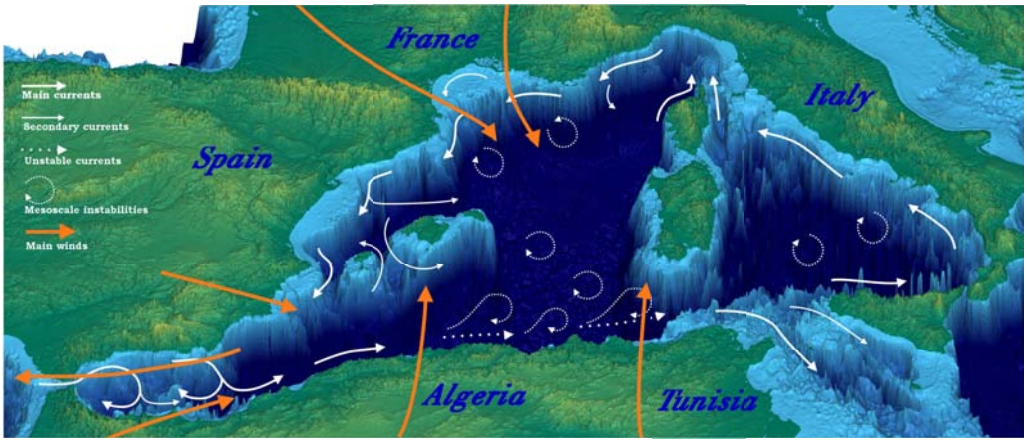

Figure 2.1: An overview of the Western Mediterranean

The Mediterranean Sea is an almost enclosed sea between 5°W and 36°E in longitude and 30°N and 46°N in latitude with a total area of 3,000,000 km^2. It separates Europe from the African continent.

The narrow (22 km) and shallow (300 m) Gibraltar Strait at the south of Spain connects the Sea with the Atlantic Ocean. The Mediterranean Sea is composed of two main basins linked by the Sicilian Strait: the Eastern Basin and the Western Basin.

The Western basin (hereafter WMed) which is the focus of this thesis is shown on figure 2.1. It is composed of various sub-basins : the Alboran Sea, the Algerian basin, the Balearic Sea, the Liguro-Provencal basin and the Tyrrhenian Sea. As shown on the figure, the topography is rugged and the coastlines are jagged.

To study the WMed, it is useful to separate the basin into different regions according to their general circulation patterns. Figure 2.2 shows these regions defined by Manca et al. (2004)

that we will use in this thesis.

2.2 Forcings

The Gibraltar Strait forcing is crucial to the Western Mediterranean circulation as it is the source of fresh water that will feed the entire Mediterranean thermohaline circulation. The transport through the strait has three components: two mostly barotropic components and a baroclinic one. The first barotropic component is tidal induced with velocities of about 2.5 $m.s^{-1}$. The other one is due to atmospheric difference of pressure over the Mediterranean (Gomis et al., 2006) creating velocities of about 0.4 $m.s^{-1}$ (Candela et al., 1989). The long-term baroclinic component is driven by the water budget of the Mediterranean which is a concentration basin and thus needs some input from the Atlantic, inducing velocities of about 0.5 $m.s^{-1}$. Astraldi et al. (1999) made a review on the estimated transport through the strait from observation up to 1999 but the estimates vary greatly depending on the method used to compute it. The methods can be direct measurements or indirect computations by the Mediterranean budget, hydrodynamic properties of the strait or computation of geostrophic balance. The uncertainty about these estimates also comes from the fact that most of them are computed from short data series (less than 1 year) or have strong assumptions. Estimates of the Atlantic inflow range between 0.72 and 1.60 Sv (1 Sv = 10^6 $m^3.s^{-1}$), the outflow ranges between 0.80 and 1.68 Sv and the net exchange is of the order of tenths of Sv. More recently, using in-situ observations Soto-Navarro et al. (2010) measured the outflow at -0.78 $\pm$ 0.05 Sv and the resulting inflow at 0.81 $\pm$ 0.06 while Criado-Aldeanueva et al. (2012) estimated the inflow

to be around 0.82 ± 0.05 Sv. The transport in the Gibraltar Strait has also been studied using numerical models such as the work by Beranger et al. (2005) or Sannino et al. (2009).

The high mountain chains around the basin (Pyrenees, Alps, Atlas) constrain the lower atmospheric layer and create very strong local winds that flow over the Mediterranean. These winds, in the western part of the basin, can come from the north such as the Tramontane, Mistral and Bora, or from the south such as the Sirocco (figure 2.1). The circulation in the Mediterranean Sea is strongly constricted by these local winds but interconnections with large scale atmospheric forcings have been found (Xoplaki et al., 2004; Josey et al., 2011).

Northerly winds bring cold and dry air above the sea, causing strong evaporation and therefore latent heat loss. This effect is the dominant one in the Mediterranean whose net water and heat flux is negative. This loss is compensated at the Gibraltar Strait by the water and heat transport described above where a little warmer and fresh Atlantic waters enter the Mediterranean Sea. With in-situ observations from moored instruments Macdonald et al. (1994) estimated the heat transport into the Mediterranean through the strait at 5.2 ± 1.3W.m^2. Other authors gave estimations ranging from 5 W.m^2 (Bunker et al., 1982) to 8.5 W.m^2 (Bethoux, 1979). A more complete budget of the area with more that 40 years of reanalysis is given by Ruiz et al. (2008). They confirmed the importance of latent heat in the budget and gave new estimates of the different terms. In the Western Mediterranean, they show that the heat budget is actually positive which means a heating of the Sea with a value of 5 W.m^2 in the basin whereas the whole basin has a net heat flux of -1 W.m^2.

Estimation of the loss of water is more uncertain due to

the difficulties to have good estimates of the evaporation and precipitation fluxes. (Bethoux, 1979) gives a value of -0.95 m.year^{-1} on the surface of the Mediterranean Sea (2.5 10^{12} m^2). Since then many authors have taken on the task of estimating these fluxes for the whole Mediterranean basin, Bryden et al. (1994) made a review of these estimates ranging between 0.47 m.year^{-1} and 1.31 m.year^{-1}. This water loss is compensated by the net water coming into the Mediterranean at the Gibraltar Strait.

Another external influence on the Mediterranean Sea is river inflow. In the WMed, the main rivers are the Rhône (mean discharge : 1710 m^3.s^{-1}) and the Ebro river (mean discharge : 426 m^3.s^{-1}). These discharges are not trivial as the Rhône, for example, injects the equivalent of 0.02 m of water to the surface of the whole Mediterranean Sea per year (Tomczak and Godfrey, 2001). This is to be compared to precipitation values of around 0.34 m.year^{-1} and E-P-R around -1 m.year^{-1}. Bethoux and Gentili (1999) also show that Mediterranean rivers could play an important role in climate by studying the trends in salinity and temperature in the basin and linking these trends to changes in the river inflow.

2.3 General circulation and water masses

2.3.1 Surface circulation

The general surface circulation of the Western basin is mainly driven by the wind forcing in Sverdrup balance (Pinardi and Navarra, 1993; Molcard et al., 2002). This is shown in figure 2.1 and has been described by Millot (1999). Entering the WMed from the Gibraltar Strait to compensate the deficit of water

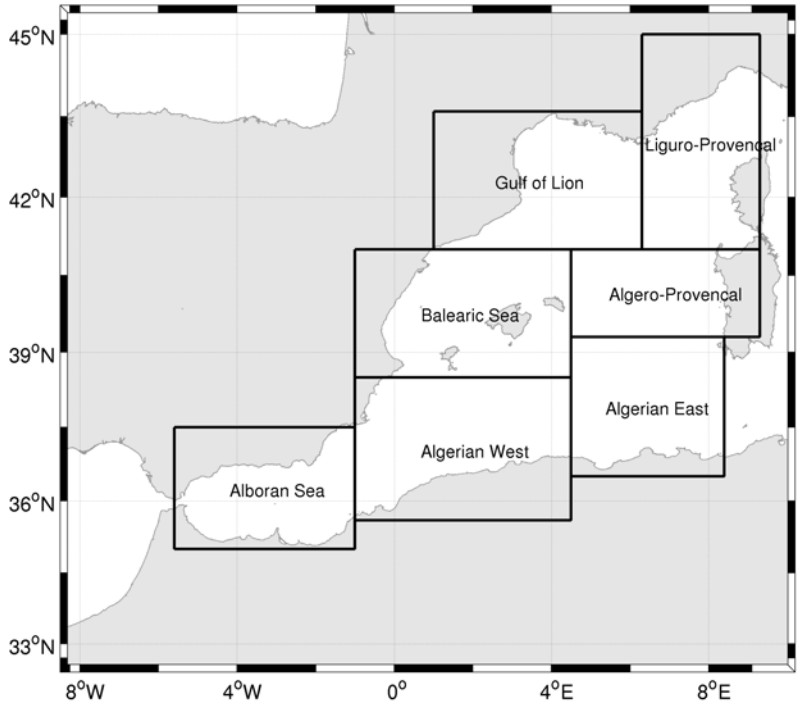

Figure 2.2: Different areas of the WMed as defined by Manca et al. (2004)

due to the wind-induced high evaporation, fresh Atlantic Water (AW)[1] forms the Atlantic jet. This strong current meanders through the Alboran gyres, the quasi permanent Western Alboran Gyre (WAG) and the intermittent Eastern Alboran Gyre (EAG). It then becomes the relatively narrow Algerian Current, flowing along the coast at first but becoming less clearly defined nor narrow as it progresses eastward. This is due to baroclinic instabilities that cause meanders and, eventually, eddies that detach from the main current (Olita et al., 2011).

In the Tyrrhenian Basin, west of Corsica and Sardinia, the circulation is mainly cyclonic over the entire water column (Millot, 1987). Rinaldi et al. (2010) argue that the circulation

[1]The acronyms for the water masses in the Mediterranean follow the convention decided by the CIESM round table in Monte Carlo, 26 September 2001

is more complex, with wind-driven cyclones in the northwest Tyrrhenian (Marullo et al., 1994) that are coupled with an anticyclonic gyre in the center of the basin.

In the Northern part of the basin, the main current is the Northern current which flows westward along the French coast in the Ligurian Provençal Basin, the Gulf of Lion and then the Spanish coast in the Balearic Sea. It is stronger and closer to the coast in winter while weaker and broader in summer due to its meanders (Conan and Millot, 1995; Birol et al., 2010). The current then splits into two branches, one going back along the Balearic northern shore (Ruiz et al., 2009a; Mason and Pascual, 2013) and the other flowing southward through the Ibiza channel (Pinot et al., 2002).

This description of the general surface circulation is in agreement with the synthetic Mean Dynamic Topography (MDT) derived by Rio et al. (2014) (figure 4.1) which was obtained by combining hydrological profiles, model outputs, altimeter observations and drifting buoy velocities. Global circulation models have been shown to be able to reproduce correctly this circulation as shown by Vidal-Vijande et al. (2012) but they lack the resolution to reproduce mesoscale features.

2.3.2 Water masses

Apart from the AW at the surface, whose origin, characteristics and circulation we have already described, there are several more characteristic water masses in the WMed (Nielsen, 1912). The Mediterranean Sea has several sites of convection where, in winter, cold and dry winds evaporate already denser water and create vertical mixing more or less deep that generate dense waters.

The north of the Levantine basin is one of them. There, a layer 300-500m deep of salty water called Levantine Intermediate Water (LIW) is formed in winter under the action of northerly winds (Robinson et al., 1991). In summer, the surface layer warms up but the LIW stays at depth (200-400m) and spreads to the whole Mediterranean marking a maximum of salinity at these depths. After passing the strait of Sicily and going northward along the Italian coast, some of the LIW goes through the Corsica strait between Corsica and France to follow the path of the Northern current at depth. Yet the majority of these waters flows southward along the eastern coast of Corsica and Sardinia and enter our area of study through the Sardinia strait where they bifurcate northward to join the rest of the LIW at the southern coast of France (Millot, 1999).

The other main convection site is the Gulf of Lion where the Western Mediterranean Deep Water (WMDW) is formed (Marshall and Schott, 1999). The process is separated into the preconditioning phase where the cyclonic circulation in the Gulf of Lion intensify bringing interior waters that are less stratified to the surface ("doming") and increasing the inflow of salty LIW waters. Surface waters are also getting denser due to loss of temperature and water due to atmospheric forcings (evaporation). Then, strong cold and dry winds events coming from the north induce loss of buoyancy that destabilizes the water column and create powerful vertical mixing which can reach the bottom of the basin. The WMDW created then spread at the bottom of the basin as observed by Send et al. (1996) forming the bottom layer of the water column in the WMed.

When the conditions are not sufficient to trigger the deep convection, the cooling induces nonetheless a mixing of the surface layer with the high-salinity LIW which form the Western

Intermediate Water (WIW), both cooler and fresher than the LIW and therefore placed above it (Send et al., 1999). This water mass, first described by Salat and Font (1987), is advected southward by mode water eddies in the Northern Current (Pinot et al., 2002). In a recent study, Juza et al. (2013) described the formation and spreading of the WIW using a high resolution model of the WMed. They showed that this water mass can propagate southward into the Alboran Sea where it is detected as a minimum of potential temperature.

2.4 Mesoscale dynamics

In the Western Mediterranean Sea, mesoscale activity is present albeit rather inhomogeneous as shown by the levels of EKE in altimetry data (Pujol and Larnicol, 2005) but also drifter data (Poulain et al., 2012). As explained in the Introduction (chapter 1), the Rossby radius is relatively small in this region which makes studying the mesoscale difficult and hence reveals the need for high resolution datasets. This explains why the most of the mesoscale dynamics of the basin have started to be described only recently.

Small mesoscale features are difficult to observe but large ones such as the Alboran gyres or the Algerian eddies have been thoroughly studied through, firstly, ship-based hydrographic cruises and, later with the help of satellite sensing or autonomous vehicles (gliders). The development of higher resolution or better spatial and temporal coverage datesets have allowed to steadily improve our knowledge of the mesoscale in the WMed. However, still most of the knowledge we have of the mesoscale in the region comes from localized surveys or simulations that describe specific eddies or low resolution models

that can only resolve the larger eddies.

2.4.1 Alboran Sea

As presented in section 2.3, the Atlantic inflow that goes through the Strait of Gibraltar forms two large anti-cyclonic gyres at the entrance of the Mediterranean Sea (Vazquez-Cuervo et al., 1996; Viúdez et al., 1996; Allen et al., 2001). Even though these structures were known about for a relatively long time, the more recent satellite data have helped to better understand the dynamics of these mesoscale gyres.

Using extensive in-situ profiles as well as Sea Surface Temperature (SST) from satellites, Viúdez et al. (1996) made the first accurate description of the gyres. Then, with more in-situ data (moorings, current meters, tide gauges) and more satellite-based SST, Vargas-Yáñez et al. (2002) described two different regimes for the circulation in the basin, one with only the WAG in winter-spring and one with the two gyres in summer-autumn. This study was completed by Renault et al. (2012) who studied the annual and interannual variability of the gyres from altimetry maps. Ship measurements allowed Allen et al. (2001) to characterize the hydrography and vertical velocities in these gyres.

Using a combination of in-situ data, SST from satellites and satellite altimetry, Flexas et al. (2006) discovered a migration of the WAG and discussed some hypotheses for its migration. In July 2008, an experiment described by Ruiz et al. (2009b) involving new glider technology that helped to calibrate altimetry data in the eastern Alboran Sea was used to evaluate vertical velocities in the gyres. Combining the high resolution hydrographic data from the glider and satellite altimetry they

were able to estimate the vertical exchanges to be about 1 m per day in the gyres.

Recently, Peliz et al. (2012) made a realistic high resolution (2 km) simulation of the basin and used it to study the mesoscale dynamics (Peliz et al., 2013). They confirmed the two modes described by Renault et al. (2012) and examined the WAG migration and its impact on the transition between the two regimes. A study on the mesoscale eddies in this region was also conducted where they found that the generated eddies were small (mean radius of 13 km), short lived (less than 3 weeks), more likely to be cyclones and they were generated preferably when the two gyres were not present. The eddies were found to be generated mostly by instabilities of the jet and strong currents along the shore and at the Strait of Gibraltar.

2.4.2 Algerian Basin

The Algerian basin is located at the south of the WMed along the Algerian coast and can be separated into a western and an eastern part (see figure 2.2). In this region, the Algerian current is highly unstable and the circulation is dominated by strong and large mesoscale eddies (Olita et al., 2011). Such mesoscale eddies, known as Algerian Eddies have been observed since the 1970s (Katz, 1972; Burkov et al., 1979) and have been described from in-situ data from oceanographic cruises (Benzohra and Millot, 1995) or drifting buoys (Font et al., 1998). The launch of earth observing satellites enabled an easier observation of these structures as well as the possibility to follow them using satellite infrared images (Millot, 1985) or altimetry (Ayoub et al., 1998). The combination of these datasets with

other sensors like drifting buoys (Salas et al., 2002; Font et al., 2004) showed the reliability of the satellite sensors and their potential to describe these large mesoscale eddies. Their influence on biology has also been studied using cruise data (Morán et al., 2001). With an extent that can reach 1000 m as observed by Ruiz et al. (2002), these features have diameters of about 100-200 km and their lifetime ranges from several months up to 3 years (Puillat et al., 2002).

Algerian eddies usually follow the main eastward flow, from which they obtain energy, until they detach from the coast and drift northward where they eventually arrive in the center of the basin. There, they tend to go westward and may go back into the Algerian current and thus make a loop (Puillat et al., 2002). When the eddies detach from the Algerian coast, they transport water mass properties northward instead of eastward by the current. Isern-Fontanet et al. (2004) used altimetry in combination with hydrographic data from cruises to describe the spatial 3D structure of these large anticyclonic eddies.

The Algerian mesoscale eddies are usually generated as a result of baroclinic instability (Millot, 1985; Beckers and Nihoul, 1992).

2.4.3 Algero-Provençal basin

In the Algero-Provençal basin, there are no well defined mean currents. However, maps of altimetry derived EKE (see figure 4.15) show that transient features are common.

In this part of the WMed, mesoscale activity is mainly associated with the large Algerian eddies that formed from the instabilities of the Algerian current that goes northward into this basin. There are also anticyclones called Sardinian ed-

dies that are at an intermediate depth, formed by intermediate water coming westward from the Sardinian Strait and going northward along the Sardinian coast. These are generated at 39°N and travel westward; their signature is difficult to differentiate from Algerian eddies without in-situ measurement of the characteristics of the eddy cores (Testor et al., 2005).

2.4.4 Liguro-Provençal basin and Gulf of Lion

The main permanent characteristic of the Liguro-Provençal basin and Gulf of Lion is the Northern current. Mesoscale activity has been observed in this region (Robinson et al., 2001) with a strong increase in autumn (Font et al., 1995). The Northern Current has been shown to make intrusions on the shelf which are responsible for exchanges between open waters and the shelf (Petrenko et al., 2005). Millot et al. (1980), with meteorological data from a station and satellite infrared images, determined the role of south-easterly winds in these intrusions. Analysing an improved coastal along-track altimetry product in the gulf, Bouffard et al. (2011) was able to observe these features in altimetry data which allows a better monitoring of them.

On the western part of the current, anticyclonic mesoscale eddies have been detected by hydrological and current meter observations (Estournel et al., 2003; Millot, 1982). A project called LATEX, combining data from an inert tracer release (SF6), Lagrangian drifters, satellites and Eulerian moorings with numerical modelling, was initiated in 2008 to study these mesoscale dynamics. Results from the model (Hu et al., 2009), as well as the other sensors (Hu et al., 2011) give an improved picture of the mesoscale activity in this area. An anticyclonic eddy lasting at least 50 days was observed with a radius of

about 20 km, similar to what had been also observed in 2001. With the help of the high resolution (3 km to 1 km) model, the death of the eddy was linked to its interaction with the Northern Current while its formation was hypothesized to be due to the combined effect of strong Tramontane winds and the Northern Current (Millot, 1982; Hu et al., 2009).

Rubio et al. (2009) used a high resolution regional model of the North-western Mediterranean Sea to study the generation and evolution of eddies in this basin. They found two different sites of eddy formation : near the city of Marseilles and at the same place as the LATEX experiments (Roussillon site). In the Marseilles site, the generation of eddies is related to the current that separates from the coast and creates eddies from barotropic instabilities. In the Roussillon site, the separation of the current is also the origin of the eddies but the wind also plays a role and the generation of the eddies is a combination of barotropic and baroclinic instabilities. (Garreau et al., 2011) using another high resolution model explained the generation of the LATEX eddies and also how they are linked to offshore eddies propagating in the Catalan seas.

2.4.5 Balearic Sea

In the Balearic Sea, the general circulation (Font et al., 1988) is composed of the Northern Current flowing along the Catalan coast that then separates in two branches, one going through the Ibiza channel (Pinot et al., 2002) and the other recirculating into the Balearic Current, which flows eastward along the Northern shore of the Balearic Islands (Mason and Pascual, 2013). This circulation is modulated by mesoscale activity that, at first, was underestimated (La Violette et al., 1990) but later

was found to be similar to the Algerian current (García et al., 1994).

In the Balearic Current, many studies have shown the existence of mesoscale structures by analysing satellite data, drifting buoys, oceanographic cruises or gliders (*e.g.* Pinot et al. 1995; Ruiz et al. 2009a; Bouffard et al. 2010). In particular, Pascual et al. (2002) used SST data from satellites as well as SLA from altimetry to infer the formation, life and decay of a strong anticyclone north of Mallorca that blocked the usual circulation in the Balearic Sea. A smaller anticyclonic eddy was also found in this area by Pascual et al. (2010) in 2009 during a multi-sensor experiment. More recently, Amores et al. (2013) used a mooring to describe the characteristics of an eddy appearing in the same area. The eddy evolved from a front detected and described by Balbín et al. (2012) using Conductivity Temperature Depth (CTD), satellite and mooring data. The size of these eddies ranged between 15 km (Pascual et al., 2010; Amores et al., 2013) and 100 km (Pascual et al., 2010).

The formation of such eddies has been hypothesized to be due to instabilities of the Balearic Current, the formation of a meander and then a coherent vortex (Amores et al., 2013) for the smaller eddies. Direct action of the wind can also transmit anticyclonic vorticity from the negative curl associated with the shear of the Mistral downstream of the Pyrenees forming the larger eddy as proposed by Pascual et al. (2002) and Mason and Pascual (2013).

2.5 Recent advances in modelling and global observations of the mesoscale in the WMED

2.5.1 Observing systems

As stated earlier, the Mediterranean Sea is an area that has been intensively investigated due to its unique location and importance for a large population. The mesoscale dynamics can be and have been investigated by very diverse observing systems.

2.5.1.1 Ships surveys

First, there are the regular ship cruise campaigns that can be designed to observe the mesoscale by doing high density CTD sampling in small areas allowing the construction of a 3D image of the ocean state. As an example, in a campaign in May 2009, Pascual et al. (2010) were able to study an eddy event occurring at the north shore of Mallorca. The dynamic height computed from the ship CTDs allows a reconstruction of this eddy which was also detected in SST from satellite, drifter data and gliders. Another example is the LATEX campaign mentioned earlier in which the combination of ship measurements consisting of Acoustic Doppler Current Profiler (ADCP) and CTD sensors as well as SST satellite images and Lagrangian drifter trajectories detected the presence of an eddy and enabled the study of its characteristics described in Hu et al. (2011). However, these cruises are costly and can only sample a small area of the ocean over a given time, as a larger area means lower sampling density or high inhomogeneity in time. Such cruises are useful to study a particular mesocale eddy or structure.

2.5.1.2 Surface drifters

Lagrangian floats are an inexpensive and convenient tool to study surface currents. They are buoys with a drogue at about 15 m depth that passively follow the horizontal flow at the surface. Their position is known via satellite and they can carry temperature or air pressure sensors. They can be deployed easily in high numbers and can provide information for large spatial domains. Poulain et al. (2012) compiled and analyzed a database of these drifters in the Mediterranean to study the mean circulation and energy. Despite these advantages, due to their nature, drifters cannot be controlled and the sampling is highly inhomogeneous. These drawbacks preclude a global analysis of the mesoscale from drifter data.

2.5.1.3 Moorings

Moorings with temperature, salinity or current sensors produce a very high temporal resolution view of the water column. These time-series have the temporal resolution (less than an hour) to detect mesoscale and sub-mesoscale dynamics and have successfully been used to describe mesoscale eddies such as the work by Amores et al. (2013) or Zhang et al. (2013). Amores et al. (2013) studied data from a mooring north of Mallorca revealing the passage of an eddy that affected the whole water column for one month. The analysis of the data showed that the eddy's core was formed by WIW. However, the observational data provided by this sensor is limited to a single point in space and therefore can only describe temporal and, to a more limited degree vertical variability. It has to be combined with other observing systems as it is too limited for a regional monitoring of the mesoscale.

2.5.1.4 Gliders

Underwater gliders are autonomous vehicles with various sensors (CTD, oxygen sensor, chlorophyll,...) that can sample 2D fields with high spatial resolution (1 km) down to depths typically around 1000 meters along a previously defined sawtooth trajectory. They can be deployed to efficiently sample the mesoscale activity within a predefined area as shown by L'Hévéder et al. (2013) in an Observing System Simulation Experiment (OSSE). However, gliders are expensive and only cover relatively small areas for a limited time. The data from a glider in combination with along-track altimetry enabled Bouffard et al. (2010) to describe an intense mesoscale eddy found in the Balearic Sea. Heslop et al. (2012) used a repetitive sampling of the Ibiza Channel to characterize the transport and the mesoscale activity in the strait. The dataset provided very useful information but the temporal resolution was still not sufficient to fully characterize the mesoscale.

2.5.1.5 Coastal radars

High frequency (HF) radars measure wave heights but also surface currents by measuring the Doppler shift of the Bragg scattering of the radar signal. Positioned in coastal areas they are adequate to monitor mesoscale activity providing a high spatial (3 km) and temporal (20 minutes) resolution view of the currents (Quentin et al., 2013). However, HF radar ranges are limited (50-100 km) and thus they are only viable for coastal studies.

2.5.1.6 Observatory centers

As all these observing systems have different strengths and weaknesses, high quality information can be extracted from the combination of multiple sensors (Pascual et al., 2010; Ruiz et al., 2009a). However, such studies tend to be local and cover short periods of time. Two main observatory centers, located in the Western Mediterranean are dedicated to the continuous monitoring of the basin: MOOSE (Mediterranean Ocean Observing System for the Environment) for the Northern part of the basin and SOCIB (Sistema d'observació i predicció costaner de les Illes Balears) for the Balearic Sea. These observatory centers aim to develop a network of observations combining all the observations cited above and their objective is to make the data easily available for the user. The MOOSE network comprises two HF radars located at the south of France, gliders which sample regularly two transects in the Gulf of Lion, at least two deep moorings in the region, coastal stations of meteorology and regular ship campaigns. The SOCIB facility has a HF radar on the Ibiza and Formentera islands, several gliders which regularly sample the Ibiza Channel and also perform one-time missions (Troupin et al., 2014), drifters that are launched for campaigns, an oceanographic ship and an operational forecast model of the Western Mediterranean Sea at 1/32°. Efforts made with these initiatives greatly improve our knowledge of the Mediterranean Sea and its dynamic at various scales including mesoscale. Still, these observation systems are not suited for our goal of a systematic characterization of the region which need a relatively homogeneous spatial and temporal coverage at high resolution.

2.5.1.7 Satellite observations

In order to make synoptic observations of mesoscale activity in the Western Mediterranean, remote sensing data from satellites is a promising alternative as it provides very good spatial coverage and temporal frequency. Two broad type of sensors are placed on these satellites, radiometers (passive sensor) and radars (active sensor). They have to work at wavelengths that are not absorbed by the atmosphere and therefore the spectral bands available are visible/near infrared (ocean color), thermal infrared (SST) and microwaves (microwave radiometry for SST, radars for Sea Surface Height (SSH)). Images from visible/near infrared and thermal infrared have high spatial resolution and have been used in many studies, many of them which we already described in the previous section. Yet, these datasets have two main limitations. First, the observed quantity is only a tracer and for SST, not a passive one which means that the motions can not be directly recovered. Methods have been constructed such as the one proposed by Vigan et al. (2000) to compute velocities from SST data but they are not completely reliable. Gaultier et al. (2013) proposed an innovative approach combining these images with radar altimetry from satellite to generate high resolution altimetry data. Yet this method is also limited for our objectives by the second limitation of these datasets, which is the fact that they are sensitive to cloud coverage. When there are clouds in the area, the ocean color or SST information cannot be retrieved, preventing the consistent analysis we want to perform. Microwave radiometry are not affected by clouds and thus provide an homogeneous coverage of the ocean but it has a much coarser resolution of about 50 km (Wentz et al., 2000) which is not sufficient to study mesoscale

in our region. The last available remote sensing dataset is then radar sea surface height from altimetry that we used in our study and will describe below.

2.5.2 Altimetry

2.5.2.1 Along-track data

Radar altimeter from a satellite allows to observe the dynamic topography of the ocean or SSH by calculating the propagation time of a transmitted signal and then the distance R between the satellite and the sea. The SSH is deduced by knowing the satellite distance to an ellipsoid reference (S) and the geoid distance to this ellipsoid (h_g): :

$$\eta = S - h - h_g \tag{2.1}$$

The value of S is determined by the combination of several locating systems like the Global Positioning System (GPS) or the Doris system, a network of 50 ground beacons, worldwide, transmitting to the satellite which use Doppler shift to accurately know its velocity and then its position by dynamic orbitography models.

The Earth's geoid is the SSH without any disturbance (current, tide, wind,...) only due to difference of gravity. Estimating this geoid has been the goal of two satellite missions, first GRACE (Gravity Recovery and Climate Experiment) launched in 2002 and GOCE (Gravity field and steady-state Ocean Circulation Explorer) launched in 2009. GRACE data has a horizontal resolution of around 500 km (Tapley et al., 2003) for the geoid which is not enough for our purpose. GOCE has a higher horizontal accuracy of 100 km but is still not sufficient for mesoscale in the WMed. The solution to this limitation has

been to substract the temporal mean of the observed SSH to obtain the Sea Level Anomaly (SLA) which is the time evolving part of the SSH. The SSH is then reconstructed by adding the MDT, the mean value of the SSH, to the SLA in order to obtain the total height of the sea surface. A description of how the MDT is computed for the Mediterranean is presented in section 4.2.

Several corrections need to applied to the raw signal in order to use it for geophysical applications. The first corrections are applied in order to correct the errors due to the signal atmospheric propagation.

- **Ionosphere :** When the signal passes through the ionosphere (70 km to 1000 km), its speed is reduced due to dispersion which imply an error in the distance $\delta R = \frac{A}{f}$ with A a value characteristic of the state of the ionosphere and f the frequency of the signal. Since δR depends on the frequency, the solution is to send 2 signals with different frequency and the difference in the measured distance allows to find the value of A. The positioning system (Doris) can be used in complement as it measures the correction between the satellite and a station on Earth.

- **Wet troposphere :** The troposphere contains large quantities of water which induce a delay of the signal. Since the medium is not dispersive, the corresponding error of distance does not depend on the frequency and we cannot use the same method as for the ionosphere. The water vapor corrections are made based on multi-frequency microwave radiometers.

- **Dry troposphere :** Other gases such as nitrogen or oxygen can modify the propagation of the signal in the tropo-

sphere. For these corrections, a meteorological model of the area is used to estimate the correction.

Then, corrections directly linked to the geophysical application of the user are applied.

- **Sea state bias :** When the signal arrives to the sea surface, it is reflected both by wave troughs and wave crests but dispersion at wave crests is stronger due to the convexity of the surface (Fu et al., 1994). The signal has therefore a bias towards troughs and is corrected with an estimation of the sea swell by the dispersion of the return signal (Gaspar et al., 1994).

- **Tides :** The tide signal is removed from the raw signal with a tide model.

- **Inverse barometer :** Variations of atmospheric pressure over the ocean create a variation of the SSH. Since these variations are not related to the oceanic circulation, this effect is removed for low frequencies by an inverse barometer correction based on surface pressure fields from atmospheric models. For the high frequencies variations, the MOG2D barotropic correction (Carrère and Lyard, 2003) is used which takes into account wind and pressure effects from the European Centre for Medium-Range Weather Forecasts (ECMWF) analysis. MOG2D correction has been shown to improve representation of high frequency effects on sea level (Pascual et al., 2008).

Finally correction of the orbit errors have to be accounted for. A global multi-mission crossover minimization is performed as proposed by Le Traon and Ogor (1998) on the data.

2.5.2.2 Gridded fields

The raw information given by the satellite is the SLA along its track which is then optimally interpolated to produce the 2D maps containing the signature of mesoscale eddies (Le Traon et al., 1998) (see section 4.2 for a description of the dataset in the Mediterranean).

On figure 2.3, the satellite missions that can be used in the interpolation are summarized. These altimeters are on 3 different types of orbits with different repeat period and distance between neighboring tracks. The Geosat missions have a repeat period of 17 days and a distance between tracks of 1.45°or 125 km at the Mediterranean latitude, then ERS/ENVISAT satellites have a longer period of 35 days and a small distance inter-track of 0.7°or 60 km, finally TOPEX/Poseidon and Jason altimeters have a short period of 10 days but a high inter-track distance of 2.8°or 240 km. As indicated in figure 2.3, the number of satellites available for the Optimal Interpolation (OI) is not the same throughout the 1992-2012 period with, for example, high density (four satellites) between 2002 and 2005 and lower density (two satellites) between 1992 and 2000. The density of tracks in the Mediterranean for the two configurations is shown in figure 2.4. In the worst case (two satellites), we see that the distance between two tracks is irregular and can be quite large (reaching 100 km) but in the best case (four satellites), the distance between the track is much smaller and the distance between one point and the nearest track does not exceed 50 km. In figure 2.5, we present the evolution of this distance over the WMed, it shows that even though the satellite constellation changes, the distance stays below 50 km for 90% of the domain.

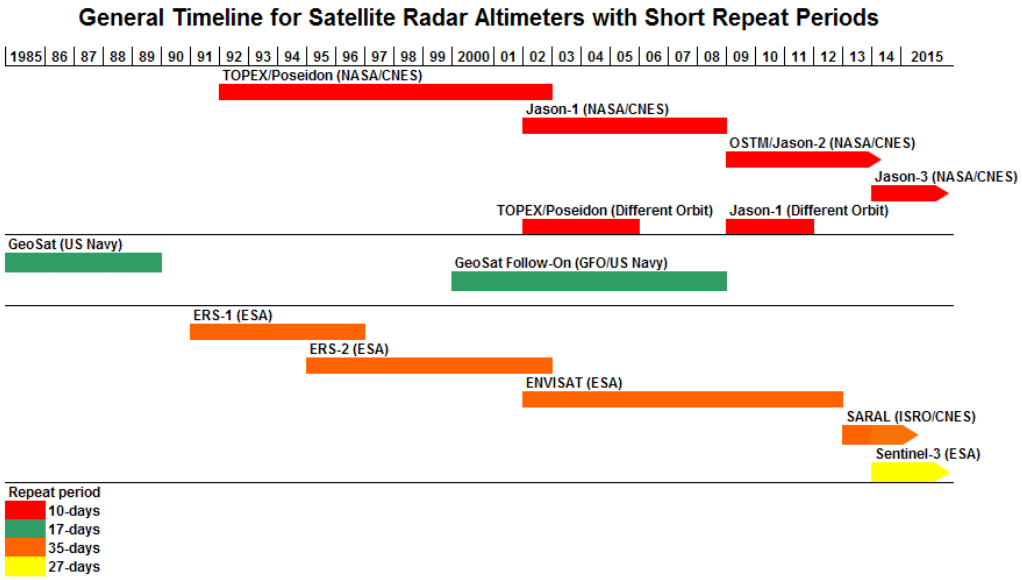

Figure 2.3: Overview of the satellite altimeters missions.

To compute the gridded maps, the OI uses correlation scales adapted to this distribution of tracks as described in Pujol and Larnicol (2005) (100 km for spatial correlation and 10 days for temporal). The spatial correlation function is the one proposed by Arhan and De Verdiere (1985) which correspond to a smoothing of around 50 km (see Annex C). These correlation scales, and more fundamentally the distance between the tracks, are strong limitations in terms of spatial resolution of the altimetry maps. The observable scales in altimetry are therefore limited and only large (>30km) and relatively stable mesoscale structures can be acurately detected. This is particularly crucial for the study of mesoscale in the WMed since the structures observed have smaller dimensions than in the global ocean.

Other limitations can include errors of measurement, atmospheric corrections or orbital errors.

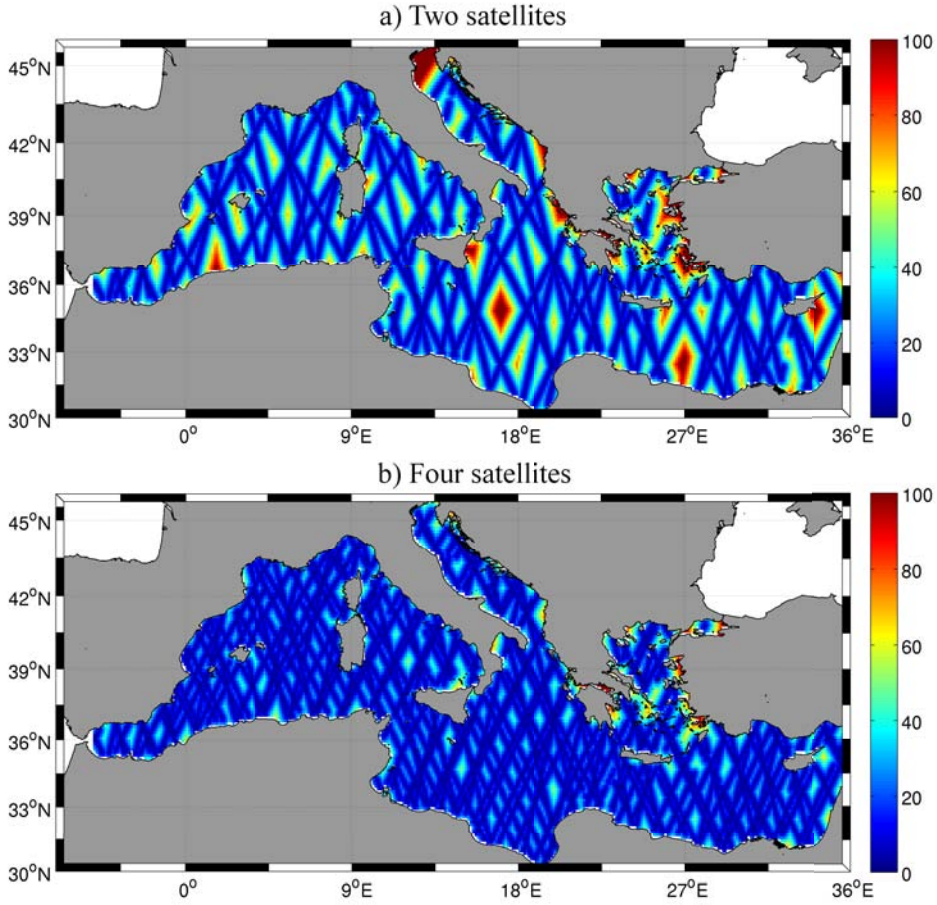

Figure 2.4: Distance between grid point and next available tracks in the optimal interpolation for 2 different configurations. The maps are plotted for the same particular day as in figure 1 of Pascual et al. (2007) (12 November 2002). The distance is shown in kilometers.

2.5.2.3 Studies

Concerning remotely sensed global observations of eddies in the Mediterranean, the work of Iudicone et al. (1998) opened the field. Using the first altimeter data from TOPEX/POSEIDON, they described the mesoscale features of the Mediterranean finding high seasonal variability, and northward transport of momentum due to the Algerian eddies.

Later, a study by Isern-Fontanet et al. (2006) made the first automated detection of eddies in the Mediterranean that he

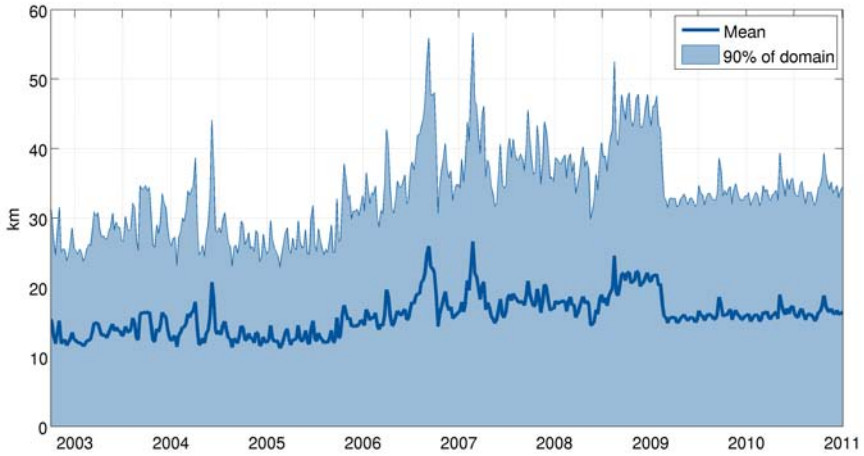

Figure 2.5: Evolution of the mean distance between gridpoints and the next available track in the WMed. The distance is in kilometers.

applied to 7 years of gridded altimetry data. They used the Okubo-Weiss method that relies on the eponymous parameter which gives information on the relative dominance of strain and vorticity in the fluid. The detected vortices have a mean size of 30 km with a standard deviation of 25 km, the bigger eddies corresponding to stronger ones. Selecting only the strongest eddies (amplitude above twice the standard deviation of the Okubo-Weiss parameter), they did not find any seasonal variability. Finally, the path of the detected eddies is examined showing some clear patterns of propagation.

2.5.3 Modelling

Concerning numerical modelling, efforts have increased a lot in recent years. Two different type of numerical models have been designed.

2.5.3.1 Long-term simulations

First, long term simulations of the Mediterranean Sea exist aiming at inter-annual and climatic studies. In this category, there is NEMOMED12 developed by Beuvier et al. (2012) with the Nucleus for European Modelling of the Ocean (NEMO, Madec and the NEMO Team 2008) model. This model is applied to the Mediterranean with a 1/12°horizontal resolution (with a NEMOMED36 in preparation at 1/36°horizontal resolution) and ran for a period of 50 years in hindcast (without assimilation). This simulation covers the period desired for our study but the resolution (about 8 km) is not sufficient to fully resolve the mesoscale in the region.

Then there is the reanalysis simulations that include data assimilation. The operational models MFS (Mediterranean Forecasting System) has a resolution of 1/16°and provides a reanalysis of the last 25 years with data assimilation. MERCATOR also offers a reanalysis of the last 20 years of the global ocean (including the Mediterranean Sea) at a resolution of 1/12°. These simulations are still too coarse and furthermore does not serve our purpose since the use of data assimilation prevents a study of the processes involved in the mesoscale dynamics as it does not let the model run freely.

2.5.3.2 Short studies

On the other hand, high resolution models are designed for smaller areas and shorter time spans. One example is the SYMPHONIE model that runs for the Gulf of Lion area at a resolution of 1 km (Marsaleix et al., 2006). Herrmann et al. (2008) studied the impact of the atmospheric resolution for the deep convection in the Gulf of Lion with this model. Another high

resolution simulation is GLAZUR 64, based on the NEMO code that covers the North Western Mediterranean with an horizontal resolution of 1/64°and 130 vertical levels. The simulation was run for several years and has been used, in combination with in-situ data, to study an anti-cyclonic eddy in the Gulf of Lion (Guihou et al., 2013). The regional model MARS3D developed by Lazure and Dumas (2008) has been also applied at a horizontal resolution of 1.2 km in the Northern WMed in a study we discussed above by Garreau et al. (2011). In the Alboran Sea, the simulation cited earlier by Peliz et al. (2013) using the ROMS core revealed insights into the mesoscale activity in the Alboran Sea.

The lack of an existing simulation with a high enough resolution to describe the mesoscale dynamics over the entire WMed motivated us to design our own simulation. The simulation covers the Western Mediterranean and is run for a long period of time in order to have statistically robust results and to study annual and inter-annual variability. The details of this model are summarized in chapter 3.

Chapter 3

A high resolution model of the area

Contents

3.1 Objective

To study the mechanisms that govern our oceans, oceanographers used to rely only on in-situ observations that are costly and scarce. With the development of satellite observational capacity, a better temporal and spatial coverage was achieved as seen in the previous chapter. However, these data still lack the resolution (temporal and spatial) to effectively monitor mesoscale activity and only provide information at the surface. The development of electronic computing enabled us to add a new tool for this endeavor: numerical modelling which complements the input given by observations, allowing global analyzes, forecasts and hindcasts.

To attain the objective of the thesis, which is the characterization of mesoscale eddies in the WMed, we need a simulation of the region that satisfies two broad criteria. First, it has to have a high spatial resolution to be able to resolve mesoscale dynamics in this area where the deformation radius is small. Considering the current computing power available, a simulation of around 3 km is a good candidate. Then, we want a long period of simulation in order to have reliable statistics (more than 10 years). Finally, since the objective would also be to look at the processes of formation and evolution, the simulation has to behave freely without assimilation.

In section 2.5, we reviewed the existing simulations of the WMed but none of them corresponds to our needs. We therefore decided to make our own simulation at 1/32° of the region comprised between 7°W and 10°E of the Mediterranean for the 20 years of altimetry period (1992-2012). This period will allow us to compare to the altimetry products available. A long term simulation like this is a challenge as it has to be stable and

realistic, even long after the initialization (Vidal-Vijande et al., 2012) which is why we will validate extensively the simulation in chapter 4.

The simulation is built upon the WMOP (Western Mediterranean sea - Balearic Operational) system, the forecasting subsystem component of SOCIB, the Balearic Islands Coastal Observing and Forecasting System (Renault et al., 2013). This solution provides daily forecasts of the Western Mediterranean since the end of 2010 using atmospheric forcing derived from AEMET/Hirlam and daily boundary conditions provided by MFS2 from MyOcean/MOON. However, this model configuration is designed for short term forecasts which does not suit our longterm simulation objectives and therefore was heavily modified as described below.

3.2 ROMS model

As explained above, the simulations were performed using the Regional Ocean Modeling System (ROMS) core, which is a community model designed for regional realistic applications (e.g., Shchepetkin and McWilliams 2005). We adopted the 3.0 version of the ROMS_AGRIF version (Penven et al., 2006) maintained by IRD and INRIA, French institutes working on environmental sciences and applied mathematics. ROMS kernel is a 3D free-surface, sigma-coordinate, split-explicit primitive equation model with Boussinesq and hydrostatic approximations.

The choice of ROMS is motivated by several factors. First, the core of the model has been built specifically for regional studies such as the WMed. As detailed in Shchepetkin and McWilliams (2009a), the model is based on multiple-time-level

time-stepping (short time steps for barotropic dynamics such as SSH or 2D momentum and much larger time steps for baroclinic dynamics such as T,S or 3D momentum) and high-order upstream-biased advection schemes which help to better resolve turbulent processes. A comparison performed by Ilıcak et al. (2012) showed that the definition of the advection scheme in ROMS reduced spurious dianeutral mixing (mixing through layers of different buoyancy) which can be problematic for high resolution simulations that are eddy resolving.

It also uses sigma coordinates on the vertical which allow an easier definition of the bottom boundary condition and are well suited for studies with complex bathymetries such as the WMed, a semi-enclosed sea strongly constrained by its topography. Finally, the constant increase of users of this numerical code has led to the implementation of several pre- and post-processing tools such as the ROMSTOOLS (Penven et al., 2008), making it relatively easy to implement in a non numerical model-oriented laboratory.

3.2.1 Primitive equations

The equations solved by the model are the Reynolds averaged Navier-Stokes equations with hydrostatic and Boussinesq hypothesis. They can then be written in the Cartesian coordinates (conservation of momentum):

$$\frac{\partial u}{\partial t} + \vec{v}.\vec{\nabla} u - fv = -\frac{\partial \phi}{\partial x} - \frac{\partial}{\partial z}(\overline{u'w'} - \nu \frac{\partial u}{\partial z}) + \mathcal{F}_u + \mathcal{D}_u \quad (3.1)$$

$$\frac{\partial v}{\partial t} + \vec{v}.\vec{\nabla} v + fu = -\frac{\partial \phi}{\partial y} - \frac{\partial}{\partial z}(\overline{v'w'} - \nu \frac{\partial v}{\partial z}) + \mathcal{F}_v + \mathcal{D}_v \quad (3.2)$$

$$\frac{\partial \phi}{\partial z} = -\frac{\rho g}{\rho_0} \quad (3.3)$$

The continuity equation (conservation of mass) is:

$$\frac{\partial u}{\partial x} + \frac{\partial v}{\partial y} + \frac{\partial w}{\partial z} = 0 \tag{3.4}$$

and the scalar transport of the variable C (advective-diffusive equation):

$$\frac{\partial C}{\partial t} + \vec{v}.\vec{\nabla}C = -\frac{\partial}{\partial z}(\overline{C'w'} - \nu_\theta \frac{\partial C}{\partial z}) + \mathcal{F}_C + \mathcal{D}_C \tag{3.5}$$

We close the problem with an equation of state:

$$\rho = \rho(T, S, P) \tag{3.6}$$

Variable	Description
$C(x, y, z, t)$	scalar quantity, i.e. temperature, salinity, nutrient concentration
D_u, D_v, D_C	optional horizontal diffusive terms
F_u, F_v, F_C	forcing/source terms
$f(x, y)$	Coriolis parameter
g	acceleration of gravity
$h(x, y)$	depth of sea floor below mean sea level
$H_z(x, y, z)$	vertical grid spacing
ν, ν_θ	molecular viscosity and diffusivity
K_M, K_C	vertical eddy viscosity and diffusivity
P	total pressure $P \approx -\rho_0 g z$ (Boussinesq approximation)
$\phi(x, y, z, t)$	dynamic pressure $\phi = (P/\rho_0)$
$\rho_0 + \rho(x, y, z, t)$	total in situ density
$S(x, y, z, t)$	salinity
t	time
$T(x, y, z, t)$	potential temperature
u, v, w	the (x,y,z) components of vector velocity $\vec{v}$
x, y	horizontal coordinates
z	vertical coordinate
$\zeta(x, y, t)$	surface elevation

Table 3.1: Variables used in the description of the ocean model

3.2.2 Vertical boundary conditions

The vertical boundary conditions are:

$$\begin{aligned} \text{top: } (z = \zeta(x,y,t)) \quad & K_m \frac{\partial u}{\partial z} = \tau_s^x(x,y,t) \\ & K_m \frac{\partial v}{\partial z} = \tau_s^y(x,y,t) \\ & K_C \frac{\partial C}{\partial z} = \frac{Q_C}{\rho_0 C_P} \\ & w = \frac{\partial \zeta}{\partial t} \end{aligned} \tag{3.7}$$

with τ_s^x, τ_s^y the surface wind stress and Q_C the surface concentration flux. The first two equations are the momentum input from the wind stress, the third represents the input of a tracer, C, and the last is the free surface.

$$\begin{aligned} \text{bottom: } (z = -h(x,y)) \quad & K_m \frac{\partial u}{\partial z} = \tau_b^x(x,y,t) \\ & K_m \frac{\partial v}{\partial z} = \tau_b^y(x,y,t) \\ & K_C \frac{\partial C}{\partial z} = 0 \\ & -w + \vec{v}.\nabla h = 0 \end{aligned} \tag{3.8}$$

with τ_b^x, τ_b^y the bottom stress. The first two equations are the input of momentum from bottom friction, the third is the absence of tracer transfer at the bottom, and the last is the impermeable bottom condition. The bottom stress is, in our solution, a linear function of the velocities:

$$\begin{cases} \tau_b^x = \gamma u \\ \tau_b^y = \gamma v \end{cases} \tag{3.9}$$

with γ the linear drag coefficient.

3.2.3 Terrain-following coordinate system

As said before, ROMS is a sigma-coordinate model. This means that it uses a stretched vertical coordinate system which essentially "flattens out" the variable bottom at $z = h(x,y)$. The new coordinate for the vertical direction is $s \in [-1;0]$ which

follows the topographic geometry. Several ways of defining the depths of the vertical levels are available depending on the topography and SSH. We tested two of them and decided on the following as it behaves better in shallow regions and we found that it reduces the pressure gradient errors (see next section):

$$z = \zeta + (\zeta + h)S \tag{3.10}$$
$$S = \frac{h_c s + hC(s)}{h_c + h}$$

where h_c is the depth above which we want an increased of the vertical resolution. The vertical stretching function, $C(s)$ is then defined as (Shchepetkin and McWilliams, 2009b):

Surface refinement function:

$$C_s(s) = \frac{1 - \cosh(\theta_S s)}{\cosh(\theta_S) - 1}, \text{ for } \theta_S > 0$$
$$C_s(s) = -s^2, \text{ for } \theta_S \leq 0 \tag{3.11}$$

Bottom refinement function:

$$C(s) = \frac{\exp(\theta_B C_s(s) - 1)}{1 - \exp(-\theta_B)}, \text{ for } \theta_B > 0 C(s) = C_s(s), \text{ for } \theta_B \leq 0 \tag{3.12}$$

The parameters θ_S and θ_B determine the stretching of the grid at the surface (θ_S) and at the bottom (θ_B). They range between 0 (no increase of resolution at the boundary layer) and 10 for θ_S or 4 for θ_B.

The vertical grid of our solution has 32 levels, representing a good compromise between computation time/storage size and an accurate representation of the ocean dynamics. A test with increased number of vertical levels was performed and the results were very similar but for a much higher cost. We used a value of 6.5 for θ_S to have a refined resolution in the upper levels which is where we want to study mesoscale dynamics.

For the deeper levels, a value of 1.5 is imposed for θ_B because, even though bottom layers are not the interest of the study, the complicated bathymetry of the region needs a sufficient representation of the vertical levels at depth. The size of the upper level range from 2 meters to 7.5 meters and at depth from 4 meters to 280 meters (see figure (3.1 for three different bottom topography depths).

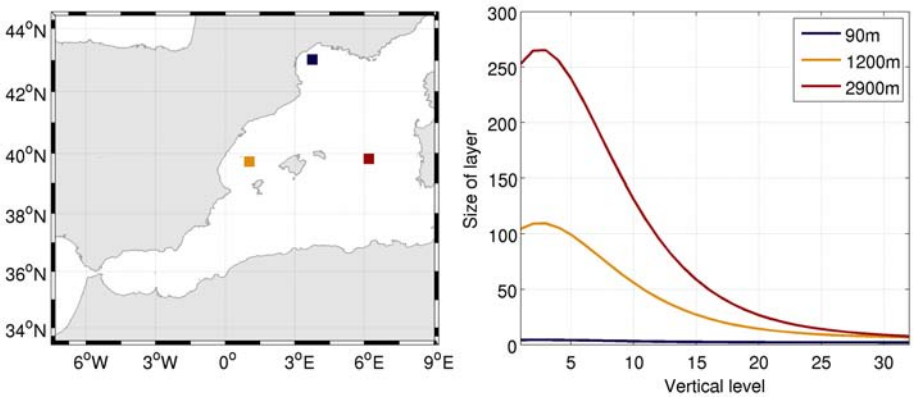

Figure 3.1: Size of vertical levels at different points in the model area. The bottom depth at the grid point is indicated in the legend.

An example of the resulting grid is presented in figure 3.2 where the mean section of water transport for the Ibiza Channel is plotted for the partial step 50 zeta vertical levels of NEMOMED12 (see section 3.6) and for the 32 sigma vertical levels of our ROMS simulation. This parameterization has several advantages in our relatively small basin with complex coastline and topography because:

- In shallow regions, the vertical levels are equally spaced which avoids having too much resolution in these areas.

- In deep regions, the vertical levels are largely independent of the bathymetry and thus behave like geopotential coordinates.

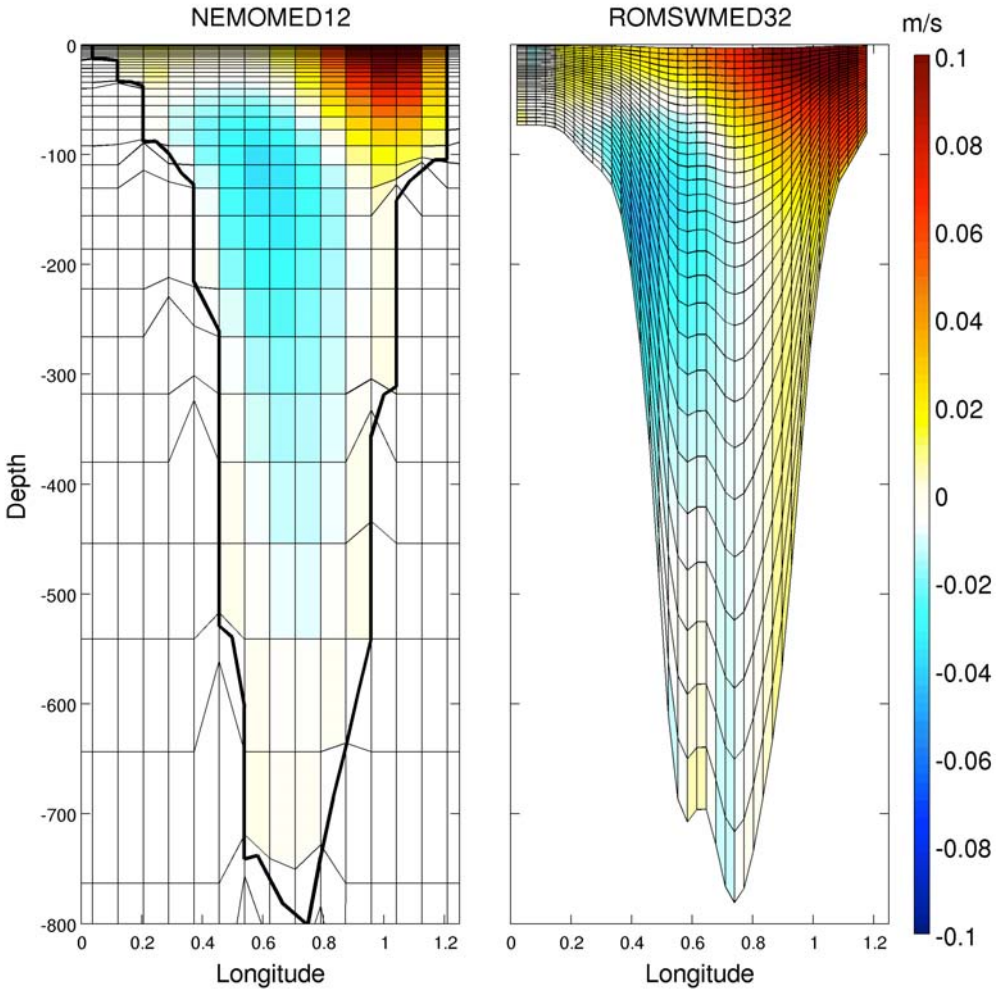

Figure 3.2: Mean zonal velocity at the Ibiza Channel for NEMOMED12 (left) and the ROMS simulation (right). The difference in the parameterization of vertical levels is clearly shown by the grids plotted in black.

3.3 Physical parameterizations

3.3.1 Advection schemes

As said in the introduction of the model, ROMS has high order advection schemes to better represent turbulent activity. These schemes allow the generation of steep gradients, are weakly diffusive and reduce dispersion errors (Shchepetkin and McWilliams, 1998).

For horizontal advection, a third-order upstream-biased advection scheme is used for the momentum. The tracers are advected by a split and rotated third-order upstream-biased advection scheme which strongly reduces diapycnal mixing (Marchesiello et al., 2009) and therefore is adapted when there is variable bathymetry. This scheme has also been adapted to further reduce errors as explained in Lemarié et al. (2012). In this scheme, the third-order upstream-biased advection scheme is split into fourth-order centered advection and rotated bi-laplacian diffusion with grid-dependent diffusivity, which avoids the need for an explicit diffusion scheme (Shchepetkin and McWilliams, 1998).

Vertical advection is done with a spline advection scheme for momentum. This scheme reconstructs vertical derivatives with parabolic splines, which is equivalent to a conventional scheme of order 8. For tracers, a fourth-order Akima scheme is implemented.

3.3.2 Boundary layer parameterization

The vertical diffusion scheme used is a non-local, K-profile planetary (KPP) boundary layer Large-McWilliams-Doney (LMD) scheme (Large et al., 1994) which represents the unresolved

physical vertical subgrid-scale processes. It was developed from atmospheric boundary layer models to include nonlocal transport terms in the mixing parameterization. The goal of this diffusion scheme is to find the profile of the K parameter of the turbulent mixing defined as:

$$\overline{u'w'} = -K_m \frac{\partial u}{\partial z} \quad \text{and} \quad \overline{v'w'} = -K_m \frac{\partial v}{\partial z} \tag{3.13}$$

with similar definitions for K_s of temperature, salinity and other tracers.

In the LMD parameterization scheme, the oceanic water column is separated into three different layers (see figure 3.3). In the interior of the ocean, mixing is governed by shear generated mixing, internal wave activity, and double diffusive processes. The surface and bottom boundary layers have separate parameterizations for the vertical mixing. The LMD scheme computes the depth of these layers based on a critical value of turbulent processes parameterized by a bulk Richardson number, and then the value of K is computed according to the wind stress at the surface boundary layer and the bottom shear at the bottom boundary layer. A shape function in the form of a third order polynomial is fitted between the mixing values in the boundary layers and the interior, creating the total profile of K (see figure 3.3).

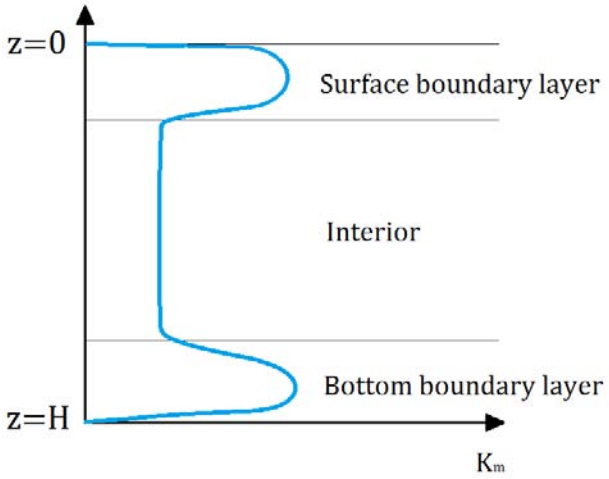

Figure 3.3: Schematic view of the KPP turbulent closure.

3.4 Spatial and temporal discretization

The spatial discretization of the model is done using a centered scheme on an Arakawa C-grid (Arakawa and Lamb 1977, see figure 3.4). This grid performs very well for high resolution models, where horizontal spacing is smaller than the deformation radius. As indicated on the figure, the free-surface (ζ), density (ρ), and active/passive tracers are located at the center of the cells whereas the horizontal velocities (u) and (v) are located to the western/eastern and southern/northern edges of the cells, respectively. These staggered grids allow the use of flux formulation, limiting the number of operations and better conserving momentum and tracer concentrations.

In the vertical direction, the grid is also staggered so that horizontal momentum (u, v), (ρ), and active/passive tracers are located at the center of the grid cell. The vertical velocity (ω, w) and vertical mixing variables (K_t, K_v, etc) are located at the bottom and top faces of each cell.

In order to optimize computation time, equations are solved by a split-explicit time-step. The principle is simple, the

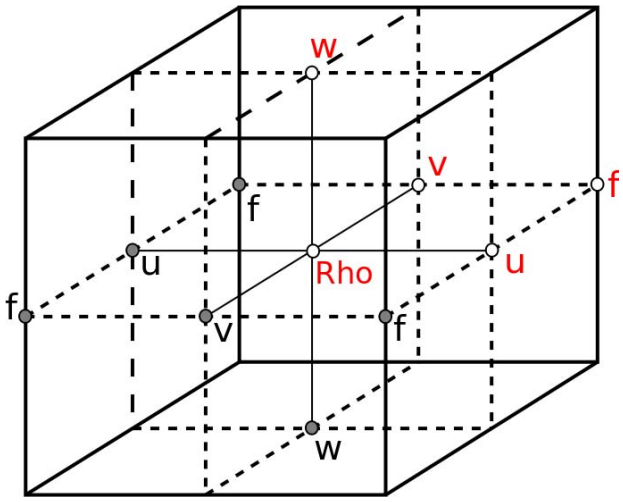

Figure 3.4: Arakawa grid. A single cell is highlighted in red.

barotropic component (depth-integrated) of the equations is integrated at a shorter time-step than the full 3D baroclinic equations (see Shchepetkin and McWilliams 2005; Shchepetkin and McWilliams 2009a for detailed description).

3.5 Topography

A crucial input for the simulation is the topography. This is especially the case for models such as ROMS that have a sigma vertical coordinate (see previous section). Sigma-coordinates present great advantages for regional applications because they allow the continuous representation of variables horizontally and follow the bathymetry. Yet, this parameterization exhibits stronger sensitivity to topography, which results in pressure gradient errors that we will discuss below. Due to the special circulation of the Mediterranean, it is very sensitive to the topography in the Gibraltar Strait as discussed below.

3.5.1 Pressure gradient error

The pressure gradient in the terrain-following coordinate system is given as follows:

$$\begin{aligned} -\frac{1}{\rho_0}\left.\frac{\partial P}{\partial x}\right|_z &= -\frac{1}{\rho_0}\left.\frac{\partial P}{\partial x}\right|_s + \frac{1}{\rho_0}\left.\frac{\partial z}{\partial x}\right|_s \frac{\partial P}{\partial z} \\ &= -\frac{1}{\rho_0}\left.\frac{\partial P}{\partial x}\right|_s + \frac{1}{H_z}\frac{1}{\rho_0}\left.\frac{\partial z}{\partial x}\right|_s \frac{\partial P}{\partial s} \end{aligned} \tag{3.14}$$

with $H_z = \frac{\partial z}{\partial s}$

In equation 3.14, we see that the pressure gradient is decomposed into: the pressure gradient along the surface where s is constant and a term that corrects the vertical gradient created by the first term. In areas of strong topographic gradients, these two terms have high values but opposite signs, which means that a small error in the finite difference can induce large errors of the estimation of the gradient (Mellor et al., 1994; Haney, 1991). This error, called the truncation error, is therefore higher on strong topography gradients and thus iso-sigma gradients, which occurs when:

$$\epsilon = \frac{\left|\left.\frac{\partial P}{\partial x}\right|_s - \left.\frac{\partial z}{\partial x}\right|_s \frac{\partial P}{\partial s}\right|}{\left|\left.\frac{\partial P}{\partial x}\right|_s\right| + \left|\left.\frac{\partial z}{\partial x}\right|_s \frac{\partial P}{\partial s}\right|} \ll 1 \tag{3.15}$$

In ROMS, improved calculation of the horizontal pressure gradient have been implemented to reduce the weight of these errors in the calculations (Shchepetkin and McWilliams, 2003). Yet these errors are still present and they need to be taken into account and reduced as much as possible. One solution to reduce these errors is to smooth the bathymetry in order to avoid too steep topography. A useful parameter introduced by Beckmann and Haidvogel (1993) is the stiffness parameter

$r_{x0} = \frac{\Delta h}{h}$, which measures the model resolution compared to topographic variations. This parameter should stay small to avoid strong truncation errors. The method is then to perform an iterative smoothing of the bathymetry until the maximum value of r_{x0} is below a threshold $r_{x0(max)}$. Auclair et al. (2000) found that a stiffness parameter of $r_{x0} \leq r_{x0(max)} = 0.2$ was sufficient to significantly reduce these errors.

As done in other studies (*e.g.* Ly and Jiang 1999), we performed a test simulation called PGEROMS (Pressure Gradient Experiment in ROMS) where the model is initialized with the same temperature and salinity profile at each grid point, we close the boundaries and remove atmospheric forcing. In this way, there should not be any current in the simulation due either to horizontal density gradients or wind forcing. Figures 3.5 and 3.6 present the results of this experiment with different values of the maximum stiffness parameter $r_{x0(max)}$. They show a significant decrease of erroneous currents when the $r_{x0(max)}$ value is decreased. After 80 days, the mean KE in the domain is 1.10^{-4} $m^2.s^{-2}$ for the simulation with $r_{x0(max)} = 0.5$, which corresponds to mean currents of around 1 $cm.s^{-1}$ in the domain. The value of the maximum velocity for this simulation shows that these currents are not homogeneous and can attain 16 $cm.s^{-1}$ after this time. For the simulation with $r_{x0(max)} = 0.2$, on the other hand, the mean KE is ten times smaller, around 1.10^{-5} $m^2.s^{-2}$, which corresponds to currents of around 3 $mm.s^{-1}$ in average and the maximum currents are around 2 $cm.s^{-1}$. The values given by the simulation with $r_{x0(max)} = 0.2$ are considered small enough to be able to run the model with this bathymetry.

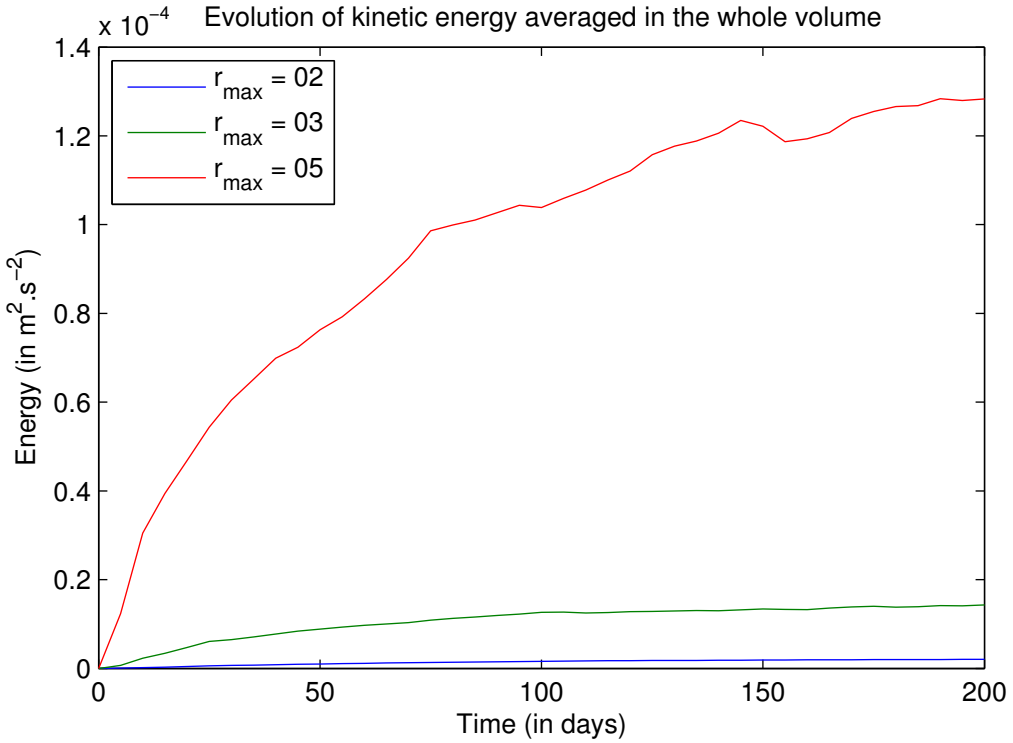

Figure 3.5: Evolution of the volume averaged KE for different topographical smoothing in PGEROMS. Values of $r_{x0(max)}$ tested are 0.2 (blue), 0.3 (green) and 0.5 (red).

3.5.2 Gibraltar

A key region for the WMed is the Strait of Gibraltar since the exchange with the Atlantic Ocean goes through this channel. As realistic as possible geometry in the strait is therefore crucial in order to have realistic transports between the Mediterranean Sea and the Atlantic Ocean. Yet, as explained in the previous section, the topography must be smoothed in order to avoid the gradient pressure errors. We therefore paid special attention to the specification of the topography in the Strait.

In this perspective, we combine two databases to compute the model depths: the one from Smith and Sandwell (1997) for the whole basin and a detailed one for the Gibraltar region (Sanz, 1991). For the Gibraltar channel, the same filtering used

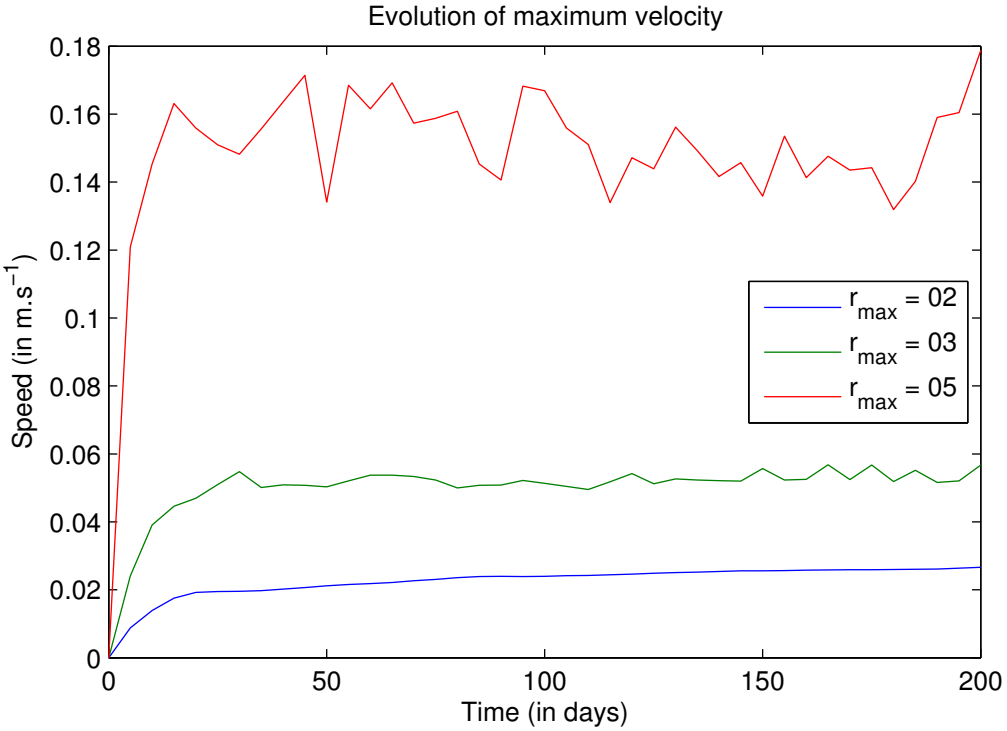

Figure 3.6: Evolution of the maximum velocity in the domain for different topographical smoothing in PGEROMS Values of $r_{x0(max)}$ tested are 0.2 (blue), 0.3 (green) and 0.5 (red).

by Peliz et al. (2012) was applied to conserve the characteristics and depth of the Strait while applying enough smoothing to avoid pressure gradient errors. Figure 3.7 shows how the different filters impact the bathymetry and the highest peak of the strait. At the junction of the two bathymetries, an additional filter is applied to remove possible spurious features induced by the combination.

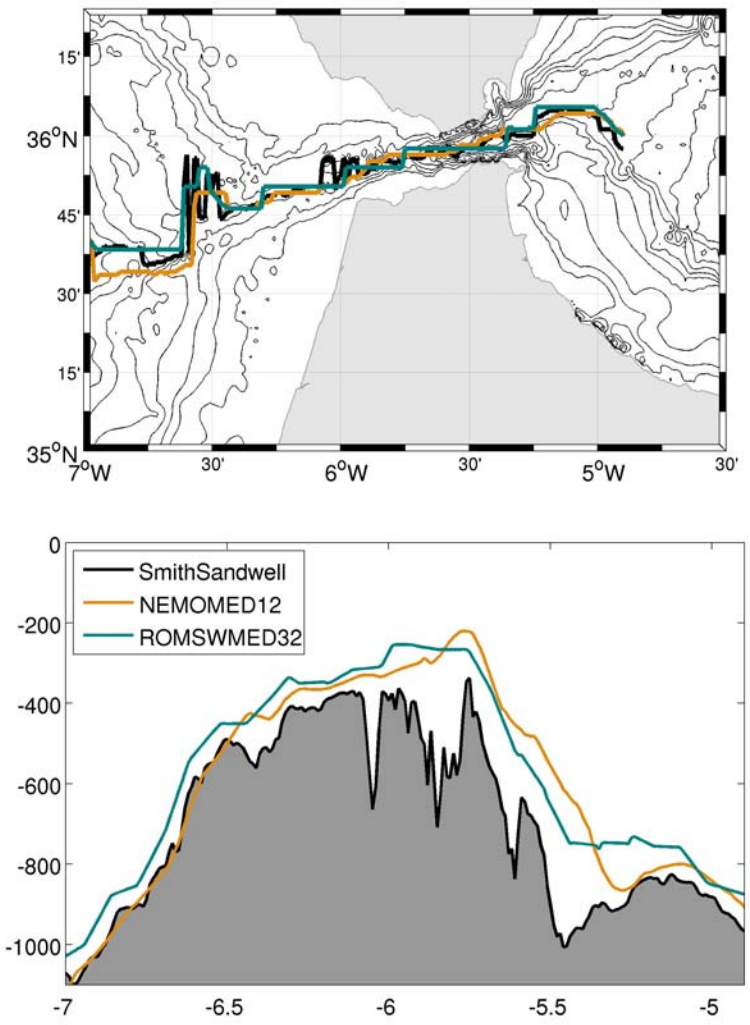

Figure 3.7: Section of topography in the Strait of Gibraltar. Similar to figure 2 of Peliz et al. (2012).

3.6 Initial state and boundary conditions

For the initial and boundary conditions as well as the forcings, we used the highest resolution, validated simulation available for our period and region at the time of the study. In this case, the simulation is NEMOMED12, a 50-year simulation of the entire Mediterranean basin with a 1/12° horizontal resolution designed by Beuvier et al. (2012).

3.6.1 NEMOMED12 simulation

The core model of the NEMOMED12 simulation is NEMO (Madec and the NEMO Team, 2008) in a regional configuration called MED12. This simulation has 50 stretched z-vertical levels (Δz is 1 m at the surface and 500 m at the bottom) with partial step parameterization (the bottom layer thickness can vary to adapt to the bathymetry). It was initialized with the 10-year filtered 3D temperature and salinity climatology provided by MEDATLAS-II covering the period 1955-1965, for the month of October 1958 and an ocean at rest. At the boundary, which is only open on the west side since the model covers the whole Mediterranean Sea, there is a buffer zone from 11°W to 7.5°W where temperature and salinity are restored toward the climatology of Levitus et al. (2005). In addition, a damping of SSH is done in this area towards a prescribed SSH given by a previous version of the model that assimilates satellite altimetry data to ensure volume conservation. River runoff is simulated as freshwater increase at the grid point near to the river mouths. The values of the 33 main Mediterranean rivers is taken from the RivDis database (Vörösmarty et al., 1996) and the rest is added as a coastal runoff along the coast from the climatological average of the interannual data of Ludwig

et al. (2009). The Black Sea is considered as a river with runoff values given by Stanev and Peneva (2001).

NEMOMED12 is forced by ARPERA, a product obtained by performing a dynamical downscaling of European Centre for Medium-Range Weather Forecasts (ECMWF) products over the European-Mediterranean region (Herrmann and Somot, 2008). The downscaling is done by spectral nudging using the atmospheric model ARPEGE-Climate (Déqué and Piedelievre, 1995), where large scales (above 250 km) are spectrally driven by ECMWF fields and small scales can develop freely. This way, the model possesses realistic synoptic as well as high resolution structures. ERA40 reanalysis (Simmons and Gibson, 2000) fields are used for the period 1992-2001 while ECMWF operational analyses are used for the period 2002-2012, the latter being downgraded to the ERA40 resolution to ensure consistency between the two periods. ARPERA provides daily fields of momentum, freshwater and heat fluxes to NEMOMED12.

A more detailed description of the simulation as well as its validation can be found in Beuvier et al. (2012).

3.6.2 Initial conditions

In order to have a realistic initial state that can reduce the spin-up time of our simulation, we take the outputs of NEMOMED12 for the start date (1st of January 1992). At this date, the NEMOMED12 simulation has run more than 30 years and therefore we are not in its spin-up. NEMOMED12 temperature, salinity and currents are linearly interpolated in 3D to the ROMS grid to serve as the initial state of our simulation.

3.6.3 Boundary parameterization

The northern and southern boundaries of the simulation are the coastlines of Europe and Africa, respectively, whereas for the eastern and western boundaries we require external forcing. These boundaries are situated in the west at 7.5°W in the Cadiz Gulf in the Atlantic and in the east at 9.5°E at the longitude of Sardinia and Corsica.

The boundary conditions are prescribed by the outputs of the NEMOMED12 simulation and different parameterizations were tested (cf table 3.2). Due to the mode-splitting used in the time-stepping of the code, the barotropic and baroclinic mode have different parameterizations. After some sensitivity test, we finally opted for the following schemes. The Flather-type characteristic method as described in Mason et al. (2010) is used for barotropic velocities. For baroclinic velocities and tracers, a radiative open boundary condition (Orlanski, 1976) with adaptive strong (weak) nudging for inflow (outflow) (Marchesiello et al., 2001) is used, which is appropriate for waves leaving the domain. A barotropic correction on the barotropic and baroclinic transport at the open boundaries is applied to ensure volume conservation (see Mason et al. (2010) for details)

We conducted some sensitivity tests using a 3D nudging of temperature and salinity towards the values of NEMOMED12 in a buffer zone of around 110 km at the boundaries where relaxation time increases going toward the interior of the domain. This buffer zone did not improve the accuracy of the model and even created some instabilities. It was therefore not included in the final simulation. This also allowed a reduction of the pre-processing time and data storage as this buffer zone needed 3D interpolated fields of temperature and salinity from

NEMOMED12.

Within a band of 15 grid points (around 45 km) at all the boundaries, an increased viscosity is added to the background value, ranging from 125 $m^2.s^{-1}$ at the boundary to 0 inside the domain. This area of increased viscosity, called a sponge layer, acts to prevent numerical instabilities at the boundaries as well as spurious currents due to the differences between the simulation and the value from the boundary condition.

3.7 Atmospheric forcings

In ocean models, atmospheric forcings are very important; they are the boundary conditions at the surface that are needed by the primitive equations (Barnier, 1998). There are two ways to apply the forcings to the ocean: one method is to impose the heat fluxes to the model (flux mode), the other one lets the model compute the heat fluxes according to the atmospheric state but also the ocean state (bulk mode). Each of these methods is discussed below.

3.7.1 Flux forcing

In a configuration with flux forcing, the model is given the direct value of the ocean-atmosphere heat, water and momentum fluxes. Since most of the fluxes depend on the atmospheric variables but also on the ocean state, they are often calculated from another model or from an observation climatology. This method reduce the degrees of freedom of the model by forcing it with fluxes independent of the model state.

In our case, the first simulations were done with flux forcing, the fluxes being taken from the output of NEMOMED12

that takes ARPERA as input atmospheric forcing (see previous section). They are daily means of the variables. A retroaction term $dQ/dSST$ is implemented in the heat flux that allows a relaxation of SST toward the values of a climatology. For this coefficient, a constant coefficient of $dQ/dSST = -40W.m^{-2}.K^{-1}$ was tested (as in NEMOMED12). However, the simulation was not stable and a space dependent climatological value of $dQ/dSST$ was computed from the Comprehensive Ocean-Atmosphere Data Set (COADS) climatology (Slutz et al., 1985). With this coefficient, the simulation reached a stable state.

3.7.2 Bulk parameterization

Another way to define the forcing is the bulk formulation: the model is given the state of the atmosphere, humidity, temperature, wind... and it computes the heat fluxes itself from this information and the state of the ocean.

The ARPERA forcing extracted from the NEMOMED12 outputs had some issues due to the spatial interpolation of the wind field. Indeed, the computed wind curl was null except on the edges of the mosaic tiles that are the ARPERA grid (see figure 3.8). Since this unrealistic input could impact our study of the mesoscale at the surface, we decided to try another forcing. We used the NCEP-CFSR (Saha et al., 2010) dataset, which is available for our period, with a bulk formulation for the fluxes. The Climate Forecast System Reanalysis (CFSR) is a reanalysis of the state of the ocean-atmosphere for the last 35 years made by the National Centers for Environmental Prediction (NCEP). This is done by running a constant model with a constant data assimilation scheme retrospectively, from

1979 through the present. This dataset has a spatial resolution of 35 km and is available every 6 hours.

Figure 3.9 shows how the change of atmospheric input impacted the mean vorticity of the simulation, which no longer has non-realistic pattern of vorticity, especially in the vicinity of the Northern Current.

We made some qualitative validation of the NCEP-CFSR dataset for our region and period of study and concluded that it represents correctly the atmospheric state over the Mediterranean (not shown).

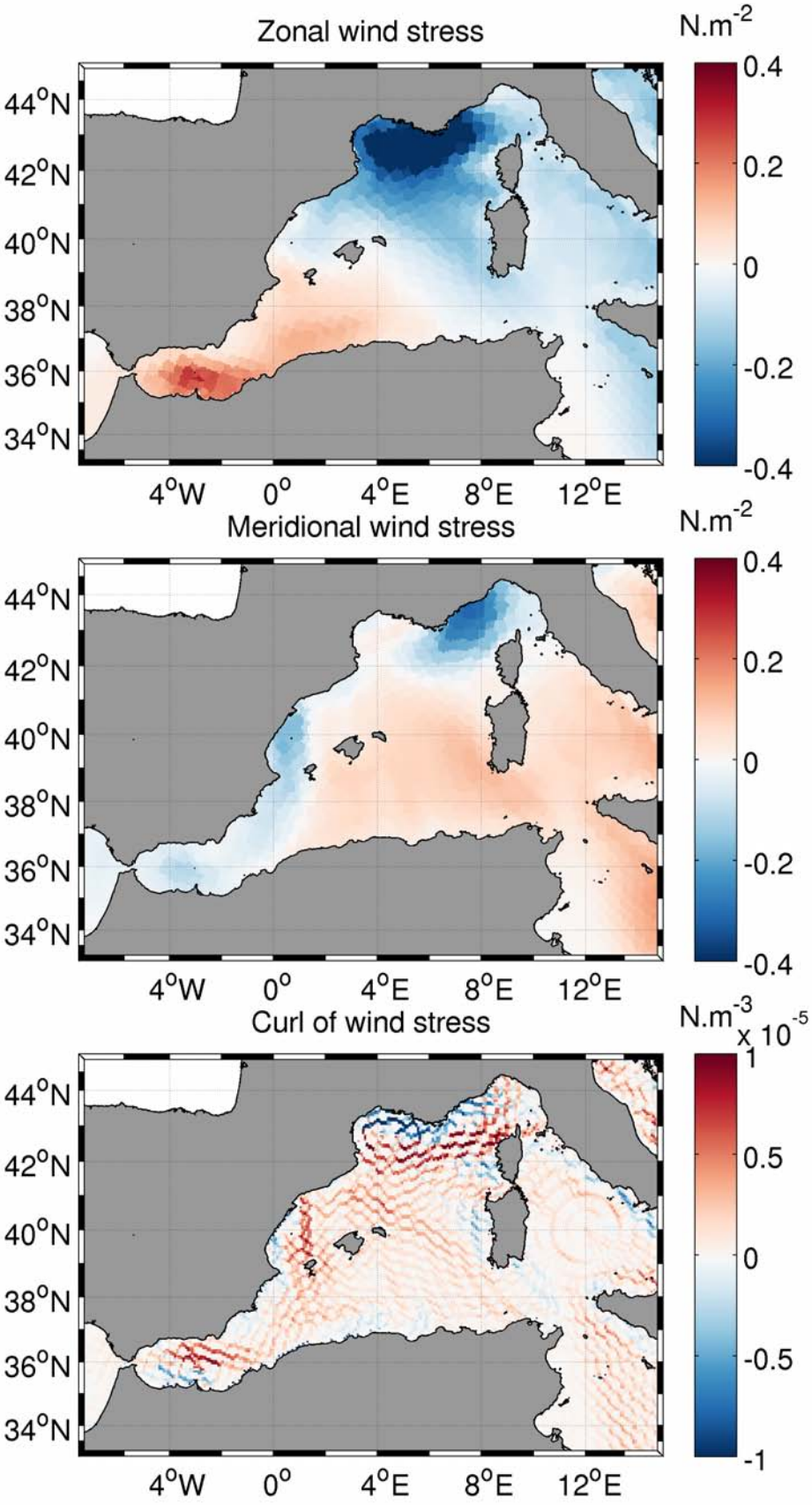

Figure 3.8: Wind stress input from ARPERA (zonal on the top, meridional in the center and curl on the bottom). Example for the 23/01/1992.

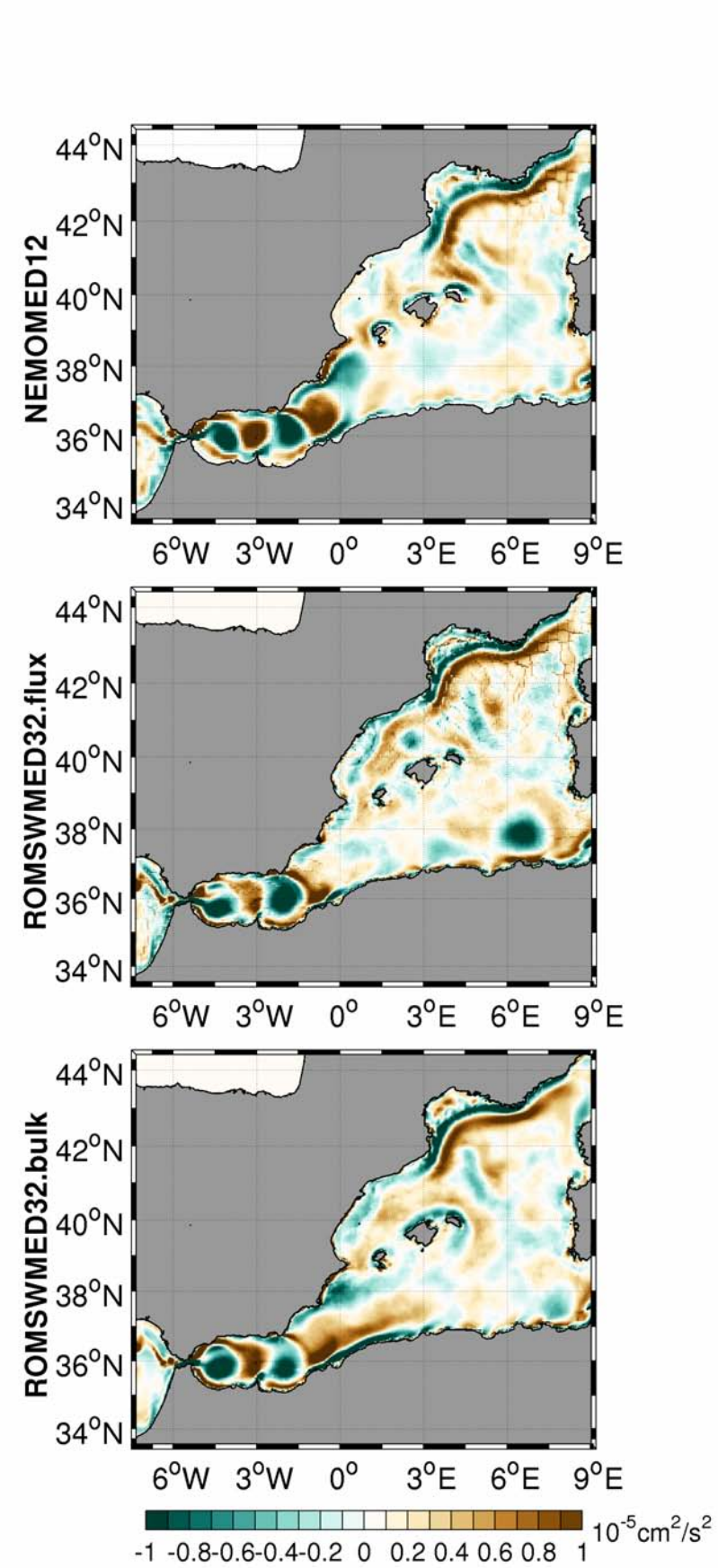

Figure 3.9: Mean vorticity for the period 1992-2012 for NEMOMED12 and two simulations with ROMS (flux and bulk forcing)

3.8 Rivers

River input is done through the artificial increase of precipitation at the rivers mouths to account for the freshwater input due to the rivers.

In order to maintain the stability of the high resolution simulation, we had to, unlike the NEMOMED12 simulation, spread the river input fluxes on a disc of 150 km of radius with a decreasing gaussian from the coastline. This spreading also allows to compensate for the difficulty of the model simulation of the offshore transport of river runoff. An example of how the river input looks in the E-P-R fluxes is shown in figure 3.10. For our simulation, we used the monthly climatology from Dai et al. (2009).

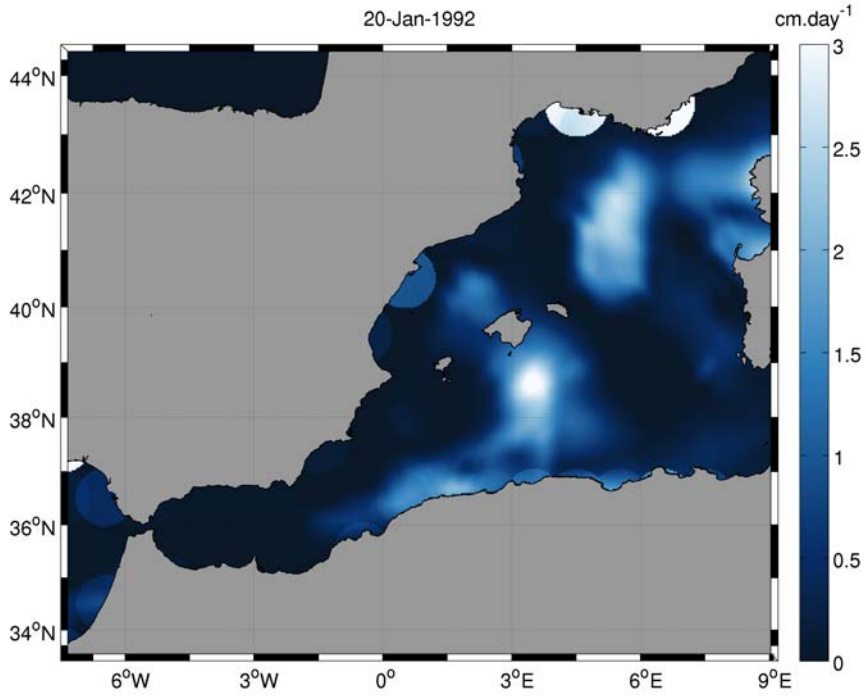

Figure 3.10: Precipitation rate input including river spreading.

3.9 Set of simulations

To tune the model parameterizations and obtain a realistic and correct simulation of the WMed for our period of 1992-2012, we performed over 30 simulations with different configurations, the more relevant of which are described in table 3.2. This table illustrates the difficulties of achieving a good simulation as there are a lot of parameters to take into account that also interact together. The final simulation of 21 years, which will hereafter be called ROMSWMED32, is summarized in table 3.3. It is realistic and its long duration allows robust statistical comparisons.

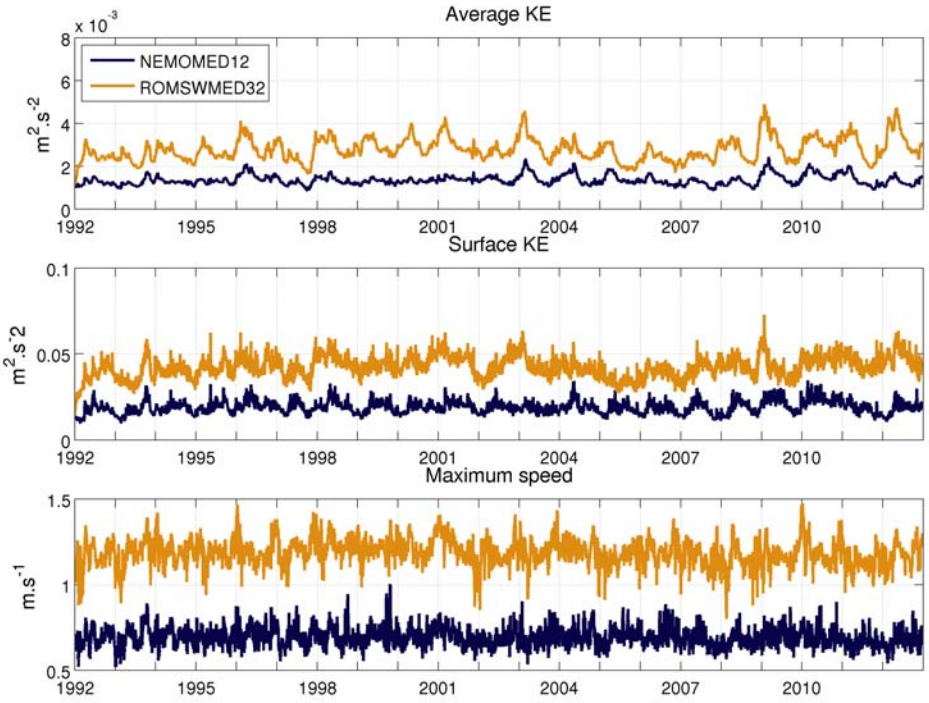

Figure 3.11: Time evolution of kinetic energy (KE), surface KE and maximum velocity of the different simulations.

The stability of the simulation is examined in figure 3.11: the KE appears to stabilize between 20 and 40 cm^2/s^2 after 6 months and the surface KE at around 450 cm^2/s^2. The spin-

up time of the model is therefore estimated to be around 6 months, but analysis will be done after 1 year (1993-2012) to be sure that the model is stabilized. The energy in our high resolution simulation is higher than in NEMOMED12, which is expected since mesoscale and sub-mesoscale processes are not fully resolved by NEMOMED12. ROMSWMED32 simulation also appears to have higher variability, especially at the annual scale. The maximum velocity in the domain is stable in all the models and higher for the ROMS simulation while still being in a reasonable range for this region.

Test	Name	Period	Description
Boundary conditions	bnd_gib	3 yrs	Test with eastern boundary at Gibraltar Strait
	bnd_3Dnudg	3 yrs	Test with 3D nudging at boundaries
	bnd_no3Dnudg	3 yrs	Test without 3D nudging
	bnd_close	6 months	Test with closed boundaries
	bnd_spg2	6 months	Stronger sponge area
	bnd_radnud	1.5 yrs	Test a new boundary parametrization (Radiation + nudging)
	bnd_corrflux	9 yrs	Adding of the barotropic correction of velocities
Model	agrif	1 yr	Changing the model version (from RUTGERS to AGRIF)
Bathymetry	topo_smoo03	9 yrs	Topography smoothed for rx0max = 0.3
	topo_smoo015	14 yrs	Topography smoothed for rx0max = 0.15
	topo_newmask	9 yrs	Change of land mask in Algerian coast
	topo_gibnew	1 yr	New topography at the Strait of Gibraltar
	topo_gibnew2	1 yr	New topography better smoothed at the Strait of Gibraltar
Vertical levels	vert_old	3 yrs	Test with another function for stretching of vertical levels
	vert_n40	5 yrs	Test with 40 vertical levels
Lateral diffusion	smago	3 yrs	Test with lateral diffusion (Smagorinski)
Forcings	flux	21 yrs	Test with ARPERA forcing of NEMOMED12 as flux forcing
	flux_Tsrelax	1 yr	Test with small temperature and salt relaxation for flux forcings
	flux_Trelax	9 months	Test without salt relaxation for flux forcings
	flux_dQdSST	9 yrs	Relaxation parameter space and time dependent (climatology) + rivers are spreaded
	bulk	21 yrs	Using new forcing (CFSR) in bulk
	flux_mixte	1 yr	Using mixte forcings (ARPERA for wind +CFSR)

Table 3.2: Summary of the simulations performed. The final simulation is in red.

Area	Wmed: 7.4°W to 10°E 34.6°N to 44.7°N
Horizontal resolution	1/32°
Forcings	NCEP-CFSR (6 hours)
Boundaries	NEMOMED12 (daily)
Sponge	yes (45 km)
Nudging	2D at boundaries
Period	1992-2012
Outputs	daily
Vertical levels: Number (θ_S,θ_B)	32 (6.5,1.5)
$r_{x0(max)}$	0.2
Δt	240s
Nb barotropic steps	25
Background vertical mixing	0
Bottom drag	linear (γ = 0,0003 m.s^{-1})

Table 3.3: Characteristics of the final simulation.

3.10 Computing resources

The model was run at IDRIS (Institut du développement et des ressources en informatique scientifique) in France. It used 121 cores and with its 32x461x532 grid, 1 month was computed in 1 hour, which makes the whole simulation available after around 20 000 single processor hours. The whole 21 years simulation with daily outputs uses 1.2 TB of hard disk drive storage.

3.11 Conclusion

In this chapter, we presented the development of a 20 years, high resolution simulation of the Western Mediterranean. This development was a challenge because the simulation needs to be stable and realistic for a long period of time. The model was at first taken from an existing operational model but the different goals and exigencies of this hindcast required a lot of changes in the parameterizations. The steps that led to the final simulation are explained, as well as the choices that have been made. A final stable simulation is selected and is validated in chapter 4 for use in the study of mesoscale variability in the Mediterranean.

Chapter 4

Analysis and validation of a 20-years simulation at 1/32° resolution

Contents

4.1 Objective

In the previous chapter, we developed a stable and realistic simulation called ROMSWMED32. With an horizontal resolution of 1/32° it simulates the behavior of the Western Mediterranean Sea over the period of altimetry (1992-2012). In this chapter, we determine the realism of this simulation and how it reproduces the mesoscale dynamics in the region, We analyze the outputs of our simulation and therefore its adequacy to represent the known dynamics and features of the region. The simulation is validated with the objective of a good representation of the mesoscale structures.

The simulation will be compared to available in-situ or satellite observational data to validate its realism. We also compare results from NEMOMED12, which can be considered to be a state of the art simulation.

First, a general validation of the simulation is performed (sections 4.3 to 4.7) by comparisons with observations. Observations often have a lower resolution, which is why we need the numerical model for our study, but we can look at the synoptic structures to assess the accuracy of ROMSWMED32. Then we focus on the mesoscale performance of our model (sections 4.8 to 4.10) and how it compares to the previous, lower resolution model solution: NEMOMED12.

4.2 Observational products used for the validation

In this section, we describe the observations used for the validation. However, observations can also be useful for direct characterization of ocean processes, and some will be also used

in other parts of the thesis (drifters, altimetry). Indeed, in chapter 5, an attempt at an improvement of the satellite SLA maps will be conducted. Automated eddy detection algorithms (chapter 6) will also be applied to altimetry maps in order to compare the model results with observations. Finally, observations can be assimilated into numerical models with the aim of getting as close to reality as possible. This, however, is not within the scope of this thesis as we want the model to freely simulate the mesoscale features in order to understand their mechanisms.

4.2.1 Altimetry

Satellite altimetry provides a quasi global coverage and "high" temporal resolution of SSH observations, which makes it a suitable tool to validate the surface circulation of numerical models.

4.2.1.1 Along-track data

Along-track data are the first level altimetry product that is usable for oceanographers. These are the direct measurements from each satellite on its orbit around the globe. The dataset from multiple altimeters is homogeneous and inter-calibrated with a global crossover adjustment using TOPEX/Poseidon as the reference mission (Le Traon et al., 1998). Standard geophysical corrections are applied (see section 2.5) and a cubic spline interpolation is used to obtain equally spaced values every 7 km. The 7-year mean of 1993-1999 is removed to obtain SLA data as explained in section 2.5.

4.2.1.2 AVISO gridded (AVISOMED08)

The along-track data are interpolated to obtain 2D gridded fields. In this chapter, we used merged, delayed-time gridded maps of optimally interpolated SLA provided by Archiving, Validation and Interpretation of Satellite Oceanographic (AVISO) (http://www.aviso.oceanobs.com). This product is specially designed for the Mediterranean Sea with adapted (smaller) correlation scales (see Pujol and Larnicol (2005) for details) and a higher resolution grid (1/8°). To obtain this product, all available satellites are used in the OI (TOPEX/Poseidon, Jason-1/2, ERS 1/2, Envisat, Geosat-Follow On, see figure 2.3). The along-track data described previously are filtered with a Lanczos filter to remove measurement noise (cut-off wavelength of 42 km) and then interpolated with an optimal analysis every 7 days. The spatial and temporal correlation scale are constant and set at 100 km and 10 days with a correlation function proposed by Arhan and De Verdiere (1985) (see Annex C). The OI is set to correct long-wavelength errors and measurement noise. Details of the mapping procedure for the Mediterranean Sea can be found in Pujol and Larnicol (2005).

This dataset will hereafter be called AVISOMED08.

4.2.1.3 Mean Dynamic Topography

As explained before, uncertainty in the geoid prevents us from knowing the SSH and so we only have the SLA. To reconstruct the total SSH, a mean state of the SSH called the MDT has to be computed. For this study we used the regional MDT of the Mediterranean Sea from Rio et al. (2014).

This MDT is constructed using an average of the outputs of

an ocean model as a first guess. In this case, the ocean model is NEMOMED8, the previous version of NEMOMED12 with a horizontal resolution of 1/8° (Beuvier et al., 2010). Then, an inverse technique is used to improve the first guess using in-situ datasets. The observational data used are hydrological profiles from CTDs, moorings, Argo floats and gliders, as well as geostrophic velocities computed from drifters. This MDT has been validated with independent observations that have shown its validity in many areas (Rio et al., 2014).

4.2.2 SST

SST provides very useful information about the state of the ocean at its interface with the atmosphere, providing data about ocean features as well as thermal fluxes between the ocean and atmosphere.

The SST used in this study comes from a high resolution analysis for the global ocean (Stark et al., 2007; Donlon et al., 2012) called OSTIA (operational sea surface temperature and sea ice analysis) and available on the MyOcean website (`http://www.myocean.eu/`). It uses satellite data provided by the GHRSST project, together with in-situ observations to determine the sea surface temperature. The analysis is performed using a variant of OI described by Martin et al. (2007) and produced daily on a 1/20° grid (approx. 5km) but the effective resolution is lower (Reynolds et al., 2013).

4.2.3 Temperature and salinity fields

The observed 3D state of the Mediterranean Sea is obtained from the gridded ENACT-ENSEMBLE version 4 (EN4) product (Good et al., 2013). It was produced by an OI of the tem-

perature and salinity profiles from different datasets. The main source of profiles is the World Ocean Database 05, to which is added data from the Arctic Synoptic Basin Wide Oceanography project (ASBO), the Global Temperature and Salinity Profile Program (GTSPP), and Argo data from the Argo global data assembly centres (GDACs). It contains observations from bathythermographs (XBTs and MBTs), hydrographic profiles (CTDs and predecessors), moored buoys and ARGO drifters. These data are processed with quality control and then used to produce a monthly potential temperature and salinity objective analysis on a 1°x1° grid. This dataset provides very useful information as it is global, for the 3D ocean and available over a long period of time (1900-2014) even if the first maps have very few observations. It is also useful as it gives an estimate of the error for its gridded fields given by the interpolation. However, the scarcity of the raw profiles induces a low spatial resolution of 1° and the fields are monthly means which prevents its use for the study of mesoscale.

Another dataset available for the Mediterranean Sea is provided by the MEDAR Group (2002). Temperature and salinity profiles from 1945 to 2002 are interpolated into annual fields of 1/4°x1/4°grid and 25 standard vertical levels (Rixen et al., 2005). The interpolation is done by the Variational Inverse Method (VIM, Brasseur 1991, Brasseur1996b) and a Generalised Cross validation (Brankart and Brasseur, 1996) is applied to calibrate the correlation length and the signal to noise ratio.

It is important to note that, for these datasets, the raw data come from isolated profiles that are not sampled regularly in time and space. This means that there is a bias toward the areas of deep and intermediate water formation where many cruise campaigns have occured. They are also seasonally biased

as more profiles are available for the spring and summer seasons (Tsimplis and Rixen, 2002).

4.2.4 Drifters

The drifting buoy dataset used in this study is a compiled database of drifters in the Mediterranean Sea from the MedSVP program (Poulain et al., 2012). There are three different drifters, the Surface Velocity Program (SVP) drifter designed for the Global Drifter Program, the CODE drifter aimed at measuring coastal surface currents and the Compact Meteorological and Oceanographic Drifters (CMOD) or XAN-1 from the US Navy. The localization, data and status of the drifters is transmitted to Argos Data Collection and Location System (DCLS) polar-orbiting satellites, although some drifters are equipped with GPS to provide more accurate positions.

Editing to remove outliers and spikes is performed using statistical and manual techniques with criteria based on maximum distance, maximum speed and maximum angle between consecutive points. The positions are then interpolated with Kriging optimal interpolation and velocities are estimated using centered finite differences between interpolated positions. A low-pass Hamming filter of 36 hours is applied to velocities and positions to remove high frequency motions such as inertial oscillations, and the data are supsampled every 6 hours. These processed data can be accessed through the MedSVP web site (`http://nettuno.ogs.trieste.it/sire/medsvp/`).

4.3 Surface circulation

4.3.1 Mean circulation

The mean SSH presented in figure 4.1 shows that the simulations that we performed succeed in reproducing the patterns found in the literature, as described in section 2.3. On the figure, we also plot the mean SSH calculated from the MDT and adding the average for our period of study, to serve as a reference as well as the mean circulation from NEMOMED12. The mean circulation of the new simulation ROMSWMED32 is then plotted for its validation. We can identify some discrepancies between the different datasets (observations and different model simulations) that we will discuss below.

Alboran gyres As noted in chapter 2, a key area for the WMed is the Alboran Sea with the permanent WAG and the semi-annual EAG. Seasonal variability will be discussed later but we can already see that in the observations, here taken from AVISOMED08, the two gyres are present but the eastern one is much weaker because of its semi-annual presence. In the NEMOMED12 simulation, both gyres are apparent in the mean with equal strength suggesting that the second one may be permanent. The ROMSWMED32 simulation, in turn, exhibits a stronger western gyre and a weaker eastern one closer to what is observed by the altimetry data.

Algerian Current Flowing eastward out of the Alboran Sea, the Algerian Current is quite strong and narrow in the observations as we can see in figure 4.1 and in other studies such as described by Millot (1999). This current is not very well defined in the mean SSH of NEMOMED12, with the forma-

tion of meanders just outside of the Alboran Sea leading to the formation of eddies and the main branch of the current flowing much more to the north below the Balearic Islands. The ROMSWMED32 simulation is closer to the observations, with the narrow Algerian Current close to the coast as far as 3°E.

This current is then quite unstable, which results in weaker velocities that are farther offshore in the temporal mean, as is also apparent in the satellite observations but farther to the east than otherwise observed (Millot, 1999). This current instability is well reproduced by both models and we can see the weakening of the mean current that is directed away from the coastline due to the strong formation of meanders and eddies.

Northern Current Along the French coast, the Northern Current flows from the Tyrrhenian Sea to the Balearic Sea, as clearly seen in the observed mean SSH. The current is well represented by all model simulations but, in the ROMS model solution, the current is stronger, narrower and closer the coast, which is more realistic according to the literature (*e.g.* Sammari et al. 1995).

Balearic Sea In the Balearic Sea, altimetry data show that the Northern Current can reach the Ibiza channel, with some mesoscale structures altering its path to make it less well defined. As described in section 2.3, the flow can either go southward through the Ibiza channel or follow the Balearic islands northern coast forming the Balearic Current. However, in this plot, we see that some of the Northern Current also bifurcates southward earlier, at 3°E, reaching the Mallorca coast and joining the Balearic Current towards Sardinia, which completes the northern gyre of the basin.

The Northern Current in NEMOMED12 does not, on average, reach the Ibiza channel and most of it bifurcates southward at 5°E and the rest no farther west than 2°E. ROMSWMED32 reproduces a Northern Current going further west than in NEMOMED12 with a strong Balearic Current. Both simulations generate quite correctly the current at the Balearic front that completes the southern part of the northern gyre, with ROMSWMED32 resembling more closely the observations from satellite altimetry.

Even if, in average, the new simulation does not have a current flowing southward through the Ibiza channel, individual maps show that this circulation can happen.

4.3.2 Focus on the Alboran Sea

As we detailed before, the realistic reproduction of AW coming through the Strait of Gibraltar is essential to have a realistic simulation of the Mediterranean Sea. Therefore, we look at the gyres in the Alboran Sea and their variability which is constrained by this inflowing current, to assess the realism of the simulation. A useful tool to analyze the variability of a 2D field and highlight its primary modes is Empirical Orthogonal Functions (EOF) analysis. The method consists of decomposing the dataset into a reduced set of functions, with time series and spatial patterns, which account for the variance as efficiently as possible. This way, we can study the variability of our complex 2D field just by looking at a few modes. The practical computation of these modes is done by finding the eigenvectors of the covariance matrix of the dataset.

In figure 4.2 we reproduce the figure from Renault et al. (2012) where the three main modes of variability of the SLA

measured by altimetry in the Alboran Sea are depicted. The first mode explains nearly 60% of the variance, representing the steric contribution to the annual signal. In this mode, both gyres intensify in spring-summer and weaken in fall-winter, with stronger variation for the East Alboran Gyre. The weakening can even lead to the formation of a cyclonic gyre, the Central Cyclonic Gyre (CCG). The second mode, accounting for 15% of the variance, reveals a dipole between the EAG and a cyclonic gyre to the east. The third mode, explaining 10% of the variance, represents the variation of intensity in opposite phase to the WAG and EAG, as well as the creation of a cyclonic or anticyclonic eddy next to the EAG. The last two modes have 2-2.5 year cycles identified in the spectra as well as, for the second one, a significant peak at 5 year frequency. Details on how these modes explain the circulation can be found in Renault et al. (2012).

The same EOF analysis was done for the ROMSWMED32 simulation in figure 4.3. The first mode is the same as in AVISOMED08 but explains less variance, which may be due to the increase of mesoscale variability in the high resolution model. It has the same annual cycle which, as described earlier, explains the annual variability of the EAG. As for the two other modes, they are very similar to those of the altimetry data but in a different order. The third (second) mode of observations is the second (third) mode of the model, explaining 21% (11%) of the variance. This shows that the model is able to reproduce very well the variability of the surface currents in this region, albeit not exactly like in the altimetry observations.

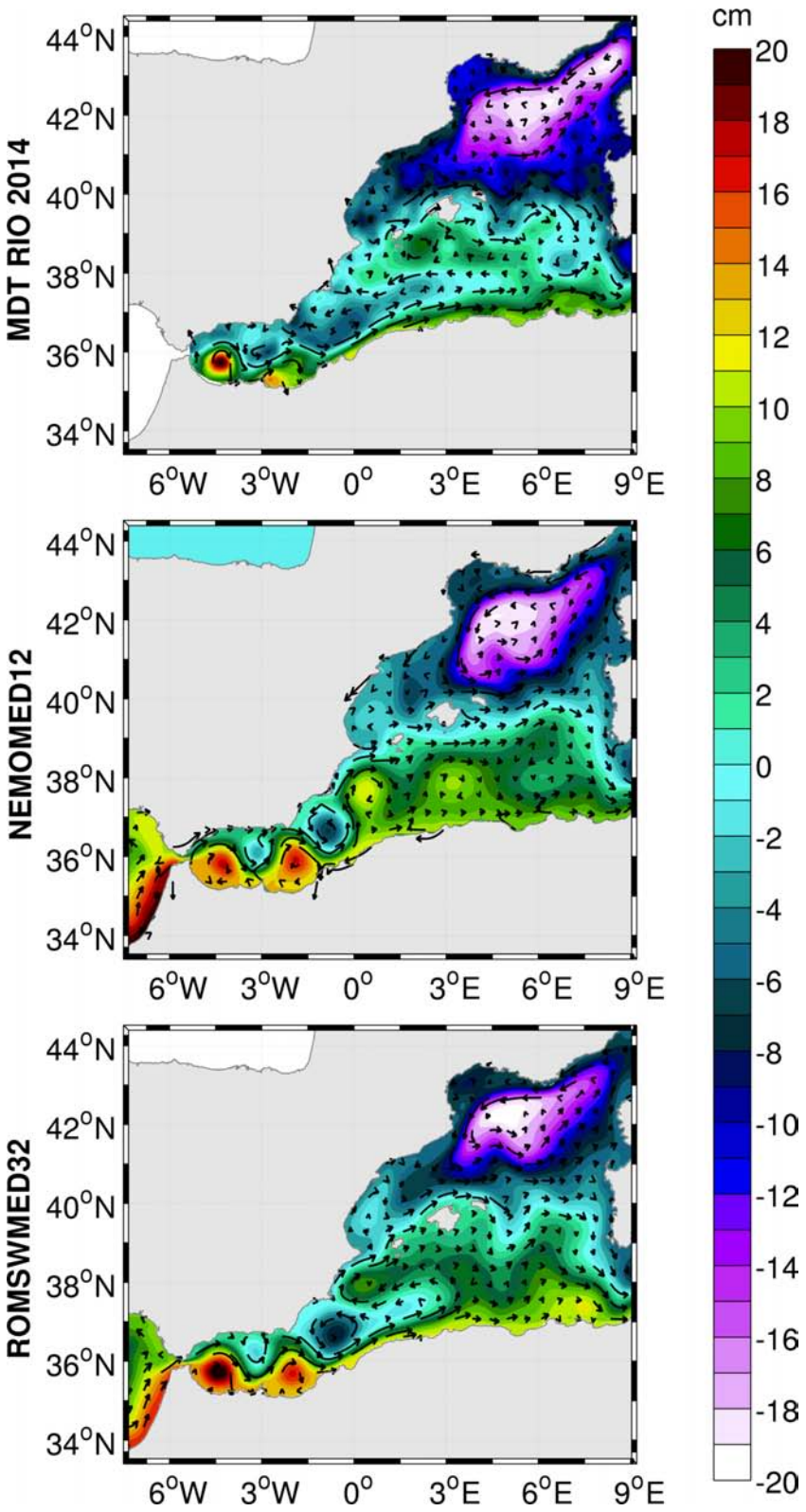

Figure 4.1: Mean SSH for the period 1992-2012 for the two models ROMSWMED32 and NEMOMED12, and mean SSH from AVISOMED08 computed as the mean of SLA + MDT. Vectors are the geostrophic velocities computed from the respective SSH.

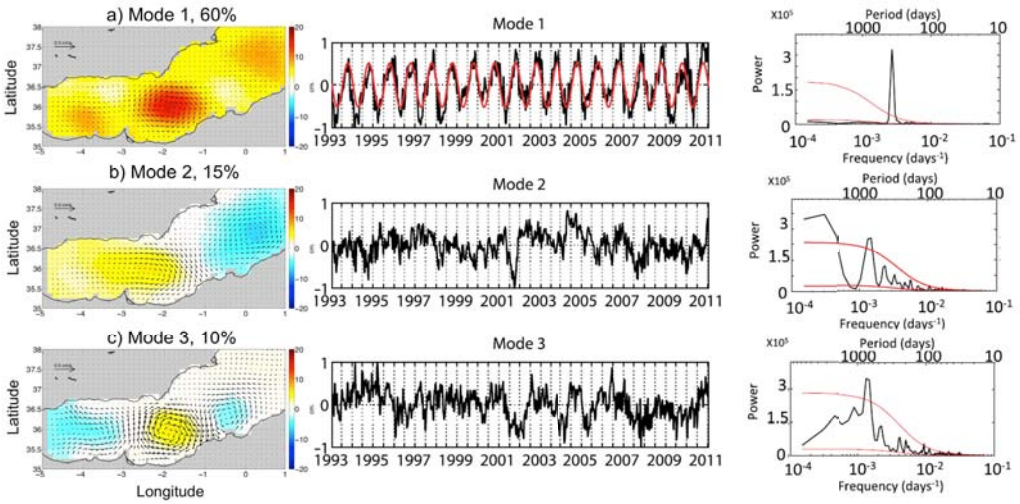

Figure 4.2: EOF of the SLA in the Alboran Sea: observations. Figure extracted from Renault et al. (2012). The EOF are computed from AVISOMED08. The first column is the spatial variations of the EOF, the second column is the time series associated and the third column is the spectra of the time series. For the spectra, the red lines represent the 5% and 95% confidence interval estimated from a red noise (Markov).

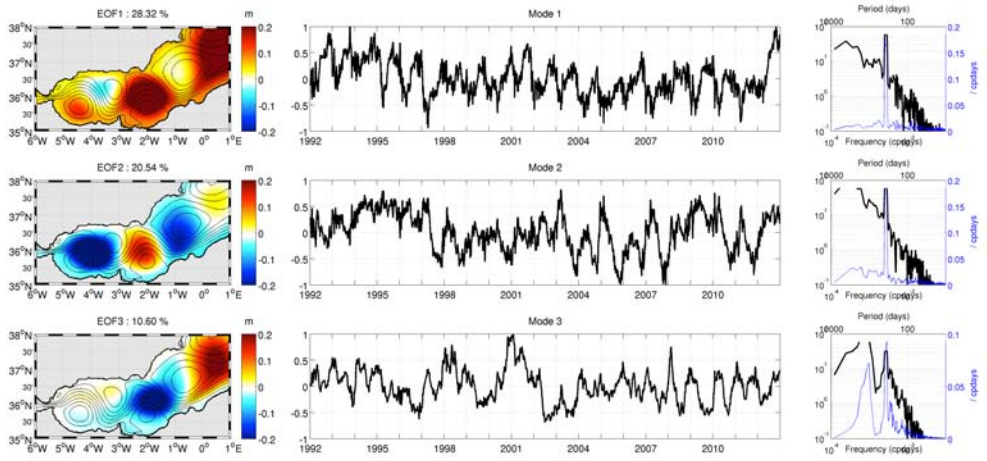

Figure 4.3: EOF of the SLA in the Alboran Sea: ROMSWMED32 simulation. The EOF computation is applied to the SLA of the model. The columns are the same as in figure 4.2. For the spectra, the scale is logarithmic and the variance preserving spectra is plotted in blue.

4.4 Surface variables

4.4.1 Sea Surface Temperature

The temporal means of SST from the different simulations are compared with the temporal mean of SST from satellites (see section 4.2) in the left panels of figure 4.4. This reveals that, in the northern part of the basin, simulations are in good agreement with observations. The Gulf of Lions presents the coldest waters (up to 16.5°C) due to the northern winds blowing over the region (Mistral). A strip of warmer water coming from the east along the French coast reveals the presence of the Northern Current bringing warmer waters from the Tyrrhenian Sea. The Balearic front in its eastern part is well defined in both simulations and located at the same place as the observations whereas the western part of the Balearic front is better represented in the ROMS simulation.

In the southern part, there is a positive bias in temperature between NEMOMED12 and the observations; the ROMS simulation also has a bias, albeit a smaller one. It may come from the forcings since the bias was different for two ROMS simulations that had different forcings (not shown). While both models present similar biases in the eastern Algerian Basin, in the Alboran region both gyres reveal much warmer waters at the surface than the observations for NEMOMED12 and less so for the ROMS simulation. This is probably due to the shortwave fluxes that are stronger in NEMOMED12 in the region (see figure 4.5).

4.4.2 Sea Surface Salinity

Another surface variable that we can examine to assess the validity of the models is the SSS. In this case, recently produced satellite data sets such as SMOS are available but do not have the appropriate spatial resolution nor the temporal coverage to be used here. We therefore used the MEDAR climatology computed from in-situ profiles. A comparison of temporal mean SSS is presented in the right panels of figure 4.4. The range of the values is the same for all the data as well as the general patterns corresponding to the surface circulation discussed above. Still there are some discrepancies, such as a negative bias of salinity in the center of the Gulf of Lions in ROMSWMED32 which may be related to the way the rivers are spread in the forcing of the model. The signature of the Rhône river is present in the models and the observations. The Ebro river effect can also be observed in all the datasets but is weaker due to a lesser discharge.

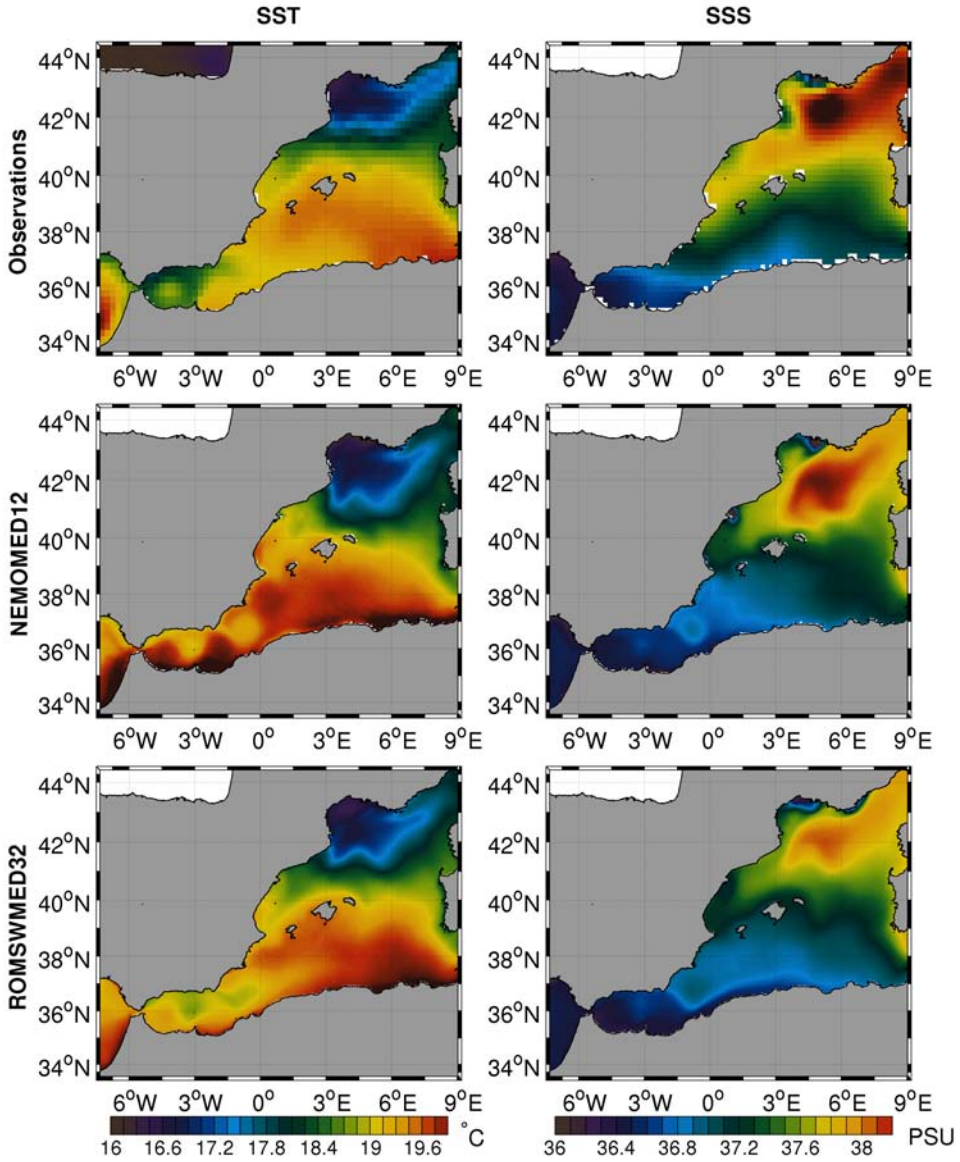

Figure 4.4: Comparison of mean SST (left) and Sea Surface Salinity (SSS) (right) over the period 1992-2012 for observations (top), NEMOMED12 (center) and ROMSWMED32 (bottom). For SST, observations are taken from OSTIA product and for SSS from the MEDAR climatology (see text for details).

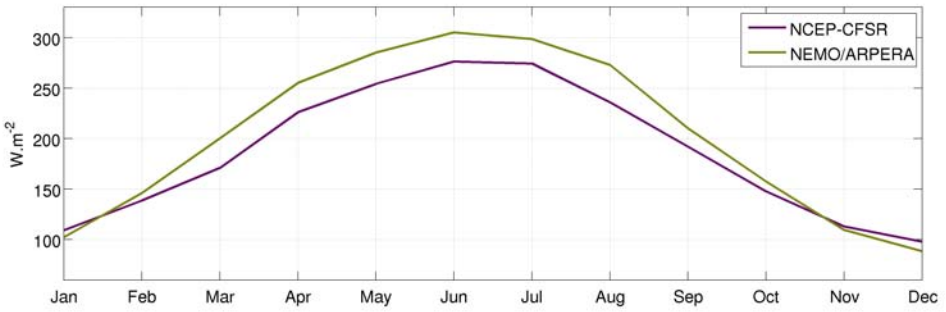

Figure 4.5: Comparison of shortwave fluxes in the Alboran Sea for the two different atmospheric forcings: APERA (forcing NEMOMED12) and NCEP-CFSR (forcing ROMSWMED32).

4.5 Under the surface

4.5.1 Heat and salt content

To investigate how the models behave at depth, one can compute the volume average of temperature and salinity for different depths as an estimation of the thermohaline content. Figure 4.6 presents the evolution of the volume averaged temperature and salinity for 3 layers: from 0 to 150, 150 to 600, and 600 to 3000 meters as in Rixen et al. (2005). This mean is computed from the EN4 gridded product as well as from NEMOMED12 and our simulation. The gridded product includes an estimation of the standard deviation of the error for each grid point. We estimate the error of the estimation of the mean heat and salt content as the volume averaged mean of this error.

First, we note that the observed heat content for the WMed in the upper layer is between 14˚and 17°C with a very strong seasonal cycle. The models reproduce this cycle quite well but we observe a small positive bias of around 0.5°C with respect to observations. In the layer below, observations no longer display the seasonal cycle and the value is stable around 13.25°C but with variability that may be due to the lack of temporal homogeneity in the observations. The models, in turn, still have a weak seasonal signal at these depths and they warmer by about 0.5°C. NEMOMED12 appears to have a small negative trend, while ROMSWMED32 is stable at around 13.75°C. In the deeper layer, as expected, observed water is colder with little variability at around 12.7°C. NEMOMED12 also exhibits little variability but, as in the upper layers, there is a warm bias which is smaller here (about 0.15°C). As for the ROMS simulation, we see that there is a positive trend. The simu-

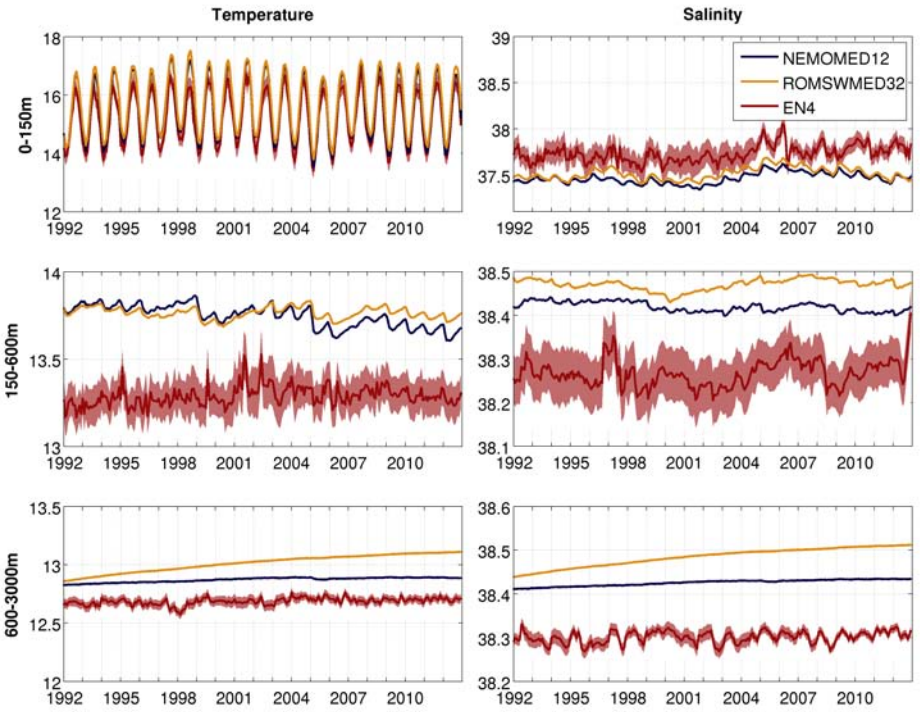

Figure 4.6: Time evolution of the volume averaged temperature (left, °C) and salinity (right) for EN4 observations in red the two simulations (NEMOMED12 in blue and ROMS in yellow) in the upper (top), intermediate (center) and deep (bottom) layer. The depths of the layers are indicated to the left of the plots. For the observations, the volume averaged mean of the standard deviation of the error is plotted as a confidence interval (area in red).

lation started with almost the same bias of about 0.15°C as NEMOMED12 but it increased over the 20 years of simulation to reach a value of 0.4°C. The possible reasons for this trend are discussed below.

Regarding the salt content, there is a weak seasonal cycle in the upper layer for the observations, but they exhibit high variability and an inter-annual signal. The model simulations, in contrast, appear to have a seasonal cycle with saltier waters in spring and less salty waters in autumn somewhat stronger, which is consistent with the observed climatology of the fresh-water input that is stronger in autumn and weaker in spring

(Mariotti et al., 2002). The simulations display a negative bias of about 0.4, the mean being 37.4 whereas the mean observed value is 37.8. The observed salt content in the intermediate layer is stable but presents a high variability at intra- and inter-annual time scales. NEMOMED12 salt content is higher by about 0.18 and the ROMS simulation is higher by about 0.2. The variability in the model simulations is smaller but there is a signal. At greater depths, while observed values are relatively constant at 38.33, NEMOMED12 values are around 38.42 with a slight increasing trend. The ROMS simulation, similar to what was observed for heat content in the deep water, presents a notable positive trend going from values of 38.44 to 38.51 in 20 years.

Concerning the trend of heat and salt content in the deep water in the ROMSWMED32 simulation, one hypothesis is that this is attributable to the transports at the boundaries, mainly the eastern boundary, which are slightly different in ROMS than in NEMOMED12. The ROMS model would transport too much saline and warm water into the basin at depth. With the objective of reducing this trend, we made some improvements to the simulation, such as changing the boundary topography to resemble more closely that of NEMOMED12, as well as a correction on the barotropic water flux at the boundaries (Mason et al., 2010) and an increase of the number of vertical levels. These efforts did not succeed in reducing the trend. The difference between NCEP surface fluxes but APERA-related boundary fluxes (from NEMOMED12) is not the culprit either as the trend is also present with ARPERA forcing. Furthermore, when we plotted the heat content of the bottom layer, this time for different regions as defined in chapter 2, it appeared that the trend occurs throughout the basin, increasing

in magnitude from east to west (figure 4.7) indicating that the problem may be at the Gibraltar Strait. This suggests that getting the right transport through Gibraltar is a crucial and difficult task that will need further improvement in the future. However, we succeeded in reducing this trend by decreasing the maximum r-value for the topography (see section 3.5)

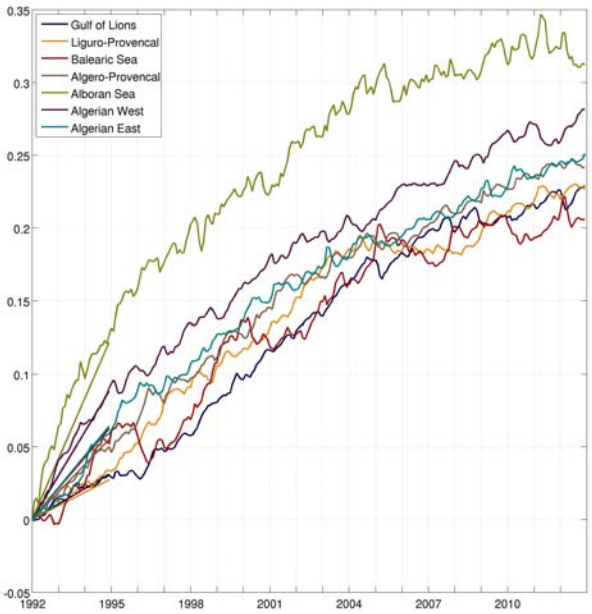

Figure 4.7: Time evolution of the volume averaged temperature of the deep layer (600 m to bottom) in the different regions defined in section 2.3. The values at the start of the simulation have been removed from each region to better see the trends.

As noted above, there is some inter-annual signal in the data (observations and models,) which is extracted in figure 4.8 by removing the mean and averaging the thermohaline content at yearly values. The figure shows that both simulations reproduce some of this inter-annual content. In table 4.1, correlation between these yearly estimates of the heat and salt content in simulations and the observations are indicated. In the upper layer, the correlation is high for heat content in both models

(0.8) and for salt content, NEMOMED12 has a higher correlation (0.81) than ROMSWMED32 (0.66). In the intermediate layers, the correlation is much higher with ROMSWMED32 for temperature and salinity than with NEMOMED12 for which it is essentially 0. In the lower layers, the correlations are similar for both models at around 0.6 for temperature and 0.5 for salinity.

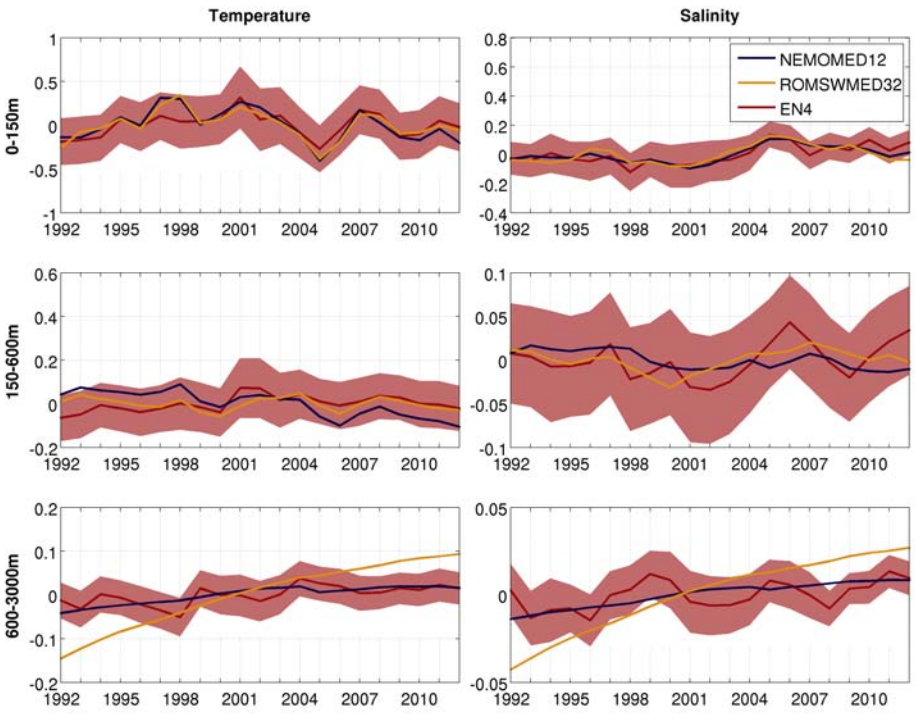

Figure 4.8: Time evolution of the anomalies of the volume averaged temperature (left) and salinity (right) for EN4 observations in red the two simulations (NEMOMED12 in blue and ROMS in yellow) in the upper (top), intermediate (center) and deep (bottom) layer. The yearly mean of these anomalies are plotted to remove the seasonal cycle. The depths of the layers are indicated at the left of the plots. For the observations, the volume averaged mean of the standard deviation of error is plotted as confidence interval (area in red).

Layer & Simulation		Temperature	Salinity
0-150 m	NEMOMED12	0.81	0.81
	ROMSWMED32	0.80	0.66
150-600 m	NEMOMED12	-0.08	0.06
	ROMSWMED32	0.32	0.50
600-3000 m	NEMOMED12	0.63	0.46
	ROMSWMED32	0.65	0.49

Table 4.1: Correlations between the models (ROMSWMED32 and NEMOMED12) and observations (EN4) for heat and salt content.

4.5.2 Water masses

Figure 4.9 presents T/S diagrams of mean profiles in the different regions of the WMed and allows us to describe the various water masses. In the Alboran Sea region, we can identify fresh AW entering through the Gibraltar Strait. Although the picture is not very clear because of the lack of good observations, AW can be identified in the observations as the fresh (around 37.2) waters that constitute the upper layer of the profiles. Two profiles obviously depicting Atlantic water which, at depth, is cold (below 13°C) and fresh (37) are included erroneously in the region likely because of erroneous longitude coordinates for the profiles. In both models, profiles show fresh waters that correspond to AW. They seem to exhibit a bias in salinity with respect to the observations at the surface, since the AW is between 36 and 37. However, other observations such as Gascard and Richez (1985) confirm that these values are realistic.

AW is then advected through the Alboran Sea joining the eastward Algerian Current as explained in section 2.3. This current flows beneath strong surface winds that induce high evaporation of the surface waters. In the observed T/S data, we can see the shift of the previously described AW toward higher salinity from the Alboran Sea (around 37.2), to western Algerian (37.5) and then to the eastern Algerian region (37.9). The two models also reproduce this behaviour, with salinity at the surface shifting from ∼36.5 to ∼37.5. The main branch of the circulation then flows south of Sardinia and through the Sicilian channel into the Eastern Mediterranean.

When the AW returns to the northern part of the WMed through the Corsica channel, it is much saltier because of strong evaporation in the Eastern Mediterranean Sea. The diagram

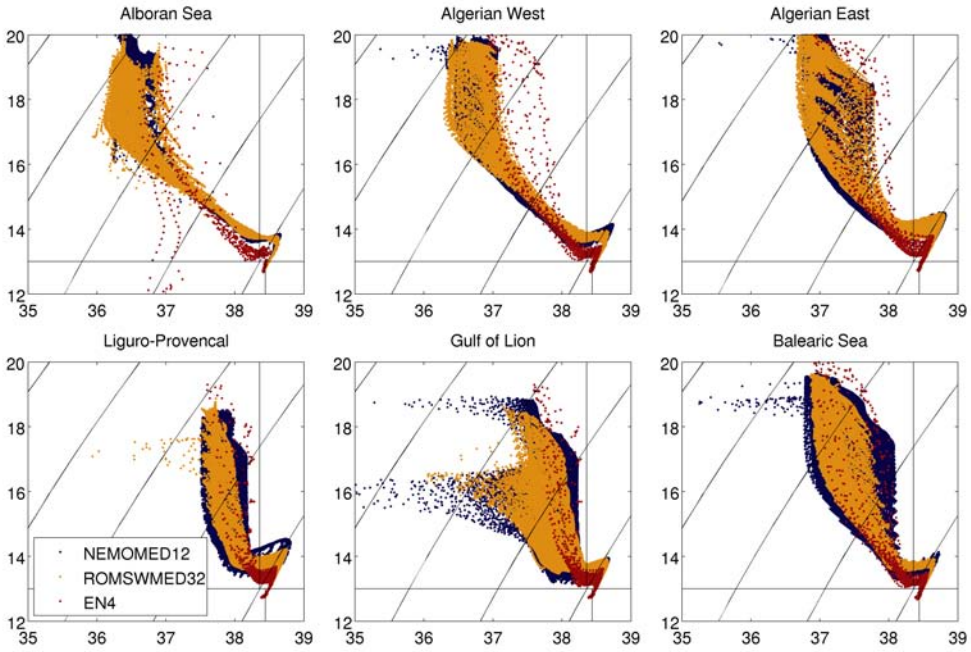

Figure 4.9: T/S diagrams of various regions of the WMed for the models (ROMSWMED32 and NEMOMED12) and observational data (EN4). The data are profiles of temporal means over the 20 years for all datasets. Observations are from the gridded product of EN4.

of observed profiles in the Liguro-Provencal region represents these waters very well, with salinity between 37.8 and 38.3. The models exhibit similar characteristics, although still with slight negative biases of salinity. During its journey in the eastern basin the surface AW can cool and evaporate, in winter, leading to an increase in density that allows it to sink; these dense water formation processes occur in specific regions such as the Levantine basin. The water mass that is created is called Levantine Intermediate Water (LIW), which is characterized by a local maximum of temperature and a maximum of salinity in profiles at 250 m depth. The LIW travels back to the western basin in the same way as the AW, but at a deeper level (200-400 m). It is easily identified in observed T/S diagrams of the Liguro-Provencal region by the "scorpion-

tail" feature that represents the local maximum in temperature (above 13°C) and global maximum of salinity (38.5). This remarkable shape is also found in the models, and the maxima are even more marked (14°C and 38.7).

The situation is similar in the Gulf of Lion region with only one notable difference that is the formation of Western Intermediate Water (WIW) (see section 2.3) in this area. This can explain the decrease in the observations of the local temperature and salinity minimum reaching 13°C in the mean. This minimum is the tracer for these particular waters. The model data are in good agreement with observations for the AW, LIW, and also the WIW, but we can see low to very low salinity points that deviate from the bulk of the other points and are not depicted in the observations. These are the signature of the Rhône river, which is the largest river of the region with discharges of fresh water up to 20000 m^3s^{-1} (Naudin et al., 1997). To simulate the river inputs, the NEMOMED12 injects relatively high quantities of fresh water at the river mouths corresponding to these discharges; this creates the low salinity points. They are at the surface and the two main temperature values for these points correspond to summer and winter. In the case of the ROMS model, the freshwater input is spread along the coast (see section 3.8), which is why we also see this effect in the Liguro-Provençal region that is upstream of the Northern Current and not in NEMOMED12 where it is advected downstream by the current. The observations are too far from the coast to see the effect of the Rhône river, which explains why we don't have these feature in EN4.

The Balearic Sea is where modified AW that comes from the Northern Current meets recent AW coming from the south and the Ibiza channel. In the observed T/S diagram of this

region, profiles present relatively fresh waters (from 37) and saltier waters (up to 38). The effect of the WIW is present as well as the strong signature of the LIW. The T/S diagrams for the models offer very similar pictures but we can note that the effect of the river inputs is still visible in the NEMOMED12 model.

Finally, as described in Millot (1999), LIW flows westward through the Gibraltar Strait but also recirculates eastward at depth along the Algerian coast explaining the "scorpion-tail" pattern in the T/S diagrams of the three southern regions.

4.6 Deep water convection

As described in chapter 2, a particular feature of the WMed is that deep water convection that occurs in this basin and, in particular, in the Gulf of Lion. In this area, deep water formation is triggered by latent heat loss by the ocean due to strong local winds (Mistral and Tramontane) in winter (Schott et al., 1996). WMDW is then formed in the center of the cyclonic gyre of the Gulf of Lion where convection may reach the bottom of the basin (2400 meters). This water mass, characterized by a density over 29.10 $kg.m^{-3}$ plays an important role in the thermohaline circulation of the Mediterranean.

To assess the ability of the simulations to reproduce this phenomenon, the evolution of the mean and maximum of the MLD for an area covering the center of the cyclonic gyre in the Gulf of Lion is presented in figure 4.10. The MLD is computed with a criterion based on the shallowest extreme curvature of near surface layer temperature profiles (Lorbacher et al., 2006) and similar results are found with the Δ criteria on density. For the NEMOMED12 simulation, the MLD increases in wintertime and, in some years, deepens down to the bottom. However, although it reaches the bottom in 14 of the 21 years, the mean MLD shows for most of these years that it may be at only a few grid points and there is no deep convection at all such as in years 1992 or 1993. As documented by observations, we can see that there is deep convection in years 2006, 2009 and 2012 and an especially strong event in year 2005 . Results from the ROMSWMED32 simulation indicate that, even though the MLD reached the bottom of the basin in several years (1992, 2005, 2006 and 2012), the mean MLD stayed around climatological values and there was no deep convection.

Figure 4.11 illustrates that the region where the MLD reaches the ocean bottom is very small for the ROMS model compared to NEMOMED12.

The possible reasons for this difference between the two models are the following. First, we know that there is a strong role of the atmospheric forcing in the triggering of the deep water convection. ARPERA forcings are colder than NCEP-CFSR, which increases the density of the surface layers and facilitates the deep convection. In a previous simulation with ROMS that was identical to this one but using the forcings by ARPERA (ROMSWMED32.flux) it was possible to simulate some deep convection events. Another reason can be the positive trend of salinity of the deeper layers in the ROMS simulation as described in section 4.5, which gradually increases the stability of the water column making it more difficult to have a deep convection event. Finally, NEMOMED12 uses daily atmospheric forcing while ROMSWMED32 uses diurnal forcing and the use of diurnal atmospheric forcing has been shown to reduce the deep water convection (Lebeaupin Brossier et al., 2011).

This limitation of the simulation is not critical as it should not strongly affect the focus of our study, which is the mesoscale eddies. Indeed, as observed by Testor and Gascard (2006) and simulated by Herrmann and Somot (2008), eddies formed by the convection event are quite small (cores of about 5 km diameter) and can be considered sub-mesoscale eddies that are not resolved by either NEMOMED12 or ROMSWMED32.

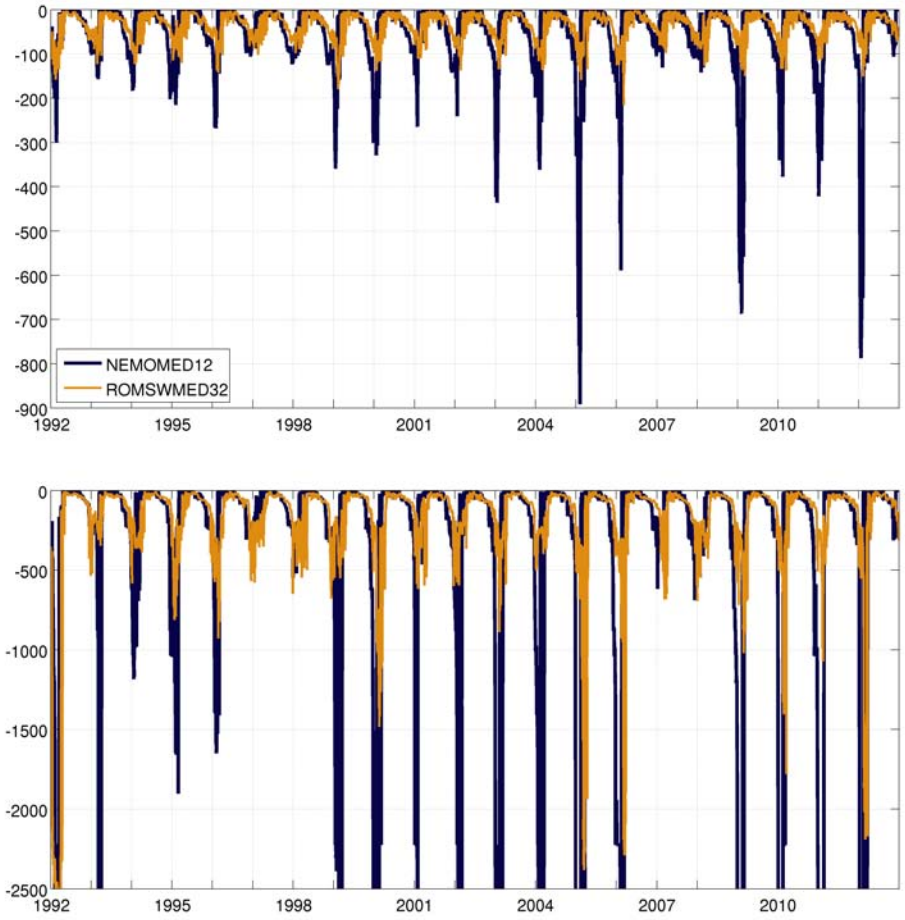

Figure 4.10: Time evolution of the spatially averaged (top) and maximum (bottom) mixed layer depth in the Gulf of Lion for NEMOMED12 in blue and the ROMS simulation in yellow.

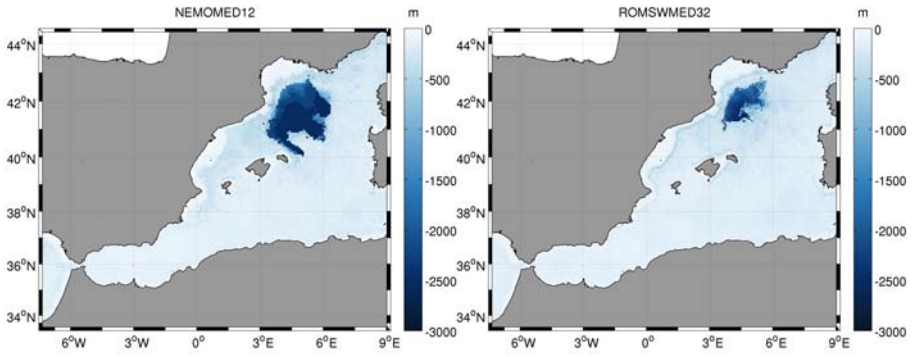

Figure 4.11: Spatial distribution of the maximum of the MLD in the basin for NEMOMED12 (left) and the ROMSWMED32 simulation (right).

4.7 Transports

4.7.1 Time evolution

The transport through the Gibraltar Strait is, as noted in chapter 2, essential to correctly simulate the circulation of the basin. Lots of work have been done to estimate the inflow, outflow and net water transport toward the Mediterranean. Estimates range from +0.72 to +1.01 Sv for the inflow, from -0.68 to -0.97 Sv for the outflow and from +0.04 to +0.13 Sv for the net flow (Tsimplis and Bryden, 2000; Lafuente et al., 2000; Sánchez-Román et al., 2009; Baschek et al., 2001). In figure 4.12, the time evolutions of the water transport into and out of the basin are compared for the different simulations as well as the value of the latest estimate from observations computed by Criado-Aldeanueva et al. (2012). Mean values as well as the variability of both simulations are quite similar, although ROMSWMED32 has somewhat smaller values of inflow and outflow. However, these transports in the models are weaker than the observations. The net transport is well reproduced by NEMOMED12 and slightly overestimated by ROMSWMED32.

4.7.2 Velocity section

Figure 4.13 shows sections of mean zonal velocities from NEMOMED12 and ROMSWMED32 along longitude 5.8°W. It shows that, despite similar water transport through the strait, the bathymetry sections are different and therefore the velocities have different values. In NEMOMED12, the upper half of the 300 m section is an eastward flow with velocities reaching 50 $cm.s^{-1}$ near the surface. The depth of the shear interface is around 150 m, which is what has been observed by acoustic

doppler current profilers (ADCP) as reported by Tsimplis and Bryden (2000). In the bottom half of the water column, the flow is westward at velocities around 30 $cm.s^{-1}$. The situation in ROMSWMED32 is similar for the upper 100-150 m where a mean eastward current flows at about 30 $cm.s^{-1}$. In the deeper water, however, the bottom depth is much shallower, meaning that westward velocities must be much stronger in order to export the same amount of water. They can reach 1 $m.s^{-1}$ and are concentrated in the bottom 30 meters of the water column.

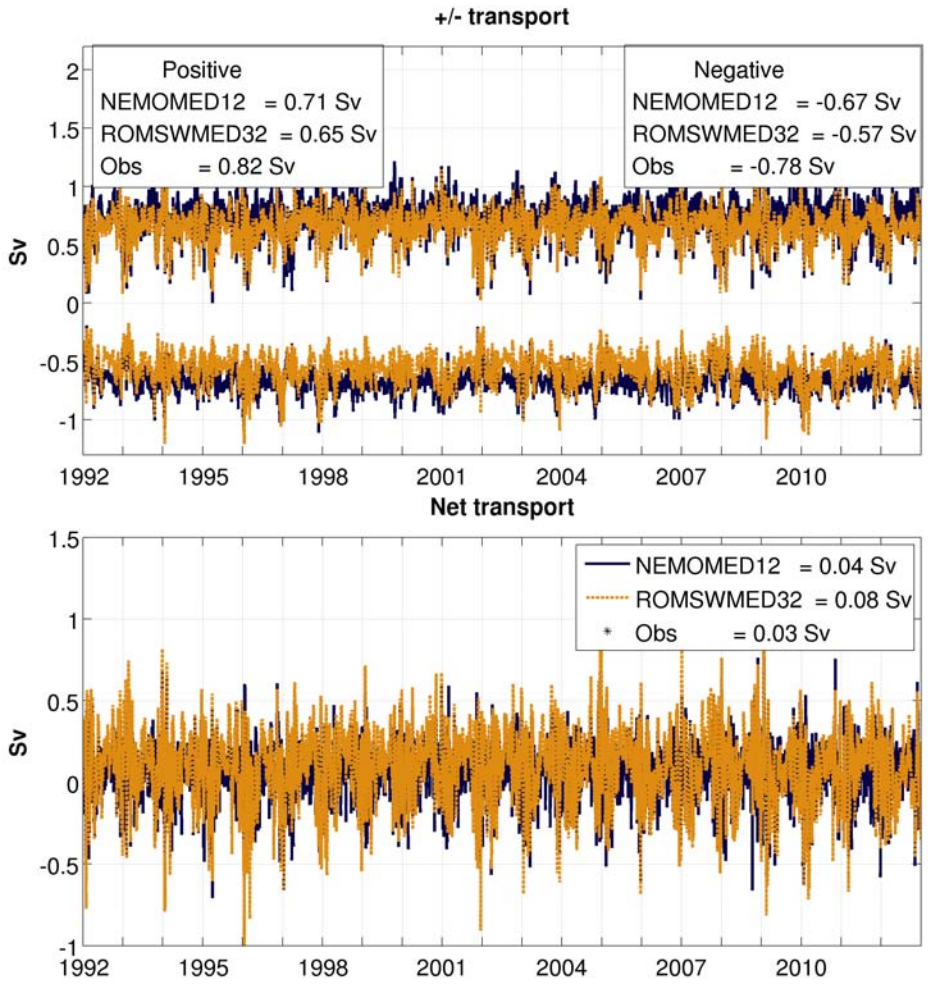

Figure 4.12: Transport of water through the Gibraltar Strait. Positive (inflow) and negative (outflow) are plotted on the right hand side and the net transport is on the left hand side. NEMOMED12 transport is indicated in blue while ROMS transport is in yellow. Observations estimates are taken from (Criado-Aldeanueva et al., 2012).

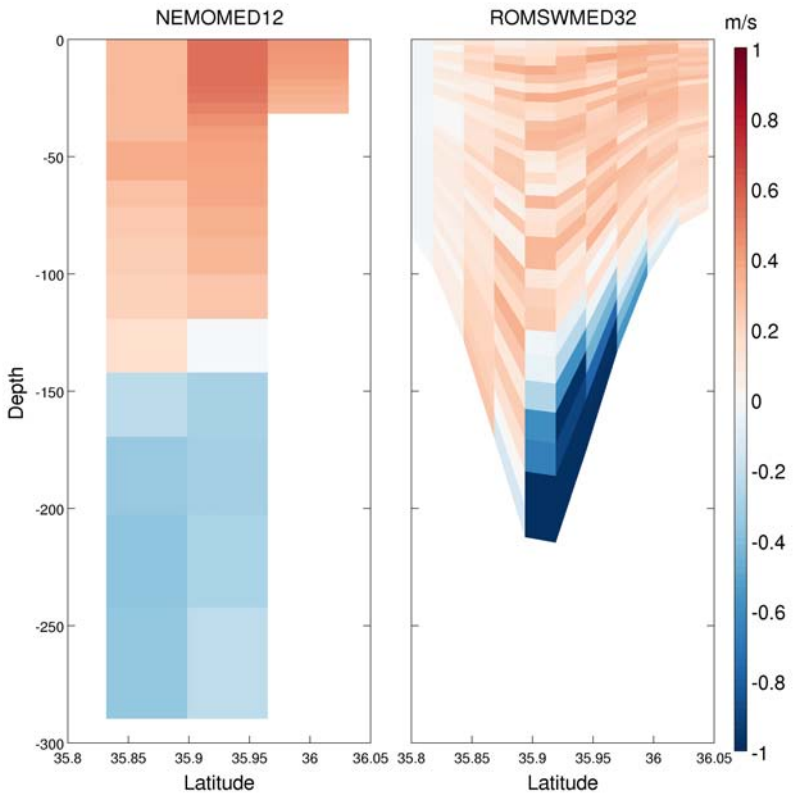

Figure 4.13: Mean section of zonal velocities in the Gibraltar Strait for the two different simulations (NEMOMED12 and ROMSWMED32) at longitude 5.8°W.

4.8 Spectra

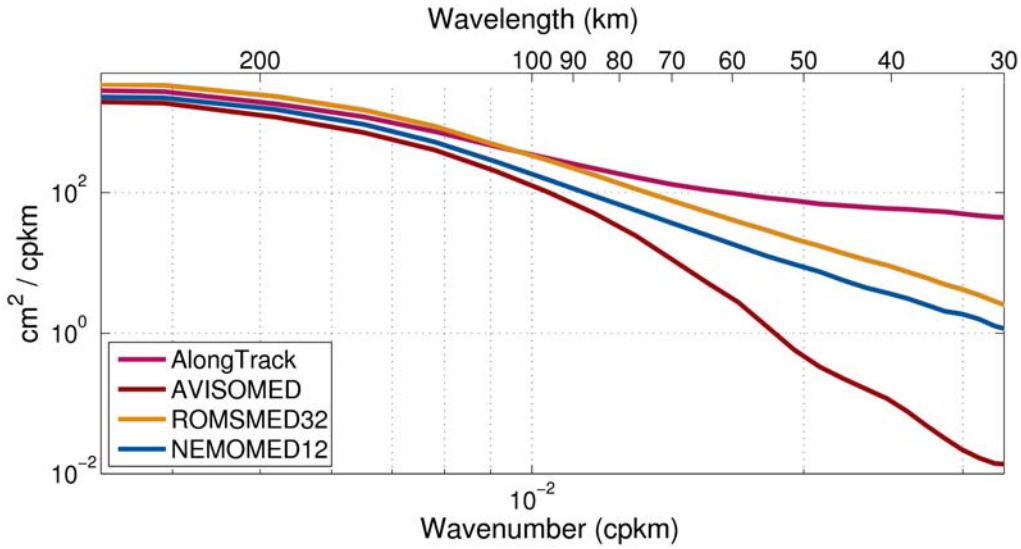

Figure 4.14: Power spectra of the SLA at the altimetric track location for different datasets.

The spatial scales represented in the different simulations are examined with the power spectrum of SLA from each of the different datasets (figure 4.14). The along-track data display the most energy at all wavenumbers, these being the unfiltered data with only the atmospheric and the orbit corrections. The power spectrum decreases at a steady rate for the large scales and then becomes relatively flat at wavelengths shorter than about 60 km which corresponds to observational noise. We focus on the 30-90 km band which is where we want to improve the representation in the simulation. For this range, the energy from AVISOMED08 exhibits a sharp decline due to the smoothing applied to the dataset (Pujol and Larnicol, 2005). ROMSWMED32, on the contrary, has a regular decrease of energy that seems to correspond to the decrease of the along-track for larger scales (out of the noise band). NEMOMED12 has less energy in this band, which is explained by the lower

grid resolution of the model that does not allow it to fully resolve the mesoscale variability in this region. However, since there is no smoothing applied, the energy level in both models is higher than AVISOMED08.

4.9 EKE

The EKE is defined as the KE that is due to transient dynamics. The KE is given by:

$$KE = \frac{1}{2}(u^2 + v^2) \tag{4.1}$$

and therefore, we can compute EKE by:

$$EKE = \frac{1}{2}((u - \bar{u})^2 + (v - \bar{v})^2) \tag{4.2}$$

with $\bar{u}$ and $\bar{v}$ the mean currents. Figure 4.15 shows the mean EKE computed from geostrophic velocities u_g and v_g defined in terms of SSH ζ as:

$$\begin{aligned} u_g &= -\frac{g}{f}.\frac{\partial \zeta}{\partial y} \\ v_g &= \frac{g}{f}.\frac{\partial \zeta}{\partial x}, \end{aligned} \tag{4.3}$$

whrere g is the gravitational acceleration and f is the coriolis parameter. Although the levels of EKE in figure 4.15 are quite different between the datasets, the geographical distributions are similar. As described in the introduction, the strong EKE is found at the locations of strong KE associated with mean currents meaning that the principal origin for these eddies are baroclinic or barotropic instabilities of permanent currents. EKE computed from AVISOMED08 is much weaker than EKE from drifters. The drifters may overestimate the energy due to residual wind-driven and non-geostrophic currents (Poulain et al., 2012) but this cannot explain all the differences. The levels of EKE in NEMOMED12 are also weaker, close to the values of altimetry, but the new high resolution simulation gives energy values that are more consistent with drifters estimates. This will have to be verified in the future but altimetry (and NEMOMED12) clearly underestimates the energy of mesoscale

dynamics in the region. This is likely attributable to the inability of gridded altimetry to resolve wavelength scales shorter than about 50 km (see figure 4.14).

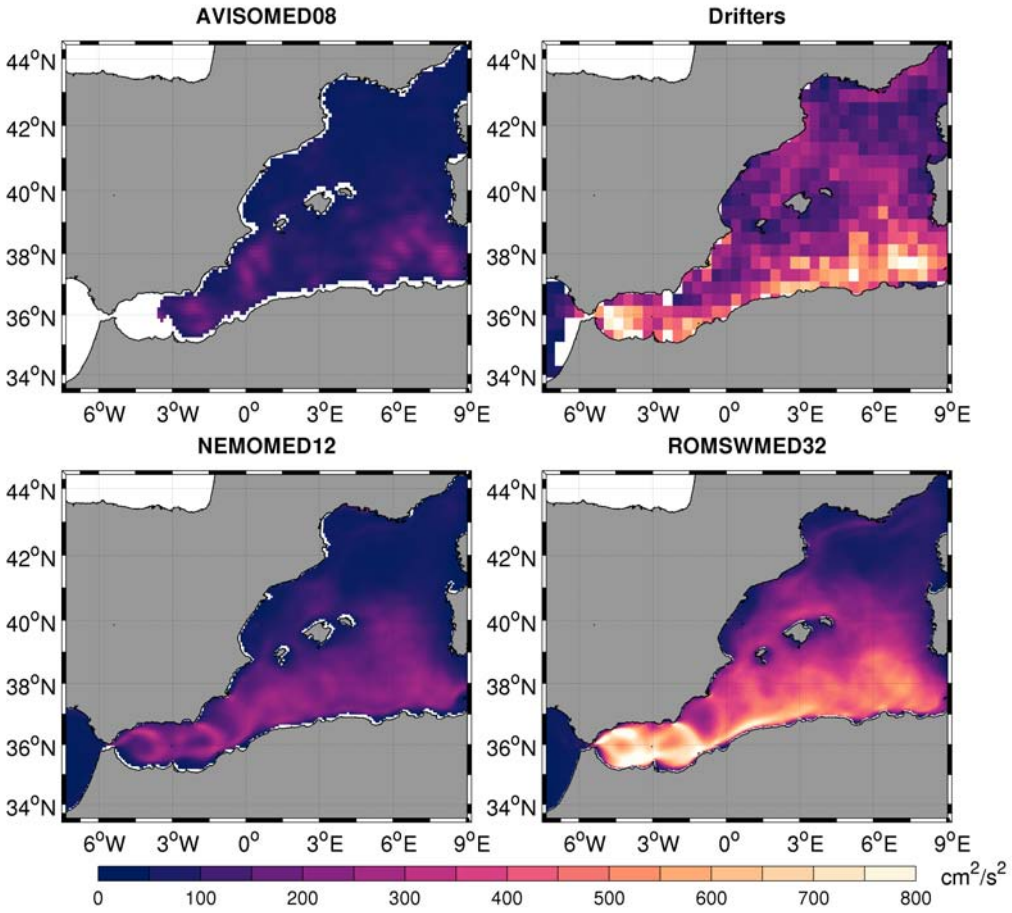

Figure 4.15: Comparison of mean EKE over the period 1992-2012 for AVISOMED08 (top left), drifter data (top right), NEMOMED12 (bottom left) and ROMSWMED32 (bottom right). Drifter data come from the database compiled by Poulain et al. (2012).

4.10 Eddy heat transport

With the high values of mesoscale activity shown in figure 4.15, it is interesting to look at the heat and salt transports due to these structures which since they impact the climate and characteristics of the region. The time-mean oceanic heat balance integrated over the upper ocean is:

$$\mathcal{T} = \mathcal{A} + \mathcal{Q}_{atm} + \mathcal{D} \tag{4.4}$$

where $\mathcal{Q}_{atm}$ is the net heat flux coming from the atmosphere, the heat storage trend $\mathcal{T}$ is:

$$\mathcal{T} = \int_{z_0}^{\eta} \rho_0 C_p \partial_t \overline{T} dz \tag{4.5}$$

and tends to 0 when averaged over long time periods. The boundary condition at the depth z_0 is:

$$\mathcal{D} = -\rho_0 C_p \overline{\kappa_\nu \partial_z T}|_{z_0} \tag{4.6}$$

and is negligible below the boundary layer. The last component of the equilibrium is then the heat advection $\mathcal{A}$ defined as:

$$\mathcal{A} = -\int_{z_0}^{\eta} \rho_0 C_p \nabla . \overline{\mathbf{u}T} dz \tag{4.7}$$

This advection term can be separated into the mean component and the eddy component and therefore:

$$\begin{array}{ccccc} \mathcal{A} = & -\int_{z_0}^{\eta} \rho_0 C_p \overline{\mathbf{u}}\,\overline{T} dz & - & \int_{z_0}^{\eta} \rho_0 C_p \overline{\mathbf{u}'T'} dz \\ = & \mathcal{A}_{mean} & + & \mathcal{A}_{eddy} \end{array}$$

Zonal and meridional heat transports by the main currents and by eddy dynamics are presented in figure 4.16. The heat transport by mesoscale dynamics is much stronger (one order of magnitude) than the transport by the mean currents. Values of meridional and zonal transport almost compensate because

horizontal transport is the main component of the heat budget in the region (vertical heat transport is weaker).

Figure 4.17 shows the integrated heat transport. The meridional heat transport is integrated along constant latitudes and the zonal heat transport is integrated along constant longitudes. This figure confirms that eddy heat transport is much higher than the transport by the mean currents but there is no increase in the transport from NEMOMED12 to ROMSWMED32 in spite of higher levels of EKE. This is due to the fact that, on average over a long period, atmospheric forcings constrain the heat transport so that there is no net heat storage. The main difference between the simulations, in the meridional heat transport is a southward shift of the transport in ROMSWMED32, which in the southern region is explained by the closer proximity to the coast of the Algerian Current. For the zonal transport, even though the large scale patterns are similar between both simulations, ROMSWMED32 has high varibility with strong spikes.

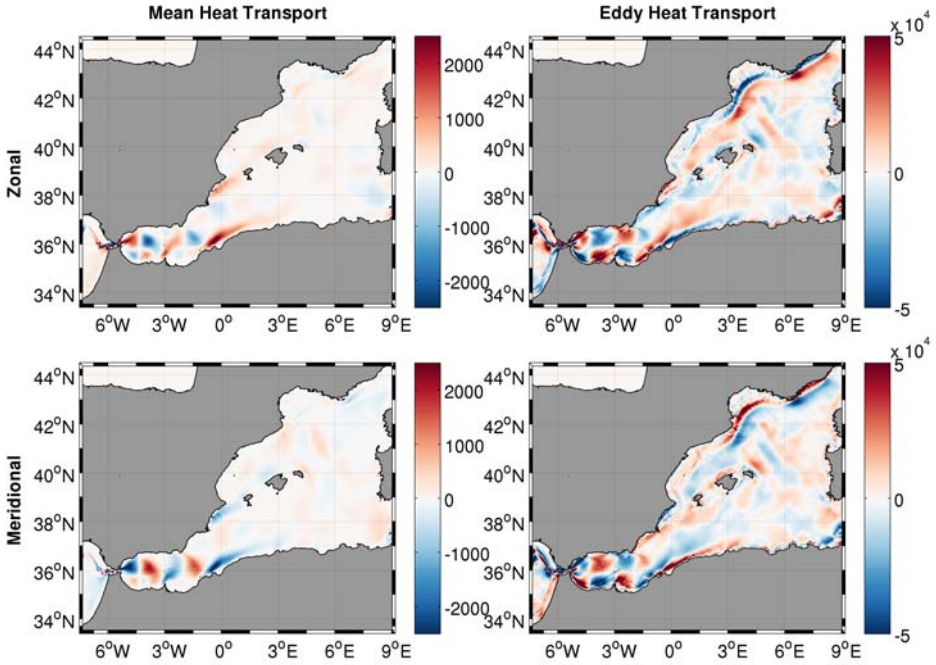

Figure 4.16: Heat transport by mean currents (left) and anomalies (right). The transport is separated into zonal (top) and meridional (bottom) components. The heat transport is given in W.m^{-2}

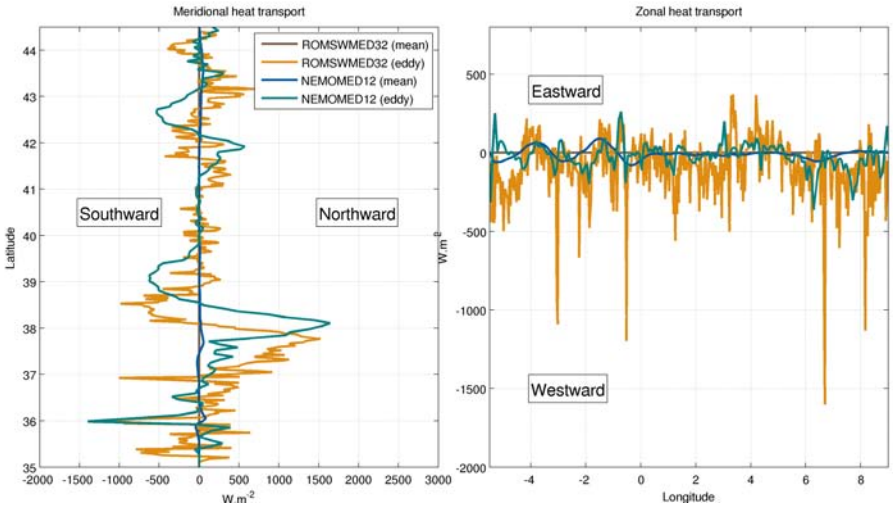

Figure 4.17: Zonal and meridional integrated heat transport in the WMed in the first 200 m.

4.11 Conclusion

In this chapter, we have used different observations (remote sensing, in-situ, drifters) and results from a realistic model (NEMOMED12) to validate the general characteristics of the ROMSWMED32 simulation. The general circulation of ROMSWMED32 outputs is coherent with data from satellite altimetry but also with previous knowledge from in-situ measurements. The transport in the Gibraltar Strait are consistent with NEMOMED12 but a little weaker than observations. The temperature and salinity patterns are realistic at the surface, and the values are stable and similar to observations the upper layers (down to 600 meters).

However, in the ROMSWMED32 simulation, there is a positive trend of heat and salt content in the deeper layers that may be due to the weaker transport in the Gibraltar Strait accumulating of warm and salty waters formed in the Western Mediterranean. This trend may also explain the very weak deep water convection when compared to NEMOMED12. Yet, these limitations of the simulation do not impact our study as we are interested in the mesoscale eddies at the surface of the ocean. The simulation performs very well in this regard and we obtained a stable, long-term, ROMS simulation without data assimilation of the WMed.

Finally, the simulation exhibits more energy in the mesoscale frequency band than smoothed gridded altimeters SLA maps and NEMOMED12 which is what was intended by the design of this high resolution simulation. The levels of EKE are much higher than altimetry (two or three times higher) and are comparable to the EKE computed from drifters, meaning that previous studies based on altimetry have been underestimating

mesoscale activity in the region. Indeed, the small Rossby radius in the area makes it difficult for altimetry to detect all the mesoscale activity.

Chapter 5

One step towards better observational data: High resolution altimetry

Contents

5.1 Objective

In the previous chapter we have shown that, although gridded altimetry data (AVISOMED08) gives relevant information on the surface ocean currents, it lacks resolution for the study of mesoscale in areas with small Rossby radius like the Mediterranean (Nencioli et al., 2011). Yet, the along-track data contains information about the mesoscale (see also Bouffard et al. 2010) that is filtered out in the OI process. Studies on along-track data do not allow automatic identification and tracking of coherent structures and optimal mapping techniques tailored to the WMed dynamics are required. In this study, we aim at the design of a new method of optimal interpolation of the altimeter along-track data to make 2D maps of SSH with a higher resolution of the mesoscale in the WMed. Since this region is strongly constrained by the topography and coastline, we include a bathymetric constraint in the optimal interpolation.

5.2 Escudier et al. 2013

This chapter was published in Geophysical Research Letters (Escudier et al., 2013). It is available at `http://onlinelibrary.wiley.com/doi/10.1002/grl.50324/full`

5.3 Conclusions and perspectives

In this study, we showed that is was possible to improve the gridded altimetry maps by adding small scale information that is smoothed by the standard processing and including a bathymetry constraint. The method was tested in the North WMed and results reveal that the new maps compare better

with drifter data and have higher EKE. The resulting EKE can also be compared to the one we obtained for the model and we see that the higher levels of energy are coherent with the model and the locations of the increased energy are also consistent with the simulation, *e.g.*, the Northern Current area.

However, the gridded fields we obtained do not have homogeneous resolution and accuracy, and the improvements are mainly concentrated around the along-track data around the time of the satellite passage. This can be useful for specific studies that are close in space and time to altimetry tracks. For our objective of synoptic study of mesoscale however, the inhomogeneity of this higher resolution altimeter dataset is not adequate.

These gridded fields have also been used in a study by Bouffard et al. (2014) whose article is repoduced in annex A. In this study, the authors used a lagrangian method to compare the different altimetry-based maps. This method compares the result of the advection of particles with an advection scheme and the altimetry fields with the actual trajectories of in-situ drifters. The results confirm the improvement of the representation of mesoscale with bathymetry constraint we developed. However, there are still some issues, mainly due to the coastal difficulties and the intrinsic limitation of altimetry, due to the spatial and temporal resolution of the actual constellation of altimeters (the distance between tracks and the time between passage of the satellites).

Another study used the method described in this chapter in a different region. In an article submitted to Advances in Space Research and reproduced in annex B, Gómez-Enri et al. (2015) used the datasets computed with the same method to detect the discharges of the river Guadalquivir in the Gulf of Cadiz.

Strong discharges of this river were shown to be associated with an increase of the water level which is not detected by the standard altimetry product. In the new product, however, the inclusion of along-track residuals allows the recovery of the lost signals of these discharges. Comparisons with remote-sensing ocean color show that the new dataset also reproduces the river plume.

In summary, an innovative method has been developed and successfully tested in different areas for specific studies but the altimetry data still possess some fundamental limitations for the global study of mesoscale variability in the Mediterranean Sea. The combination with other remote sensors, including wide swath altimetry and in-situ measurements is the promising method to obtain "eddy resolving" observations of the Mediterranean Sea.

Chapter 6

Eddy detection and tracking

Contents

6.1 Objective

In the previous chapters, we developed high resolution datasets of the WMed, the objective of this chapter is to characterize mesoscale eddies in these datasets. In this perspective, we apply automatic eddy detection algorithms to the data. The automatic detection of eddies is a powerful tool that allows us to extract relevant information about mesoscale eddies in datasets that contain a wide range of complex structures, scales and information. The results of these algorithms inform us about the number of eddies detected, and also their size, amplitude, position, etc. Statistical analysis can then be applied to the results to characterize mesoscale eddies in the region.

This type of study has been done in other areas, but in the Mediterranean, only the study by Isern-Fontanet et al. (2006) described an automated eddy detection applied to the first 7 years of altimetry data. This is mainly due to the small size of the mesoscale structures in the area that makes their systematic study difficult.

The datasets used are standard altimetry data maps (AVISOMED08), the numerical simulation NEMOMED12 (see section 3.6), and also the products we have developed: the high resolution model of the WMed (ROMSWMED32, see chapters 3 and 4) and, in a separate study due to differences in the area covered (only the NWMed) and period (2002-2012), the High Resolution (HR) altimetry product described in chapter 5. The study is focused on the 20 years of satellite altimetry (1993-2012) and on the WMed domain (7°W to 10°E, 34°N to 45°N).

The detection and tracking of eddies is performed with a modified version of the method described by Chelton et al.

(2011) but, in addition, two other methods are applied to validate the results. The goal is to characterize mesoscale eddies in the WMed, their size, amplitude, periodicity, distribution and vertical structure. Altimetry results will be our starting point but, as shown earlier, ROMSWMED32 has a better representation of the mesoscale in this region and will hopefully provide a more accurate description. The model also gives a 3D view of the detected eddies and allow us to study their vertical structure.

6.2 Methods and data

In this section, we will explain briefly the respective algorithms for the three methods that we used as well as how they were applied to the datasets. To limit the detection of spurious eddies, eddies with a lifetime shorter than 7 days are removed for all methods. This limit is somewhat arbitrary but is backed up by experience of observation of eddies in the region that have been shown to last only one week (Pascual et al., 2010). The tracking of eddies is used for the lifetime characterization and the selection of eddies but, in most of the analyse, we are not interested in the trajectories of particular eddies. Instead, we count an eddy each time (in this case, each day) it is detected on a map. This is motivated by the difficulties of tracking eddies in the area where there is no clear preferred direction of propagation and where mean currents can be strong. This can be considered as an Eulerian view in contrast to a Lagrangian one.

6.2.1 Detection method: Closed contours of SLA

The first method used to detect and track eddies in the datasets is the one developed by Chelton et al. (2011). This approach consists of detecting closed contours of SLA that include a local extremum and several other criteria, detailed below, to identify and track mesoscale eddies. In this method, an eddy is viewed as a coherent isolated vortex and therefore the corresponding SLA has the form of a bump or a hole. A detailed description of the method can be found in Chelton et al. (2011) but we present here its main steps (for anticyclonic eddies):

1. An upper threshold of SSH is fixed (100 cm)
2. The algorithm looks for a connected set of points that satisfy the following conditions:
   - They are all above the threshold specified.
   - There are at least 8 connected pixels and less than 1000.
   - In the region there are at least one local maximum.
   - The eddy amplitude is greater than 1 cm.
   - The distance between two points is less than a predefined maximum.
3. Any identified eddies are removed from the SSH field.
4. The threshold is decreased by 1 cm and steps 2 to 4 are repeated until reaching a threshold of 0.

The same process is used for cyclonic eddies but with a negative threshold (from -100 cm to 0 cm) and the connected points are below the threshold with a local minimum instead of a maximum.

This method was successfully applied to the global ocean and the global dataset is available at http://cioss.coas.oregonstate.edu/eddies/. However, a preliminary study of the results of this eddy detection and tracking method when applied to the Mediterranean Sea revealed that the method needed some adjustments to adapt to this region. Several issues were identified and modifications were applied to the algorithm in collaboration with Prof. D. Chelton and M. Schlax to the method to obtain a reliable dataset.

This method will be thereafter named the Modified eddy detection method from Chelton et al. (2011) (CHE11).

6.2.1.1 Contour closing and coastal issues

The first issue that appeared on the detected eddies can be seen clearly on figure 6.1 (top) that plots the centers of all the detected eddies. When compared to other detection methods such as the Okubo-Weiss method used by Isern-Fontanet et al. (2006), the method performs poorly in detecting eddies near the coast.

This issue comes from the need of the algorithm for a closed contour of SLA to identify an eddy. Therefore, an interpolation to a grid with a $1/12^\circ$ horizontal resolution and an extrapolation to the coast is performed prior to the detection process. This change permits the detection of eddies in regions much closer to the coast (see figure 6.1, bottom).

6.2.1.2 Tracking issues

Another issue we noted was the difficulty for the algorithm to properly track an eddy. In many cases, a movie of the eddy position with the SLA in the background showed the eddy center

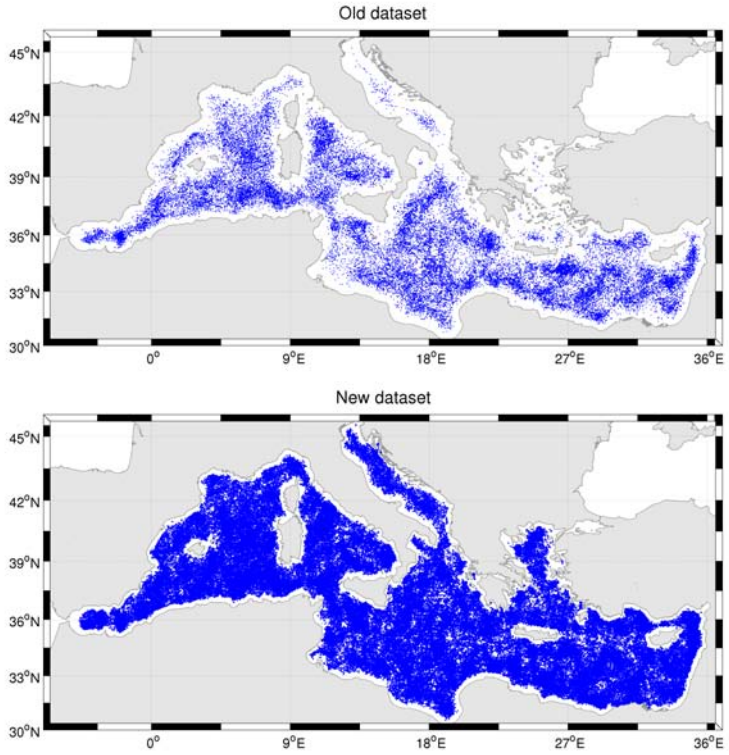

Figure 6.1: Position of the center of all detected eddies during the period 2002-2010. The top figure represents the eddies detected with the algorithm without the modification applied to address coastal issued. The positions presented in the bottom figure are of the eddies detected with the modified algorithm.

"jumping" from one eddy to another. Two main approaches were considered to try to solve this problem that is very tricky in this region since the eddies do not have a preferred direction of propagation.

- **Decreasing the search radius and isotropy**. The isotropy of the propagation of the eddies in this region called for a circular search rather than an ellipse as used for the global ocean (Chelton et al., 2011). The search radius was also decreased to account for the relatively slow propagation speeds of the eddies.

- **Use of daily products**. The most effective way to avoid the errors in the tracking was to use the daily product (new product in the AVISO website) instead of the weekly one (standard product). This allows a reduction the distance travelled by the eddies and therefore the possibility of errors.

6.2.1.3 Removal of non-eddy shapes

Some of the shapes detected by the algorithm seemed to be non eddy-like: long filaments or crescents instead of more round or oval shapes. Therefore another criterion was added to the method that is defined as following (see also figure 6.2). Two values were considered, the aspect ratio (x-axis of the plot on the right) and the effective radius-based ratio (y-axis of the plot on the right). The aspect ratio is the ratio of the major to minor semi-axes of the ellipse constructed from the detected eddy (in red on the left of the figure). The effective radius-based ratio is the percentage of pixels of the eddy that lie outside the effective radius when centered on the maximum (minimum) of the ellipse (in purple on the left of the figure). The contours on the plot show the fraction of their bivariate histogram that lies above each contour, which means that 70% of the eddies have an aspect ratio and effective radius-based ratio that lie within the 0.7 contour. Eddies are rejected then when they are outside the 0.7 contour and therefore, 30% of the originally detected eddies are rejected. In the example in the figure, the top eddy is kept whereas the bottom one is rejected. This means that the algorithm will move to the next step of the detection and detect two eddies instead of one in the example. This criterion also has the advantage of removing a lot of cases where two

eddies where detected as only one large eddy.

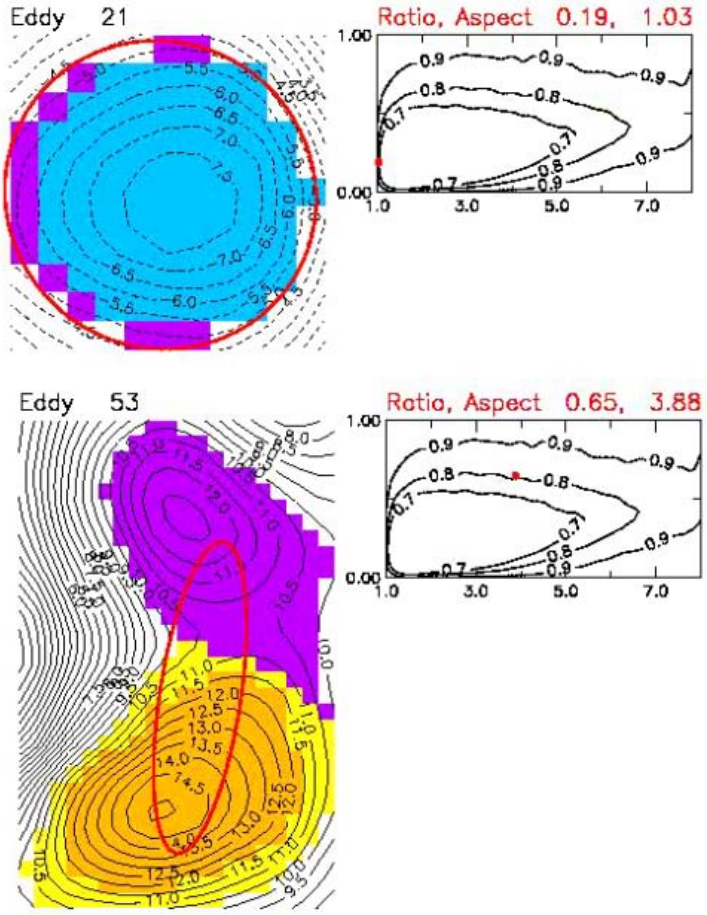

Figure 6.2: Example of the non-eddy shape criterion. The top panel shows an accepted eddy and the bottom one a rejected one.

6.2.2 Other methods

To give more robustness to the results obtained with the CHE11 method, we used two other algorithms for eddy detection and tracking.

6.2.2.1 Method 2: Inversion of velocities

The second method used to detect and track eddies in the WMed is based on the geometry of surface velocities. The description of the algorithm and its application can be found in Nencioli et al. (2010) but we will try to summarize the method. The objective is to detect a region where the velocity field rotates around a center. Therefore, four constraints are defined that the detected centers have to respect:

1. Along an east-west (EW) section, y must reverse sign across the eddy center and its magnitude has to increase away from it;

2. Along a north-south (NS) section, u must reverse sign across the eddy center and its magnitude has to increase away from it: the sense of rotation has to be the same as for y;

3. Velocity magnitude has a local minimum at the eddy center;

4. Around the eddy center, the directions of the velocity vectors have to change with a constant sense of rotation and the directions of two neighboring velocity vectors have to be within the same or two adjacent quadrants (the four quadrants are defined by the north-south and west-east axes: the first quadrant encompasses all the directions

from east to north, the second quadrant encompasses the directions from north to west, the third quadrant encompasses the directions from west to south, and the fourth quadrant encompasses the directions from south to east).

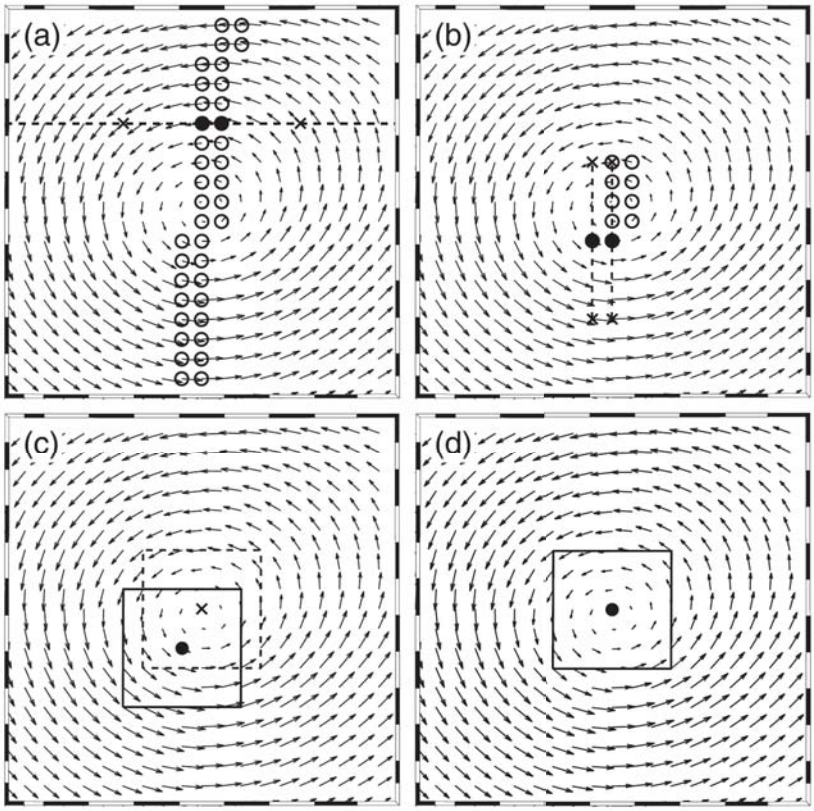

Figure 6.3: Image extracted from Nencioli et al. (2010).(a) First, (b) second, (c) third, and (d) fourth constraint applied to the vectors within the box of an example. The first constraint is applied to all latitudinal sections (the one indicated by a dashed line is used as example in the text). The second and third constraints are applied only to the points for which the previous one is satisfied. The point for which the fourth constraint is satisfied [the dot in (d)] indicates the position of an eddy center.

These constraints are tuned by two parameters a and b. The number of points inspected for the inversion in EW or NS (constraints 1. and 2.) as well as for the curve for constraint 4 is

given by a. The other parameter b determines the size of the area in which we look for the local minimum in constraint 3

Since we are comparing this method with others that rely on SLA and we want to apply it to altimetry maps, the velocities used in this study are geostrophic velocities computed from the SLA with the equation of the geostrophic equilibrium:

$$u_g = -\frac{g}{f}.\frac{\partial \zeta}{\partial y} \tag{6.1}$$

$$v_g = \frac{g}{f}.\frac{\partial \zeta}{\partial x} \tag{6.2}$$

with g the acceleration of gravity, f the Coriolis parameter and ζ the SSH. The discretization of the equations are done with a centered difference scheme.

The MATLAB code proposed by Nencioli et al. (2010) did not give an estimation of the radius of the detected eddies. Since we wanted to compare different methods, and the other methods we use do have this estimate, we used the same formula to compute it as the method by Chelton et al. (2011). The radius R is defined as that of a circle that has the same area as the detected region,

$$R = \sqrt{\frac{\mathcal{A}_{eddy}}{\pi}} \tag{6.3}$$

The tracking is done in a classical manner. After eddy detection over the whole period of interest, the algorithm goes back to time $t = 1$ and for each eddy, the next position of the eddy (with the same rotational direction) is searched for at the next time step in an area of NxN grid points centered at the position of the eddy. The value of N is very important as the tracking accuracy is very sensitive to it, an estimate is made by multiplying the average current speed by the time step. If the continuation of the eddy is missed at time $t + 1$, a search

is made at $t+2$ with an increased search radius to avoid losing the eddy track. In the case of more than one eddy being found in the search area at $t+1$, the closest one is selected.

This method will be named hereafter as the Eddy detection method from Nencioli et al. (2010) (NEN10).

6.2.2.2 Method 3: Okubo-Weiss and geometry

The third method employed is the one described by Halo et al. (2013). This method combines the geometric criteria as in the method of Chelton et al. (2011) and traditional methods (*e.g.* Isern-Fontanet et al. 2006, Chelton et al. 2007, Penven et al. 2005) based on local deformation properties of the flow such as the Okubo-Weiss parameter. The Okubo-Weiss (Okubo, 1970; Weiss, 1991) parameter is defined as:

$$W = S_n^2 + S_s^2 - \xi^2 \qquad \text{with} \qquad \begin{cases} S_n &= \frac{\partial u}{\partial x} - \frac{\partial v}{\partial y} \\ S_s &= \frac{\partial v}{\partial x} + \frac{\partial u}{\partial y} \\ \xi &= \frac{\partial v}{\partial x} - \frac{\partial u}{\partial y} \end{cases} \tag{6.4}$$

where S_n and S_t are the normal and shear components of the strain and ξ, the relative vorticity. In this method, a geostrophic or mesoscale eddy is contained within a closed loop of SLA and dominated by vorticity ($W < 0$). Therefore, the algorithm works as follows:

1. After two passes of a Hanning filter, the W field is used to find regions where vorticity dominates.

2. Regions inside a closed loop of SLA are selected.

3. Regions that combine the two criteria are determined to be geostrophic eddies.

In their article, Halo et al. (2013) advise using the algorithm on SSH data rather than SLA but, to be more coherent with the other methods such as CHE11, we decided to use SLA data. The main reasons they present which advocate for the use of SSH are the detection of spurious meanders and permanent eddies. In our region, the only permanent eddies are the Alboran

gyres which we will not study and we did not see the detection of spurious meanders.

In this method, the only parameter to tune is the interval between the contours for closed loop detection which we fixed at 1 cm as in the CHE11 method.

The tracking algorithm was proposed by Penven et al. (2005) and relies on a generalized distance between the two eddies $e1$ and $e2$ defined as:

$$X_{e1,e2} = \sqrt{\left(\frac{\Delta X}{X_0}\right)^2 + \left(\frac{\Delta R}{R_0}\right)^2 + \left(\frac{\Delta \xi}{\xi_0}\right)^2} \tag{6.5}$$

where ΔX is the distance between the two eddies, ΔR is the variation of diameter and $\Delta \xi$ is the variation of vorticity. We fixed the value of the parameters at $X_0 = 100km$ for the characteristic length scale, $R_0 = 50km$ for the characteristic radius and $\xi_0 = 2.10^{-5}$ for the characteristic vorticity. $X_{e1,e2}$ is considered infinite if there is a change of sign in the vorticity to make sure a cyclonic eddy cannot turn into an anticyclonic eddy (and vice-versa).

This method will be named hereafter as the Eddy detection method from (Halo et al., 2013) (HAL13).

6.2.3 Datasets

We recall here the datasets used for this study which are synthesized in table 6.1.

6.2.3.1 AVISOMED08

The first dataset to which we applied the detection methods is the gridded altimetry maps provided AVISO. These maps are obtained by an OI of the along-track data from satellite altimetry as explained in section 4.2. The data represented by

these maps is the SLA of the Mediterranean and the algorithms of detection and tracking are performed in the WMed region. The period of altimetry data covers 1993-2012.

6.2.3.2 NEMOMED12

We used the SSH outputs of the NEMOMED12 simulation described in section 3.6 from which we extracted the SLA. This simulation's resolution is 1/12° which is not high enough to fully resolve mesoscale dynamics in a region where the Rossby radius is around 10km. Indeed, a study on a similar simulation (PSY2V4, model NEMO with 1/12° resolution) by MERCATOR-OCEAN found that the effective resolution was 45 km at the latitudes of the Mediterranean Sea (Mercator Quaterly Newsletter #49, April 2014) Although the simulation covers all of the Mediterranean, we focus here on the WMed area.

6.2.3.3 ROMSWMED32

The last dataset comes from the simulation (ROMSWMED32) developed in the framework of this thesis (see chapter 3). It is a high resolution simulation of the WMed at 1/32° with the ROMS model. We expect this simulation to be more eddy-resolving as it was found to have more energy in the mesoscale band (see sections 4.8 and 4.9). The work of Marchesiello et al. (2011) deduced that for the ROMS simulations, the effective resolution was about seven times lower than the grid resolution which means that the effective resolution of our simulation should be around 20 km.

Dataset	AVISOMED08	NEMOMED12	ROMSWMED32	HR+BATHY
Resolution	1/8°(10-14 km)	1/12°(7-9 km)	1/32°(2.5-3.5 km)	1/16°(5-7 km)
Effective resolution	∼50 km	∼45 km	∼20 km	(40-50) km
Type	altimetry	model (NEMO)	model (ROMS)	altimetry
Variable	SLA	SLA	SLA	SLA
Area	WMed	WMed	WMed	North WMed
Frequency	daily	daily	daily	daily
Period	1993-2012	1993-2012	1993-2012	2003-2010

Table 6.1: Overview of the datasets used in the eddy tracking.

6.3 Results

The algorithms are then applied to the datasets. The outputs of these algorithms are: position of the center, radius, lifespan, direction of rotation (cyclonic or anticyclonic). Two of the algorithms (CHE11 and HAL13) also give the amplitude and rotational speed

6.3.1 Preliminary study on satellite altimetry

A first analysis was performed on the gridded satellite altimetry (AVISOMED08) with the CHE11 method in collaboration with Prof. Dudley Chelton and Mr. Michael Schlax (COAS, OSU, Oregon, United-States). We present here some results of this study that help introduce the main results.

6.3.1.1 Histograms

Figure 6.4, which should be compared with figure 9 in Chelton et al. (2011) (here reproduced in figure 6.5), shows that, for amplitude and rotational speed, the distributions of cyclonic and anticyclonic eddies are noticeably different. While the distribution of anticyclonic eddies for these parameters is similar to the whole northern hemisphere values, cyclonic eddies are less

likely to be strong in amplitude and speed. This can be explained by the presence of strong anticyclonic eddies formed in the Algerian Current that resemble the global northern ocean eddies, while in the rest of the basin, eddies (cyclonic or anticyclonic) are weaker.

There is no significant difference between the distribution of the eddy scale for cyclonic or anticyclonic eddies, but we can observe that values are very concentrated around 50 km which is the length of the spatial smoothing prior to the optimal interpolation of the gridded altimetry data (Pujol and Larnicol, 2005). This suggests that the smoothing constrains the eddies in this field to be around this value. The last panel on figure 6.4 indicates that there does not seem to be any correlation between the eddy scale and its amplitude, which is surprising as the strong Algerian eddies have been observed to be quite large.

6.3.1.2 Spatial distribution

Looking at the spatial distribution of eddies, no particular pattern seems to govern the position of eddies except that more eddies are detected in the southern region than in the north. Close to the coast, very few eddies are detected which may be due to the limitation of altimetry in the coastal band (*e.g.* Nencioli et al. 2011).

The amplitude and rotational speed spatial distribution are similar to the EKE distribution presented in figure 4.15. The high energy areas such as the Algerian Current are where the strongest eddies are generated. These strongest area are in the WMed, the Algerian Current and more acutely in its eastern part, and the Balearic Sea.

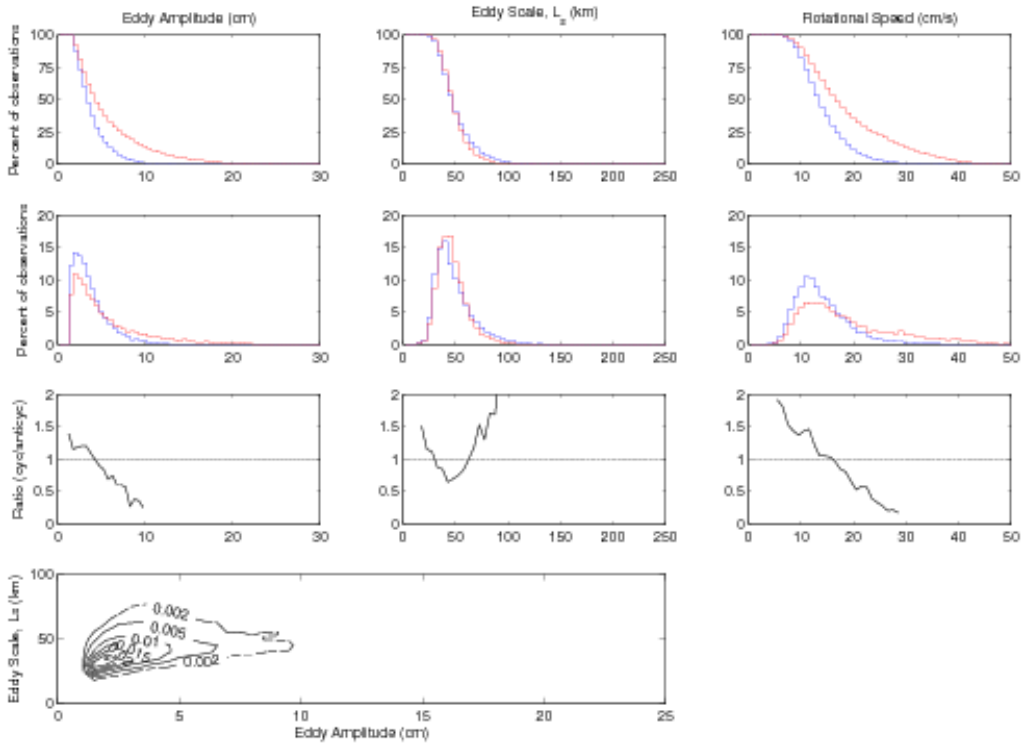

Figure 6.4: Distribution of eddy scale (left), amplitude (middle) and rotational speed (right) in the WMed. The first row panels show the upper-tail cumulative histograms while the second row panels present histograms and the third row panels show the ratios of cyclonic to anticyclonic eddies. For the two first row panels, cyclonic eddies are plotted in blue and anticyclonic eddies in red. The last panel shows the two-dimensional histogram of the joint distribution of the amplitudes A and scales L. The figure is similar to figure 9a in Chelton et al. (2011) reproduced in figure 6.5.

As for the mean radius, as expected, Algerian eddies are on average larger than eddies generated in other places, but the pattern is less comparable to the EKE.

6.3.1.3 Propagation

On figure 6.7, the spatial distribution of the preferred direction of propagation is plotted for the eddies detected in AVISOMED08. The eastward propagation of eddies advected by the Algerian current clearly appears in the figure, as well as

the northward detachment at 9°E. Along the French and Spanish coast, a south-westward direction of propagation stands out that may be correlated with the Northern Current. Other main currents, such as the eastward Balearic Current north of Mallorca also appear in this figure. In the center of the basin, a westward propagation preference is observed which is consistent with the theoretical propagation of an isolated vortex (McWilliams and Flierl, 1979). Since this region has weak permanent currents and no land, the theory could apply there.

6.3.1.4 Temporal evolution

A time series constructed from the number of detected eddies per day in the whole basin is presented on figure 6.8. This series does not take into account the tracking of the eddies since it only represents the number of eddies detected on a particular day. This means that every eddy is counted on each day of its life.

A temporal analysis of the time-series reveals a significant semi-annual cycle but no annual cycle (figure 6.9 top). To find a possible explanation for the lack of an annual cycle in the total number of eddies in the domain, we separated the eddies into short-lived eddies (lifetimes below four weeks, 65% of all eddies) and long-lived eddies (lifetimes above four weeks, 35% of all eddies). The analysis on these two subset reveals that they both have a significant annual cycle (figure 6.9) and a weaker semi-annual cycle.

Harmonic regressions of the time series onto annual and semi-annual frequencies give insight into why the annual cycle disappears in the full dataset (figure 6.10). In these regressions, we see that the annual cycles are in opposite phase for

short-lived and long-lived eddies, and that they have a similar amplitude. Therefore the sum of the two compensates to give a weak annual cycle.

In figure 6.10, we see that strong wind seasons correspond to strong short-lived eddy generation with a one to two month lag. Figure 6.11 presents another way of showing the collocation of the short-lived eddies and strong wind stress. The figure shows the mean and standard deviation of the number of eddies found in bins that have a wind stress value around the value on the axis. The decrease observed in the number of long-lived eddies when the wind stress becomes stronger suggests that they are more prevalent in weaker wind areas. Therefore, the hypothesis suggested is that short-lived eddies are shallow and unstable eddies generated by the wind, whereas long-lived eddies are deeper and more stable eddies that may come from instabilities of strong currents. An observation that tends to support this idea is that the long-lived eddies appear to be in regions where there are strong currents (e.g. Algerian current in the Western Mediterranean).

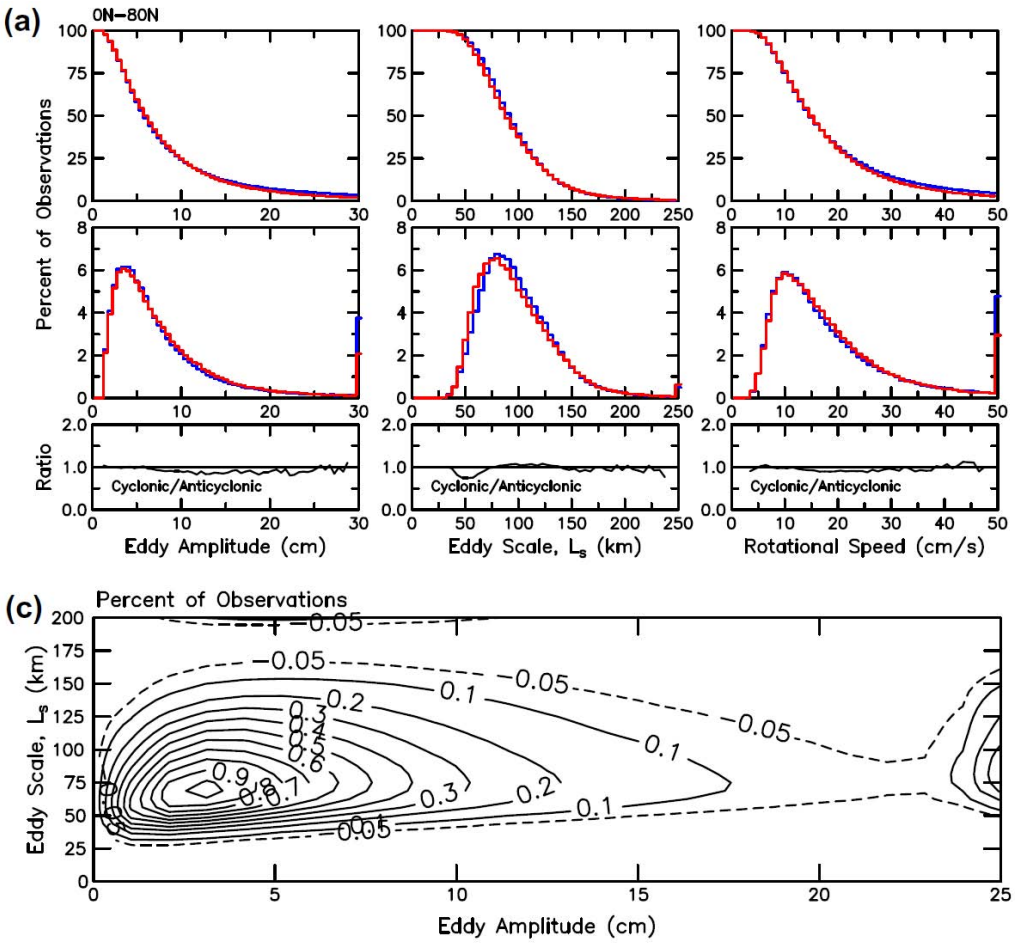

Figure 6.5: Distribution of eddy scale (left), amplitude (middle) and rotational speed (right) in the Northern hemisphere. The first row panels show the upper-tail cumulative histograms while the second row panels present histograms and the third row panels show the ratios of cyclonic to anticyclonic eddies. For the two first row panels, cyclonic eddies are plotted in blue and anticyclonic eddies in red. The last panel shows the two-dimensional histogram of the joint distribution of the amplitudes A and scales L. The figure is extracted from Chelton et al. (2011).

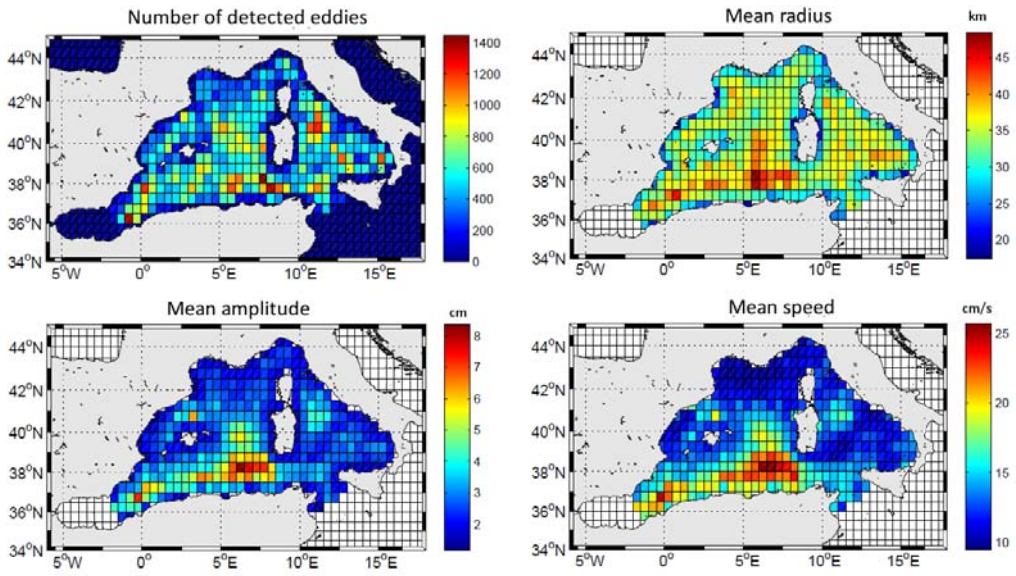

Figure 6.6: Spatial distribution of detected eddies (top left) computed by counting the number of eddies found in each cell of 1/2°. The top right panel presents the mean radius of these eddies in each cell, the bottom left panel the amplitude, and the bottom right the rotational speed.

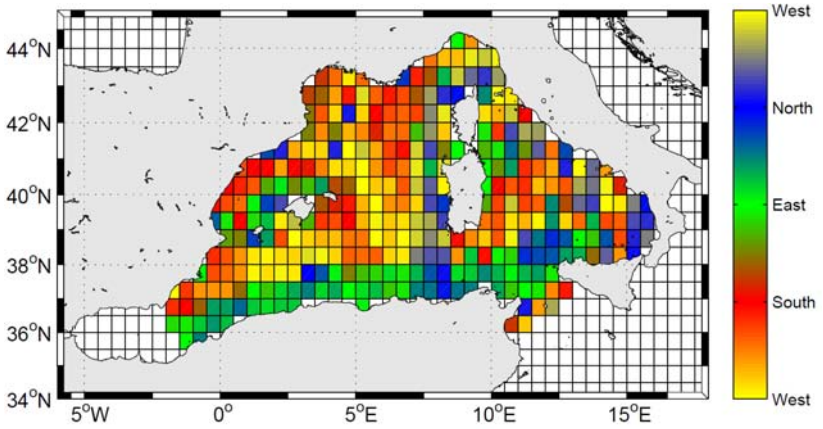

Figure 6.7: Spatial distribution of the direction of propagation of AVISOMED08 eddies computed in each cell of 1/2°.

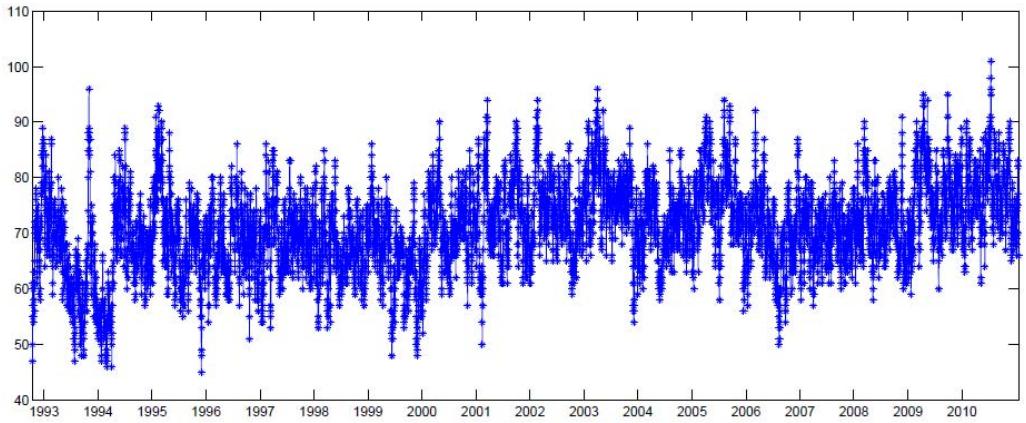

Figure 6.8: Time series of the number of detected eddies in the Mediterranean Sea from altimetry.

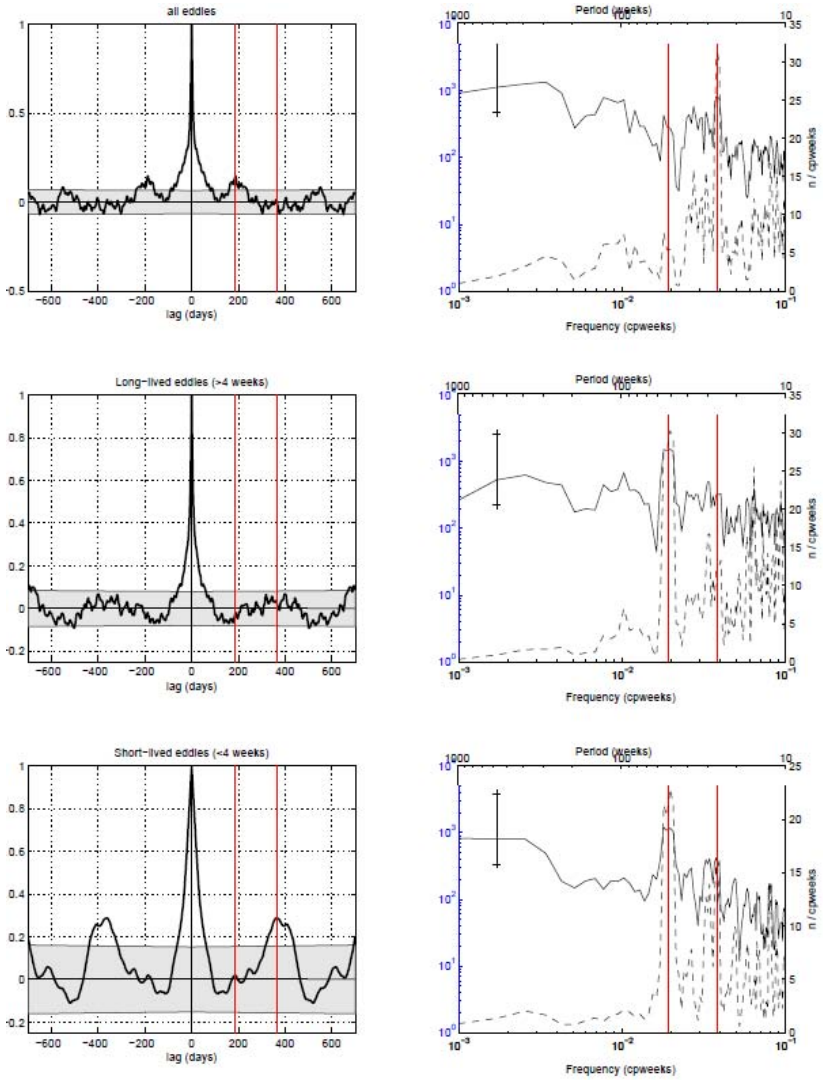

Figure 6.9: Autocorrelation (left) and power spectrum (right) of the numbers of eddies from the diifferent datasets. The annual and semi-annual cycle are shown in red. For the autocorrelation, significant correlations at the 95% level are above the grey area. For the spectra, the significance is indicated by the bar on the left. Dotted line shows the variance preserving spectra.

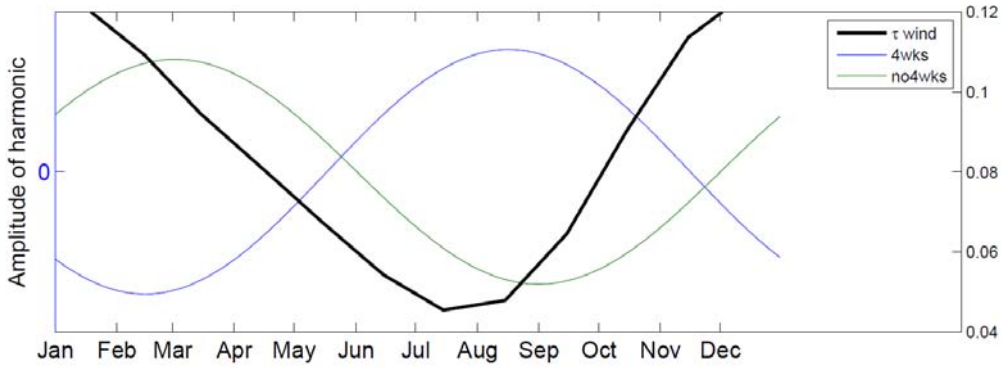

Figure 6.10: Climatology of the wind compared to the annual harmonic of the different datasets.

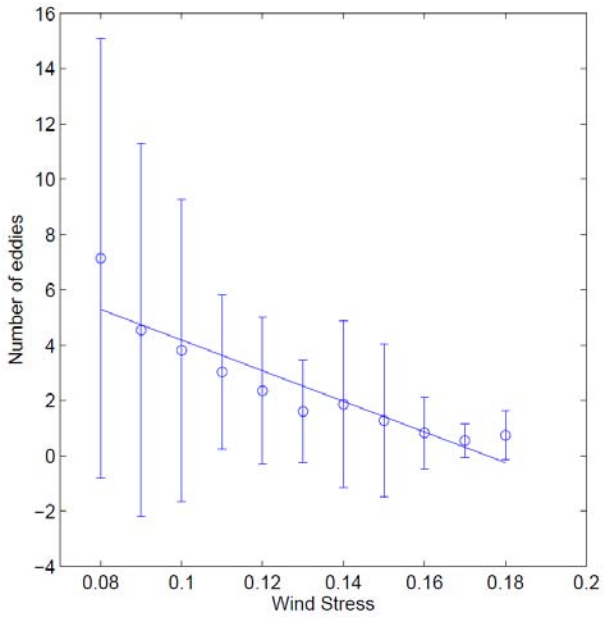

Figure 6.11: Comparison between the strength of the wind stress and the number of eddies with a lifetime longer than 4 weeks. The circle represent the mean of number of eddies in bins where the wind stress is the x-axis value. The bar is the standard deviation of the subset of eddies in each bin. The linear regression is indicated as well.

6.3.2 Application to simulations

We then applied all the detection algorithms to the three datasets available for the 20 year period: AVISOMED08 (remote sensing observations), NEMOMED12 (long-term simulation of the Mediterranean) and ROMSWMED32 (high resolution long-term simulation).

6.3.2.1 Statistics

Table 6.2 summarizes the outputs of the different eddy detection methods on the different datasets. The minimum lifetime is 7 days for all datasets and methods as we decided to remove eddies lasting for shorter times. The average lifetime and 95% point of lifetime distribution already illustrate the differences in the algorithms for the tracking of eddies. Focusing on each method independently, we remark that the lifetimes are, on average, higher in the HR model data (ROMSWMED32) than in the altimetry gridded field (AVISOMED08) and coarser model (NEMOMED12). This implies that either eddies live longer in the models or it may be that the increased resolution of the models allows for better detection and therefore tracking of the eddies.

As for the 5% minimum radii of the detected eddies, the CHE11 and HAL13 algorithms give similar values and the NEN10 algorithm gives lower values. This is probably due to the method used in the NEN10 algorithm to detect the shape of the eddies. We observe that this 5% minimum is similar in NEMOMED12 and AVISOMED08, consistent with their effective resolution being similar, and lower for the ROMSWMED32 model. This result is coherent with the increase of the resolution that enables the presence of smaller structures. The

Data & Method		Mean life (days)	95% life	5% Radius (km)	95% Radius (km)	Cyclonic precent.	Nb eddies	Nb unique eddies
AVISOMED	CHE11	36	121	23	57	49.2	105205	6181
	NEN10	30	93	13	41	49.2	98701	6211
	HAL13	55	187	23	47	50.6	104079	5029
NEMOMED12	CHE11	73	221	22	84	51.4	117708	4256
	NEN10	55	174	12	48	45.6	136581	6172
	HAL13	25	69	18	51	57.3	88943	5755
ROMSWMED32	CHE11	151	568	13	64	52.7	250771	7944
	NEN10	55	217	9	44	47.8	214325	10126
	HAL13	66	255	10	48	57.8	284123	12899

Table 6.2: Eddy detection results. The first two columns present the minimum and maximum life of detected eddies in days, the third and fourth their minimum and maximum radius, the fifth the percentage of cyclonic eddies found, the sixth the total number of eddy-shape structures identified in the maps and the seventh is the number of unique eddies revealed by the tracking.

95% value of the radii distribution varies around 50 km except for the CHE11 method on NEMOMED12 where it reaches 84 km. This value is much larger that of the others and may be an issue of the detection method. There is no increasing or decreasing pattern between datasets because the resolution should not impact the size of the largest eddies that are well above the resolution limit for the models and the smoothing for the observations.

The cyclonic percentage of detected eddies is very close to 50% in all of our data but for the CHE11 and HAL13 methods, it is greater in the models than in the altimetry data. For the NEN10 algorithm, on the contrary, the cyclonic percentage is smaller for the models than in the altimetry-detected eddies and therefore we cannot conclude anything in this regard.

The total number of detected eddies (with no tracking involved except for the rejection of eddies lasting less than 7 days) is found to be between 98,000 and 105,000 for the AVISO maps with all the methods. The number of unique eddies is around 6,000 for CHE11 and NEN10 and smaller (5,000) for HAL13, meaning that the tracking seems to work differently. On the NEMOMED12 model, we find that the number of detected eddies is not higher than in AVISOMED08 for all the methods, ranging between 90,000 and 136,000 eddies. In the ROMSMED32 simulation, on the other hand, there are more detected eddies than in the other datasets for all methods, ranging from 215,000 to 285,000. This is encouraging as we expected an increase of mesoscale eddies due to the increase of resolution of the model.

6.3.2.2 Histograms

To assess the validity of the results of the eddy detecting and tracking methods, we look at the distribution of eddies according to their size for the 3 datasets and the 3 methods (figure 6.12). The radii given by the different methods have different distributions: the NEN10 method detect always smaller eddies as noted above which is related to the way of detecting the shape of the eddies. Looking at instantaneous maps, we can see that the eddies are mostly the same but the shape has a lesser extension. The CHE11 method detected a higher number of large eddies than the other two methods with the model outputs, also highlighting differences in the detection of shapes.

We observe that, consistently with the three algorithms, smaller eddies are detected in the higher resolution model (ROMSWMED32) than in NEMOMED12 or the altimetry dataset (AVISOMED08) confirming the result found with the 5% minimum. For the altimetry product, the detected eddies are found to have radii of mainly around 30 km with both CHE11 and HAL13 and 20 km with NEN10. For NEMOMED12, the distribution maxima are between 20 km and 35 km while for ROMSWMED32, the maxima are between 20 and 25 km.

In figure 6.12, the distribution of the lifetime of eddies is also plotted. This distribution decreases rapidly, and half of the detected eddies have lifespan below 30 days for altimetry, between 20 days (HAL13), 35 days (NEN10) and 50 days (CHE11) for NEMOMED12, and 50 days (NEN10 and HAL13) or 75 days (CHE11) for ROMSWMED32. The algorithms give different results but the shape of the distribution is similar and there are eddies with higher lifetimes for the ROMSWMED32 simu-

lation as already noted above.

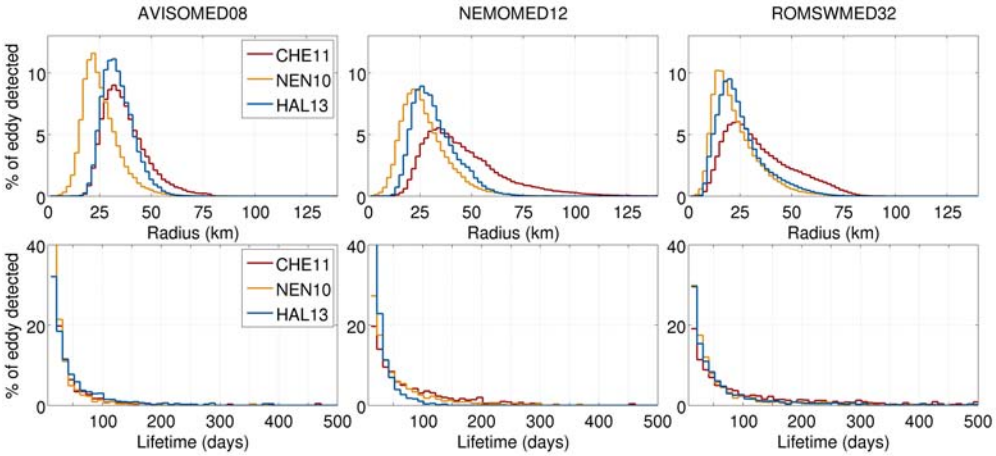

Figure 6.12: Distribution of the detected eddies according to size (1st row) and lifetime (2nd row) for AVISOMED08 (altimetry, 1st column), NEMOMED12 model (2nd column) and ROMSMED32 (3rd column)

6.3.2.3 Spatial distribution

We can also study the spatial distribution of the detected centers for the whole 1993-2012 period (figure 6.13). For the AVISOMED08 data, the location of the detected eddies is very comparable between the 3 methods. We can note that the NEN10 method detects more eddies in the northern part of the basin, namely the Balearic Sea and the Liguro-Provencal basin. For NEMOMED12, the three algorithms present a similar picture except for the Gulf of Lion where very few eddies are detected in the case of HAL13. Still, the NEN10 method detects more eddies than the others as noted previously. In the ROMSMED32 simulation, the previous result that more eddies were detected is again clearly noticeable (notice the change of scale), but this time, the figure allows us to see that the increase in eddy numbers is concentrated in the northern part of

the basin. The Northern Current seems to generate a higher number of eddies in ROMSWMED32.

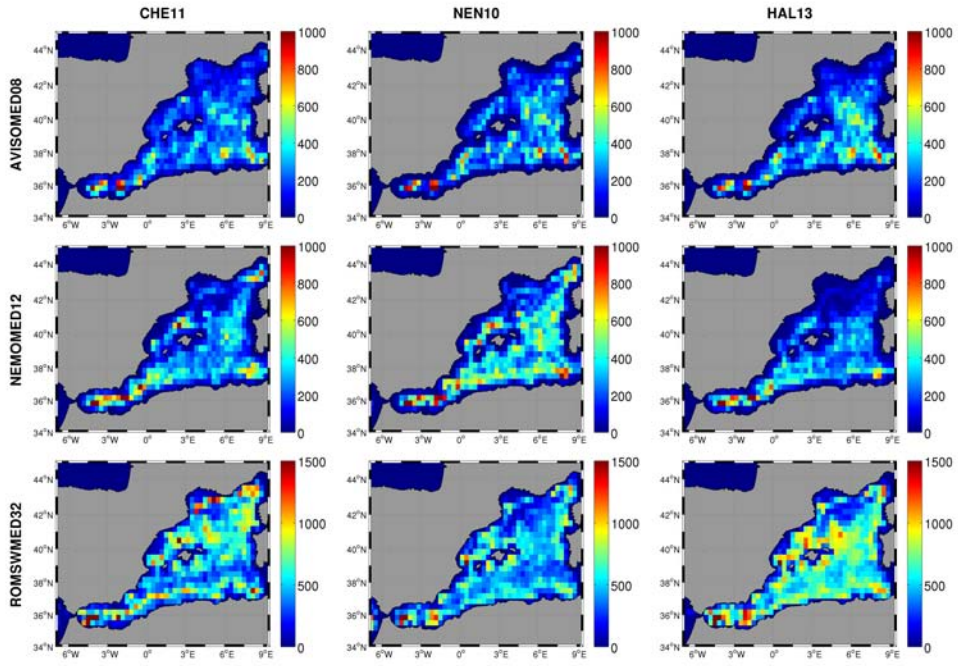

Figure 6.13: Total number of detected eddies in each cell of 1/3° x 1/3° of the domain for all datasets and methods. Each eddy is counted in the cell that contains its center.

Overall, there are some discrepancies between the methods of detection but the general patterns are consistent. The areas with high densities of eddies are generally the same and the increased number of eddies in the high resolution simulation is mainly in the northern part of the basin. Between datasets, similar results also emerge in the spatial distribution of eddies. We observe that the Algerian Current, the Balearic Sea and the Algero-Proveçal basin are consistently areas of high density of detected eddies.

The detection algorithms detect both cyclonic and anticyclonic eddies, so we can investigate whether there is an organized spatial distribution to the number of cyclonic or anti-

cyclonic eddies. Figure 6.14 displays the spatial distributions of the percentages of cyclonic eddies. It shows that there is no clear pattern in this distribution for any of the methods or datasets. Regions that appear to have a tendency toward cyclones or anticyclones like in NEMOMED12 with HAL13, are those which have too few detected eddies to be significant. The only area which can be noted is the Northern Current where there is a lower percentage of cyclonic eddies for both numerical models but this area has a low density of eddies and the result does not appear in the altimetry data (AVISOMED08). In the ROMSMED32 simulation, the figure reveals that the tendency toward cyclonic eddies in HAL13 is homogeneously distributed over the basin.

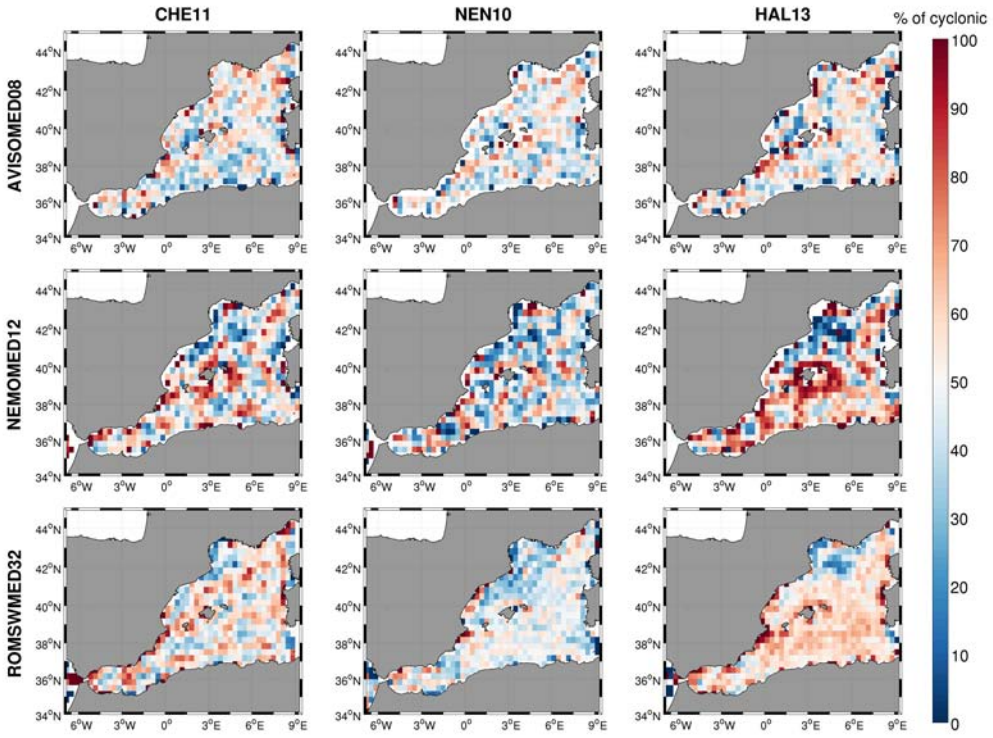

Figure 6.14: Percentage of cyclonic eddies in each cell of 1/3° x 1/3°of the domain.

Maps in figure 6.15 show how large eddies are distributed

in the region in each dataset. In this case, all datasets and methods appear to agree in putting the largest eddies along the Algerian Current with higher value along the north eastern coast of Algeria. In both simulations, large eddies are also found at the northern shore of Mallorca in the Balearic Sea, whereas this is less clear in the altimetry maps. Both the large Algerian and Balearic eddies have been studied in depth in the literature (see section 2.4).

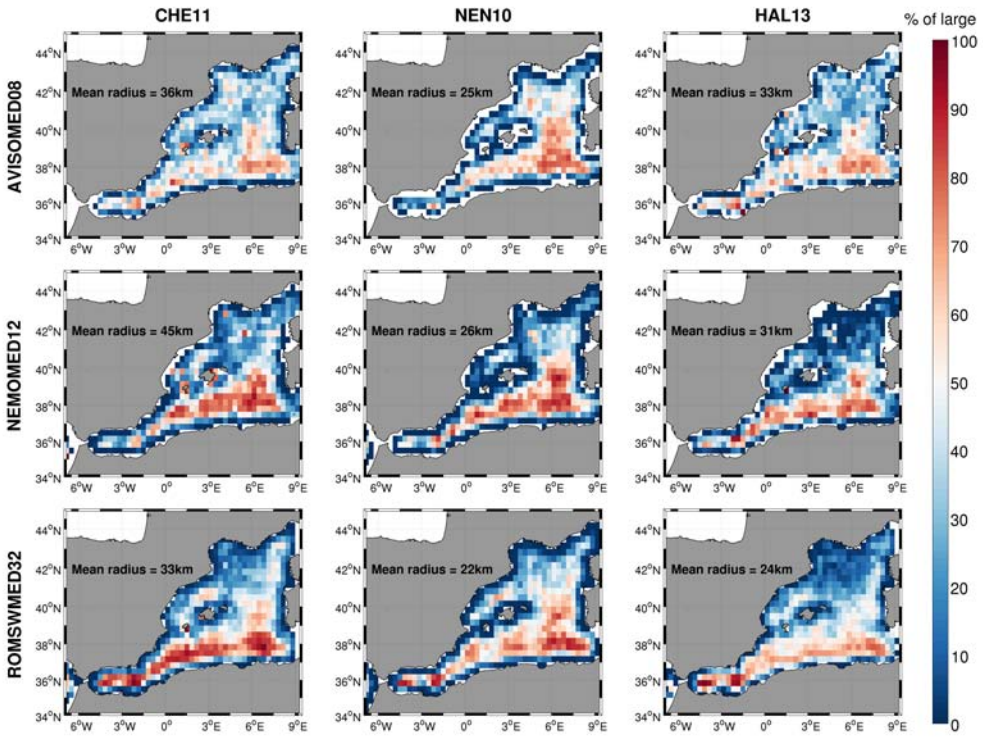

Figure 6.15: Percentage of large eddies in each cell of 1/3° x 1/3°of the domain. For each method and each dataset, an eddy is considered large if its radius is above the mean radius of the dataset for the method (indicated on the map).

This figure (6.15) can be compared to figure 6.16 where the distribution of the percentage of eddies with a lifetime over 4 weeks is examined. First, we can note that this percentage increases when going from altimetry to NEMOMED12 and to

ROMSMED32 in the CHE11 method. It is also the case for the NEN10 method whereas for HAL13 it increases from altimetry to ROMSMED32 but decreases in the NEMOMED12. However, the general pattern is roughly maintained between the datasets and methods. As for the size of the eddies, eddies generated near the Algerian Current and those found north of Mallorca are more likely to be long-lived.

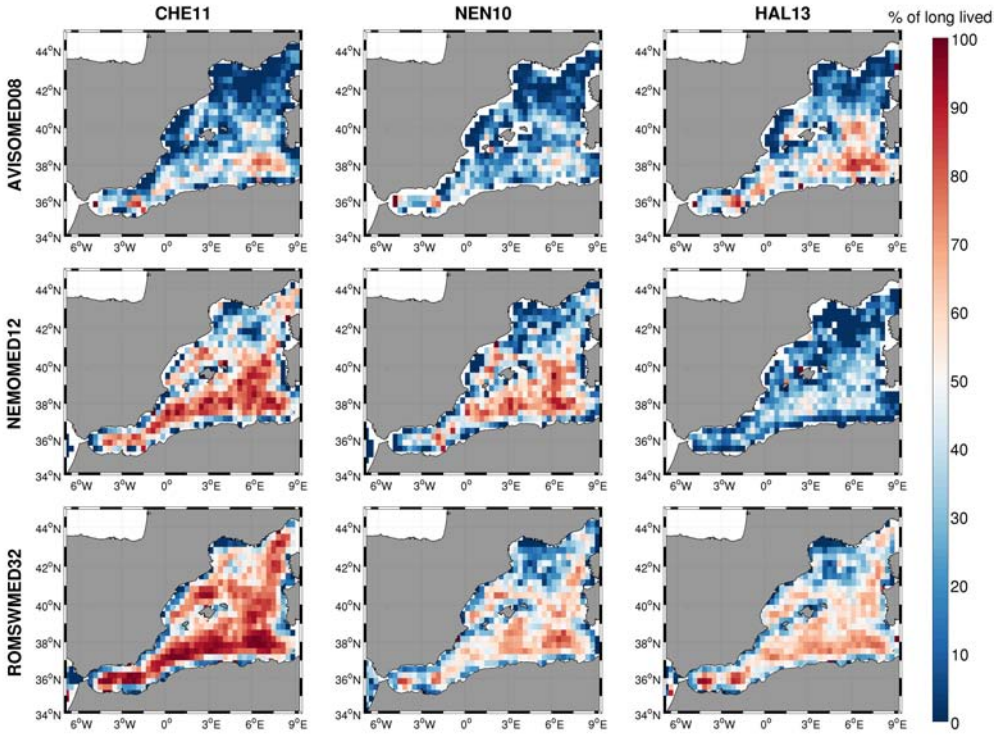

Figure 6.16: Percentage of long-lived eddies in each cell of 1/3° x 1/3°of the domain. A long-lived eddy is an eddy with a lifetime longer than 4 weeks.

This similar distribution of the large size and long-lived eddies suggests that there may be a correlation between the two characteristics of the eddies. However, the computed correlation are small (0.2 to 0.4) and not significant enough to conclude anything about their correlation.

6.3.2.4 Focus on eddy radii and durations

To investigate even further this relationship between the two characteristics of the detected eddies, a scatter plot of the maximum (or 95% percentile, the value of the distribution at 95%) radius of each eddy versus its duration can be found in figure 6.17. The shape of this scatter plot is not a strait line, as would be expected if the two variables were highly correlated. But it is not a random shape either, having the form of a triangle on a logarithmic scale. This means that, for a given radius, there is a maximum duration for the eddy, and small eddies cannot live as long as big eddies. Our assumption for this is that the two variables are correlated and the triangular shape is due to inadequacies in the tracking. Indeed, if we assume that larger eddies are living longer, the points in the bottom right of the plots may be eddies that are lost and found again by the tracking algorithms.

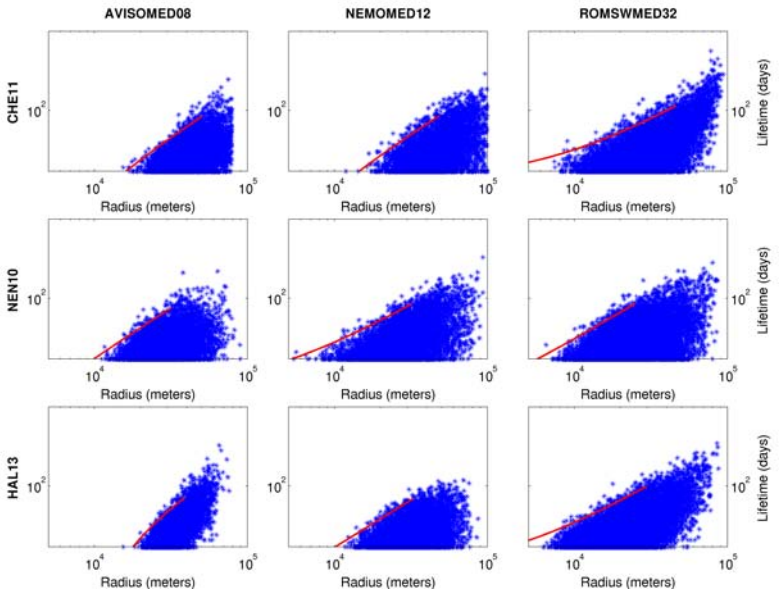

Figure 6.17: Maximum radius of detected eddies (in km) in function of their duration (in days). The scale is logarithmic for both axis. In red is plotted the regression of the upper limit.

Since possible issues in the tracking of the eddies prevent us from directly studying the relationship between the radii and duration of the detected eddies, we focus on the upper limit of duration for a given maximum size of the eddy. A regression for this limit (in red in the figure) shows that for every dataset from observations and models and with all the algorithms, the radii are significantly (at the 95% level) related to duration by a root square function:

$$R|_{lim} = A + B * \sqrt{T} \tag{6.6}$$

with $R|_{lim}$, the maximum radius (95% percentile) of the eddies at the desired limit and T the duration of the eddies. The value for the parameter B is between 3 and 4 $kms^{-1/2}$ for all the datasets.

Two hypothesis can then be formulated: is this relationship related to an increase of the size during the life of the eddy, or are large eddies formed at their larger size and live longer due to a higher stability? The latter hypothesis has been tested by making the same plot as before but this time the minimum radius of each eddy is compared to its duration (figure 6.18). In this plot, the lack of a relationship between the two variables is apparent meaning that we can discard this hypothesis. A similar behavior is observed with the 5% percentile.

The other hypothesis is then that the eddies increase in size with time; to test this hypothesis, we compute the mean radius of the eddies for each age (in days) of the eddies lifetime. The results are depicted in figure 6.19. The size of the eddies appears to indeed increase with age; the evolution seems to follow a square root of time since the first detection for the "early life" (0-100 days for AVISOMED08, 0-150 days for NEMOMED12 and 0-200 days for ROMSWMED32). Then, the pattern is less

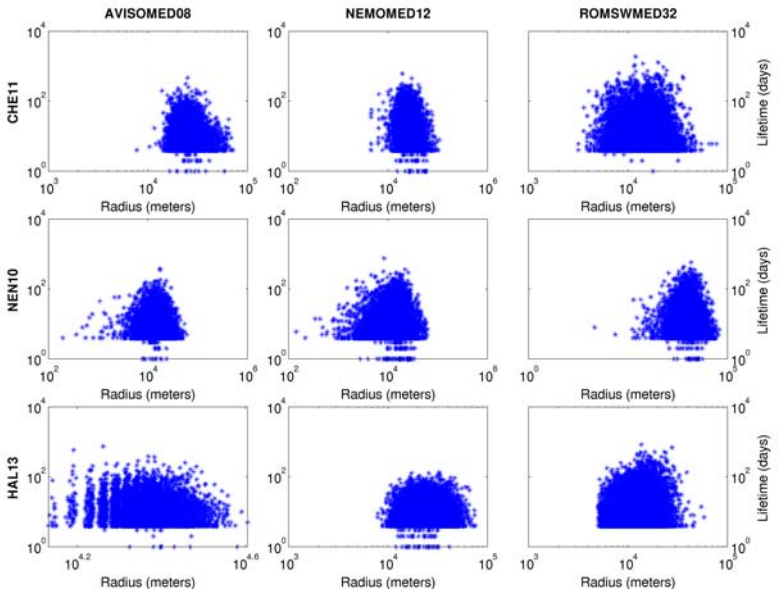

Figure 6.18: Minimum radius of detected eddies (in km) in function of their duration (in days). The scale is logarithmic for both axis.

clear, probably due to the lack of sufficient data for long-lived eddies. A square root regression, similar to equation 6.6 applied to the maximum radii versus duration dataset, is significant at the 95% level for all datasets. Yet, the value of the B parameter is, in this case, lower than before (between 1 and 2 times lower) which is hard to explain.

The final answer may be given by figure 6.20. Indeed, in figure 6.19, the number of eddies used to compute the size at each age on the x-axis is not the same and is likely to skew the results. To account for this, we plot the size of the detected eddies as a function of their dimensionless age t'. The dimensionless age is given by: $t' = (t-1)/T$ with T the lifespan of the eddy and t its age. We then regroup the eddies by age class: 4-25 days, 25-50 days, 50-100 days, 100-150 days, 150-200 days and 200-300 days. The mean of each class is plotted in figure 6.20, the dimensionless axis is multiplied for each class by the median of the lifespan (*e.g.* 75 for the 50-100 day class) to

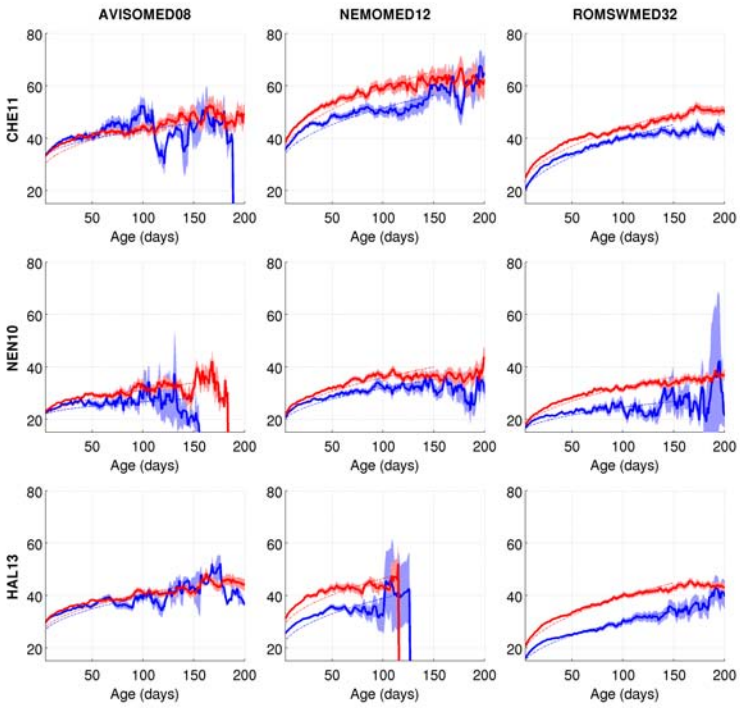

Figure 6.19: Mean eddy radius in function of its age (in days) for the different datasets. Cyclonic eddies are plotted in blue and anticyclonic in red. The estimation of the error of the mean is indicated as the shaded area. The square root regressions are plotted in dotted lines.

better represent the evolution. The results show that indeed, eddies that have longer timespan tend to be larger but that their size does not increases monotonically. On the contrary, the eddies, on average, seem to first grow quickly, then stabilize, and then decrease rapidly. This result is found in all the datasets but is clearer for the models where we have more data.

A bibliographic research of the subject enabled us to find that these results strongly resemble what is found for the global ocean dataset of eddies detected from altimetry provided by Chelton et al. (2011). In a recent article, Samelson et al. (2014) made a very similar study on this global dataset as well as on a global numerical ocean circulation model and, surprisingly, were able to reproduce the pattern with a simple stochastic

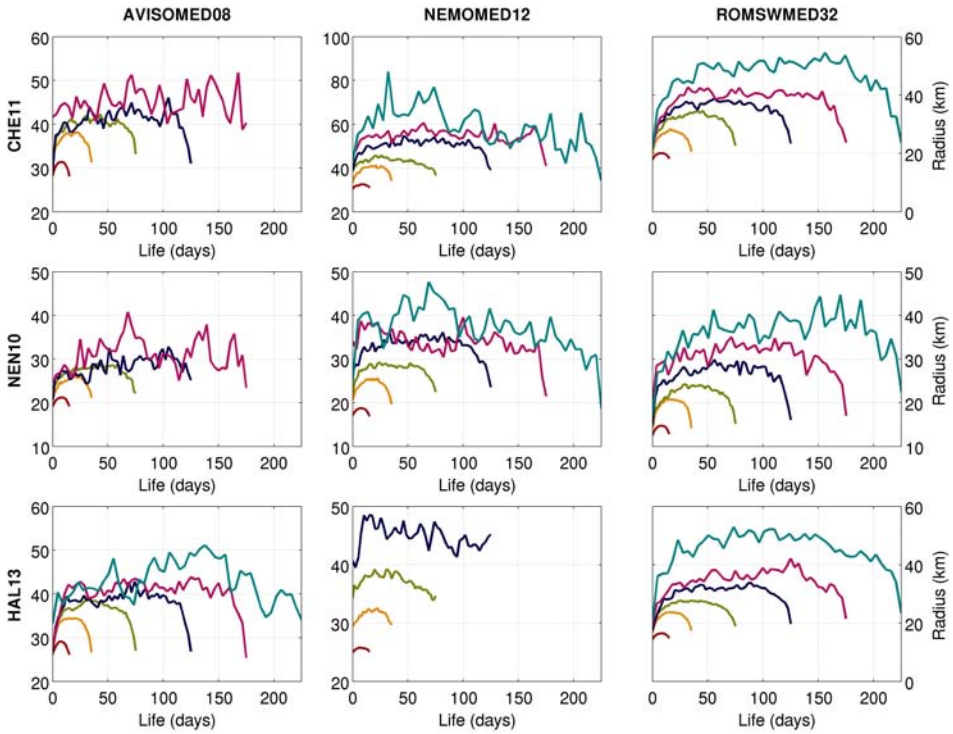

Figure 6.20: Evolution of eddy radii as a function of its age by lifespan class.

model. Similar plots to the ones in that article are presented in figure 6.21 where the similarities appear very clearly for all the datasets and maybe more clearly for ROMSWMED32. In these plots, the x-axis is the dimensionless age and the y-axis is the dimensionless radius defined as $R' = R/R_{mean}$ with R_{mean} the mean radius of the eddy.

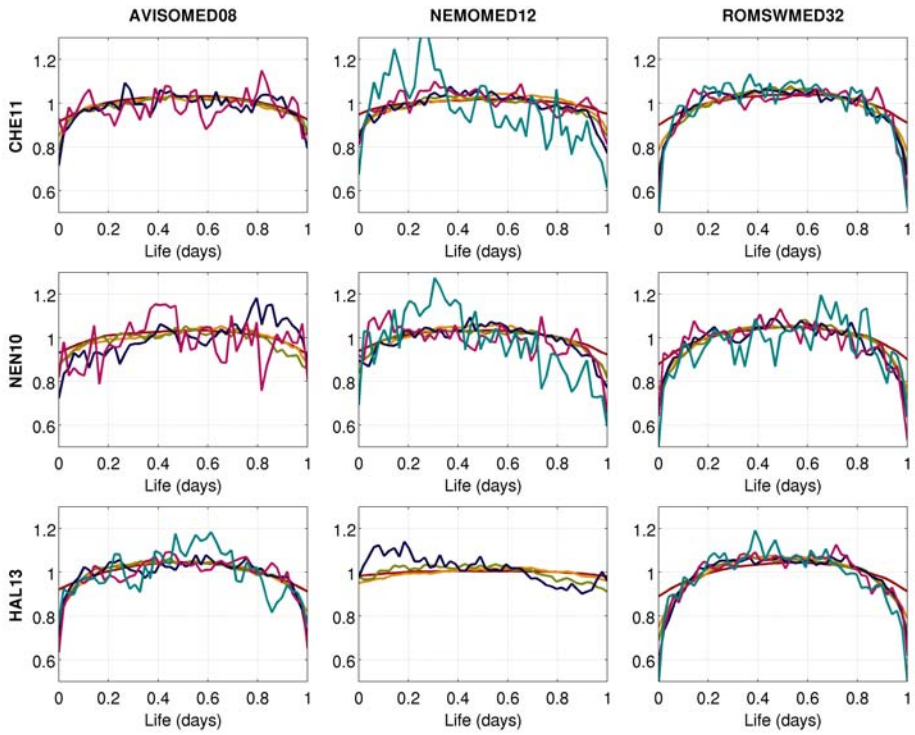

Figure 6.21: Evolution of dimensionless eddy radii as a function of its dimensionless age by lifespan class.

6.3.2.5 Propagation of eddies

In figure 6.22, where all the trajectories of the eddies are plotted with the same starting point, we observe that eddies in altimetry maps do not travel very far away from their origin while for ROMWMED32, they travel further away from their initial positions. This is the case for all detection methods (not shown) and illustrates the limits of eddy tracking with satellite altimetry data. The spatial and temporal distances between the satellite ground tracks make it difficult to correctly follow small mesoscale eddies. Increasing the simulation resolution also seems to increase the distance traveled by the eddies and it may be related to the increased lifetime of eddies in the high resolution simulation (ROMSWMED32).

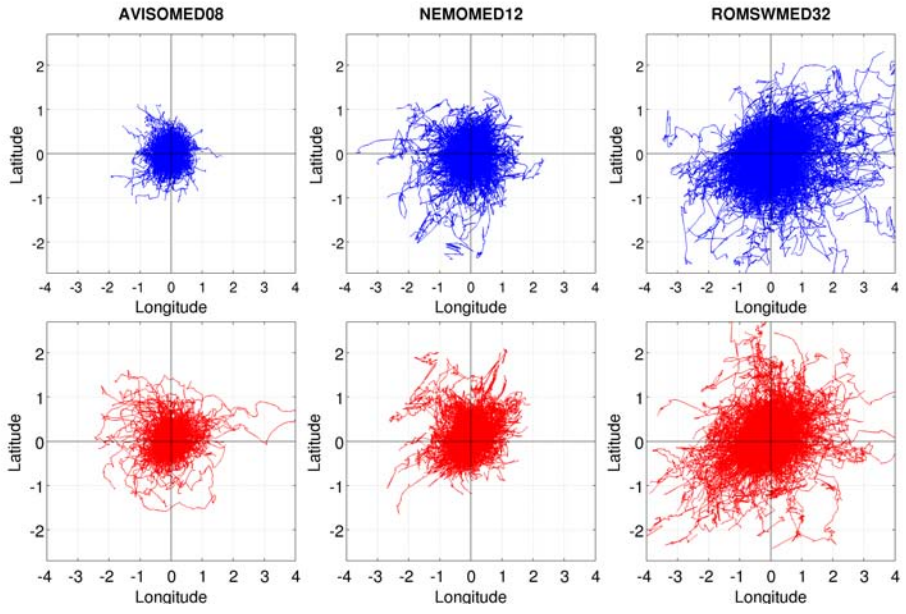

Figure 6.22: Trajectories of all detected eddies if they had the same starting point for the different datasets. These are the eddies detected with the CHE11 method. The top panels in blue are cyclonic eddies and the bottom ones are anticyclonic eddies in red.

The direction of propagation of the detected eddies as well as their velocity is presented in figure 6.23. Only results from

the CHE11 method are presented for clarity and they are easier to interpret as the algorithm gives position in continuous space whereas others give the nearest grid point. The velocity of propagation of the detected eddies is quite small, most of the eddies moving at speeds below 8 cm s^{-1} in all the regions.

Over the whole WMed basin, while there is an east-west preference in the propagation of eddies in altimetry data, it is shifted toward a slightly northeast-southwest propagation in the simulations (with an angle of around 15°). This inclination may be due to the geometry of the basin with the Spanish and French coast going from south-west to north-east. This anisotropy of the eddy propagation is stronger in the ROMSMED32 simulation.

In the south of the basin (Algerian region, second column in the figure), satellite detected eddies have a clear tendency to go eastward with the Algerian Current. This is also strongly pronounced in the ROMSMED32 simulation with greater speeds whereas, in NEMOMED12, the preference is not apparent and the eddies go mostly eastward or westward. For the latter simulation, this can be explained by a much weaker simulated Algerian Current (see section 4.3).

In the northern region, the Northern Current appears to drive eddies, resulting in an eastward (with a small inclination southward) propagation of the mesoscale structures in all the datasets. In the simulations results, the eastward preference is stronger and the inclination southward is more pronounced. NEMOMED12 reproduces the Northern Current well and therefore its effect on the eddies is visible.

The central region is interesting for the AVISOMED08 dataset where the previous result about the westward tendency in propagation is still present. However, this is not that

clear in the simulations: in the NEMOMED12 simulation the preferred direction of propagation seems to be eastward, and in ROMSMED12 the directions are both westward and eastward with only a weak preference toward westward propagation. Since we saw that eddies are mostly advected by mean currents, it may be due to differences in the mean state of the currents in the region, which are weaker and therefore harder to reproduce well than in other region of the WMed.

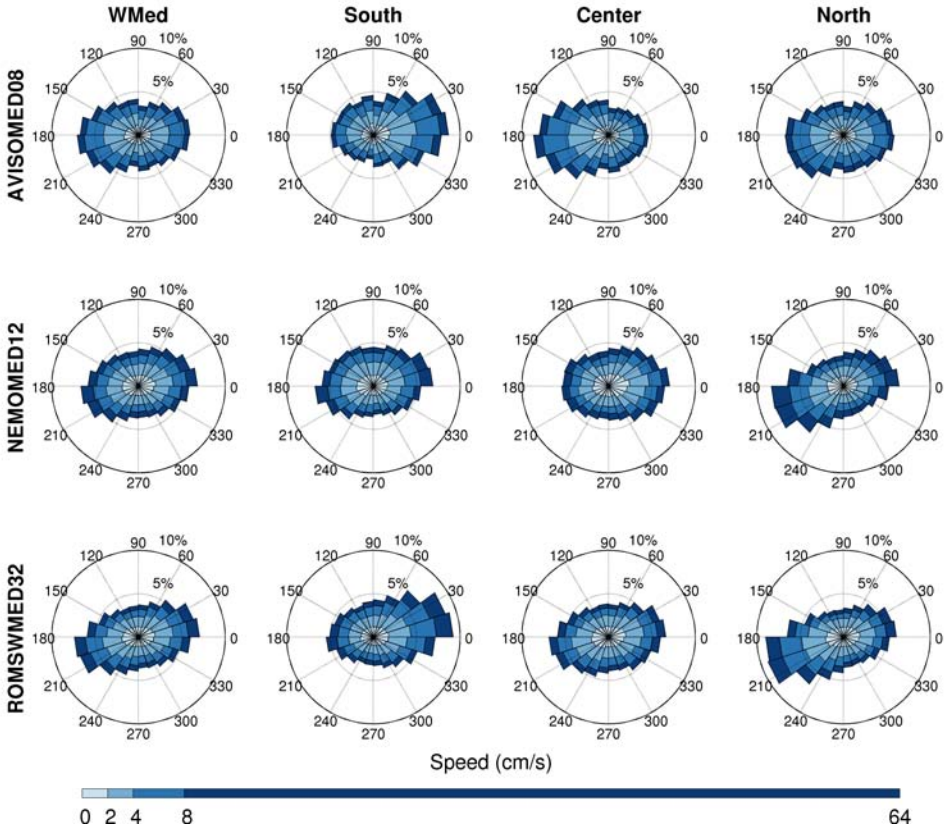

Figure 6.23: Polar histogram of the direction of propagation of the detected eddies. In color is the distribution of velocities in each direction. Eddies from altimetry gridded data are plotted on the first row, eddies from NEMOMED12 on the second row and eddies from ROMS are on the last row. The eddies presented here are only the ones detected by CHE11. The WMed is separated in three different regions: south (Algerian basins), center (Algero-Provençal basin) and north (Gulf of Lion and Balearic Sea).

6.3.2.6 Temporal analysis

Time series To analyze the temporal evolution of the eddy field in the WMed, as done in the previous section from altimetry, we look at the total number of detected eddies each day. These time series for the different datasets and methods are plotted in figure 6.24.

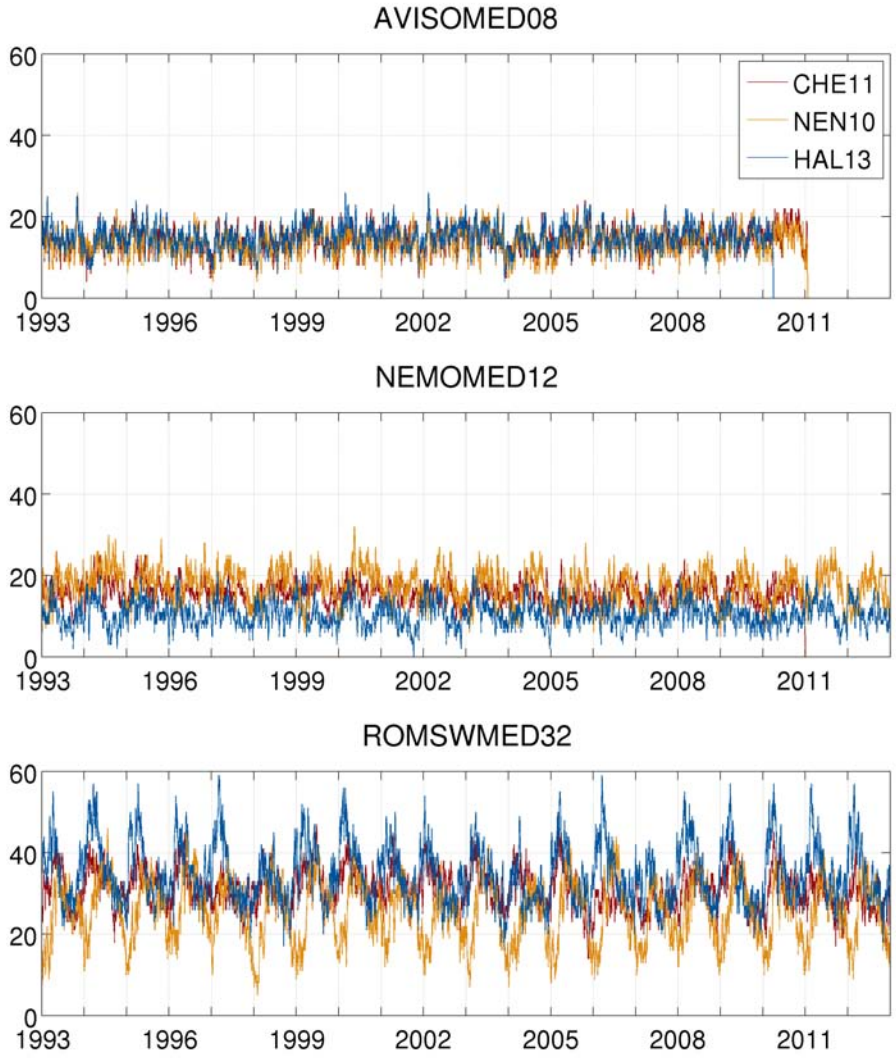

Figure 6.24: Time series of the number of detected eddies per day.

First, the mean number of detected eddies per day is consistent between the methods as seen already in the total num-

ber of eddies detected for the whole period (see table 6.2), being around 15 for altimetry, 16 for NEMOMED12 and 34 for ROMSMED32. In the altimetry data, we see that there are high frequencies but also an interannual signal with a standard deviation of around 3 for all algorithms. Eddies detected in NEMOMED12 also have some high frequency variability, but the annual cycle stands out visually; the standard deviation is a little higher between 3 and 4. The ROMSMED32 eddies, in addition to being more numerous, also exhibit a higher variability (standard deviation between 5 and 8), which is highly seasonal. Altimetry data seem therefore to be the only one without a well defined seasonal cycle. Yet, as described in the previous section from the preliminary study, altimetry data do have an annual variability, but it is for different type of eddies (long-lived and short-lived) and the cycles compensate in the total shown in figure 6.24.

Spectral analysis Computed spectra of the previous time series are shown in figure 6.25. They confirm that the two simulations of the WMed have a clear annual cycle with all the methods. In the altimetry data, the peak at the frequency equivalent to the annual cycle is not significant, as found in the preliminary study.

Climatology To investigate the annual cycle, anomalies of the climatology of the number of detected eddies are plotted in figure 6.26. As in the preliminary study, the annual cycle is present for the eddies when they are separated into long-lived and short-lived structures. This is confirmed for AVISOMED08 with all the algorithms. In the simulations, this phenomenon is also observed but maybe less clearly. Also, the annual cy-

cles do not exactly compensate in the models because they are not in perfect phase opposition and so the annual cycle is present when looking at the whole dataset. The reasons for this can be that the models do not perfectly reproduce the mesoscale dynamics in the region or that the limits of the altimetry based observations prevent from having the complete field of mesoscale eddies. Finding the mechanism behind these cycles should give an answer to this question.

Wind As was done for the preliminary study from altimetry data, it is useful to look at the wind forcing to explain the annual cycle of the long-lived eddies. In figure 6.27, the climatologies of the numbers of short-lived eddies are compared with the the wind stress intensity average over the domain. The increase of eddy number seems to follow the increase of wind but the results are not clear, especially for the NEN10 method in the models. Some future work including a sensitivity test to the wind must be be performed to investigate this further.

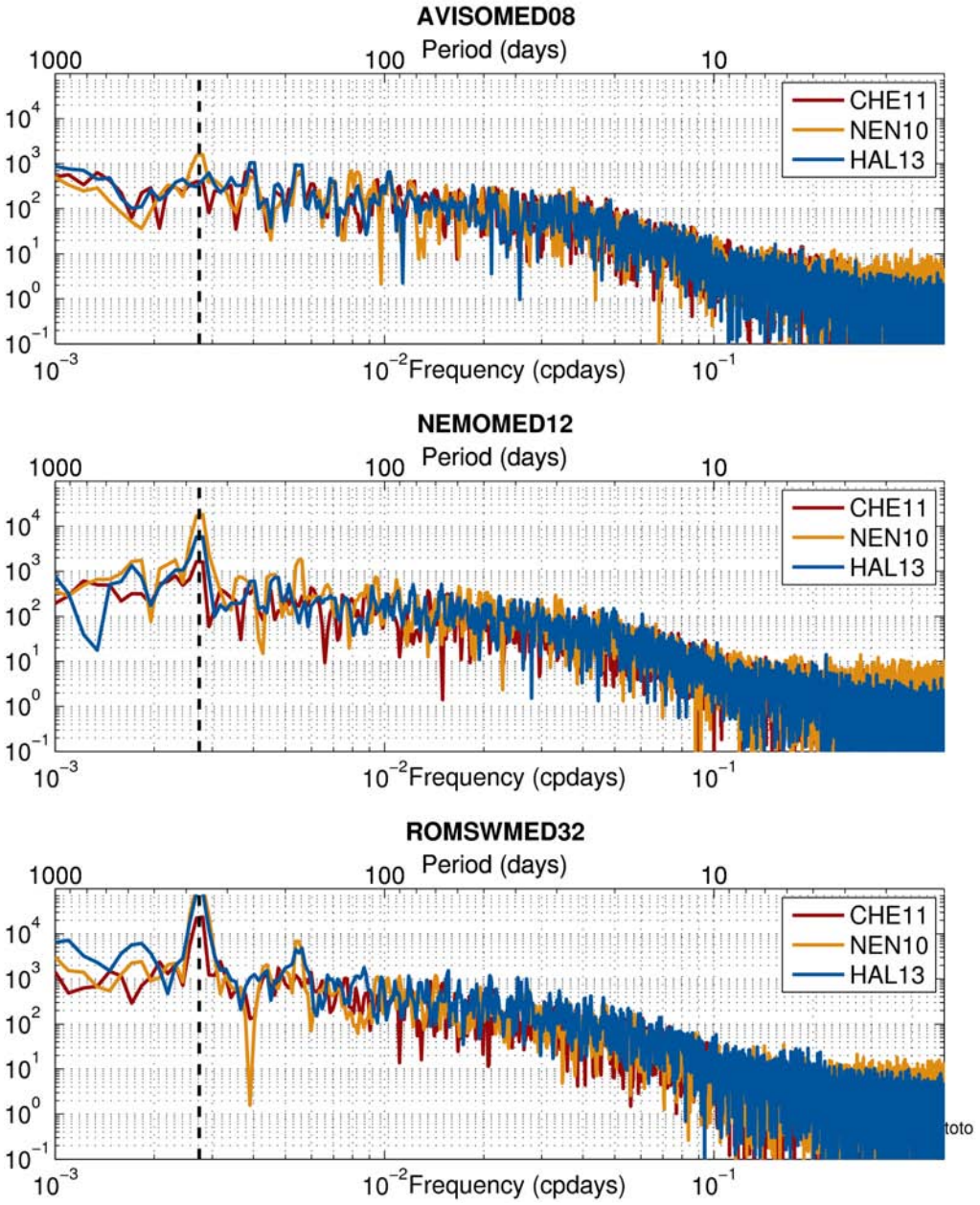

Figure 6.25: Spectra of the time series of the number of detected eddies per day. On the top panel are the spectra for altimetry maps, in the center for NEMOMED12 and on the bottom for ROMSMED32. Colors indicate the different methods.

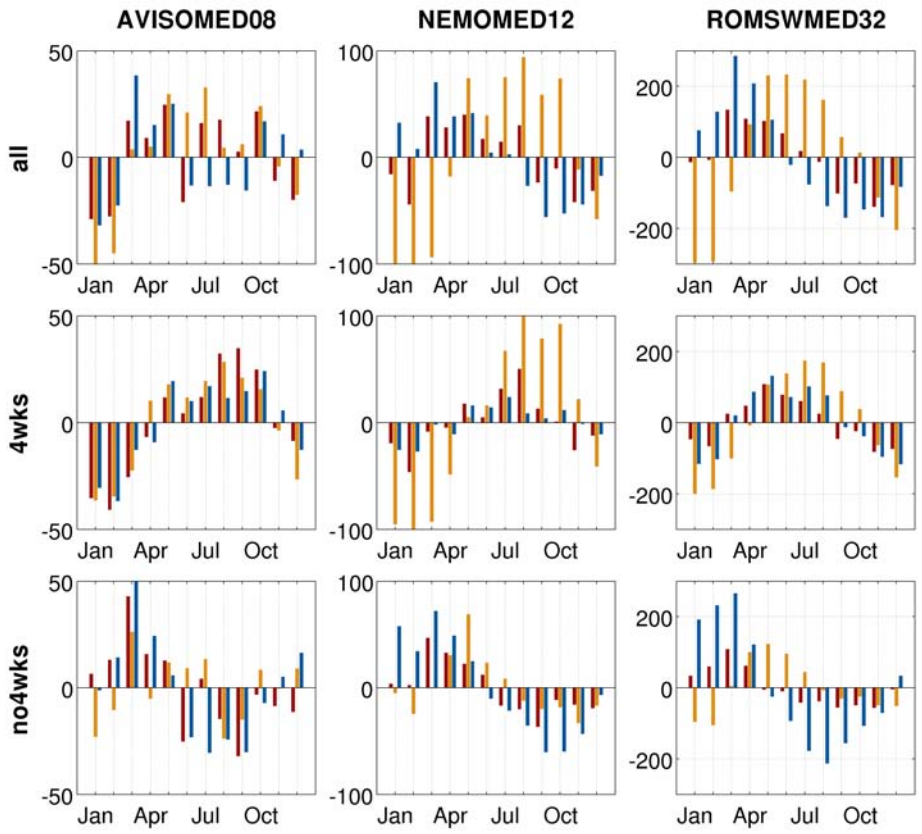

Figure 6.26: Anomalies of climatology of number of detected eddies. Climatology (mean number of detected eddies for all January, Frebruary,...) are computed for each dataset. Then we substract the mean number of eddies per month to this climatology to obtain this plot. The result for all eddies is on the first row while on the second row are the long-lived ($>$ 4 weeks) eddies and the third row are the short lived eddies. The colors represent the different eddy detection methods: red is CHE11, yellow is NEN10 and blue is HAL13.

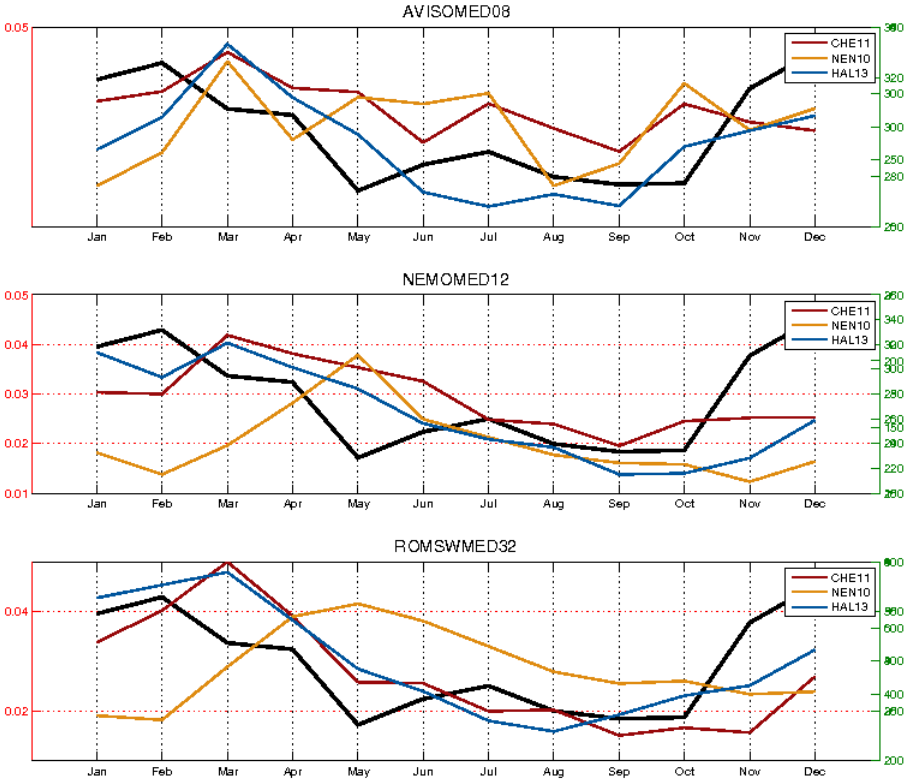

Figure 6.27: Climatology of the number of detected eddies compared to a climatology of the wind stress intensity averaged on the domain. The wind stress (in black) is from NCEP-CFSR dataset used as a forcing for ROMSWMED32.

6.3.2.7 Composites

As presented in the introduction, the use of models allows us to have information of the 3D structure of the detected eddies. An easy way to extract this information is to look at composites of the profiles of various water properties in the centers of the eddies. The composites are created by taking the mean of the vertical profiles of every eddy at its center. Figure 6.28 shows these average vertical profiles. The averaged profiles are anomalies with respect to the climatological profile at this grid point for this month of the year.

In this figure, the results show that there are some differences in structure between the eddies detected in the different areas of the WMed. As expected, cyclonic eddies induce negative anomalies of temperature and/or positive anomalies of salinity and therefore positive anomalies of density. This is because cyclones tend to uplift the pycnocline, which results in these structures in the anomalies. The effect is the opposite for anticyclonic eddies which lower the pycnocline. The maximum of the anomalies is also deeper for anticyclones. The lowered pycnocline in anticyclones will create a maximum of the temperature anomaly below the mean depth of the pycnocline whereas an uplifted pycnocline in cyclones will create a minimum above. We can note from figure 6.28 that long-lived eddies are associated with stronger anomalies of density. The effect of the changes in density are transmitted to the Brunt-Vaisala frequency.

We can also look at the averaged 2D sections of the detected eddies. In figure 6.29, the composites of zonal sections going through the center of the eddies are shown. To account for the change of radius of the different eddies, the sections are

taken as function of depth and a dimensionless distance from the center set 1 at the computed radius of the eddy. In this figure, the previous results on the density are confirmed with positive anomaly for cyclones and negative for anti-cyclones. The anomalies extend horizontally quite far, until more than twice the radius. The composite sections of meridional velocities confirms the rotation direction of the two type of eddies. They also show that the radius detected by the HAL13 detection method is not where the velocities are maximum. The maximum of velocities is found at around 1.5 times the radius. A similar result is found for the NEN10 method but the with the CHE11 method which may explain the differences observed in the histograms presented previously. The Okubo-Weiss parameter defines the shape of the eddy since it is positive within it and negative outside. It shows that, on average, anticyclones extend deeper than cyclones. The shape of the vertical extension of the two types of eddies is also different with cyclones having a rounder aspect and anticyclones a more conic shape.

In figure 6.30, only the Okubo-Weiss parameter is plotted for different areas of the WMed in order to look at the different shapes of the detected eddies. It shows that the shapes differ from one area to another. In the southern region, the cyclones are the most shallow while anticyclones are deeper on average. This may explain why in-situ observation have difficulties observing cyclones in this region. In the northern region, both cyclones and anti-cyclones have similar mean depth but the anticyclones still have a radius that decreases more rapidly with depth than the cyclones (conic shape). The center region is an intermediate between both extremes.

6.3.2.8 Depth of eddies

Principle The method used to estimate the depth of the detected eddies is based on the Okubo-Weiss parameter. We compute this parameter W in a profile at the center of each eddy from the velocity fields (see section 6.2). The depth at which W changes sign and becomes positive is determined to be the depth of the eddy. The principle is the same as for the eddy detection methods that rely on the Okubo-Weiss parameter: W is positive inside the eddy and negative outside. Except, in this case, the detection is done vertically. The depths of eddies, and consequently the results below, are computed only for the ROMSWMED32 simulation.

Results On figure 6.31, the distribution of detected eddies according to their depth is presented. First, it appears that both algorithms used for this diagnostic (NEN10 and HAL13) present similar results. Then these distributions show that most of the eddies have depths shallower than 400 m. Even in the Algerian region where eddies have been observed to reach 1000 m, the distribution is centered around 200 m. There are some differences between the different areas but not as marked as expected.

Figure 6.32 presents the spatial distribution of the mean depth of detected eddies. It shows that long-lived eddies are, on average, deeper than short-lived eddies. In the Balearic Sea, eddies tend to be deeper than in the rest of the region. Another area where eddies are deeper on average is the western part of the Algerian Current where many Algerian eddies are created.

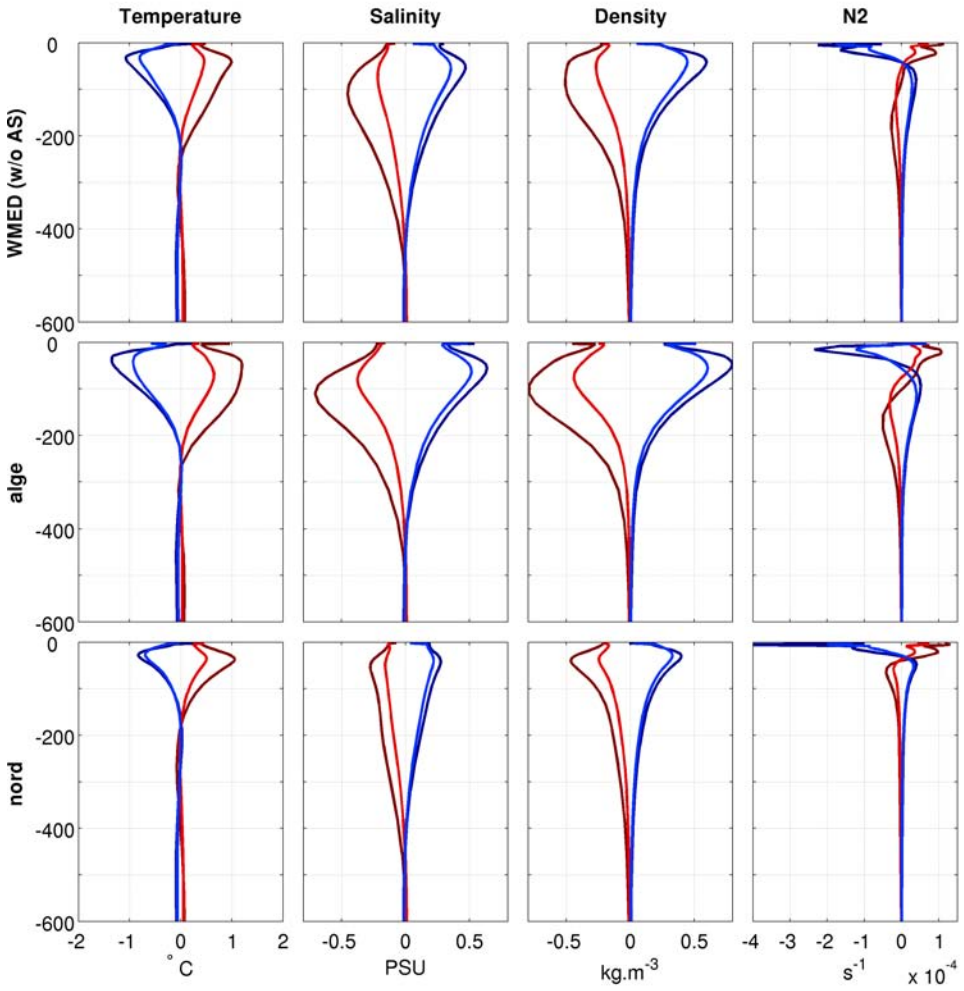

Figure 6.28: Composites of different characteristics (temperature, salinity, density and Brunt-Vaisala frequency) taken in the center of each eddies in the different regions. These composites are the mean of anomalies with respect to climatology of the profiles in the center of the eddies. Cyclonic eddies are in blue and anticyclonic eddies are in red. Darker colors are for long-lived eddies and brighter colors are for short-lived eddies.

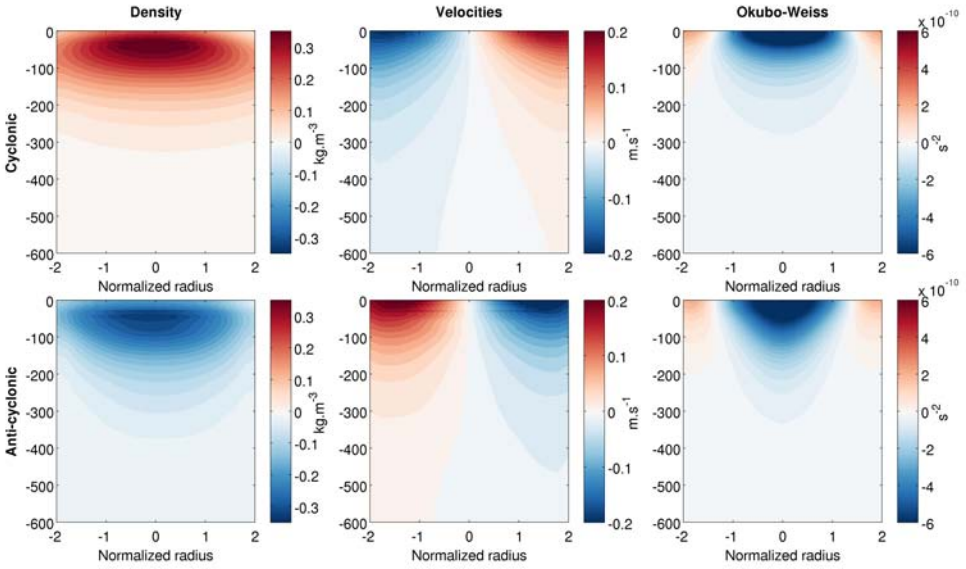

Figure 6.29: Composites of the zonal section of the detected eddies for the anomaly of density, of meridional velocities and the Okubo-Weiss parameter. The density and velocity composites are the mean of anomalies with respect to the climatology. Cyclones are pictured in the first row and anticyclones in the second row. The y-axis of the plots is the depth while the x-axis is a dimensionless distance from the center.

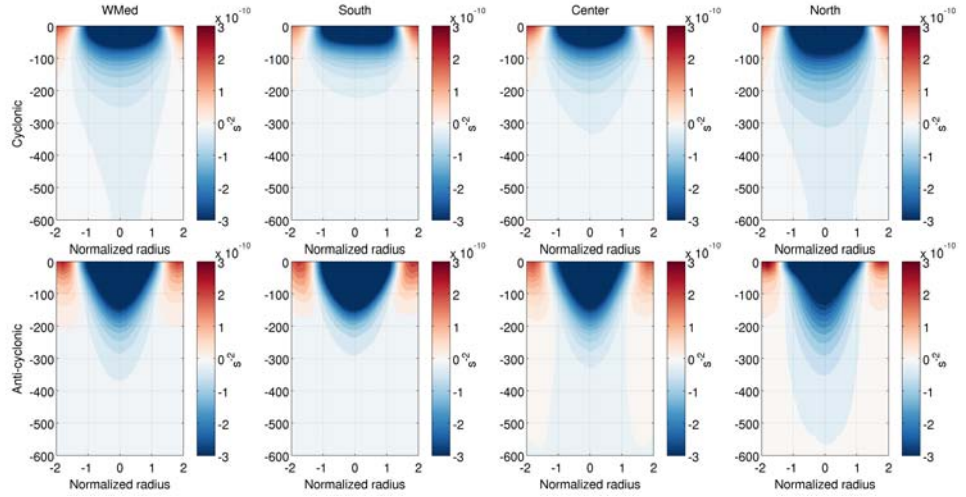

Figure 6.30: Composite section of the Okubo-Weiss parameter of the detected eddies. This composite is computed for different areas of the region. Cyclones are pictured in the first row and anticyclones in the second row. The y-axis of the plots is the depth while the x-axis is a dimensionless distance from the center.

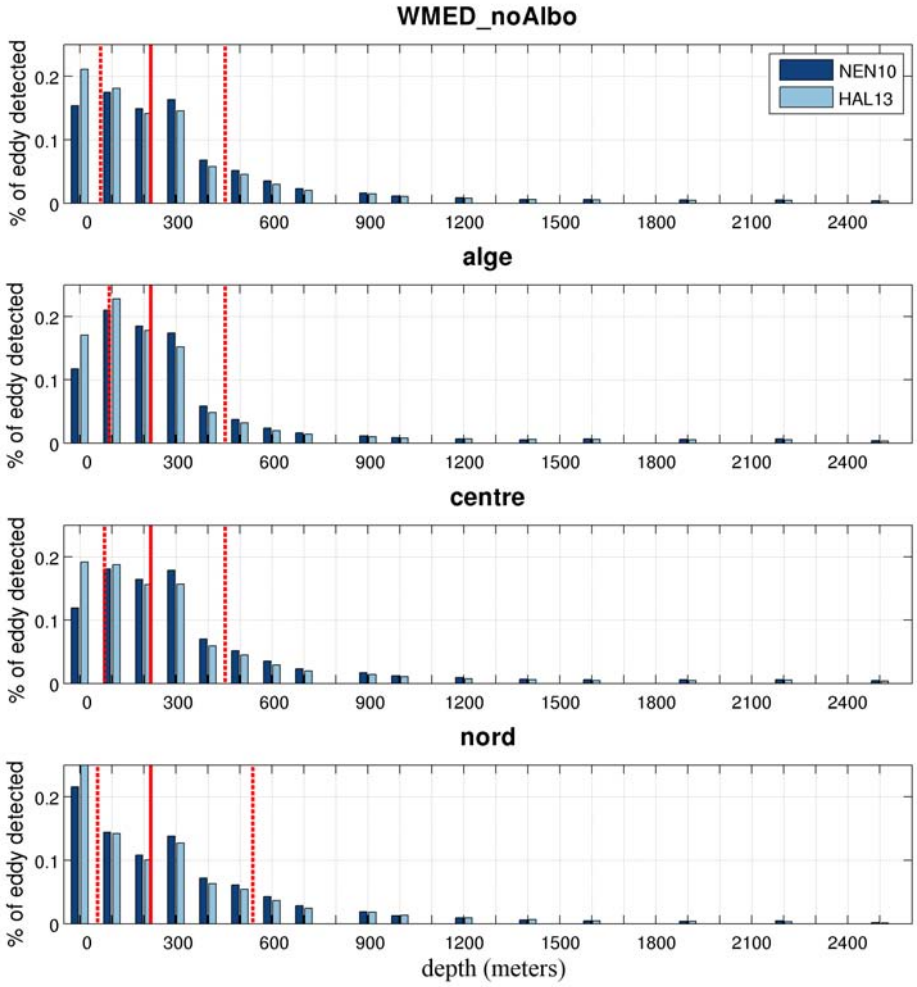

Figure 6.31: Distribution of detected eddies according to their depth in the ROM-SWMED32 simulation. Results from the NEN10 algorithm are in dark blue and results from the HAL13 algorithm are in light blue. Different areas of the basin are plotted. The median (solid line) and the 17 and 83 percentiles (dotted lines) of the distribution are indicated in red.

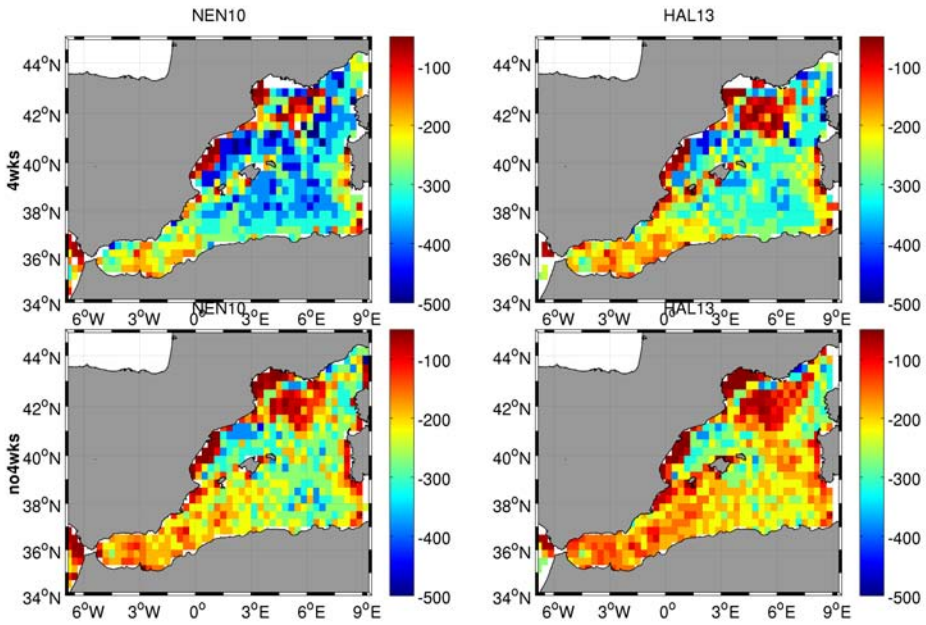

Figure 6.32: Spatial distribution of mean depth of detected eddies in the ROMS-WMED32 simulation. The mean is computed in bins of 1/3°x1/3°. Long-lived eddies are studied in the top row and short-lived eddies are in the second row.

6.3.3 Application to the high resolution altimetry

We then applied two detection methods (NEN10 and HAL13) to the HR+BATHY fields of chapter 5 and to AVISOMED08 in the region of the HR+BATHY data. A higher number of detected eddies as well as a reduction of the average radius is expected. However, as discussed in the discussion of chapter 5, this method improves the resolution mainly near the satellite track. As we do not have any information for the inter-track areas, this improvement is not spatially homogeneous and therefore not well suited for the tracking of eddies.

6.3.3.1 Statistics

In table 6.3, the same statistics as in previous section are presented. From these statistics, we observe that there are no significant differences between the two products. The different metrics are almost the same for both altimetry products except for the number of eddies which, surprisingly is reduced for the HR+BATHY product with both methods. For the HAL13 method, the change is quite dramatic with 30% fewer eddies detected. This may be due to the reduction of the size of some structures that are consequently no longer detected by the detection methods. As for the number of unique eddies, it increases for the NEN10 method and decreases for the HAL13 method.

6.3.3.2 Histograms

As previously, we begin by looking at the distribution of the number of eddies according to their size and lifetime (figure 6.33). The NEN10 method once again gives smaller eddy sizes but on average, eddies are smaller in this area than in the

Data & Method		Mean life	Max life	Min Radius (km)	Max Radius (km)	Cyclonic percent.	Nb eddies	Nb unique eddies
AVISOMED08	NEN10	35	259	0.1	83	51.6	69917	3611
	HAL13	33	211	6.6	71	51.5	95185	5164
HR+BATHY	NEN10	27	253	0.2	86	51.5	66658	4210
	HAL13	21	200	6.6	70	49.4	61363	4800

Table 6.3: Eddy detection results for the HR altimetry. The first two columns present the minimum and maximum life of detected eddies in days, the third and fourth their minimum and maximum radius, the fifth the percentage of cyclonic eddies found, the sixth the total number of eddy-shape structures identified in the maps and the seventh is the number of unique eddies revealed by the tracking.

whole WMed (mean radius of 19 for NEN10 and 23 for HAL13). The HR+BATHY fields appears to have less eddies that are above the average and more eddies concentrated around the peak of the distribution. The eddies detected in the new fields are also more short-lived, especially with the HAL13 method where almost 70% of the detected eddies last less than 20 days. This may due to the shorter temporal correlation scale in the mapping analysis that was performed for these maps or more probably to the inhomogeneous accuracy of the SSH fields

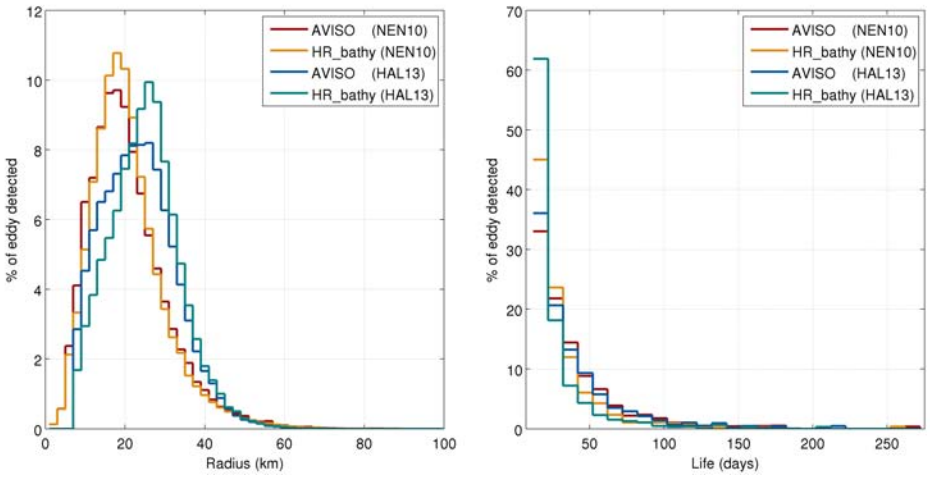

Figure 6.33: Distribution of detected eddies according to their size (left panel) and lifetime (right panel) for AVISOMED08 and HR+BATHY datasets.

6.3.3.3 Spatial distribution

Regarding spatial distribution (figure 6.34), the number of detected eddies is rather homogeneous and no clear spatial pattern is found in this area for either AVISOMED08 data or HR+BATHY. In the case of NEN10, the distribution is even more homogeneous for the HR+BATHY dataset.

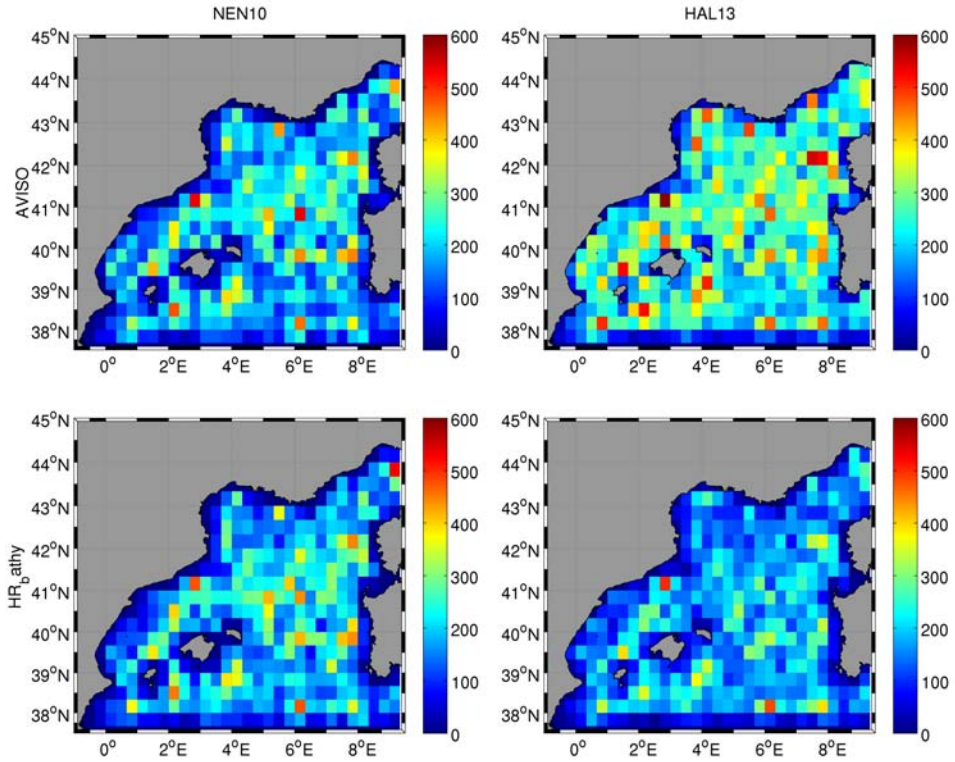

Figure 6.34: Total number of detected eddies in each cell of 1/3° x 1/3° of the domain. Each eddy is counted in the cell that contains its center.

6.3.3.4 Temporal analysis

In figure 6.35, we can see that the number of eddies detected does not increase for the HR+BATHY field in the NEN10 method but is higher for the HAL13 method. The annual and inter-annual variability are very similar for the different datasets and methods.

Indeed, this is illustrated by figure 6.36 where the spectra of the time series are very similar between the different datasets. In this region, the annual cycle is weak but present and a semi-annual cycle may be significant.

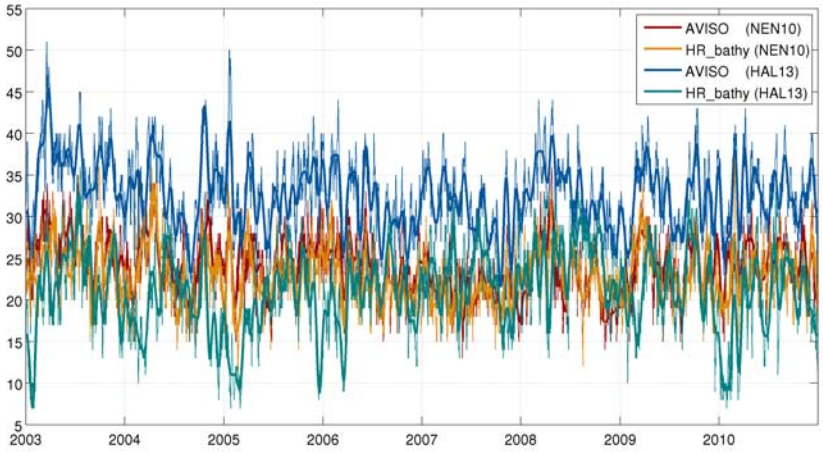

Figure 6.35: Time series of the number of detected eddies in the Mediterranean Sea in AVISOMED08 and HR+BATHY.

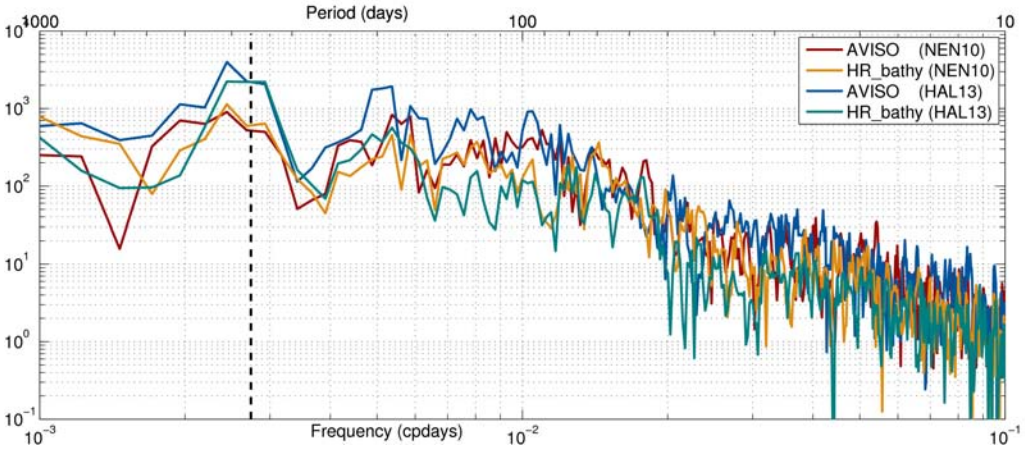

Figure 6.36: Spectra of the time series of the number of detected eddies per day.

6.4 Conclusion

In this chapter, we modified an existing eddy detection method for the specificity of the WMed. We then applied it to our observational data (satellite altimetry) and numerical model outputs, one existing simulation and a high resolution simulation developed in the course of this thesis. The algorithm was then compared to other eddy detection methods in order to isolate robust results. The methods are quite different in their functioning and therefore perform differently on the datasets.

We observed an increase of the lifetimes of the eddies in the simulations that may be due to the fact that eddies can be lost because of inadequate sampling when they stray between altimetry tracks and that it is easier to detect eddies in simulation outputs. The number of detected eddies is increased in the case of the high resolution simulation, which demonstrates that high resolution numerical models are needed to resolve mesoscale dynamics in this region. In this simulation, the distribution of mesoscale eddies is shifted towards smaller scale eddies and the peak of the distribution is closer to the Rossby radius for the region. Yet, this simulation may not be sufficient to fully resolve mesoscale dynamics. Future comparisons with higher resolution models would therefore be interesting.

The methods also show that the geographical distinction of eddies is essential in this region. The different regions of the WMed have separate mesoscale dynamics and the resulting eddies are different in scale, amplitude, lifetime and vertical structure. In consequence, it appears important to separate studies of the mesoscale into subregions even if it means reducing the significance of the statistical results. These differences may be due to the eddy formation processes; this that can be studied

further with the models.

However, a time series analysis of the number of detected eddies showed consistent results between algorithms and datasets for the whole region. The time series of the detected eddies has a annual cycle that is different for long-lived and short-lived eddies. This annual cycle is in opposite phase between the two types of eddies in altimetry, which results in its disappearance in the whole dataset. For the numerical simulations, the cycles do not compensate but have a similar phase to the altimetry results. The origins of this annual cycle are still unknown but an hypothesis about an effect on the wind has been studied. The results of this study are not yet convincing enough but open the way for future studies.

Two of the eddy identification methods have been applied to the HR altimetry dataset developed for this thesis (chapter 5). As noted in the discussion of chapter 5, the HR product is not suited for global mesoscale studies as it still has the sampling limitations of altimetry, *i.e.*, a lack of data between different altimeter tracks. The results from these datasets show no real change in the automated detection of eddies.

Chapter 7

Conclusions and perspectives

7.1 Conclusions

Mesoscale eddies are ubiquitous in the ocean and have an impact on the mean ocean circulation, heat fluxes with the ocean and atmosphere and biological processes. The Western Mediterranean Sea is a key area to study these processes as it is under strong anthropogenic pressure and is central to the climate in Europe. In this region, mesoscale eddies have not yet been systematically studied due to the small size of the Rossby radius that characterizes the horizontal scales of the eddies. In this thesis we therefore developed tools to study mesoscale dynamics in this basin in a statistical approach.

First, we developed a regional simulation of the region with the ROMS model (ROMSWMED32). The high horizontal spatial resolution (1/32°) enables the resolution of finer scales and the long duration of the simulation (20 years: 1993-2012) makes the diagnostics more robust and offers the possibility to look at interannual variations. The outputs of the final version of this new high-resolution simulation were then validated by the comparisons with observational data which show that the mean surface circulation, temperature and salinity are coherent. The

water masses are well reproduced but a positive trend in the heat and salt content is found that may explain a weak deep water convection in the Gulf of Lion, which can be related to weak transport in the Strait of Gibraltar. Energy levels in the mesoscale band are higher in the simulation than in observational data (altimetry) and another coarser resolution model (NEMOMED12), which was the objective of developing the high-resolution model since these data underestimate fine scale energy levels. Yet eddy induced heat and salt transports are similar with the lower resolution simulation.

We investigate the improvement of satellite altimetry gridded maps to recover more of the mesoscale signal. A new method involving an optimal interpolation in two steps to separate large scales and finer scales was designed and tested in the north-western Mediterranean. To improve the results in the coastal areas, we performed a test with a bathymetry constraint added on the second interpolation. The maps generated with this method yield higher levels of eddy kinetic energy with a spatial pattern that is consistent with known dynamics of the region and maps generated from drifting buoy velocities. The statistical representation of geostrophic currents in the new maps is closer to the one given by the lagrangian drifters. Comparisons with satellite sea surface temperature and in-situ data reveal that the method better represents the mesoscale in specific cases. A lagrangian comparison with drifting floats shows that the new fields provide a better estimation of their trajectories than the standard product (Bouffard et al., 2014). A study of river discharges in the Gulf of Cadiz also demonstrates the ability of these fields to detect the strong discharges (Gómez-Enri et al., 2015). However, the improvement is limited to the vicinity in time and space of an altimeter track, which means

that the quality and resolution of generated gridded fields are not spatially homogeneous.

We applied three eddy detection methods to altimetry gridded maps, the ROMSWMED32 simulation and a coarser simulation NEMOMED12. These algorithms extract useful information (number, position, size, amplitude) of the eddies from the gridded fields. The results for the different detection and tracking methods are quite different, highlighting the difficulty of studying mesoscale eddies in the region. However, some of the results are found to be consistent between the methods and are studied in this thesis. As expected, the number of detected eddies is higher for the high resolution model (ROMSWMED32) than for the other datasets (from 18 per day in AVISOMED08 and NEMOMED12 to 30 in ROMSWMED32). The mean radius of the detected structures decreases from 30 km (AVISOMED08 and NEMOMED12) to 25 km. The spatial distribution of the number of detected eddies is highly non uniform and follows well defined patterns that are quite consistent between the datasets that may be a consequence of eddy formation processes. A temporal analysis of the number of detected eddies per day reveals that there are different seasonal cycles in all of the datasets for long-lived (more than four weeks) and for short-lived (less than four weeks) eddies. The influence of wind is investigated but the results are not robust enough to make definitive conclusions. A more in-depth study of this phenomenon will be conducted in the future. The detected eddies have no clear propagation direction but seem to follow the main currents. The relationship between the size of an eddy and its duration was also examined. Results show that, on average, the size of an eddy first increases and then decreases during its life. Long-lived eddies tend to grow more rapidly toward bigger

size.

Composites of the vertical structure of the eddies in the ROMSWMED32 simulation show that eddies found in different areas have different structures. Also, anticyclones appear to have a more conic shape than cyclones and long-lived eddies present, on average, stronger anomalies of temperature and density. The spatial distribution of the mean penetration depth of the detected eddies emphasizes again the differences between the areas of the basin. For long-lived eddies in the Balearic Sea, for example, eddies have a mean penetration depth of more than 400 meters while in the Gulf of Lion, it is around 100 meters. The mean eddy penetration depth for the whole basin is 300 meters.

7.2 Perspectives

In this thesis, we showed that mesoscale dynamics are energetic in the WMed while the horizontal scales of these structures are small due to a small Rossby radius (Robinson et al., 2001). Therefore, the need for higher spatial resolution observations is stressed. This could be addressed with a higher density of satellite altimeters but also coastal radar and more fine grid in-situ data. The launch of the satellite SWOT will also allow increased observational knowledge of fine mesoscale in this region (Fu et al., 2009).

Satellite data have to be used in synergy with alternative sensors (Pascual et al., 2013) and modelling. Concerning numerical models, as we demonstrated, the computational capabilities are now sufficient to represent mesoscale variability in our area of study. Still, we can wonder if there might be a need to increase even more the resolution to represent the finer

scales that could reach 10 km, the Rossby radius. A future study should be conducted to determine the model resolution that is most well suited for the study of mesoscale eddies in the region.

Regarding the eddy detection algorithms and results, more studies should be undertaken by separating the region into different areas which, as we have shown, have different properties that are linked to the formation processes. In this thesis, we have extracted characteristics from the eddies in the region using observations and models. Future work will involve the study of the mechanisms behind the different characteristics if the eddies in different areas of the WMed. The study of the seasonal cycle, the relation between size and duration of an eddy and the vertical structures all implied some questions about the origins of the eddies that need further investigation. A focus on the location and time of the eddy formations and terminations would be a good starting point.

List of Figures

List of Tables

Bibliography

Allen, J., Smeed, D., Tintoré, J., and Ruiz, S. (2001). Mesoscale subduction at the almeria–oran front: Part 1: Ageostrophic flow. *Journal of Marine Systems*, 30(3):263–285. 21

Amores, A., Monserrat, S., and Marcos, M. (2013). Vertical structure and temporal evolution of an anticyclonic eddy in the balearic sea (western mediterranean). *Journal of Geophysical Research: Oceans*, 118(4):2097–2106. 26, 28

Arakawa, A. and Lamb, V. R. (1977). Computational design of the basic dynamical processes of the ucla general circulation model. *Methods in computational physics*, 17:173–265. 53

Arhan, M. (1987). On the large scale dynamics of the mediterranean outflow. *Deep Sea Research Part A. Oceanographic Research Papers*, 34(7):1187–1208. 12

Arhan, M. and De Verdiere, A. C. (1985). Dynamics of eddy motions in the eastern north atlantic. *Journal of Physical Oceanography*, 15(2):153–170. 36, 79, 285

Astraldi, M., Balopoulos, S., Candela, J., Font, J., Gacic, M., Gasparini, G., Manca, B., Theocharis, A., and Tintoré, J. (1999). The role of straits and channels in understanding the characteristics of mediterranean circulation. *Progress in oceanography*, 44(1):65–108. 14

Auclair, F., Marsaleix, P., and Estournel, C. (2000). Sigma coordinate pressure gradient errors: Evaluation and reduction by an inverse method. *Journal of Atmospheric and Oceanic Technology*, 17(10):1348–1367. 56

Ayoub, N., Le Traon, P.-Y., and De Mey, P. (1998). A description of the mediterranean surface variable circulation from combined ers-1 and topex/poseidon altimetric data. *Journal of Marine Systems*, 18(1):3–40. 22

Balbín, R., Flexas, M. d. M., López-Jurado, J. L., Peña, M., Amores, A., and Alemany, F. (2012). Vertical velocities and biological consequences at a front detected at the balearic sea. *Continental Shelf Research*, 47:28–41. 26

Barnier, B. (1998). Forcing the ocean. In *Ocean Modeling and Parameterization*, pages 45–80. Springer. 63

Baschek, B., Send, U., Lafuente, J. G., and Candela, J. (2001). Transport estimates in the strait of gibraltar with a tidal inverse model. *Journal of Geophysical Research: Oceans (1978–2012)*, 106(C12):31033–31044. 106

Beckers, J.-M. and Nihoul, J. C. (1992). Model of the algerian current's instability. *Journal of marine systems*, 3(4):441–451. 23

Beckmann, A. and Haidvogel, D. B. (1993). Numerical simulation of flow around a tall isolated seamount. part i: Problem formulation and model accuracy. *Journal of Physical Oceanography*, 23(8):1736–1753. 55

Benzohra, M. and Millot, C. (1995). Hydrodynamics of an open sea algerian eddy. *Deep Sea Research Part I: Oceanographic Research Papers*, 42(10):1831–1847. 22

Beranger, K., Mortier, L., and Crpon, M. (2005). Seasonal variability of water transports through the straits of gibraltar, sicily and corsica, derived from a high resolution model of the mediterranean circulation. *Progress in Oceanography*, 66(2-4):341–364. 15

Bethoux, J. (1979). Budgets of the mediterranean sea-their dependance on the local climate and on the characteristics of the atlantic waters. *Oceanologica Acta*, 2(2):157–163. 15, 16

Bethoux, J. and Gentili, B. (1999). Functioning of the mediterranean sea: past and present changes related to freshwater input and climate changes. *Journal of Marine Systems*, 20(1):33–47. 16

Bethoux, J., Gentili, B., Morin, P., Nicolas, E., Pierre, C., and Ruiz-Pino, D. (1999). The mediterranean sea: a miniature ocean for climatic and environmental studies and a key for the climatic functioning of the north atlantic. *Progress in Oceanography*, 44(1):131–146. 12

Beuvier, J., Beranger, K., Lebeaupin Brossier, C., Somot, S., Sevault, F., Drillet, Y., Bourdalle-Badie, R., Ferry, N., and Lyard, F. (2012). Spreading of the western mediterranean deep water after winter 2005: Time scales and deep cyclone transport. *Journal of Geophysical Research: Oceans (1978–2012)*, 117(C7). 8, 39, 60, 61

Beuvier, J., Sevault, F., Herrmann, M., Kontoyiannis, H., Ludwig, W., Rixen, M., Stanev, E., Beranger, K., and Somot, S. (2010). Modeling the mediterranean sea interannual variability during 1961–2000: focus on the eastern mediterranean transient. *Journal of Geophysical Research: Oceans (1978–2012)*, 115(C8). 80

Birol, F., Cancet, M., and Estournel, C. (2010). Aspects of the seasonal variability of the northern current (NW mediterranean sea) observed by altimetry. *Journal of Marine Systems*, 81(4):297–311. 18

Bouffard, J., Nencioli, F., Escudier, R., Doglioli, A. M., Petrenko, A. A., Pascual, A., Poulain, P.-M., and Elhmaidi, D. (2014). Lagrangian analysis of satellite-derived currents: Application to the north western mediterranean coastal dynamics. *Advances in Space Research*, 53(5):788–801. 121, 188

Bouffard, J., Pascual, A., Ruiz, S., Faugre, Y., and Tintor, J. (2010). Coastal and mesoscale dynamics characterization using altimetry and gliders: A case study in the balearic sea. *Journal of Geophysical Research*, 115:17 PP. 26, 29, 120

Bouffard, J., Roblou, L., Birol, F., Pascual, A., Fenoglio-Marc, L., Cancet, M., Morrow, R., and Ménard, Y. (2011). Introduction and assessment of improved coastal altimetry strategies: Case study over the northwestern mediterranean sea. In *Coastal altimetry*, pages 297–330. Springer. 24

Brankart, J.-M. and Brasseur, P. (1996). Optimal analysis of in situ data in the western mediterranean using statistics and cross-validation. *Journal of Atmospheric and Oceanic Technology*, 13(2):477–491. 81

Brasseur, P. P. (1991). A variational inverse method for the reconstruction of general circulation fields in the northern bering sea. *Journal of Geophysical Research: Oceans (1978–2012)*, 96(C3):4891–4907. 81

Broecker, W. S. et al. (1991). The great ocean conveyor. *Oceanography*, 4(2):79–89. 12

Bryden, H. L., Candela, J., and Kinder, T. H. (1994). Exchange through the strait of gibraltar. *Progress in Oceanography*, 33(3):201–248. 16

Bunker, A., Charnock, H., and Goldsmith, R. (1982). A note on the heat balance of the mediterranean and red seas. *Journal of Marine Research*, 40:73–84. 15

Burkov, V., Krivosheya, V., Ovchinnikov, I., and Savin, M. (1979). Eddies in the current system of the western mediterranean sea. *Oceanology*, 19(1):9–13. 22

Candela, J., Winant, C. D., and Bryden, H. L. (1989). Meteorologically forced subinertial flows through the strait of gibraltar. *Journal of Geophysical Research: Oceans (1978–2012)*, 94(C9):12667–12679. 14

Carrère, L. and Lyard, F. (2003). Modeling the barotropic response of the global ocean to atmospheric wind and pressure forcing-comparisons with observations. *Geophysical Research Letters*, 30(6). 34

Chelton, D. B., Deszoeke, R. A., Schlax, M. G., El Naggar, K., and Siwertz, N. (1998). Geographical variability of the first baroclinic rossby radius of deformation. *Journal of Physical Oceanography*, 28(3):433–460. 5

Chelton, D. B., Schlax, M. G., and Samelson, R. M. (2011). Global observations of nonlinear mesoscale eddies. *Progress in Oceanography*, 91(2):167–216. 124, 126, 127, 128, 133, 135, 138, 140, 143, 160, 287

Chelton, D. B., Schlax, M. G., Samelson, R. M., and de Szoeke, R. A. (2007). Global observations of large oceanic eddies. *Geophysical Research Letters*, 34(15):L15606. 3, 6, 135

Colas, F., McWilliams, J. C., Capet, X., and Kurian, J. (2012). Heat balance and eddies in the peru-chile current system. *Climate dynamics*, 39(1-2):509–529. 7

Conan, P. and Millot, C. (1995). Variability of the northern current off marseilles, western mediterranean-sea, from february to june 1992. *Oceanologica Acta*, 18(2):193–205. 18

Criado-Aldeanueva, F., Soto-Navarro, F. J., and García-Lafuente, J. (2012). Seasonal and interannual variability of surface heat and freshwater fluxes in the mediterranean sea: Budgets and exchange through the strait of gibraltar. *International Journal of Climatology*, 32(2):286–302. 14, 106, 108

Dai, A., Qian, T., Trenberth, K. E., and Milliman, J. D. (2009). Changes in continental freshwater discharge from 1948 to 2004. *Journal of Climate*, 22(10):2773–2792. 68

Déqué, M. and Piedelievre, J. P. (1995). High resolution climate simulation over europe. *Climate dynamics*, 11(6):321–339. 61

Donlon, C. J., Martin, M., Stark, J., Roberts-Jones, J., Fiedler, E., and Wimmer, W. (2012). The operational sea surface temperature and sea ice analysis (ostia) system. *Remote Sensing of Environment*, 116:140–158. 80

Ducet, N., Le Traon, P.-Y., and Reverdin, G. (2000). Global high-resolution mapping of ocean circulation from topex/poseidon and ers-1 and-2. *Journal of Geophysical Research: Oceans (1978–2012)*, 105(C8):19477–19498. 6

Escudier, R., Bouffard, J., Pascual, A., Poulain, P.-M., and Pujol, M.-I. (2013). Improvement of coastal and mesoscale observation from space: Application to the northwestern mediterranean sea. *Geophysical Research Letters*. 120

Estournel, C., Durrieu de Madron, X., Marsaleix, P., Auclair, F., Julliand, C., and Vehil, R. (2003). Observation and modeling of the winter coastal oceanic circulation in the gulf of lion under wind conditions influenced by the continental orography (fetch experiment). *Journal of Geophysical Research: Oceans (1978–2012)*, 108(C3). 24

Feliks, Y. (1985). On the rossby radius of deformation in the ocean. *Journal of Physical Oceanography*, 15(11):1605–1607.

Feng, M., Majewski, L. J., Fandry, C., and Waite, A. M. (2007). Characteristics of two counter-rotating eddies in the leeuwin current system off the western australian coast. *Deep Sea Research Part II: Topical Studies in Oceanography*, 54(8):961–980. 7

Flexas, M. d. M., Gomis, D., Ruiz, S., Pascual, A., and León, P. (2006). ¡ i¿ in situ¡/i¿ and satellite observations of the eastward migration of the western alboran sea gyre. *Progress in Oceanography*, 70(2):486–509. 21

Font, J., Garcialadona, E., and Gorriz, E. (1995). The seasonality of mesoscale motion in the northern current of the western mediterranean-several years of evidence. *Oceanologica Acta*, 18(2):207–219. 24

Font, J., Isern-Fontanet, J., and De Jesus Salas, J. (2004). Tracking a big anticyclonic eddy in the western mediterranean sea. *Scientia Marina*, 68(3):331–342. 23

Font, J., Millot, C., Salas, J., Julia, A., and Chic, O. (1998). The drift of modified atlantic water from the alboran sea to the eastern mediterranean. *Scientia marina*, 62(3):211–216. 22

Font, J., Salat, J., and Tintoré, J. (1988). Permanent features of the circulation in the catalan sea. *Oceanologica Acta*, 9:51–57. 25

Frankignoul, C. and Müller, P. (1979). Quasi-geostrophic response of an infinite β-plane ocean to stochastic forcing by the atmosphere. *Journal of Physical Oceanography*, 9(1):104–127. 7

Fu, L.-L., Alsdorf, D., Rodriguez, E., Morrow, R., Mognard, N., Lambin, J., Vaze, P., and Lafon, T. (2009). The swot (surface water and ocean topography) mission: spaceborne radar interferometry for oceanographic and hydrological applications. In *OCEANOBS09 Conference*. 190

Fu, L.-L., Christensen, E. J., Yamarone, C. A., Lefebvre, M., Menard, Y., Dorrer, M., and Escudier, P. (1994). Topex/poseidon mission overview. *Journal of Geophysical Research: Oceans (1978–2012)*, 99(C12):24369–24381. 34

García, M., Millot, C., Font, J., and García-Ladona, E. (1994). Surface circulation variability in the balearic basin. *Journal of Geophysical Research: Oceans (1978–2012)*, 99(C2):3285–3296. 26

Garreau, P., Garnier, V., and Schaeffer, A. (2011). Eddy resolving modelling of the gulf of lions and catalan sea. *Ocean Dynamics*, 61(7):991–1003. 25, 40

Gascard, J.-C. and Richez, C. (1985). Water masses and circulation in the western alboran sea and in the straits of gibraltar. *Progress in Oceanography*, 15(3):157–216. 99

Gaspar, P., Ogor, F., Le Traon, P.-Y., and Zanife, O.-Z. (1994). Estimating the sea state bias of the topex and poseidon altimeters from crossover differences. *Journal of Geophysical Research: Oceans (1978–2012)*, 99(C12):24981–24994. 34

Gaultier, L., Verron, J., Brankart, J.-M., Titaud, O., and Brasseur, P. (2013). On the inversion of submesoscale tracer fields to estimate the surface ocean circulation. *Journal of Marine Systems*, 126:33–42. 31

Gómez-Enri, J., Escudier, R., Pascual, A., and Mañanes, R. (2015). Heavy guadalquivir river discharge detection with satellite altimetry: the case of the eastern continental shelf of the gulf of cadiz (iberian peninsula). *Advances in Space Research*. 121, 188

Gomis, D., Tsimplis, M. N., Martín-Míguez, B., Ratsimandresy, A. W., García-Lafuente, J., and Josey, S. A. (2006). Mediterranean sea level and barotropic flow through the strait of gibraltar for the period 1958–2001 and reconstructed since 1659. *Journal of Geophysical Research: Oceans (1978–2012)*, 111(C11). 14

Good, S. A., Martin, M. J., and Rayner, N. A. (2013). En4: Quality controlled ocean temperature and salinity profiles and monthly objective analyses with uncertainty estimates. *Journal of Geophysical Research: Oceans*, 118(12):6704–6716. 80

Guihou, K., Marmain, J., Ourmières, Y., Molcard, A., Zakard-

jian, B., and Forget, P. (2013). A case study of the mesoscale dynamics in the north-western mediterranean sea: a combined data–model approach. *Ocean Dynamics*, pages 1–16. 40

Halo, I., Backeberg, B., Penven, P., Ansorge, I., Reason, C., and Ullgren, J. (2013). Eddy properties in the mozambique channel: A comparison between observations and two numerical ocean circulation models. *Deep Sea Research Part II: Topical Studies in Oceanography*. 135, 136, 288

Haney, R. L. (1991). On the pressure gradient force over steep topography in sigma coordinate ocean models. *Journal of Physical Oceanography*, 21(4):610–619. 55

Herrmann, M., Somot, S., Sevault, F., Estournel, C., and Dqu, M. (2008). Modeling the deep convection in the northwestern mediterranean sea using an eddy-permitting and an eddy-resolving model: Case study of winter 19861987. *Journal of Geophysical Research: Oceans*, 113(C4):n/a–n/a. 39

Herrmann, M. J. and Somot, S. (2008). Relevance of era40 dynamical downscaling for modeling deep convection in the mediterranean sea. *Geophysical Research Letters*, 35(4). 12, 61, 104

Heslop, E. E., Ruiz, S., Allen, J., López-Jurado, J. L., Renault, L., and Tintoré, J. (2012). Autonomous underwater gliders monitoring variability at choke points in our ocean system: A case study in the western mediterranean sea. *Geophysical Research Letters*, 39(20). 29

Holland, W. R. (1978). The role of mesoscale eddies in the general circulation of the ocean-numerical experiments using

a wind-driven quasi-geostrophic model. *Journal of Physical Oceanography*, 8(3):363–392. 8

Hu, Z., Doglioli, A., Petrenko, A., Marsaleix, P., and Dekeyser, I. (2009). Numerical simulations of eddies in the gulf of lion. *Ocean Modelling*, 28(4):203–208. 24, 25

Hu, Z., Petrenko, A., Doglioli, A., and Dekeyser, I. (2011). Study of a mesoscale anticyclonic eddy in the western part of the gulf of lion. *Journal of Marine Systems*, 88(1):3–11. 24, 27

Hulme, M., Barrow, E. M., Arnell, N. W., Harrison, P. A., Johns, T. C., and Downing, T. E. (1999). Relative impacts of human-induced climate change and natural climate variability. *Nature*, 397(6721):688–691. 12

Ilıcak, M., Adcroft, A. J., Griffies, S. M., and Hallberg, R. W. (2012). Spurious dianeutral mixing and the role of momentum closure. *Ocean Modelling*, 45:37–58. 45

Iorga, M. C. and Lozier, M. S. (1999). Signatures of the mediterranean outflow from a north atlantic climatology: 1. salinity and density fields. *Journal of Geophysical Research: Oceans (1978–2012)*, 104(C11):25985–26009. 12

Isern-Fontanet, J., Font, J., García-Ladona, E., Emelianov, M., Millot, C., and Taupier-Letage, I. (2004). Spatial structure of anticyclonic eddies in the algerian basin (mediterranean sea) analyzed using the okubo–weiss parameter. *Deep Sea Research Part II: Topical Studies in Oceanography*, 51(25):3009–3028. 23

Isern-Fontanet, J., García-Ladona, E., and Font, J. (2006). Vortices of the mediterranean sea: An altimetric perspec-

tive. *Journal of Physical Oceanography*, 36(1):87–103. 37, 124, 127, 135

Iudicone, D., Santoleri, R., Marullo, S., and Gerosa, P. (1998). Sea level variability and surface eddy statistics in the mediterranean sea from topex/poseidon data. *Journal of Geophysical Research*, 103(C2):2995–3011. 37

Jayne, S. R. and Marotzke, J. (2002). The oceanic eddy heat transport. *Journal of Physical Oceanography*, 32(12). 7

Josey, S. A., Somot, S., and Tsimplis, M. (2011). Impacts of atmospheric modes of variability on mediterranean sea surface heat exchange. *Journal of Geophysical Research: Oceans (1978–2012)*, 116(C2). 15

Juza, M., Renault, L., Ruiz, S., and Tintoré, J. (2013). Origin and pathways of winter intermediate water in the northwestern mediterranean sea using observations and numerical simulation. *Journal of Geophysical Research: Oceans*, 118(12):6621–6633. 20

Katz, E. J. (1972). The levantine intermediate water between the strait of sicily and the strait of gibraltar. In *Deep Sea Research and Oceanographic Abstracts*, volume 19, pages 507–520. Elsevier. 22

Keeling, R. F. and Peng, T.-H. (1995). Transport of heat, co _{2} and o _{2} by the atlantic's thermohaline circulation. *Philosophical Transactions of the Royal Society of London. Series B: Biological Sciences*, 348(1324):133–142. 13

La Violette, P. E., Tintoré, J., and Font, J. (1990). The surface circulation of the balearic sea. *Journal of Geophysical Research: Oceans (1978–2012)*, 95(C2):1559–1568. 25

Lafuente, J. G., Vargas, J. M., Plaza, F., Sarhan, T., Candela, J., and Bascheck, B. (2000). Tide at the eastern section of the strait of gibraltar. *Journal of Geophysical Research: Oceans (1978–2012)*, 105(C6):14197–14213. 106

Large, W. G., McWilliams, J. C., and Doney, S. C. (1994). Oceanic vertical mixing: A review and a model with a nonlocal boundary layer parameterization. *Reviews of Geophysics*, 32(4):363–403. 51

Lazure, P. and Dumas, F. (2008). An external–internal mode coupling for a 3d hydrodynamical model for applications at regional scale (mars). *Advances in Water Resources*, 31(2):233–250. 40

Le Traon, P., Nadal, F., and Ducet, N. (1998). An improved mapping method of multisatellite altimeter data. *Journal of Atmospheric and Oceanic Technology*, 15(2):522–534. 35, 78

Le Traon, P.-Y. and Ogor, F. (1998). Ers-1/2 orbit improvement using topex/poseidon: The 2 cm challenge. *Journal of Geophysical Research: Oceans (1978–2012)*, 103(C4):8045–8057. 34

Lebeaupin Brossier, C., Béranger, K., Deltel, C., and Drobinski, P. (2011). The mediterranean response to different space–time resolution atmospheric forcings using perpetual mode sensitivity simulations. *Ocean Modelling*, 36(1):1–25. 104

Lemarié, F., Debreu, L., Shchepetkin, A., and McWilliams, J. (2012). On the stability and accuracy of the harmonic and biharmonic isoneutral mixing operators in ocean models. *Ocean Modelling*, 52-53(0):9 – 35. 51

Levitus, S., Antonov, J., and Boyer, T. (2005). Warming of the world ocean, 1955–2003. *Geophysical Research Letters*, 32(2). 60

Levy, M., Mémery, L., and Madec, G. (1998). The onset of a bloom after deep winter convection in the northwestern mediterranean sea: mesoscale process study with a primitive equation model. *Journal of Marine Systems*, 16(1):7–21. 7

L'Hévéder, B., Mortier, L., Testor, P., and Lekien, F. (2013). A glider network design study for a synoptic view of the oceanic mesoscale variability. *Journal of Atmospheric and Oceanic Technology*, 30(7):1472–1493. 29

Llinás, L., Pickart, R. S., Mathis, J. T., and Smith, S. L. (2008). The effects of eddy transport on zooplankton biomass and community composition in the western arctic. *Deep Sea Research Part II: Topical Studies in Oceanography*. 7

Lorbacher, K., Dommenget, D., Niiler, P., and Köhl, A. (2006). Ocean mixed layer depth: A subsurface proxy of ocean-atmosphere variability. *Journal of Geophysical Research: Oceans (1978–2012)*, 111(C7). 103

Lozier, M. S. (1997). Evidence for large-scale eddy-driven gyres in the north atlantic. *Science*, 277(5324):361 –364. 8

Ludwig, W., Dumont, E., Meybeck, M., and Heussner, S. (2009). River discharges of water and nutrients to the mediterranean and black sea: major drivers for ecosystem changes during past and future decades? *Progress in Oceanography*, 80(3):199–217. 60

Ly, L. N. and Jiang, L. (1999). Horizontal pressure gradient

errors of the Monterey bay sigma coordinate ocean model with various grids. *Journal of Oceanography*, 55(1):87–97. 56

Macdonald, A. M., Candela, J., and Bryden, H. L. (1994). An estimate of the net heat transport through the strait of gibraltar. *Seasonal and Interannual Variability of the Western Mediterranean Sea*, pages 13–32. 15

Madec, G. and the NEMO Team (2008). Nemo ocean engine. *Note du Pôle de modélisation.*, 27. Institut Pierre-Simon Laplace (IPSL), France. 39, 60

Mahadevan, A., DAsaro, E., Lee, C., and Perry, M. J. (2012). Eddy-driven stratification initiates north atlantic spring phytoplankton blooms. *Science*, 337(6090):54–58. 7

Manca, B., Burca, M., Giorgetti, A., Coatanoan, C., Garcia, M.-J., and Iona, A. (2004). Physical and biochemical averaged vertical profiles in the mediterranean regions: an important tool to trace the climatology of water masses and to validate incoming data from operational oceanography. *Journal of Marine Systems*, 48(1):83–116. 13, 17

Marchesiello, P., Capet, X., Menkes, C., and Kennan, S. C. (2011). Submesoscale dynamics in tropical instability waves. *Ocean Modelling*, 39(1):31–46. 137

Marchesiello, P., Debreu, L., and Couvelard, X. (2009). Spurious diapycnal mixing in terrain-following coordinate models: The problem and a solution. *Ocean Modelling*, 26(3):156–169. 51

Marchesiello, P., McWilliams, J. C., and Shchepetkin, A. (2001). Open boundary conditions for long-term integration of regional oceanic models. *Ocean Modelling*, 3(1):1–20. 62

Mariotti, A., Struglia, M. V., Zeng, N., and Lau, K. (2002). The hydrological cycle in the mediterranean region and implications for the water budget of the mediterranean sea. *Journal of climate*, 15(13):1674–1690. 95

Marsaleix, P., Auclair, F., and Estournel, C. (2006). Considerations on open boundary conditions for regional and coastal ocean models. *Journal of Atmospheric and Oceanic Technology*, 23(11):1604–1613. 39

Marshall, J. and Schott, F. (1999). Open-ocean convection: Observations, theory, and models. *Reviews of Geophysics*, 37(1):1–64. 19

Martin, M., Hines, A., and Bell, M. (2007). Data assimilation in the foam operational short-range ocean forecasting system: A description of the scheme and its impact. *Quarterly Journal of the Royal Meteorological Society*, 133(625):981–995. 80

Marullo, S., Santoleri, R., and Bignami, F. (1994). The surface characteristics of the tyrrhenian sea: Historical satellite data analysis. *Coastal and Estuarine Studies*, 46:135–154. 18

Mason, E., Molemaker, J., Shchepetkin, A. F., Colas, F., McWilliams, J. C., and Sangrà, P. (2010). Procedures for offline grid nesting in regional ocean models. *Ocean Modelling*, 35(1):1–15. 62, 95

Mason, E. and Pascual, A. (2013). Multiscale variability in the balearic sea: An altimetric perspective. *Journal of Geophysical Research: Oceans*, 118(6):3007–3025. 18, 25, 26

McWilliams, J. C. (1985). Submesoscale, coherent vortices in the ocean. *Reviews of Geophysics*, 23(2):165–182. 7

McWilliams, J. C. and Flierl, G. R. (1979). On the evolution of isolated, nonlinear vortices. *Journal of Physical Oceanography*, 9(6):1155–1182. 141

MEDAR Group et al. (2003). Medatlas/2002-database: Mediterranean and black sea database of temperature, salinity and bio-chemical parameters. climatological atlas. *[4 CD]*. 8

Mellor, G., Ezer, T., and Oey, L. (1994). The pressure gradient conundrum of sigma coordinate ocean models. *Journal of Atmospheric and Oceanic Technology*, 11(4):1126–1134. 55

Millot, C. (1982). Analysis of upwelling in the gulf of lions. *Hydrodynamics of Semi-enclosed Sea*, pages 143–154. 24, 25

Millot, C. (1985). Some features of the algerian current. *Journal of Geophysical Research: Oceans (1978–2012)*, 90(C4):7169–7176. 22, 23

Millot, C. (1987). Circulation in the western mediterranean-sea. *Oceanologica Acta*, 10(2):143–149. 12, 17

Millot, C. (1999). Circulation in the western mediterranean sea. *Journal of Marine Systems*, 20(1-4):423–442. 16, 19, 83, 84, 102

Millot, C., Wald, L., et al. (1980). The effect of mistral wind on the ligurian current near provence. *Oceanologica Acta*, 3(4):399–402. 24

Molcard, A., Pinardi, N., Iskandarani, M., and Haidvogel, D. (2002). Wind driven general circulation of the mediterranean sea simulated with a spectral element ocean model. *Dynamics of Atmospheres and Oceans*, 35(2):97–130. 16

Molemaker, M. J., McWilliams, J. C., and Yavneh, I. (2005). Baroclinic instability and loss of balance. *Journal of Physical Oceanography*, 35(9):1505–1517. 3

Morán, X. A. G., Taupier-Letage, I., Vázquez-Domı?nguez, E., Ruiz, S., Arin, L., Raimbault, P., and Estrada, M. (2001). Physical-biological coupling in the algerian basin (sw mediterranean): influence of mesoscale instabilities on the biomass and production of phytoplankton and bacterioplankton. *Deep Sea Research Part I: Oceanographic Research Papers*, 48(2):405–437. 23

Naudin, J., Cauwet, G., Chretiennot-Dinet, M.-J., Deniaux, B., Devenon, J.-L., and Pauc, H. (1997). River discharge and wind influence upon particulate transfer at the land–ocean interaction: case study of the rhone river plume. *Estuarine, coastal and shelf science*, 45(3):303–316. 101

Nencioli, F., Dong, C., Dickey, T., Washburn, L., and McWilliams, J. C. (2010). A vector geometry-based eddy detection algorithm and its application to a high-resolution numerical model product and high-frequency radar surface velocities in the southern california bight. *Journal of Atmospheric and Oceanic Technology*, 27(3):564–579. 131, 132, 133, 134, 289

Nencioli, F., d'Ovidio, F., Doglioli, A., and Petrenko, A. (2011). Surface coastal circulation patterns by in-situ detection of lagrangian coherent structures. *Geophysical Research Letters*, 38(17). 120, 139

Nielsen, J. N. (1912). Hydrographic of the mediterranean and adjacent waters. *Report of the Danish Oceanographic Expe-*

dition 1908-1910 to the Mediterranean and Adjacent Waters, 1, page 72191. 18

Okubo, A. (1970). Horizontal dispersion of floatable particles in the vicinity of velocity singularities such as convergences. In *Deep sea research and oceanographic abstracts*, volume 17, pages 445–454. Elsevier. 135

Olita, A., Ribotti, A., Sorgente, R., Fazioli, L., and Perilli, A. (2011). Sla–chlorophyll-a variability and covariability in the algero-provençal basin (1997–2007) through combined use of eof and wavelet analysis of satellite data. *Ocean dynamics*, 61(1):89–102. 17, 22

Orlanski, I. (1976). A simple boundary condition for unbounded hyperbolic flows. *Journal of Computational Physics*, 21(3):251–269. 62

Oschlies, A. and Garçon, V. (1998). Eddy-induced enhancement of primary production in a model of the north atlantic ocean. *Nature*, 394(6690):266–269. 7

Pascual, A., Bouffard, J., Ruiz, S., Buongiorno Nardelli, B., Vidal-Vijande, E., Escudier, R., Sayol, J. M., and Orfila, A. (2013). Recent improvements in mesoscale characterization of the western mediterranean sea: synergy between satellite altimetry and other observational approaches. *Scientia Marina*, 77(1):19–36. 190

Pascual, A. et al. (2010). Combining new and conventional sensors to study the balearic current. *Sea Technology*, 51:32–36. 26, 27, 30, 125

Pascual, A., Gomis, D., Haney, R. L., and Ruiz, S. (2004). A quasigeostrophic analysis of a meander in the palams canyon:

Vertical velocity, geopotential tendency, and a relocation technique. *Journal of Physical Oceanography*, 34(10):2274–2287.

Pascual, A., Marcos, M., and Gomis, D. (2008). Comparing the sea level response to pressure and wind forcing of two barotropic models: Validation with tide gauge and altimetry data. *Journal of Geophysical Research: Oceans (1978–2012)*, 113(C7). 34

Pascual, A., Nardelli, B. B., Larnicol, G., Emelianov, M., and Gomis, D. (2002). A case of an intense anticyclonic eddy in the balearic sea (western mediterranean). *Journal of Geophysical Research*, 107:14 PP. 26

Pascual, A., Pujol, M.-I., Larnicol, G., Le Traon, P.-Y., and Rio, M.-H. (2007). Mesoscale mapping capabilities of multi-satellite altimeter missions: First results with real data in the mediterranean sea. *Journal of Marine Systems*, 65(1-4):190–211. 37

Peliz, A., Boutov, D., Cardoso, R., Delgado, J., and Soares, P. M. (2012). The gulf of cadiz-alboran sea sub-basin: Model setup, exchange and seasonal variability. *Ocean Modelling*. 22, 58, 59

Peliz, A., Boutov, D., and Teles-Machado, A. (2013). The alboran sea mesoscale in a long term high resolution simulation: Statistical analysis. *Ocean Modelling*. 22, 40

Penven, P., Debreu, L., Marchesiello, P., and McWilliams, J. C. (2006). Evaluation and application of the roms 1-way embedding procedure to the central california upwelling system. *Ocean Modelling*, 12(1):157–187. 44

Penven, P., Echevin, V., Pasapera, J., Colas, F., and Tam, J. (2005). Average circulation, seasonal cycle, and mesoscale dynamics of the peru current system: A modeling approach. *Journal of Geophysical Research*, 110(C10):C10021. 135, 136

Penven, P., Marchesiello, P., Debreu, L., and Lefèvre, J. (2008). Software tools for pre-and post-processing of oceanic regional simulations. *Environmental Modelling & Software*, 23(5):660–662. 45

Petrenko, A., Leredde, Y., and Marsaleix, P. (2005). Circulation in a stratified and wind-forced gulf of lions, nw mediterranean sea: in situ and modeling data. *Continental Shelf Research*, 25(1):7–27. 24

Pinardi, N. and Navarra, A. (1993). Baroclinic wind adjustment processes in the mediterranean sea. *Deep Sea Research Part II: Topical Studies in Oceanography*, 40(6):1299–1326. 16

Pinot, J.-M., López-Jurado, J., and Riera, M. (2002). The canales experiment (1996-1998). interannual, seasonal, and mesoscale variability of the circulation in the balearic channels. *Progress in Oceanography*, 55(3):335–370. 18, 20, 25

Pinot, J.-M., Tintoré, J., and Gomis, D. (1995). Multivariate analysis of the surface circulation in the balearic sea. *Progress in Oceanography*, 36(4):343–376. 26

Potter, R. A. and Lozier, M. S. (2004). On the warming and salinification of the mediterranean outflow waters in the north atlantic. *Geophysical Research Letters*, 31(1). 12

Poulain, P.-M., Menna, M., and Mauri, E. (2012). Surface geostrophic circulation of the mediterranean sea derived from

drifter and satellite altimeter data. *Journal of Physical Oceanography*. 20, 28, 82, 112, 113

Puillat, I., Taupier-Letage, I., and Millot, C. (2002). Algerian eddies lifetime can near 3 years. *Journal of Marine Systems*, 31(4):245–259. 23

Pujol, M.-I. and Larnicol, G. (2005). Mediterranean sea eddy kinetic energy variability from 11 years of altimetric data. *Journal of Marine Systems*, 58(3-4):121–142. 20, 36, 79, 110, 139

Quentin, C., Barbin, Y., Bellomo, L., Forget, P., Gagelli, J., Grosdidier, S., Guérin, C.-A., Guihou, K., Marmain, J., Molcard, A., et al. (2013). Hf radar in french mediterranean sea: an element of moose mediterranean ocean observing system on environment. *OCOSS'2013 Proceedings*, pages 25–30. 29

Renault, L., Juza, M., Garau, B., Sayol, J. M., Orfila, A., and Tintoré, J. (2013). Wmop: The socib western mediterranean sea operational forecasting system. In *EGU General Assembly Conference Abstracts*, volume 15, page 9203. 44

Renault, L., Oguz, T., Pascual, A., Vizoso, G., and Tintore, J. (2012). Surface circulation in the alborán sea (western mediterranean) inferred from remotely sensed data. *Journal of Geophysical Research: Oceans (1978–2012)*, 117(C8). 21, 22, 85, 86, 88

Reynolds, R. W., Chelton, D. B., Roberts-Jones, J., Martin, M. J., Menemenlis, D., and Merchant, C. J. (2013). Objective determination of feature resolution in two sea surface temperature analyses. *Journal of Climate*, 26(8):2514–2533. 80

Richardson, P. L. (1983). Eddy kinetic energy in the north atlantic from surface drifters. *Journal of Geophysical Research: Oceans (1978–2012)*, 88(C7):4355–4367. 6

Rinaldi, E., Nardelli, B. B., Zambianchi, E., Santoleri, R., and Poulain, P.-M. (2010). Lagrangian and Eulerian observations of the surface circulation in the tyrrhenian sea. *Journal of Geophysical Research*, 115(C4):C04024. 17

Rio, M.-H., Pascual, A., Poulain, P.-M., Menna, M., Barceló, B., and Tintoré, J. (2014). Computation of a new mean dynamic topography for the mediterranean sea from model outputs, altimeter measurements and oceanographic in-situ data. *Ocean Science Discussions*, 11(1):655–692. 18, 79, 80

Rixen, M., Beckers, J.-M., Levitus, S., Antonov, J., Boyer, T., Maillard, C., Fichaut, M., Balopoulos, E., Iona, S., Dooley, H., Garcia, M.-J., Manca, B., Giorgetti, A., Manzella, G., Mikhailov, N., Pinardi, N., and Zavatarelli, M. (2005). The western mediterranean deep water: A proxy for climate change. *Geophysical Research Letters*, 32:4 PP. 81, 93

Robinson, A., Golnaraghi, M., Leslie, W., Artegiani, A., Hecht, A., Lazzoni, E., Michelato, A., Sansone, E., Theocharis, A., and Ünlüata, Ü. (1991). The eastern mediterranean general circulation: features, structure and variability. *Dynamics of Atmospheres and Oceans*, 15(3):215–240. 19

Robinson, A. R., Leslie, W. G., Theocharis, A., and Lascaratos, A. (2001). *Mediterranean Sea circulation*. Academic Press. 8, 12, 24, 190

Rubio, A., Barnier, B., Jordá, G., Espino, M., and Marsaleix, P. (2009). Origin and dynamics of mesoscale eddies in the cata-

lan sea (nw mediterranean): insight from a numerical model study. *Journal of Geophysical Research: Oceans (1978–2012)*, 114(C6). 25

Ruiz, S., Font, J., Emelianov, M., Isern-Fontanet, J., Millot, C., Salas, J., and Taupier-Letage, I. (2002). Deep structure of an open sea eddy in the algerian basin. *Journal of Marine Systems*, 33:179–195. 23

Ruiz, S., Gomis, D., Sotillo, M. G., and Josey, S. A. (2008). Characterization of surface heat fluxes in the mediterranean sea from a 44-year high-resolution atmospheric data set. *Global and Planetary Change*, 63(2):258–274. 15

Ruiz, S., Pascual, A., Garau, B., Faugre, Y., Alvarez, A., and Tintor, J. (2009a). Mesoscale dynamics of the balearic front, integrating glider, ship and satellite data. *Journal of Marine Systems*, 78, Supplement(0):S3–S16. 18, 26, 30

Ruiz, S., Pascual, A., Garau, B., Pujol, I., and Tintore, J. (2009b). Vertical motion in the upper ocean from glider and altimetry data. *Geophysical Research Letters*, 36(14). 21

Saha, S., Moorthi, S., Pan, H.-L., Wu, X., Wang, J., Nadiga, S., Tripp, P., Kistler, R., Woollen, J., Behringer, D., et al. (2010). The ncep climate forecast system reanalysis. *Bulletin of the American Meteorological Society*, 91(8). 64

Salas, J., Millot, C., Font, J., and Garcıa-Ladona, E. (2002). Analysis of mesoscale phenomena in the algerian basin observed with drifting buoys and infrared images. *Deep Sea Research Part I: Oceanographic Research Papers*, 49(2):245–266. 23

Salat, J. and Font, J. (1987). Water mass structure near and offshore the catalan coast during the winters of 1982 and 1983. In *Annales geophysicae. Series B. Terrestrial and planetary physics*, volume 5, pages 48–54. 20

Samelson, R., Schlax, M., and Chelton, D. (2014). Randomness, symmetry, and scaling of mesoscale eddy life cycles. *Journal of Physical Oceanography*, 44(3):1012–1029. 160

Sammari, C., Millot, C., and Prieur, L. (1995). Aspects of the seasonal and mesoscale variabilities of the northern current in the western mediterranean sea inferred from the prolig-2 and pros-6 experiments. *Deep Sea Research Part I: Oceanographic Research Papers*, 42(6):893–917. 84

Sánchez-Román, A., Sannino, G., García-Lafuente, J., Carillo, A., and Criado-Aldeanueva, F. (2009). Transport estimates at the western section of the strait of gibraltar: A combined experimental and numerical modeling study. *Journal of Geophysical Research: Oceans (1978–2012)*, 114(C6). 106

Sannino, G., Herrmann, M., Carillo, A., Rupolo, V., Ruggiero, V., Artale, V., and Heimbach, P. (2009). An eddy-permitting model of the mediterranean sea with a two-way grid refinement at the strait of gibraltar. *Ocean Modelling*, 30(1):56–72. 15

Sanz, J. L. (1991). *Prospección geofísica del Estrecho de Gibraltar: resultados del programa Hércules (1980-1983)*. Number 7. Ministerio de Agricultura, Pesca y Alimentación, Secretaría General Técnica. 57

Schmitz Jr, W. J. (1996). On the world ocean circulation. vol-

ume 1. some global features/north atlantic circulation. Technical report, DTIC Document. 12

Schott, F., Visbeck, M., Send, U., Fischer, J., Stramma, L., and Desaubies, Y. (1996). Observations of deep convection in the gulf of lions, northern mediterranean, during the winter of 1991/92. *Journal of Physical Oceanography*, 26(4):505–524. 103

Send, U., Font, J., Krahmann, G., Millot, C., Rhein, M., and Tintoré, J. (1999). Recent advances in observing the physical oceanography of the western mediterranean sea. *Progress in Oceanography*, 44(1):37–64. 20

Send, U., Mertens, C., and Font, J. (1996). Recent observation indicates convection'role in deep water circulation. *Eos, Transactions American Geophysical Union*, 77(7):61–65. 19

Shchepetkin, A. F. and McWilliams, J. C. (1998). Quasi-monotone advection schemes based on explicit locally adaptive dissipation. *Monthly Weather Review*, 126(6):1541–1580. 51

Shchepetkin, A. F. and McWilliams, J. C. (2003). A method for computing horizontal pressure-gradient force in an oceanic model with a nonaligned vertical coordinate. *Journal of Geophysical Research: Oceans (1978–2012)*, 108(C3). 55

Shchepetkin, A. F. and McWilliams, J. C. (2005). The regional oceanic modeling system (ROMS): a split-explicit, free-surface, topography-following-coordinate oceanic model. *Ocean Modelling*, 9(4):347–404. 44, 54

Shchepetkin, A. F. and McWilliams, J. C. (2009a). Computational kernel algorithms for fine-scale, multi-process, long-

time oceanic simulations. *Handbook of Numerical Analysis: Computational Methods for the Atmosphere and Oceans*, 119(182):01202–0. 44, 54

Shchepetkin, A. F. and McWilliams, J. C. (2009b). Correction and commentary for ocean forecasting in terrain-following coordinates: Formulation and skill assessment of the regional ocean modeling system by haidvogel et al., j. comp. phys. 227, pp. 35953624. *Journal of Computational Physics*, 228(24):8985 – 9000. 48

Simmons, A. J. and Gibson, J. (2000). *The ERA-40 project plan*. European Centre for Medium-Range Weather Forecasts. 61

Slutz, R. J., Lubker, S. J., Hiscox, J. D., Woodruff, S., Jenne, R., Joseph, D., Steurer, P., and Elms, J. (1985). Comprehensive ocean-atmosphere data set: release 1. *I: Climate Research Program, ERL/NOAA, Boulder, CO*. 64

Smith, W. H. F. and Sandwell, D. T. (1997). Global sea floor topography from satellite altimetry and ship depth soundings. *Science*, 277(5334):1956–1962. 57

Soto-Navarro, J., Criado-Aldeanueva, F., García-Lafuente, J., and Sánchez-Román, A. (2010). Estimation of the atlantic inflow through the strait of gibraltar from climatological and in situ data. *Journal of Geophysical Research: Oceans (1978–2012)*, 115(C10). 14

Stanev, E. V. and Peneva, E. L. (2001). Regional sea level response to global climatic change: Black sea examples. *Global and Planetary Change*, 32(1):33–47. 61

Stark, J. D., Donlon, C. J., Martin, M. J., and McCulloch, M. E. (2007). Ostia: An operational, high resolution, real time, global sea surface temperature analysis system. pages 1–4. 80

Tapley, B., Chambers, D., Bettadpur, S., and Ries, J. (2003). Large scale ocean circulation from the grace ggm01 geoid. *Geophysical Research Letters*, 30(22). 32

Testor, P., Béranger, K., and Mortier, L. (2005). Modeling the deep eddy field in the southwestern mediterranean: The life cycle of sardinian eddies. *Geophysical research letters*, 32(13). 24

Testor, P. and Gascard, J.-C. (2006). Post-convection spreading phase in the northwestern mediterranean sea. *Deep Sea Research Part I: Oceanographic Research Papers*, 53(5):869–893. 104

Thomas, L. N., Tandon, A., and Mahadevan, A. (2008). Submesoscale processes and dynamics. *Ocean modeling in an eddying regime*, pages 17–38. 3, 5

Thoppil, P. G., Richman, J. G., and Hogan, P. J. (2011). Energetics of a global ocean circulation model compared to observations. *Geophysical Research Letters*, 38(15). 6

Tomczak, M. and Godfrey, J. (2001). Regional oceanography: an introduction, 1994. 16

Troupin, C., Pascual, A., Valladeau, G., Pujol, I., Lana, A., Heslop, E., Ruiz, S., Torner, M., Picot, N., and Tintoré, J. (2014). Illustration of the emerging capabilities of saral/altika in the coastal zone using a multi-platform approach. *Advances in Space Research*, in press. 30

Tsimplis, M. and Bryden, H. (2000). Estimation of the transports through the strait of gibraltar. *Deep Sea Research Part I: Oceanographic Research Papers*, 47(12):2219–2242. 106, 107

Tsimplis, M. N. and Rixen, M. (2002). Sea level in the mediterranean sea: the contribution of temperature and salinity changes. *Geophysical Research Letters*, 29(23):51–1. 82

Vargas-Yáñez, M., Plaza, F., Garcıa-Lafuente, J., Sarhan, T., Vargas, J., and Vélez-Belchi, P. (2002). About the seasonal variability of the alboran sea circulation. *Journal of Marine Systems*, 35(3):229–248. 21

Vazquez-Cuervo, J., Font, J., and Martinez-Benjamin, J. J. (1996). Observations on the circulation in the alboran sea using ersi altimetry and sea surface temperature data. *Journal of Physical Oceanography*, 26(8):1426–1439. 21

Vidal-Vijande, E., Pascual, A., Barnier, B., Molines, J. M., Ferry, N., and Tintore, J. (2012). Multiparametric analysis and validation in the western mediterranean of three global ogcm hindcasts. *Scientia Marina*, 76(S1):147–164. 18, 44

Vigan, X., Provost, C., and Podesta, G. (2000). Sea surface velocities from sea surface temperature image sequences: 2. application to the brazil-malvinas confluence area. *Journal of Geophysical Research: Oceans (1978–2012)*, 105(C8):19515–19534. 31

Viúdez, Á., Tintoré, J., and Haney, R. L. (1996). Circulation in the alboran sea as determined by quasi-synoptic hydrographic observations. part i: Three-dimensional structure of

the two anticyclonic gyres. *Journal of Physical Oceanography*, 26(5):684–705. 21

Vörösmarty, C., Fekete, B., and Tucker, B. (1996). River discharge database, version 1.0 (rivdis v1. 0), volumes 0 through 6. a contribution to ihp-v theme 1. technical documents in hydrology series. 60

Weiss, J. (1991). The dynamics of enstrophy transfer in two-dimensional hydrodynamics. *Physica D: Nonlinear Phenomena*, 48(2):273–294. 135

Wentz, F. J., Gentemann, C., Smith, D., and Chelton, D. (2000). Satellite measurements of sea surface temperature through clouds. *Science*, 288(5467):847–850. 31

Willett, C. S., Leben, R. R., and Lavín, M. F. (2006). Eddies and tropical instability waves in the eastern tropical pacific: A review. *Progress in Oceanography*, 69(2):218–238. 7

Wunsch, C. (1999). Where do ocean eddy heat fluxes matter? *Journal of Geophysical Research*, 104(C6):PP. 13,235–13,249. 7

Wüst, G. (1961). On the vertical circulation of the mediterranean sea. *Journal of Geophysical Research*, 66(10):3261–3271. 12

Wyrtki, K., Magaard, L., and Hager, J. (1976). Eddy energy in the oceans. *Journal of Geophysical Research*, 81(15):2641–2646. 6

Xoplaki, E., Gonzalez-Rouco, J., Luterbacher, J. u., and Wanner, H. (2004). Wet season mediterranean precipitation variability: influence of large-scale dynamics and trends. *Climate Dynamics*, 23(1):63–78. 15

Zhang, Z., Zhao, W., Tian, J., and Liang, X. (2013). A mesoscale eddy pair southwest of taiwan and its influence on deep circulation. *Journal of Geophysical Research: Oceans*, 118(12):6479–6494. 28

Zhurbas, V., Stipa, T., Mälkki, P., Paka, V., Golenko, N., Hense, I., and Sklyarov, V. (2004). Generation of subsurface cyclonic eddies in the southeast baltic sea: Observations and numerical experiments. *Journal of Geophysical Research: Oceans (1978–2012)*, 109(C5). 7

Appendix A

Bouffard et al. 2014

Available online at www.sciencedirect.com

ScienceDirect

Advances in Space Research 53 (2014) 788–801

ADVANCES IN SPACE RESEARCH (a COSPAR publication)

www.elsevier.com/locate/asr

Lagrangian analysis of satellite-derived currents: Application to the North Western Mediterranean coastal dynamics

Jerome Bouffard [a,b,*], Francesco Nencioli [a,b], Romain Escudier [c], Andrea Michelangelo Doglioli [a,b], Anne A. Petrenko [a,b], Ananda Pascual [c], Pierre-Marie Poulain [d], Dalila Elhmaidi [e]

[a] *Aix Marseille Université, CNRS/INSU, IRD, Mediterranean Institute of Oceanography (MIO), UM 110, 13288 Marseille, France*
[b] *Université de Toulon, CNRS/INSU, IRD, Mediterranean Institute of Oceanography (MIO), UM 110, 83957 La Garde, France*
[c] *IMEDEA (CSIC-UIB), Esporles, Spain*
[d] *OGS, Trieste, Italy*
[e] *Faculté des Sciences de Tunis, Campus Universitaire 2092 El Manar, Tunisia*

Received 9 January 2013; received in revised form 6 December 2013; accepted 19 December 2013
Available online 30 December 2013

Abstract

Optimal interpolation methods for improving the reconstruction of coastal dynamics from along-track satellite altimetry measurements have been recently developed over the North Western Mediterranean Sea. Maps of satellite-derived geostrophic current anomalies are generated using these methods, and added to different mean circulation fields in order to obtained absolute geostrophic currents. The resulting fields are then compared to standard AVISO products, and their accuracies are assessed with Lagrangian diagnostics. The trajectories of virtual particle clusters are simulated with a Lagrangian code either with new current fields or with the AVISO ones. The simulated trajectories are then compared to 16 *in situ* drifter trajectories to evaluate the performance of the different velocity fields. The comparisons show that the new current fields lead to better results than the AVISO one, especially over the shallow continental shelf of the Gulf of Lion. However, despite the use of innovative strategies, some altimetry limitations still persist in the coastal domain, where small scale processes remain sub-sampled by conventional altimetry coverage but will benefit from technological development in the near future. Some of the limitations of the Lagrangian diagnostics presently used are also analyzed, but dedicated studies will be required for future further investigations.

Keywords: Lagrangian; Satellite altimetry; Mean dynamic topography; Coastal dynamics

1. Introduction

Coastal regions are characterized by a complex dynamics, often dominated by small, rapidly evolving structures at the mesoscale. In the open ocean, mesoscale dynamics plays a key role in modulating large-scale circulation and heat fluxes as well as in enhancing primary production (McGillicuddy et al., 2007). Such hydrodynamic processes are also crucial at coastal scales, where the associated currents are known to significantly influence water-mass mixing and exchanges between the continental shelf and the open ocean (Huthnance, 1995).

The high spatial/temporal variability and complexity associated with coastal mesoscale processes make them difficult to be studied with sparse *in situ* observations. Alternative options rely on exploiting satellite data specifically adapted to the coastal domain. Satellite altimeters are well adapted to observe open-ocean mesoscale structures (Fu et al., 2010) and represent an invaluable source of data that

* Corresponding author. Address: M.I.O. Institut Méditerranéen d'Océanologie, Campus de Luminy, Case 901, 13288 MARSEILLE cedex 09, Etg: 6, Bât: TPR2, France. Tel.: +33 491829108.
E-mail address: Jerome.Bouffard@univ-amu.fr (J. Bouffard).

0273-1177/$36.00 © 2014 COSPAR. Published by Elsevier Ltd. All rights reserved.
http://dx.doi.org/10.1016/j.asr.2013.12.020

provides repetitive views of phenomena unachievable by other means (Fu and Chelton, 2001). Characterizing the influence of mesoscale dynamics on water-mass stirring, mixing and tracer transport based on satellite observations is still a challenging issue, and requires the development of diagnostics that combine 2D current fields coupled with Lagrangian tools.

Optimal interpolation of along-track altimetry Sea Level Anomaly (SLA) into 2D fields was originally based on the combination of 2 altimeter missions, which could not fully resolve dynamical features at scales of 10–100 km (Le Traon and Dibarboure, 2004, 1999). Nowadays, despite using 4 altimetry missions, the resulting AVISO regional maps (SSALTO-DUACS, 2006) may still smooth a large part of mesoscale signals, especially in the coastal domain where the spatial horizontal scales are known to be smaller and more anisotropic than in the open ocean.

This has been confirmed by recent studies which evidenced that Map of SLA (hereafter (M)SLA) still lack enough of the temporal and spatial resolution and/or accuracy required for the detection of small mesoscale features (horizontal scales of less than 50 km; Bouffard et al., 2012). Furthermore, Nencioli et al. (2011) have identified inconsistencies between surface transport patterns derived from altimetry in the western Gulf of Lion and the *in situ* structures detected through an adaptative sampling strategy, which combined ship-based ADCP velocities and Lagrangian drifter trajectories. Finally, using glider measurements, Pascual et al. (2010) as well as Bouffard et al. (2010) also highlighted limitations of standard AVISO gridded fields in characterizing coastal mesoscale dynamics.

In order to improve altimetry gridded fields, a series of alternative methods have been recently developed. For example, Gaultier et al. (2013) have exploited the information from oceanic submesoscale structures retrieved from tracer observations of sea surface temperature, in order to improve the characterization of mesoscale dynamics from altimetric (M)SLA. Dussurget et al. (2011) successfully applied another technique consisting in removing the large scale signals (~100 km) from along track altimetric data and then mapping and adding the residual with an Optimal Interpolation (OI) with regionally adjusted correlation scales.

Another critical aspect for the reconstruction of coastal mesoscale dynamics may concern the inaccuracies of the Mean Dynamic Topography (hereafter MDT) associated with the marine geoid. Although the marine geoid component dominates the altimetry signal, it is not known well enough to be removed independently. Therefore, a temporal mean altimeter height is usually constructed from several year-long time series and subtracted to eliminate the geoid component. This procedure removes not only the geoid component but also any current component with a non-zero mean. So, a MDT, i.e. the non static component of the stationary sea surface height, is generally added to the (M)SLA in order to derive absolute geostrophic currents. The AVISO products in the Mediterranean Sea typically use the MDT from Rio et al. (2007).

The analysis of satellite-based mesoscale dynamics and its impact on horizontal mixing and transport properties in the coastal domain requires not only the use of new satellite-derived fields but also relevant diagnostics in order to evaluate them. None of the previous studies (Dussurget et al., 2011; Gaultier et al., 2013; Escudier et al., 2013) have focused on the quantification of the combined impact of different OI methods and MDT products on altimetry-based approaches. This paper addresses this issue by applying an improved Lagrangian diagnostics to several satellite-derived velocity fields, regionally adapted to the North Western Mediterranean basin.

The major dynamical feature of the North Western Mediterranean (hereafter NWMed) is the so-called "Northern Current" (hereafter NC). As shown on Fig. 1, this density current arises from the junction of the Eastern and Western Corsica Current (respectively ECC and WCC on Fig. 1) and flows westward initially along the coast of the Ligurian Sea, and then along the continental slope of the Gulf of Lion, until it reaches the Balearic Sea (Millot, 1991). The NC is marked by a strong seasonal variability (Gostan, 1967). Over the Gulf of Lion (hereafter GoL), NC intrusions can bring open Mediterranean water onto the continental shelf, depending on the stratification and wind conditions (Millot, 1990; Gatti, 2008; Petrenko et al., 2005, 2008; Poulain et al., 2012b). Another key aspect related to the NC dynamics concerns the development of baroclinic and barotropic instabilities. These favor the development of coastal mesoscale structures such as meanders and eddies arising along the NC external and internal border, forced by strong wind events and/or bottom topography irregularities (Millot, 1991).

The NC mean position is within 50 km off the coast (Petrenko, 2003), where radiometer and altimeter footprints may encounter the coastline and corrupt the raw along-track remote-sensed signals (Anzenhofer et al., 1999; Strub, 2001). However, recent advances in altimetry data processing can be used to characterize small scale signals in coastal regions, specifically over the NWMed (Vignudelli et al., 2003, 2005; Bouffard et al., 2008a,b, 2010, 2011, 2012). Birol et al. (2010) analyzed ADCP current measurements and satellite across-track current anomalies at different locations on the NWMed shelf edge. The results indicated good altimeter performances at seasonal time scales, confirming that improved coastal along-track altimetry is reliable to observe low frequency variations of the NC dynamics. Along-track data have also allowed to observe the NC intrusions over the GoL continental shelf for the first time (Bouffard et al., 2011) and to characterize the inter-annual (Bouffard, 2007; Birol et al., 2010) and intra seasonal (Bouffard et al., 2008b) variability of coastal currents.

Despite such major advances in coastal altimetry (in the NWMed as well as in many other areas; refer to Vignudelli

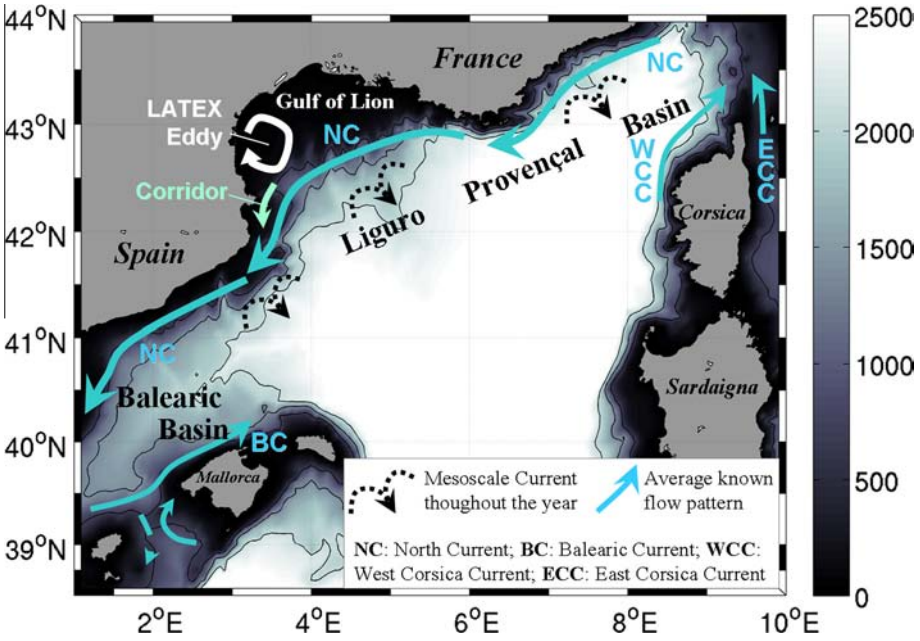

Fig. 1. Bathymetry (in m) and main surface circulation patterns of the study area. The dashed black arrows correspond to mesoscale currents throughout the year whereas the blue arrows correspond to average well known flow patterns. The coastal corridor is the one characterized by Nencioli et al. (2011). (For interpretation of the references to colour in this figure legend, the reader is referred to the web version of this article.)

et al. (2011) for an exhaustive review), most of the studies were based on Eulerian analysis of along-track altimetric measurements from which it is impossible to precisely identify and monitor in space and time coherent mesoscale features. The main objective of this study is therefore to evaluate the improvements in new coastal gridded currents through Lagrangian analysis. In particular, this work aims at assessing, for the first time, the impact of different OI methods combined with mean currents from different MDT products. This is achieved by comparing the real trajectories of drifters launched in the summers 2008, 2009, and 2010 with clusters of virtual particles advected by the different velocity fields.

The paper is organized as follow: Firstly, we present the different datasets (altimetry and drifters) and the metrics used to compute the Lagrangian trajectories from the altimetry products. Secondly, the trajectories are used to derive a Lagrangian diagnostics, whose statistics are analyzed over the NWMed basins, with a specific focus over the GoL continental shelf. Then, we discuss the ability of optimized altimetric gridded fields to reproduce specific mesoscale features identified by *in situ* observations and model results but not by standard AVISO velocity fields.

2. Material and methods

2.1. Altimetric geostrophic current anomalies

In this paper, two kinds of (M)SLA products derived from different OI methods are used and evaluated:

- The AVISO (M)SLA from Pujol and Larnicol (2005); hereafter AVISO
- The High Resolution (M)SLA with bathymetric constraint described in Escudier et al. (2013); hereafter HR+Bathy

The AVISO fields are a specific product for the Mediterranean Sea, obtained by merging delayed-time "Updated" along track altimetry (SSALTO-DUACS, 2006). They are computed weekly on a 1/8° × 1/8° Mercator grid. The spatial and temporal correlation scales used to obtain this altimetry fields are, respectively, 100 km and 10 days.

The more recent HR+Bathy fields are computed by interpolating the same along-track altimetry data but by adding smaller spatial and temporal correlation scales in the OI scheme (30 km and 3 days). For the AVISO field the spatial correlation is assumed to be isotropic. However, dynamical structures in the coastal zone are known to be anisotropic due to the strong bathymetry constraint (Liu and Weisberg, 2005). The HR+Bathy fields are thus computed modifying the correlation scales of OI in order to better take into account the shape and propagation of coastal features. The reader specifically interested in the details of the 2D mapping procedures can refer to each of the associated references.

In this study, the AVISO and HR+Bathy (M)SLA are spatially interpolated on a common horizontal grid of 1/8° × 1/8°. The AVISO maps are available only on a weekly basis, whereas the HR+Bathy maps are computed each day. Hence a daily AVISO (M)SLA is created by linear interpolation in time. The daily geostrophic current anomaly fields are then derived by applying the geostrophic balance equation.

2.2. Mean currents

As previously reminded, the long term mean (1993–1999) of the altimeter Sea Surface Height ($\overline{SSH} = \overline{(MSLA + MDT + Geoid} = MDT + Geoid$) is subtracted from SSH observations to remove the geoid contribution. However, this procedure also removes the contribution due to the MDT. Therefore, mean currents have to be estimated from an independent source and added to the (M)SLA-derived anomaly currents in order to obtain the absolute geostrophic currents. In this paper, two kinds of mean currents specifically computed for the Mediterranean Sea (see Fig. 2) are used and evaluated:

- The mean geostrophic currents derived from the MDT of Rio et al. (2007); hereafter Rio07
- The mean geostrophic currents derived from the MDT of Dobricic (2005); hereafter Dobricic05

The standard MDT from Rio et al. (2007) is built from the results of the 1/8° x 1/8° Mediterranean Forecasting System model (MFS, Pinardi et al., 2003) for the period 1993–1999 (see Fig. 2(b)). The MFS does not directly apply data assimilation. However, this MDT includes corrections from drifter velocities and altimetric SLA. These data are combined together to obtain local estimates of the mean geostrophic circulation. These estimates are then used in an inverse technique to improve the MDT computed from the model (which is used as a first guess).

The MDT from Dobricic (2005) (see Fig. 2(a)) is also estimated from the MFS model for the 1993–1999 periods, but with the assimilation of temperature from XBT observations and altimetric SLA. The MDT computation is mainly based on the assumption that the error in the MDT field appears in the assimilation system as a temporally constant but spatially variable observational bias. This error can thus be reduced by subtracting the long term average of the dynamic topography departures from the MDT first guess.

From Fig. 2, it follows that the two mean current fields show maximum intensity along the NC, confirming that this structure is the dominant dynamical feature of the NWMed (refer to Section 1). Depending on the considered field, regional differences in terms of current magnitude and direction can however be observed.

2.3. In situ data

The 16 drifter trajectories used for validation (see Table 1) were launched within the framework of the LAgrangian Transport EXperiments (LATEX) conducted in summer 2008, 2009, and 2010 by the Mediterranean Institute of Oceanography (M.I.O.) in order to study the influence of mesoscale structures on both physics and biochemistry in the western GoL. Each drifter was tethered to a holey-sock drogue centered at 15 m. In 2008 and 2010, the drifters trajectories are exploited in our analysis for a period of 60 days after their launch (T_0), during which

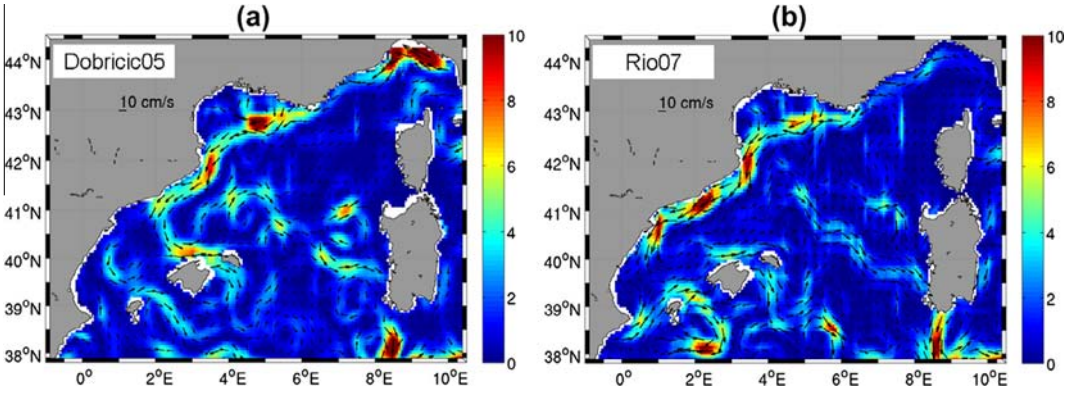

Fig. 2. Mean geostrophic current (module in cm/s) derived from the Mean Dynamic Topography of (a) Dobricic05 and of (b) Rio07 (the current intensity is in cm/s). (For interpretation of the references to colour in this figure legend, the reader is referred to the web version of this article.)

Table 1
Main characteristics of LATEX drifters.

	Drogue depth (m)	Number	Period of launching	Initial position	Maximum duration (days)
LATEX 2008 (Fig. 3(a))	15 (~surface)	3	September 01–05 2008	Western GoL	60
LATEX 2009 (Fig. 3(b))	15 (~surface)	3	August 26–28 2009	Western GoL	20
LATEX 2010 (Fig. 3(c))	15 (~surface)	10	September 11–24 2010	Western and southern GoL	60

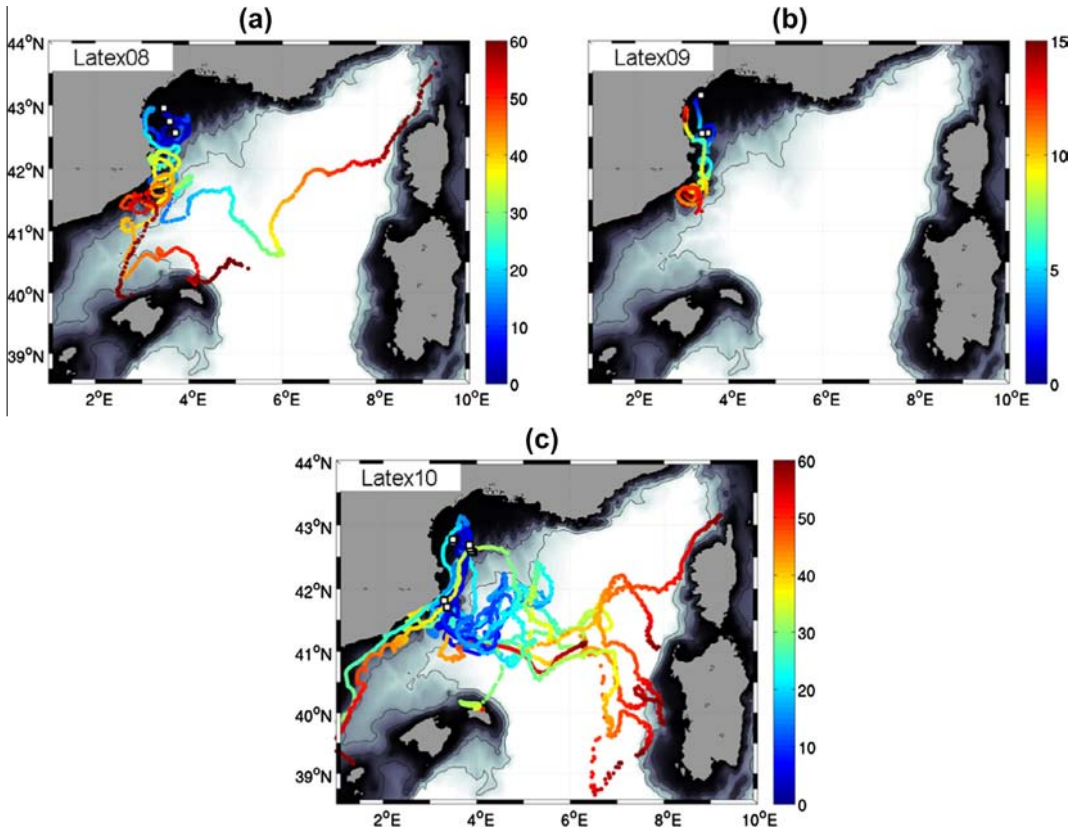

Fig. 3. Trajectories of drifters of (a) Latex08, (b) Latex09, and (c) Latex10. The color corresponds to the time of advection since the positions of origin (in day). The white square corresponds to the drifter initial positions. (For interpretation of the references to colour in this figure legend, the reader is referred to the web version of this article.)

the drifters did not strand ashore and remained inside our study area (see Fig. 3). In 2009, trajectories were exploited (Fig. 3(b)) for only 20 days, the maximum period of available data, before two of the three drifters launched were lost.

Until the present study, altimetry data have not yet been analyzed within the framework of Latex08 and Latex09 campaigns. On the other hand, the near real time AVISO data showed inconsistencies with respect to the drifter trajectories of Latex10, especially close to the GoL coast (Nencioli et al., 2011). Thus, the comparison between altimetry and drifters trajectories from Latex08, Latex09 and Latex10 gives a good opportunity to evaluate the relative performances of new altimetry products in the NWMed.

2.4. Methods of validation

Our method is principally inspired by the one of Liu and Weisberg (2011) initially developed for the evaluation of modeled trajectories over the Gulf of Mexico and successfully applied to the Norway Coast (Röhrs et al., 2012). Here, our main purpose is to diagnose the relative performances of the different combinations of OI scheme (Section 2.1) and mean current (Section 2.2) for computing absolute geostrophic currents. Our improved method, which aims at computing a Lagrangian skill score, consists of three steps:

(1) For each drifter, each day, N virtual particles (336) are launched in a square centered on the drifter initial position (grey squares on Fig. 4(a) and (b)). The square is set to a width of 30 km corresponding to the spatial correlation scale from Escudier et al. (2013). The initial intergrid spacing between each particle is about 1.5 km which is similar to previous Lagrangian-based studies over the Mediterranean Sea (e.g. D'Ovidio et al., 2004; Nencioli et al., 2011).
(2) Every day, the virtual particles are advected for a given time interval T using each of the 4 altimetry-derived currents (combinations of 2 OI methods and 2 mean currents).The advection scheme is a *fourth-order Runge–Kutta* integrator (see d'Ovidio et al. 2004) with a time-step of 3 h. The velocities are interpolated bi-linearly in space and linearly in time. The chosen time interval for advection is either $T = 10$ days (temporal correlation scale of the AVISO OI scheme) or $T = 3$ days (temporal correlation scale from Escudier et al., 2013). An illustration is provided on Fig. 4 and shows the virtual particle dispersion after 10-day advection.

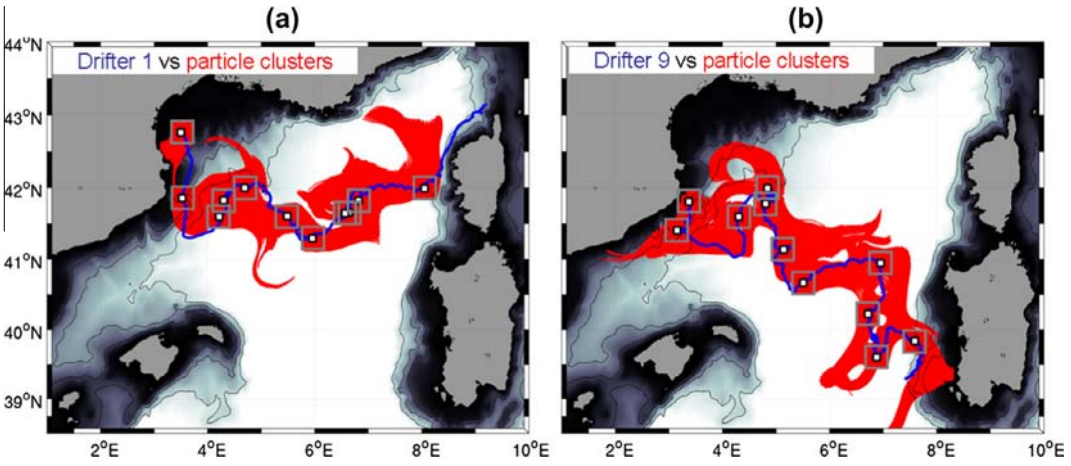

Fig. 4. Two examples ((a) Drifter 1 and (b) Drifter 9) of Latex10 drifter trajectories (in blue) versus virtual particle advected during 10 days by gridded currents using HR+Bathy (MSLA) and Dobricic (2005) mean current (in red). For more visibility, the daily particle initial positions (in grey squares) and the associated trajectories (in red) are sub-sampled every 5 days along the drifter positions. (For interpretation of the references to colour in this figure legend, the reader is referred to the web version of this article.)

(3) For each particle p and drifter D, we then compute the normalized cumulative separation distance $s_{D,p}$ defined in Liu and Weisberg (2011) as:

$$s_{D,p}(t,x) = \frac{\sum_i^T d_i}{\sum_i^T l_i} \quad (1)$$

with d_i the distance between the virtual particle p and the *in situ* drifter positions and l_i the length of the drifter trajectory after a time i of advection from the drifter initial position. $s_{D,p}$ scores are then computed every day t and position x (x,y).The procedure to compute $s_{D,p}$ is repeated each day for all the virtual particles launched around a given drifter D. For each drifter D, the daily values of $s_{D,p}$ can be averaged together to obtain the mean score $S_D(t,x)$ defined as:

$$S_D(t,x) = \frac{1}{N}\sum_{p=1}^{N} S_{D,p}(t,x) \quad (2)$$

Among the virtual particles released, only the N ones ($N \leqslant 336$) which are not stranded ashore are used in the average computation (Eq. (2)). Based on this definition, the smaller the value of S_D, the more accurate the altimetry absolute velocity field. To avoid any confusion, it is important to note that this score is similar to the "*normalized cumulative separation distance*" defined in Eq. (1)in Liu and Weisberg (2011) but generalized to particle clusters (and thus not the "skill score" defined in Eqs. (2), (3)of the same paper).

The use of particle clusters is preferred over single particles as in Liu and Weisberg (2011) since it ensures more robust statistical results (Schroeder et al., 2012). As expected, experiments using a single synthetic trajectory ($N = 1$) showed noisier results than for an ensemble of synthetic trajectories ($N = 336$) with S_D standard deviations about 20% higher (with $T = 10$ days for the whole drifters and periods). Several sensitivity tests with different number of particles were performed (not shown since the results did not provide additional information to the present ones). As mentioned before, the number of 336 particles was chosen since it provided an initial particle spacing of the order 1.5 km, in the range of previous studies.

By averaging together the S_D values of each drifter D, it is possible to compute the temporal mean score $\overline{S}_D$ for the period T_0 (60-day mean for Latex08 and Latex10, 20-day mean for Latex09).

$$\overline{S}_D = \frac{1}{T_o}\sum_{t=1}^{T_o} S_D(t,x) \quad (3)$$

Finally, by computing the average of every drifter we can retrieve $\overline{S}$, the ensemble mean per LATEX experiment.

Fig. 5 shows the temporal evolution of $S_{D=1}$ (drifter 1) and $S_{D=9}$ (drifter 9) between September and November 2010 (see Fig. 4 for their respective trajectories), in a case where the velocity field products do not show strong S differences (<1). These curves, computed with 3-day and 10-day advection, are mostly used to illustrate the variation of S_D with respect to the time of advection. For a same product, the curves show similar patterns but differences in the amplitude: the longer the time integration, the larger the score. S_D is indeed higher for 10-day advection than for the 3-day. This result, confirmed by experiments done with 60-days advection (not shown), is in agreement with Lagrangian theory and chaotic transport showing that the separation rate between two trajectories will increase exponentially for spatial scales less than the deformation radius (Garrett, 1983) or linearly at greater scales, after 10–60 days advection (Nilsson et al., 2013)

However, the increase of the score with larger T (as observed on Fig. 5), depends not only on the accuracy of the velocity field, but also on the local kinematic properties of the flow itself. In other words, since the score is computed using a cluster of particles, for a same time advection T, score differences between two products can be due to

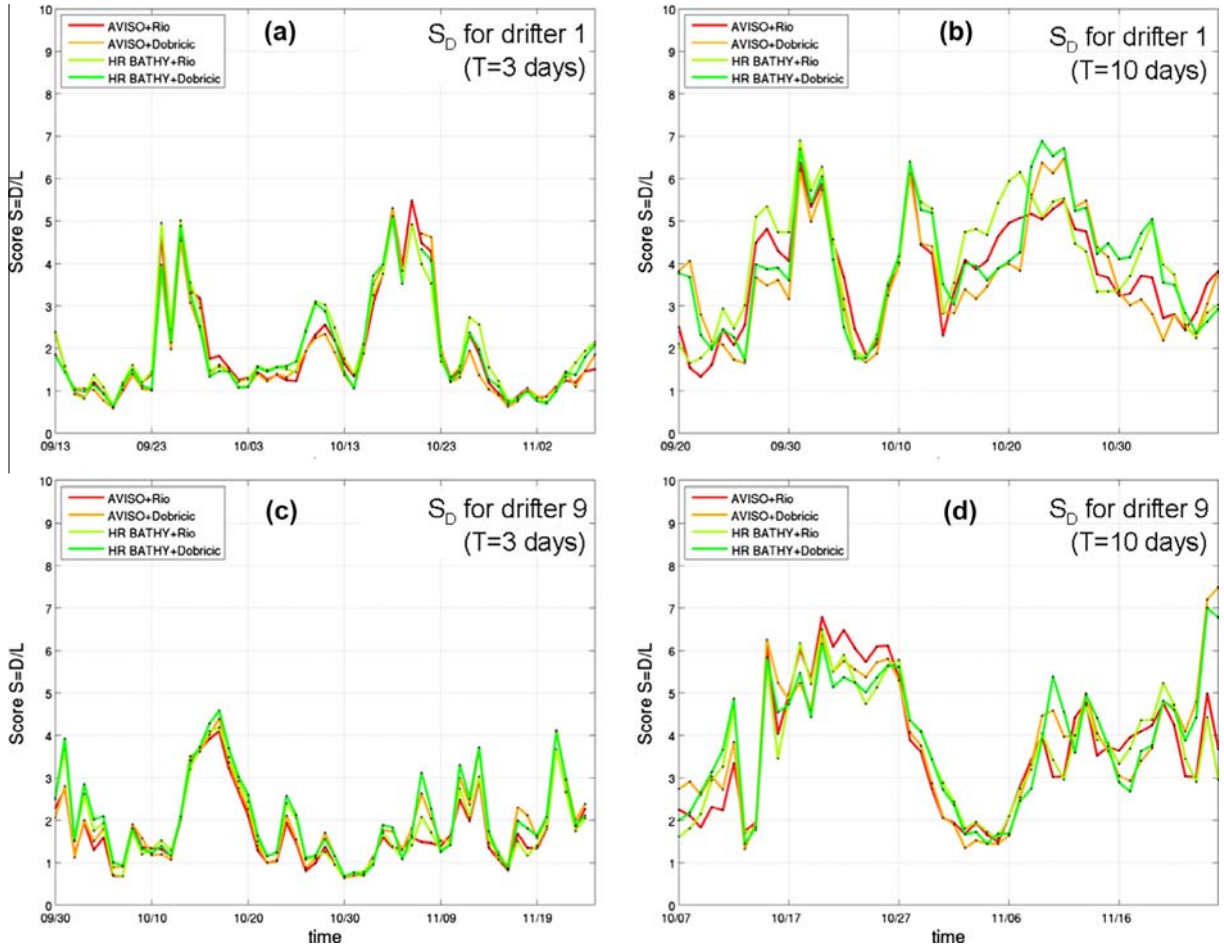

Fig. 5. Examples of time evolution of S_D scores for the 4 velocity fields along the Latex10 drifter 1 and drifter 9 with 3 days ((a),(c)) and 10 days advection ((b),(d)). (For interpretation of the references to colour in this figure legend, the reader is referred to the web version of this article.)

their respective accuracy, but also due to the dispersive characteristics of the velocity fields. In order to evaluate the dispersion rate associated with each product, we have computed the local strain rate (γ, see Eq. (4)) at all virtual particle positions.

$$\gamma_{D,p}(t,x) = \left(\frac{\partial u}{\partial x} - \frac{\partial v}{\partial y}\right)^2 + \left(\frac{\partial v}{\partial x} + \frac{\partial u}{\partial y}\right)^2 \quad (4)$$

Analogously to Lagrangian diagnostics such as the Finite Time/Size Lyapunov Exponent, the strain rate is an Eulerian diagnostic that quantifies the tendency of the flow field to disperse initially close particle trajectories (e.g. Waugh et al., 2006). The same average procedures done for $s_{D,p}$ are applied to $\gamma_{D,p}$ in order to make the mean strain rate $\overline{\gamma}$ directly comparable with $\overline{S}$ and therefore evaluate the scores of different velocity fields also in the light of their respective dispersion rate.

This point is addressed in Section 3.1 by focusing on the 2 altimetric current products which show the most statistically different results. In a second step, statistics are presented regionally, aiming at discriminating the relative influence of mean currents and OI methods (Section 3.2).

3. Results

3.1. Comparisons of current fields

3.1.1. Statistics at the basin scale

In this section we focus on the comparison between two of the products presented in Section 2: The first one (hereafter called *standard*) is the standard regional AVISO gridded field combining standard AVISO (M)SLA with geostrophic mean current derived from Rio07. The second one (hereafter called *new*) is an alternative current field which consists of the combination of geostrophic currents derived from HR+Bathy (M)SLA (Escudier et al., 2013) with the MDT Dobricic05. For the three LATEX experiments (see Table 1), the mean strain rate of the *new* product (0,70 day^{-1}) is higher than the *standard* one (0.61 day^{-1}), showing equivalent space–time variations (mean STD differences $< 8\%$). Thus, the *new* product is on average slightly more dispersive than the standard one.

The main statistical results obtained at drifters positions are summarized in Table 2 and show that the *new* surface gridded field has smaller $\overline{S}$ both with 10- and 3-day

Table 2
Mean $\overline{S}$ scores and $\overline{\gamma}$ (day^{-1}) score for LATEX drifters after 10 days (top) and 3 days (bottom in bracket) of advection with surface altimetric currents. Best $\overline{S}$ scores are in bold and underlined.

Altimetry product	Years					
	2008		2009		2010	
	$\overline{S}$	$\overline{\gamma}$	$\overline{S}$	$\overline{\gamma}$	$\overline{S}$	$\overline{\gamma}$
standard: AVISO+Rio07	3.8 (2.1)	0,64 (0,68)	4.7 (2.0)	0.49 (0,65)	4.5 (2.5)	0,74 (0,70)
New: HR+Bathy+Dobricic05	**3.6 (2.0)**	0,80 (0,84)	**3.7 (1.9)**	0.80 (0,74)	**3.9 (2.1)**	0,64 (0,64)

advection (less pronounced with 3 days) although its strain rate is higher: the average $\overline{S}$ scores ($\overline{\gamma}$) with 10-day advection for all the drifters and the three LATEX periods is of 4.3 (0.62 day^{-1}) and 3.7 (0.75 day^{-1}) for respectively the *standard* and *new* gridded geostrophic currents. This represents a mean improvement of the *new* product with respect to the *standard* one despite a larger mean strain rate.

When we look at the scatterplots of S and γ values (Fig. 6), it appears that there is no clear relation between these two quantities. Indeed, for the *standard* product (Fig. 6(a)) some strong S values (>10, see red square) are associated with low γ (<0.75 day^{-1}) whereas for the *new* product (Fig. 6(b)) some relatively low S values (<5, see blue square) can correspond to high γ (>1 day^{-1}). This means that even if a stronger strain rate tends to increase S by increasing the dispersion rate of the virtual particles, this could be compensated by a more accurate velocity field decreasing the average distance between the drifter and the virtual particles.

Having evidenced that S is more representative of the velocity field quality than of its Lagrangian dispersion (especially for high S score), we can now analyze in details the trajectories and the associated spatial distribution of S_D for 2 drifters (drifters 4 and 6 of Latex10) showing strong S_D values for a relatively low strain rate (inside the red square of Fig. 6(a)).

3.1.2. Regional differences

Both for drifter 4 and 6, the worst $S_{D=4}$ and $S_{D=6}$ are obtained between the last week of September and the first week of October. This period corresponds to a northward drifter migration not well reproduced by altimetry-derived currents despite results being significantly better with the *new* field (black curves on Fig. 7). Indeed, as observed in Nencioli et al. (2011), these two drifters – launched at the same time – are first advected in a shallow coastal area north of the GoL where the circulation dynamics might be partially ageostrophic because of intense wind and/or bathymetric effects. Other than over these particular zones, drifters 4 and 6 show relative low S_D scores (<4), especially for the *new* fields, when the drifters started to be advected southwards along the coastal corridor identified by Nencioli et al. (2011) in the south-western part of the GoL (see Fig. 1).

The analysis of $S_{D=4}$ and $S_{D=6}$ highlights significant differences between the *standard* and *new* satellite-derived velocity fields. We therefore further investigate these differences by analyzing the daily S_D score along all drifter trajectories from the LATEX experiments, and focusing in particular on its spatial distribution. For clarity we only discuss the S_D scores with 10-day advection for Latex10 and Latex08, since they are characterized by longer drifter trajectories (conclusions for Latex09 and with 3 days advection are however similar).

The southern parts of the GoL show relative good statistics with relative small S_D scores (<3 for Latex08 and Latex10) for both *new* (Fig. 8 (b) and (e)) and *standard* (Fig. 8(a) and (d)) fields (for all drifters/times). This is true even very close to the coast, along the coastal corridor

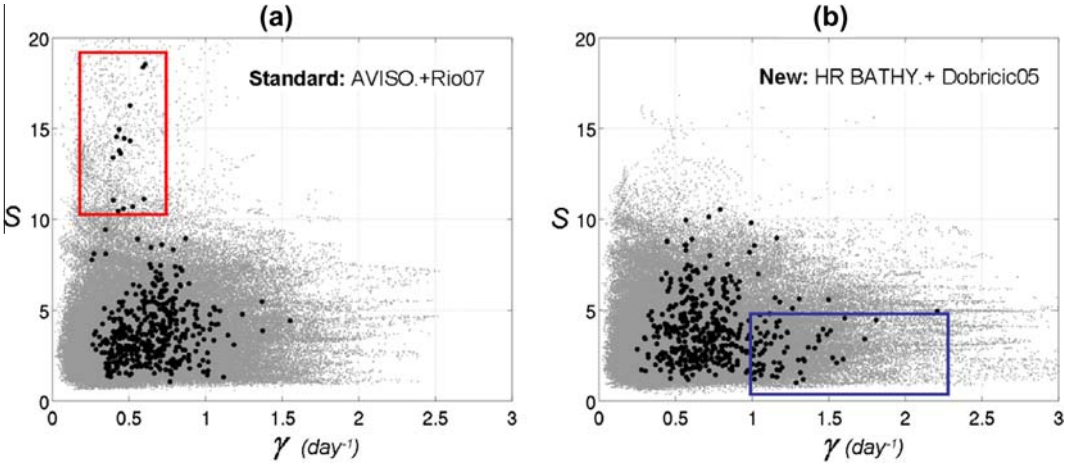

Fig. 6. Scatterplots of S_D vs γ_D (black dots) for the 10 drifters of Latex10 and of $s_{D,p}$ vs $\gamma_{D,p}$ (grey dots) for the whole corresponding particles p. (a) *Standard* product, (b) *New* product. (For interpretation of the references to colour in this figure legend, the reader is referred to the web version of this article.)

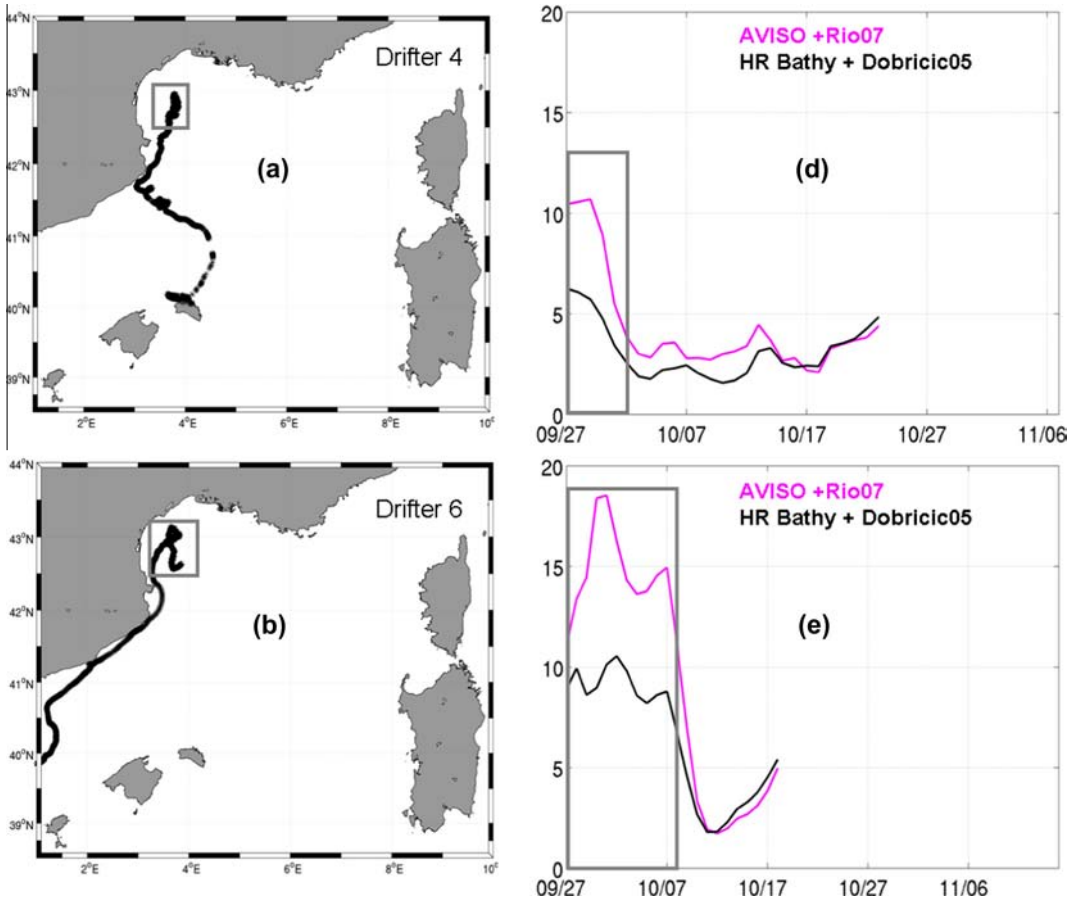

Fig. 7. Trajectories of drifters (a) 4 and (b) 6 and corresponding S_D time series (respectively (d),(e)) for the *new* – black curves - and *standard* – pink curves – altimetric products for 10 days advection-. In grey are highlighted areas (left) and corresponding periods (right) of bad S_D score. (For interpretation of the references to colour in this figure legend, the reader is referred to the web version of this article.)

(Fig. 1) described in Nencioli et al. (2011) suggesting that the dynamics over this area is quite stable and geostrophic.

Figs. 8(c) and (f) highlight the S_D difference between *standard* and *new* surface gridded currents respectively for 2008 and 2010. Except in the Catalan Sea and near the west Corsica and Sardinia coasts, the *new* fields are characterized by better statistics. The major differences are observed over the GoL continental shelf where the *new* velocity field shows lower S_D (difference > 2) for both Latex08 and Latex10.

In the north-western part of this area, high S_D scores were previously observed for drifter 4 and 6 but not for all the Latex10 drifters reaching this region. There are three possible reasons (or a combination of them): (1) the dynamical structures are maybe too small or close to the coast to be captured by the conventional along-track measurements (instrument limitation); (2) the OI methods smooth a large part of the altimetry signal even with smaller and bathymetry-constrained correlation scales (methodology limitation); (3) Episodic and small-scale ageostrophic dynamics may dominate the surface signals (see introduction and associated references).

Considering all the drifters and all the Latex periods, the mean $\overline{S}$ scores over the GoL is 3.6 against 4.5 for respectively the *new* and *standard* velocity fields. This represents a stronger regional improvement of the *new* product (>20%) with respect to result obtained over the entire NWMed domain (~15%, see Section 3.1.1). S_D along the continental shelf slope is relatively good (<3), especially for Latex 2008. There, stable dynamical features may be influenced by bathymetry and altimetry appears to be well adapted to resolve the associated geostrophic dynamics. This seems not to be always the case in shallower regions in the north-western part of the GoL, as observed during the Latex10 experiment. In order to address this issue, we now focus on a specifics event occurring at the beginning of Latex08.

3.1.3. Focus on a coastal eddy

Numerous numerical simulations and analysis of multi-source data from Latex08 and Latex09 have already identified the recurrent presence in summer of an intense anticyclonic eddy of about 20 km radius in the western side of the GoL (Fig. 1; Hu et al., 2009; Kersalé et al., 2013). It is clearly depicted in drifter trajectories of Fig. 3(a) and (b). In 2001, one such eddy was also modeled both physically (Hu et al., 2011) and biogeochemically (Campbell et al., 2012). The issue addressed here is to check if altimetry gridded fields are able to reproduce or not this coastal mesoscale feature

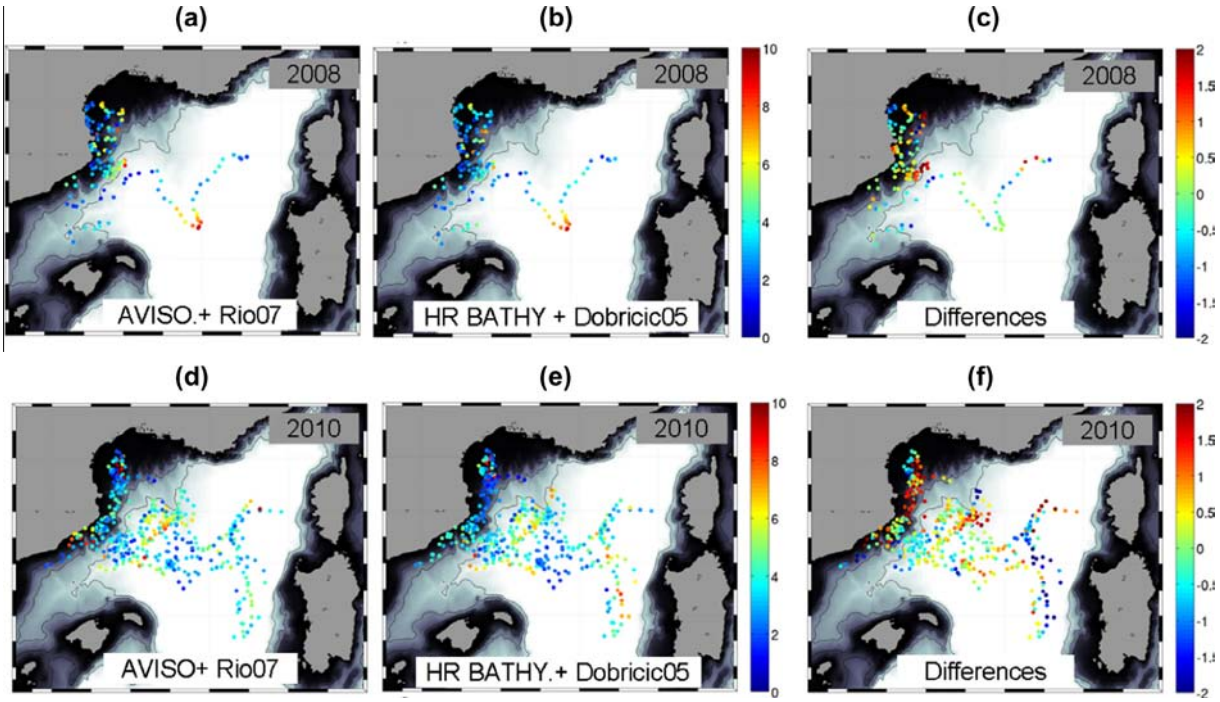

Fig. 8. Spatial distribution of S_D scores (10 days advection) along drifter daily positions for the *standard* ((a) and (d)) and *new* product ((b) and (e)) during Latex08 and Latex10. Spatial distribution of S_D differences between *standard* and *new* products for (c) Latex08 and (f) Latex10. By convention we choose each initial days of advection as drifter daily positions. (For interpretation of the references to colour in this figure legend, the reader is referred to the web version of this article.)

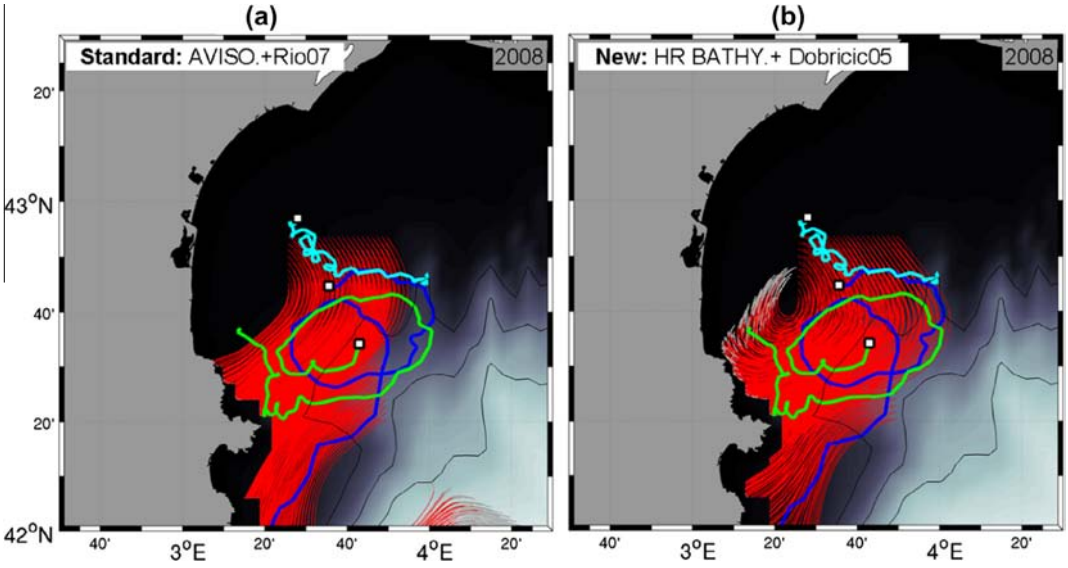

Fig. 9. Latex08 drifter trajectories (cyan, green, and blue). Two drifters are trapped by the Latex eddy (in green and blue). In red are the virtual particles initially launched at drifters' trapped initial positions and 10 days advected by (a) the *standard* and (b) *new* altimetric current field. In grey are the particles trajectories for the last day of advection. (For interpretation of the references to colour in this figure legend, the reader is referred to the web version of this article.)

For this, 336 virtual particles are launched in the 15 km neighborhood of the initial positions of the 2 drifters trapped by the eddy of Latex08. Then, the particles are advected for 10 days both with the *standard* and the *new* absolute geostrophic velocities and compared qualitatively to real drifters trajectories. From Fig. 9 it turns out that most of the particles advected by the *new* field (Fig. 9(b)) roughly follow the drifter positions (corresponding to low S scores), even if the location of the physical structure seems to be partially inaccurate. Concerning the *standard* AVISO currents (Fig. 9(a)), all the particles go directly southward, without following the observed eddy loop (corresponding to high S scores).

Analysis of this event proves that the *new* field, using a bathymetric constraint and the Dobricic05 mean current, better represents well developed, stable, coastal geostrophic mesoscale features such as the one observed during Latex08. A similar conclusion is found by Escudier et al. (2013) by comparing drifter-derived currents, glider and altimetry north of Mallorca with Eulerian approaches. However, for Latex09 (not shown) neither the *new* nor the *standard* velocity field are able to reproduce such an eddy-like structure. This structure is too small and/or too close to the coast to be captured with conventional altimetry or reproduced by the 2D fields, even by the use of innovative OI techniques and alternative MDT.

3.2. Influence of mean currents and optimal interpolation methods

3.2.1. Statistics at the basin scale

The previous results have pointed out significant differences between *new* and *standard* gridded fields both qualitatively and quantitatively. However, they did not inform on the respective influence of OI methods (see Section 2.1) and mean currents (see Section 2.2) on the Lagrangian metrics. In order to isolate the relative influence of OIs (respectively mean currents), we compute, for each OI (respectively mean currents), the average of the two $\overline{S}$ scores using the two available mean currents (respectively OIs). Table 3 shows the average $\overline{S}$ score for the different OI methods. Both with 10-day and 3-day advection, the mean $\overline{S}$ score are very close and do not allow to conclude whether one OI approach is better than another. From Table 3, it however turns out that the mean current from Dobricic05 exhibits better statistics than the Rio07 one (~12% of improvement with 10-days advection).

This shows that mean currents have a stronger influence than the OI methods on our Lagrangian diagnostics. However, even if this is true at the NWMed Basin scale, alternative OI methods might still have significant regional impacts, especially in shallow areas where the smaller correlation scale and bathymetric constraints described by Escudier et al. (2013) may have stronger impacts.

3.2.2. Focus on the Gulf of Lion

We now focus on the GoL area where major differences, both quantitative and qualitative, between the *new* and *standard* product were previously observed. In order to assess the influence of the bathymetry constraint in the Lagrangian statistics, we compute the $\overline{S}$ score for three bathymetric classes (Fig. 10 right). The $\overline{S}$ score is only computed if at least 10 drifter positions are available for a given bathymetric class. Except for 2009, the number of positions is between 20 and 100, depending on the time of advection and of the LATEX mission.

For Latex08 (Fig. 10(a)) and Latex09 (Fig. 10(b)), the two OI methods show similar statistics for any of the considered bathymetric classes, despite the qualitative differences evidenced in Section 3.1.3. Concerning the mean current, the scores are quite similar for depth < 150 m ($S \sim 3.0$ for 10-day advection); but for the other bathymetric classes; Dobricic05 exhibits better score than Rio07. It is also somehow surprising to note that the score in 2008 and 2009 are generally better in shallow water areas of the GoL ($S \sim 3$ for depth < 150 m) than in deeper zones ($S \sim 4$ for depth > 150 m) where potential small scale and partially ageostrophic instabilities may arise close to the NC external borders. This confirms that circulation over the GoL continental shelf during these two cruises is in good geostrophic balance and is relatively well resolved by altimetry gridded fields.

For Latex10 (Fig. 10(c) and (f) the conclusions are quite different. In that case, the different OI methods exhibit significant differences for depth less than 150 m (located North West of the GoL). By comparison with the AVISO $\overline{S}$ score with 10-day (3-day) advection, HR+Bathy shows improvements of 13% (23%) whereas less pronounced differences are observed depending on the considered mean currents. This indicates that the new OI method can have significant impact for some specific events in shallow-water regions. In our case, this corresponds to smaller scale dynamics influenced by the bathymetry that trapped and retained drifters close to the coast. Concerning the mean currents, Dobricic05 have again smaller $\overline{S}$ for the whole bathymetric classes confirming the conclusion obtained for Latex08 and Latex09.

Table 3
Mean $\overline{S}$ scores per OI method (averages done with the two mean currents: Rio07 and Dobricic05) and per mean current (average done with the two OI methods: AVISO and HR + BATHY) after 10 (3) day advections.

Altimetry Product	Years		
	2008	2009	2010
AVISO OI	3.7 (2.1)	4.6 (2.0)	4.0 (2.1)
HR-BATHY	3.7 (2.1)	4.6 (2.0)	3.9 (2.1)
Rio07	3.8 (2.2)	5.2 (2.1)	4.1 (2.1)
Dobricic05	3.6 (2.0)	4.0 (2.0)	3.8 (2.1)

4. Discussions and conclusions

Cross-shelf exchanges are of crucial importance to study the impact of anthropogenic discharged pollutants, oil spill as well as the transport of natural biogeochemical elements and biological organisms (e.g. nutrients, larvae, jellyfishes). A quantitative understanding of coastal physical processes and associated Lagrangian transport is therefore necessary to determine how the ocean dynamics affects the biological and ecological conditions of coastal environments.

In this paper, new absolute geostrophic currents, derived from satellite altimetry observations in combination with models are processed and evaluated using a Lagrangian diagnostic based on particle cluster advection. In agreement with the finding of Escudier et al. (2013) – based on Eulerian diagnostics – our Lagrangian approaches demonstrate that the use of HR+Bathy (M)SLA generally gives a better

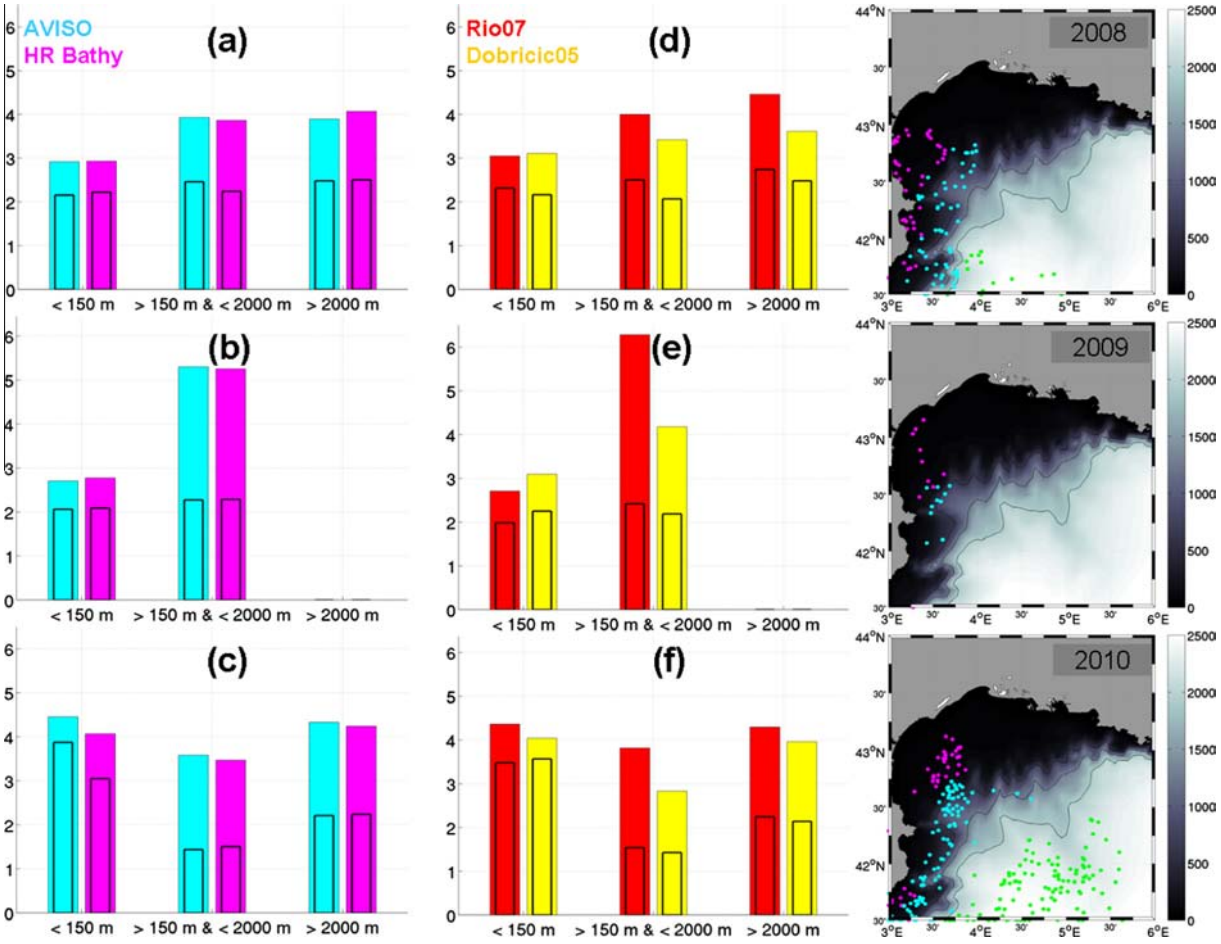

Fig. 10. (Right) Daily drifter positions used in the bathymetric classes for Latex08; Latex09 and Latex10. In pink are the points located at depths less than 150 m, in cyan the points between 150 and 2000 m and in green the points at depths higher than 2000 m. (Left). Diagram of mean $\overline{S}$ scores with respect to Latex drifters (a, b, c) for each OI methods and (d, e, f) for each mean currents function of bathymetric classes. The large (respectively thin) diagrams correspond to $\overline{S}$ score with 10 days (respectively 3 days) advection. (For interpretation of the references to colour in this figure legend, the reader is referred to the web version of this article.)

representation of transport patterns over the continental shelf (despite still evidencing some inaccuracies/limitations in the positioning of small scale structures). In addition, we have also demonstrated that the use of an alternative mean current (i.e. from Dobricic 2005) rather than the standard one (i.e. Rio et al., 2007) significantly improves the comparison with drifter trajectories, especially along the corridor located at the south west Gulf of Lion.

However, the relatively limited *in situ* dataset used in our study did not allow for more extensive Lagrangian statistical analysis requiring to compare cluster of particle trajectories with a larger number of drifters. As a perspective, it would be relevant to adopt our approach with all the available drifters in the Mediterranean Sea (>500 trajectories since 1992, Poulain et al., 2012a). This should allow the generation of a more complete and robust altimetric error map over the Mediterranean Sea than the ones obtained during the three LATEX experiments. In a second step, the whole drifter database could also be exploited in synergy with altimetry and modeling (with assimilation schemes or statistic constraints) in order to generate a new and more accurate regional Mean Dynamic Topography for coastal applications.

Concerning the Optimal Interpolation methods, the use of shorter and bathymetric constrained correlation scales is not always sufficient to significantly improve the statistics over the whole North Western Mediterranean. However, we pointed out that in some specific cases and areas, such as the continental shelf in the western part of the Gulf of Lion, improvements can be obtained (as also observed in the Balearic Sea by Escudier et al. (2013). However, the relative sparse space/time coverage of existing along track altimetric missions (such as during the 2008–2010 period) is a clear limitation for the long-term tracking and analysis of small-scale dynamics even through the development of coastal-oriented Optimal Interpolation methods. Coastal altimetry will undoubtedly benefit, in the near future, of a denser satellite constellation and new altimetry sensors. Waiting for SWOT satellite (Fu and Ferrari, 2008), Lagrangian studies of coastal mesoscale dynamics will thus

require the integration of data from the Saral/AltiKa and Cryosat-2 missions in the Optimal Interpolation schemes.

Our statistical Lagrangian analyses are in agreement with qualitative considerations and previous Eulerian studies over the North Western Mediterranean Sea. However, further investigations should be done in order to better discriminate the relative contribution to the S score due to the influence of dispersive effects (related to the strain rate) and due to the intrinsic accuracy of the velocity field. Another critical aspect concerns ageostrophic motions which could influence the transport of tracers in the surface layer but that are not included in altimetry. Their impacts – not addressed in this study – may be more important in coastal zones and could be therefore at the base of significant observed discrepancies between drifter and altimetric trajectories. For example, Liu and Weisberg (2007) show, over the Florida shelf, that the across-shelf wind effects (ageostrophic part) are secondary compared to the barotropic geostrophic currents but can be stronger than the baroclinic ones.

The relation between surface and sub-surface mesoscale is also a challenging issue requiring both the continuous development of theoretical models and high resolution 2D gridded current (Dussurget et al., 2011; Gaultier et al., 2013; Escudier et al, 2013). Our Lagrangian diagnostics applied to sub-surface drifters could also be used in a near future in order to compare results obtained from different reconstructions methods (e.g. Carnes et al., 1994; Lapeyre and Klein, 2006; LaCasce and Mahadevan, 2006; Scott and Furnival 2012). The use of 3D observation-based currents associated with Lagrangian tools is promising and might pave the way to new ecological applications for coastal altimetry such as the influence cross-shelf exchanges on fish larvae, plankton or transport and landing over the North Western Mediterranean coastal domain

Aknowledgments

The LATEX project is supported by the programs LEFE/IDAO and LEFE/CYBER of the INSU-Institut National des Sciences de l'Univers and by the Region PACA-Provence Alpes Côte dAzur. The altimeter (M)SLA were produced by SSALTO/DUACS and distributed by AVISO with support from CNES-Centre National d'Etude Spatiale. We particularly thank Milena Menna (OGS, Trieste, Italy) for processing and providing edited drifter data used within this study. The authors also acknowledge, B. Buongiorno Nardelli, M. Kersalé and R. Campbell for precious comments and useful discussions. Francesco Nencioli acknowledges support from the FP7 Marie Curie Actions of the European Commission, via the Intra-European Fellowship (FP7-PEOPLE-IEF-2011), project "Lyapunov Analysis in the COaSTal Environment" (LACOSTE-299834). Jérôme Bouffard is financed by a CNES post-doctoral grant.

References

Anzenhofer, M., Shum, C.K., Rentsh, M., 1999. Coastal Altimetry and Applications. Ohio State University, Columbus, Tech. Rep. 464, Geod. Sci. Survey.

Birol, F., Cancet, M., Estournel, C., 2010. Aspects of the seasonal variability of the northern current (NW Mediterranean sea) observed by altimetry. J. Mar. Syst. 81, 297–311. http://dx.doi.org/10.1016/j.jmarsys.2010.01.005.

Bouffard, J., 2007. Amélioration de l'altimétrie côtière appliquée à l'étude de la circulation dans la partie nord du bassin occidental méditerranéen (in French). PhD thesis under the supervision of Y. Ménard and P. De Mey.

Bouffard, J., Roblou, L., Birol, F., Pascual, A., Fenoglio-Marc, L., Cancet, M., Morrow, R., Ménard, Y., 2011. Introduction and assessment of improved coastal altimetry strategies: case study over the North Western Mediterranean sea. In: Vignudelli, S., Kostianoy, A.G., Cipollini, P., Benveniste, J. (Eds.), Coastal Altimetry. Springer-Verlag, Berlin, Heidelberg. http://dx.doi.org/10.1007/978-3-642-12796-0_12, Chapter 12, Pages 578.

Bouffard, J., Renault, L., Ruiz, S., Pascual, A., Dufau, C., Tintoré, J., 2012. Sub-surface small scale eddy dynamics from multi-sensor observations and modelling. Prog. Oceanogr. 106, 62–79.

Bouffard, J., Vignudelli, S., Cipollini, P., Ménard, Y., 2008b. Exploiting the potential of an improved multi-mission altimetric dataset over the coastal ocean. Geophys. Res. Lett. (GRL) 35. http://dx.doi.org/10.1029/2008GL033488.

Bouffard, J., Vignudelli, S., Hermann, M., Lyard, F., Marsaleix, P., Ménard, Y., Cipollini, P., 2008a. Comparison of ocean dynamics with a regional circulation model and improved altimetry in the Northwestern Mediterranean. J. Terr. Atm. Oceanic Sci. 19 (1–2), 117–133. http://dx.doi.org/10.3319/TAO.2008.19.1-2.117(SA.

Bouffard, J., Pascual, A., Ruiz, S., Faugère, Y., Tintoré, J., 2010. Coastal and mesoscale dynamics characterization using altimetry and gliders: a case study in the Balearic Sea. J. Geophys. Res. 115, C10029. http://dx.doi.org/10.1029/2009JC006087.

Campbell, R., Diaz, F., Hu, Z.Y., Doglioli, A.M., Petrenko, A.A., Dekeyser, I., 2012. Nutrients and plankton spatial distributions induced by a coastal eddy in the Gulf of Lion. Insights from a numerical model. Prog. Oceanogr. http://dx.doi.org/10.1016/j.pocean.2012.09.005.

Carnes, M.R., Teague, W.J., Mitchell, J.L., 1994. Inference of subsurface thermohaline structure from fields measurable by satellite. J. Atmos. Ocean. Tech. 11, 551–566.

D'Ovidio, F., Fernandez, V., Hernandez-Gracıa, E., Lopez, C., 2004. Mixing structures in the Mediterranean sea from finite-size Lyapunov exponents. Geophys. Res. Lett. 31. http://dx.doi.org/10.1029/2004GL020328.

Dobricic, S., 2005. New mean dynamic topography of the Mediterranean calculated from assimilation system diagnostics. Geophys. Res. Lett. 32. http://dx.doi.org/10.1029/2005GL022518.

Dussurget, R., Birol, F., Morrow, R., De Mey, P., 2011. Fine resolution altimetry data for a regional application in the Bay of Biscay. Mar. Geodesy 34 (3–4), 447–476, http://dx.doi.org/10.1080/01490419.2011.584835.

Escudier, R., Bouffard, J., Pascual, A., Poulain, P.-M., 2013. Improvement of coastal mesoscale observation from space: application to the North Western Mediterranean. Geophys. Res. Lett. 40 (10), 2148–2153. http://dx.doi.org/10.1002/grl.50324.

Fu, L.-L., Chelton, D.B., 2001. Large-scale ocean circulation. In: Fu, L.-L., Cazenave, A. (Eds.), Satellite Altimetry and Earth Sciences: A Handbook for Techniques and Applications. Academic Press, San Diego, p. 423, 133–16.

Fu, L.-L., Ferrari, R., 2008. Observing oceanic submesoscale processes from space. Eos, Trans. Amer. Geophys. Union 89 (48), 488.

Fu, L.-L., Chelton, D.B., Le Traon, P.-Y., Morrow, R., 2010. Eddy dynamics from satellite altimetry. Oceanography 23 (4), 14–25, http://dx.doi.org/10.5670/oceanog.2010.02.

Garrett, C., 1983. On the initial streakiness of a dispersing tracer in two- and three-dimensional turbulence. Dyn. Atmos. Oceans 7, 265–277.
Gatti, J., 2008. Intrusions du Courant Nord Méditerranéen sur la partie est du plateau continental du Golfe du Lion. thèse de doctorat de l'Université de Provence (PhD Thesis in french). soutenue le 16/06/2008 à Marseille.
Gaultier, L., Verron, J., Brankart, J.-M., Titaud, O., Brasseur, P., 2013. On the inversion of submesoscale tracer fields to estimate the surface ocean circulation. J. Mar. Syst. 126, 33–42, http://dx.doi.org/10.1016/j.jmarsys.2012.02.014.
Gostan, J., 1967. Etude du courant géostrophique entre Villefranche-sur-Mer et Calvi. Cahiers océanographiques XIXme année – Service Hydrographique de la Marine 4, 329–345.
Hu, Z.Y., Doglioli, A.M., Petrenko, A.A., Marsaleix, P., Dekeyser, I., 2009. Numerical simulations of eddies in the Gulf of Lion. Ocean Model. 28, 203–208, http://dx.doi.org/10.1016/j.ocemod.2009.02.004.
Hu, Z.Y., Petrenko, A.A., Doglioli, A.M., Dekeyser, I., 2011. Numerical study of eddy generation in the western part of the Gulf of Lion. J. Geophys. Res. 116, C12030. http://dx.doi.org/10.1029/2011JC007074.
Huthnance, J.M., 1995. Circulation exchange and water masses at the ocean margin. Prog. Oceanogr. 35, 353–431.
Kersalé, M., Petrenko, A.A., Doglioli, A.M., Dekeyser, I., Nencioli, F., 2013. Physical characteristics and dynamics of the coastal Latex09 eddy derived from *in situ* data and numerical modeling. J. Geophys. Res. 118, 399–409. http://dx.doi.org/10.1029/2012JC008229.
Lapeyre, G., Klein, P., 2006. Dynamics of the upper oceanic layers in terms of surface quasigeostrophy theory. J. Phys. Oceanogr. 36, 165–176.
LaCasce, J., Mahadevan, A., 2006. Estimating subsurface horizontal and vertical velocities from sea surface temperature. J. Mar. Res. 64, 695–721.
Le Traon, P.-Y., Dibarboure, G., 2004. An illustration of the contribution of the Topex/Poseidon – Jason-1 tandem mission to mesoscale variability studies. Mar. Geodesy 27, 3–13.
Le Traon, P.-Y., Dibarboure, G., 1999. Mesoscale mapping capabilities of multiple-satellite altimeter missions. J. Atmos. Oceanic Technol. 16, 1208–1223, doi: http://dx.doi.org/10.1175/1520-0426(1999)016.
Liu, Y., Weisberg, R.H., 2011. Evaluation of trajectory modeling in different dynamic regions using normalized cumulative Lagrangian separation. J. Geophys. Res. 116, C09013. http://dx.doi.org/10.1029/2010JC006837.
Liu, Y., Weisberg, R.H., 2007. Ocean currents and sea surface heights estimated across the west Florida shelf. J. Phys. Oceanogr. 37, 1697–1713.
Liu, Y., Weisberg, R.H., 2005. Patterns of ocean current variability on the West Florida Shelf using the self-organizing map. J. Geophys. Res. 110, C06003. http://dx.doi.org/10.1029/2004JC002786.
McGillicuddy, D.J., Anderson, L.A., Bates, N.R., Biddy, T.S., Buesseler, K.O., Carlson, C.A., Davis, C.S., Ewart, C., Falkowski, P.G., Goldthwait, S.A., Hansell, D.A., Jenkins, W.J., Johnson, R., Kosnyrev, V.K., Ledwell, J.R., Li, Q.P., Siegel, D.A., Steinberg, D.K., 2007. Eddy/wind interactions stimulate extraordinary mid-ocean plankton blooms. Science 316, 1021–1026.
Millot, C., 1990. The Gulf of Lions' hydrodynamics. Cont. Shelf Res. 10 (9–11), 885–894.
Millot, C., 1991. Mesoscale and seasonal variabilities of the circulation in the Western Mediterranean. Dyn. Atmos. Oceans 15, 179–214.
Nencioli, F., d'Ovidio, F., Doglioli, A.M., Petrenko, A.A., 2011. Surface coastal circulation patterns by in situ detection of Lagrangian coherent structures. Geophys. Res. Lett. 38, L17604. http://dx.doi.org/10.1029/2011GL048815.
Nilsson, J.A.U., Döös, K., Ruti, P.M., Artale, V., Coward, A., Brodeau, L., 2013. Observed and modeled global ocean turbulence regimes as deduced from surface trajectory data. J. Phys. Oceanogr. 43, 2249–2269, doi: http://dx.doi.org/10.1175/JPO-D-12-0193.1.
Pascual, A., Ruiz, S., Tintoré, J., 2010. Combining new and conventional sensors to study the Balearic current. Sea Technol. 51 (7), 32–36.
Petrenko, A.A., Dufau, C., Estournel, C., 2008. Barotropic eastward currents in the western Gulf of Lion, North-Western Mediterranean sea, during stratified conditions. J. Marine Syst. 74 (1–2), 406–428. http://dx.doi.org/10.1016/j.jmarsys.2008.03.004.
Petrenko, A.A., Leredde, Y., Marsaleix, P., 2005. Circulation in a stratified and wind-forced Gulf of Lions, NW Mediterranean sea: *in situ* and modeling data. Cont. Shelf Res. 25, 7–27. http://dx.doi.org/10.1016/j.csr.2004.09.004.
Petrenko, A.A., 2003. Circulation features in the Gulf of Lions, NW Mediterranean sea; importance of inertial currents. Oceanol. Acta 26, 323–338.
Pinardi, N., Allen, I., De Mey, P., Korres, G., Lascaratos, A., Le Traon, P.-Y., Maillard, C., Manzella, G., Tziavos, C., 2003. The Mediterranean ocean forecasting system: first phase of implementation (1998–2001). Ann. Geophys. 21 (1), 3–20.
Poulain, P.-M., Menna, M., Mauri, E., 2012a. Surface geostrophic circulation of the Mediterranean sea derived from drifter and satellite altimeter data. J. Phys. Oceanogr. 42, 973–990, doi: http://dx.doi.org/10.1175/JPO-D-11-0159.1.
Poulain, P.-M., Gerin, R., Rixen, M., Zanasca, P., Teixeira, J., Griffa, A., Molcard, A., De Marte, M., Pinardi, N., 2012b. Aspects of the surface circulation in the Liguro-Provençal basin and Gulf of Lion as observed by satellite-tracked drifters (2007–2009). Bollettino di Geofisica Teorica ed Applicata 53 (2), 261–279.
Pujol, M.-I., Larnicol, G., 2005. Mediterranean sea eddy kinetic energy variability from 11 years of altimetric data. J. Mar. Syst. 58, 121–142. http://dx.doi.org/10.1016/j.jmarsys.2005.07.005.
Rio, M.-H., Poulain, P.-M., Pascual, A., Mauri, E., Larnicol, G., Santoleri, R., 2007. A mean dynamic topography of the Mediterranean sea computed from altimetric data, in situ measurements and a general circulation model. J. Mar. Syst. 65, 484–508. http://dx.doi.org/10.1016/j.jmarsys.2005.02.006.
Röhrs, J., Christensen, K.H., Hole, L.B., Broström, G., Drivdal, M., Sundby, S., 2012. Observation-based evaluation of surface wave effects on currents and trajectory forecasts. Ocean Dyn. 62 (10–12), 1519. http://dx.doi.org/10.1007/s10236-012-0576-y.
Schroeder, K., Chiggiato, J., Haza, A.C., Griffa, A., Özgökmen, T.M., Zanasca, P., Molcard, A., Borghini, M., Poulain, P.-M., Gerin, R., Zambianchi, E., Falco, P., Trees, C.A., 2012. Targeted Lagrangian sampling of submesoscale dispersion at a coastal frontal zone. Geophys. Res. Lett. 39 (L1608), 6. http://dx.doi.org/10.1029/2012GL051879.
Scott, R.B., Furnival, D.G., 2012. Assessment of traditional and new eigenfunction bases applied to extrapolation of surface geostrophic current time series to below the surface in an idealized primitive equation simulation. J. Phys. Oceanogr. 42, 165–178.
SSALTO-DUACS., 2006. Ssalto/Duacs user handbook: (M)SLA and (M)ADT near-real-time and delayed-time products. Rep. SALP-MU-P-EA-21065-CLS, AVISO, Ramonville Saint Agne, France.
Strub, T., 2001. High-resolution ocean topography science requirements for coastal studies, in the report of the high-resolution ocean topography science working group meeting. In: Chelton, D.B. (Ed.), College of Oceanic and Atmospheric Sciences. Oregon State University, Corvallis, OR, p. 224, Ref. 2001–4.
Vignudelli, S., Cipollini, P., Reseghetti, F., Fusco, G., Gasparini, G.P., Manzella, G.M.R., 2003. Comparison between XBT data and TOPEX/Poseidon satellite altimetry in the Ligurian-Tyrrhenian area. Ann. Geophys. 21 (1), 123–135, Part 1.
Vignudelli, S., Cipollini, P., Roblou, L., Lyard, F., Gasparini, G.P., Manzella, G.M.R., Astraldi, M., 2005. Improved satellite altimetry in coastal systems: case study of the Corsica channel (Mediterranean Sea). Geophys. Res. Lett. 32, L07608, 1029/2005GL22602.
Vignudelli, S., Kostianoy, A., Cipollini, P., Benveniste, J. (Eds.), 2011. Coastal Altimetry, Springer, first ed., 2011, XII, 566, pp. 216 illus. doi: 10.1007/978-3-642-12796-0.
Waugh, D.W., Abraham, E.R., Bowen, M.M., 2006. Spatial variations of stirring in the surface ocean: a case study of the Tasman sea. J. Phys. Oceanogr. 36, 526–542.

Appendix B

Gomez Enri et al. 2014

Heavy river discharge detection with satellite altimetry: An illustration for the Guadalquivir River estuary mouth

Gómez-Enri, J. (1)*, Escudier, R. (2), Pascual, A. (2), and Mañanes, R. (1)

(1) Applied Physics Department. University of Cadiz (Spain).
(2) Instituto Mediterráneo de Estudios Avanzados (IMEDEA). CSIC-UIB (Spain).

*Corresponding author:
Jesús Gómez-Enri
jesus.gomez@uca.es
+34 956016071

Abstract

Accurate altimeter products oriented to coastal zones are increasing the number of potential applications. Present work is focused on the analysis of the sea level variability in the eastern shelf of the Gulf of Cadiz (between North Africa and the southwestern side of the Iberian Peninsula), adjacent to the Guadalquivir River estuary. Sixteen years (1994-2009) of along-track and standard AVISO maps of sea level anomalies have been used to generate a new high resolution product with increased spatio-temporal resolution. In-situ water levels in the Guadalquivir river estuary mouth demonstrate the effect of strong river freshwater discharges on the monthly means of the sea level in a yearly basis. The use of a bathymetry constraint and smaller correlation scales in the methodology developed to generate high resolution altimeter products, improves the characterization of the mesoscale signals in the coastal strip adjacent to the estuary due to strong river freshwater discharges. The daily evolution of the sea level observed with this new altimeter product has been confirmed by optical Moderate Resolution Imaging Spectrometer (MODIS) images. The spatio-temporal distribution of the altimeter tracks available in the study area might compromises the mapping capabilities to capture coastal and fine-scale features.

Key words: coastal altimetry, sea level variability, river discharge, Gulf of Cadiz.

1. INTRODUCTION

Radar altimetry has become a powerful source of accurate sea level data in the open ocean (Fu and Cazenave, 2001), and more recently in the coastal fringe (Vignudelli et al., 2011). Indeed, coastal altimeter measurements have remained largely unexploited, due to several factors: wrong characterization of the geophysical corrections and inaccurate estimates of the distance between the satellite's centre of mass and the mean reflected surface (*range*) and significant wave height (SWH). Near the shore the radar footprint might be contaminated by land and/or calm waters reflections complicating the retracking of radar waveforms, and hence the retrieval of the above mentioned parameters. Thus, sea level anomalies (SLA: corrected sea surface height) and SWH has had limited use near the coast. In addition to this a better along-track spatial resolution (from 1 to 20 Hz) might improve the extraction of finer scales in coastal areas (Vignudelli et al., 2011). A number of initiatives have been made in the last decade to improve the accuracy and availability of altimeter data in the coastal zone. They are applied to along-track measurements (Vignudelli et al., 2005; Roblou et al., 2007; Brown, 2010; Liu et al., 2012) including the use of coastal-oriented corrections and the review of the data recovery strategies near the coast (Vignudelli et al., 2003; 2005; 2011; Bouffard et al., 2008a,b; 2010; 2012, Birol et al., 2010). Alternatively, some innovative techniques for the generation of high-resolution (HR, henceforth) gridded maps of SLA have been developed by Dussurget et al., (2011) and Escudier et al., (2013). They made qualitative and quantitative comparisons with independent observations confirming that the new altimetry HR gridded products improve the characterization of coastal and fine-scale features. Thus, the number of applications exploiting accurate coastal altimeter reprocessed data has increased exponentially in the last years (Vignudelli et al., 2011, Pascual et al., 2013; Bouffard et al., 2014, among others).

Low-resolution (LR, hereinafter) (1/3º x 1/3º) gridded weekly maps of SLA routinely produced by AVISO (Archiving, Validation, and Interpretation of Satellite Oceanographic data, http://www.aviso.oceanobs.com/) have been used in the past to study the sea level variability over continental shelves at different time scales (Volkov

et al., 2007; Saraceno et al., 2008; Gómez-Enri et al., 2012; Laiz et al., 2013; Caballero et al., 2013). In particular, Gómez-Enri et al. (2012) analyzed the effect of sporadic and heavy Guadalquivir river discharges in the sea level of the eastern continental shelf of the Gulf of Cadiz. They concluded that these events could explain up to 50% of the variance of the daily mean sea level recorded by a tide gauge in the estuary mouth. No explained variance was found in the nearest LR altimeter point to the estuary (at 25 km to the mouth in the 50 m isobath). This could be indicating that the river runoff effect is restricted to the estuary mouth and along a small fringe near the coast. More recently, Laiz et al. (2013) demonstrated that LR weekly maps of SLA were unsuitable for the analysis of the Guadalquivir River sporadic discharges, due to the lack of altimeter data in the vicinity of the estuary mouth. Nencioli et al. (2011) showed that LR maps could not resolve small and coastal features because of the smoothing applied to the data merging and interpolation. Dussurget et al. (2011) improved the temporal and spatial resolution of LR maps from weekly to daily and from 1/3º x 1/3º to 1/16º x 1/16º Mercator grid, respectively. They added the short scale signals to this HR product from the along-track data. More recently, Escudier et al. (2013) presented a new approach for the generation of HR maps of SLA that clearly improves the characterization of mesoscale signals in the coastal strip by adding a bathymetry constraint.

This work focuses on the capabilities of this new daily HR product to capture coastal and mesoscale processes. We present two examples of how these maps are able to show the daily evolution of a freshwater plume in the eastern continental shelf of the Gulf of Cadiz after heavy discharges from the Guadalquivir River estuary. The paper is organized as follows. We first present the study area and the data sets used: daily means of in-situ water levels, river discharges and altimeter-derived SLA. The sea level response to heavy river discharges in terms of the monthly means is analyzed using in-situ tide gauge data in the mouth of the Guadalquivir estuary. We then focus on two events of heavy freshwater river discharges (March 2001 – December 2009) analyzing the spatio-temporal distribution of the SLA in the surrounding continental shelf of the river estuary mouth. We discuss the importance of the number and distribution of altimeter tracks in the study area during one strong event of river discharges (December 1996). The final remarks and conclusions are outlined in the last section.

2. STUDY AREA

The Gulf of Cadiz is located between North Africa and the southwestern side of the Iberian Peninsula. It connects the Atlantic Ocean with the Mediterranean Sea through the Strait of Gibraltar. Its continental shelf is located approximately in the 100 m isobath. It is divided in two halves by Cape Santa María: the western and eastern continental shelves. On the eastern side (Fig. 1) the Guadalquivir River, Tinto-Odiel system and Guadiana River are the main tributaries. The Guadalquivir River is the main contributor of freshwater discharge into the eastern shelf affecting the hydrology of the surrounding area (Prieto et al., 2009). The estuary has an extension of about 110 km between the mouth at Sanlúcar de Barrameda and the Alcalá del Río dam. The river discharge has been identified as the main forcing agent of the hydrology inside the Guadalquivir estuary (Díez-Minguito et al., 2012; Navarro et al., 2012). Díez-Minguito et al. (2012) pointed out the lack of knowledge on the exchange of water masses between the continental shelf and the river. Several works have reported a strong decrease in salinity in the estuary mouth during episodes of strong river discharges (González-Ortegón and Drake, 2012; González-Ortegón et al., 2010; Navarro et al., 2012). This might indicate that the main effect in the adjacent continental shelf is an elevation of the sea level due to the less dense freshwater over the sea level (Díez-Minguito et al., 2012). Prieto et al. (2009) analyzed the importance of heavy river discharges, together with the wind regime, in the triggering of phytoplankton growth on the shelf. In addition, the coastal warm counter surface current flowing near the shore westward (spring-summer) and eastward (late autumn - early winter) over the eastern continental shelf (Stevenson, 1977; Relvas and Barton, 2002; García-Lafuente et al., 2006; Criado-Aldeanueva et al., 2009) could also be affected by these episodes. In summary, little is known about the sea level change in the adjacent eastern continental shelf due to heavy discharges of freshwater from the Guadalquivir River estuary.

3. DATA SETS AND METHODOLOGY

3.1 High-resolution maps of sea level anomaly

Gridded LR weekly maps of SLA are generated by an optimal interpolation of the along-track data. Data were obtained from AVISO with support from CNES (Centre National d'Études Spatiales). The gridded product used was the updated "Upd" which uses up to 4 altimeters (Ducet et al. 2000). This is a better choice than the reference "Ref" (only 2 altimeters) product for mapping the mesoscale variability (Pascual et al., 2006). The data quality of this product is ensured by the quality control process based on standard raw data editing (quality flags or parameter thresholds) including detection of erroneous artifacts and crossover validation (Aviso, 2014). From these, we generate 16 years of a new daily HR product (from January 1994 to December 2009) based on the methodology described in Escudier et al. (2013). In a first step, daily HR maps were generated (HR-std, henceforth) where the larger and finer scales are given by the LR maps and the residual along-track data, respectively. In a second step a bathymetry constraint was included in the processing chain in order to improve the characterization of mesoscale and coastal signals (HR-bathy, hereinafter). The method is summarized and included as auxiliary material.

3.2 Tide gauge data

Daily means of sea level heights covering the analyzed time period were obtained from the closest tide gauge station to the estuary mouth. It is a permanent station, moored in the port of Bonanza (37º08’00”N – 6º49’56”W) at about 8 km to the mouth (Fig. 1). The instrument belongs to the Red de Mareografos (REDMAR) network of Puertos del Estado (Spain): http://www.puertos.es. The accuracy of the instrument is 2.5 mm with a resolution of 10 mm (ESEAS-RI, 2006). These data have been used in the past to validate LR weekly maps of SLA in the same area (Gómez-Enri et al., 2012; Laiz et al., 2013). These authors found a high level of agreement between both datasets at seasonal scales.

3.3 River runoff

Daily means of flow rate (Q_d in m^3/s) of the Guadalquivir River were obtained from the Automatic Hydrological Information System hosted by the Spanish Minister of Agriculture, Food and Environment (http://www.chguadalquivir.es/saih). We selected the nearest station to the estuary located at the Alcala del Río dam (about 108 km upstream).

The mean Q_d in the time period analyzed was 76.26 m^3/s. The estuary is in normal conditions (good weather) when Q_d is lower than 40 m^3/s, in extreme conditions for $400 < Q_d < 3000$ m^3/s, and is catalogued as exceptional when $Q_d > 3000$ m^3/s (Díez-Minguito et al., 2012). In normal conditions the estuary is tidally-dominated, with 400 m^3/s the limit for the river to be in a fluvially-dominated regime (Díez-Minguito et al., 2012; Navarro et al., 2012). Only 3.5% of the time period analyzed the river exceeded that value. We isolated 12 time periods with daily discharges higher than 400 m^3/s (extreme or exceptional conditions) during at least 3 days. We were interested in natural discharges avoiding sporadic outflows due to regulation activities in the dam not related to heavy rain. Table 1 summarizes some information related to these periods (number of days with discharges higher than 400 m^3/s, maximum Q_d measured in that period and altimeter missions available during these periods). From the 12 heavy river discharges, 11 reached extreme conditions and only one (December 1996) was catalogued as exceptional. We show in Fig. 2 the daily Q_d along the time period analyzed. The heavier discharges (12) mentioned in Table 1 are shown in the figure. The fluvially-dominated regime was achieved in autumn-winter seasons in all the cases. The longer periods of heavy Q_d were observed in 1997 (66 days), 1996 (54), 1998 (36), and 2001 (18). There is also a 4-years period of no heavy discharges between 2005 and 2008. This was also observed in 1994, 1995 and 2002. Thus, there is a decrease in the discharge with time in terms of amount of water and number of days. Navarro et al. (2012) analyzed a longer period of river discharges pointing out the decrease of the freshwater contribution to the estuary from 5000 hm^3/year (1931-1980) to 2000 hm^3/year (1981-2000). This reduction is greater during dry-year cycles. Discharges show a seasonal frequency and are driven by the regulation of the hydrographic basin upstream Alcala del Río dam.

3.4 Dynamic Atmospheric Correction

The static and dynamic ocean response to atmospheric forcing (pressure and wind) is modeled with the Dynamic Atmospheric Correction (DAC) developed by AVISO. The static correction basically accounts for the ocean response to low frequency atmospheric pressure variations assuming the isostatic assumption (Gil and Niiler 1973). The dynamic correction takes into account the high frequency pressure and wind signals (periods shorter than 20 days) using the MOG2D model (Carrère and Lyard, 2003; Pascual et al. 2008). Regular 6-hourly gridded maps of DAC (12:00, 6:00, 12:00, 18:00 GMT) were extracted from AVISO (http://www.aviso.oceanobs.com/index.php?id=1278). Taking into account that the daily HR maps of gridded SLA are corrected by DAC, we estimated a daily mean DAC during the analyzed time period that was subtracted to the in-situ daily water levels in order to account for the atmospheric effects removed in the altimetry data set.

3.5. In-situ monthly means

We analyzed the impact of the heavy discharge on the water level in the river estuary mouth. We estimated monthly means of daily mean water levels from the tide gauge station at Bonanza (Fig. 1). We then obtained the average of the monthly means by averaging all the monthly mean water levels in January, February, etc. The lack of in-situ water level measurements in January (1997), March to June (1999), and November (2009) precluded the estimation of the monthly mean over these years.

4. RESULTS AND DISCUSSION

We estimated the correlation coefficient between the monthly mean sea level of each year and the average of the monthly means. The correlations obtained were found not significant (95% confidence level for a p-value lower than 0.05) in the years of maximum discharges along longer periods (1996, 1998 and 2001). The highest significant correlations (95% confidence level for a p-value lower than 0.05) were found

in the years of negligible river discharges ranging between 0.92 (2007) and 0.64 (1995, 2000). We analyzed more in detail the year with the longer period of Q_d > 400 m^3/s and maximum discharge (1996), and the year with the higher correlation (2007). Note that the estuary reached exceptional conditions (Q_d > 3000 m^3/s) in December 1996 (Table 1). Fig. 3a shows the monthly means in 1996, 2007 and the average of the monthly means for the whole time period. The monthly means during 2007 fits well to the average of the monthly means. In the extreme/exceptional conditions observed in 1996 strong discrepancies were found (January and December) making the correlation not significant (95% confidence level for a p-value lower than 0.05). Fig. 3b gives the monthly mean river Q_d in 1996 and 2007 indicating that deviations observed in the monthly means in 1996 are related to the monthly river discharges during these months. The same analysis was made in 1998 and 2001 (not shown) confirming these results. Thus, heavy freshwater discharges have a definite effect on the average of the monthly means obtained in the estuary mouth during long periods of fluvial-dominated regime in the estuary.

The ability of the gridded maps of SLA to recover coastal and mesoscale signatures depends on the number of altimeter missions (Le Traon and Dibarboure, 2004; Pascual et al., 2006). Considering the spatial distribution of the altimeter tracks in the area during the episodes of heavy discharges as summarized in Table 1, we first focused on the time period in which the *Geosat Follow-On* (GFO) mission was operative (from January 2000 to September 2008). The reason for that was because this satellite presented the nearest track to the Guadalquivir estuary mouth (Fig. 1). From the 4 years of heavy discharges in that period we selected March 2001 as it showed the longer period of Q_d > 400 m^3/s (15 days) and the highest amount of water discharge (up to 2000 m^3/s).

The analysis was made from 6^{th} to 20^{th} of March 2001. In that period the correlation coefficient between daily river discharge and water level was found to be 0.70 (95% confidence level). The comparison between HR-std (no bathymetry constraint added) and HR-bathy is presented in Fig. 4 in a temporal interval of 2 days. HR-std does not show significant geographical variations of SLA in any of the days

analyzed. In the improved product, instead, there is a strong positive signal in the vicinity of the estuary mouth during about 8 days. The maximum was observed between March 12th and 14th. This signal could be related to the river discharges measured in that period, when the estuary was fluvially-dominated. The less dense freshwater plume should overlie the ocean water level increasing the sea level (Díez-Minguito et al., 2012). The improvement shown in HR-bathy is in agreement with a previous analysis in the northwestern Mediterranean Sea (Escudier et al., 2013). The authors focused on mesoscale dynamics showing an improvement in the spectral content in the HR-bathy, closer to the along-track signal demonstrating that the inclusion of the bathymetry improves the capabilities of HR products to display higher levels of energy in the mesoscale bandwidth.

A detailed analysis of the event recorded in March 2001 is presented in Fig. 5. We compared the daily SLA between 1st and 20th of March obtained from the tide gauge at Bonanza (DAC correction applied) and the nearest altimeter point available in HR-bathy (Fig. 5a): [36.8125ºN, 6.4375ºW] located at about 9 km to the station. The dates of the tracks available in the area and their geographical locations are also included. The mean daily Q_d is shown in Fig. 5b for comparison. The magnitude of the maximum SLA in the altimeter point selected is smaller than the water level measured in the tide gauge, and shows a delay of a few days. This delay might be explained by two factors: the spatio-temporal distribution of the tracks available in the area; and the temporal weighting applied to the along-track values of SLA used to generate the HR maps. To demonstrate this, Fig. 6 shows the along-track values of SLA when the satellites crossed the area between 09th and 16th of March. GFO #029 did not show high SLA probably because of the distance of the track to the coast and the fact that it was too early for the plume to be fully developed in the shelf near the estuary. One day after, the nearest track to the estuary mouth (GFO #046) showed the higher values of SLA (up to 15 cm) in the closest positions to the coast, confirming the effect of the heavy river discharge in the sea level measured by GFO. Due to the temporal scale of the interpolation that takes into account both GFO tracks, it does not appear in the 2D field. T/P #035 overpassed the zone six days later (15th) also showing high SLA near the coast. There, the interpolation uses this track and the GFO #046 to estimate the SLA. The bathymetry

constraint applied helps in that regard because even if the segments of the two tracks close to the coast are far between them, they are at a similar bathymetry. Regarding the temporal weighting applied in the interpolations made to generate the maps, the along-track values of SLA are taken into account during 10 days from T-4d to T+5d, being T the dates and times of the measurements. Thus, we expect higher values of SLA in the HR maps between 10th and 15th of March considering GFO #046 and T/P #035 tracks. All these circumstances explain the date and position of the maximum observed in HR-bathy.

This illustration evidences the potential of using advances techniques for improving the spatio-temporal resolution of altimeter fields but, at the same time, highlights the need for higher temporal repetitiveness of the altimeter constellations, especially in the coastal areas.

Other sources of information in the area might be used to show the effect of the river discharge in the continental adjacent shelf. We analyze the event of December 2009 (Table 1) in terms of daily HR-bathy SLA maps and optical RGB MODIS (Moderate Resolution Imaging Spectrometer) images (Terra) available in AERONET (http://lance-modis.eosdis.nasa.gov/imagery/subsets/?project=aeronet). Water color might indicate the presence of high concentrations of sediment related to heavy discharges of freshwater from the river. The correlation between daily river discharge and water level (from 15th to 31st) was 0.77 (95% confidence level). From the set of optical scenes in the study area we selected four days with cloud-free conditions. The RGB images and the corresponding maps of SLA are shown in Fig. 7. The river discharge started to be heavy after 22nd of December. Before that date the turbidity is scarce as shown in the optical images and the maps of SLA do not reflect any significant change in the vicinity of the estuary. A couple of days after that date the turbidity plume is clearly seen in the RGB images in the adjacent continental shelf reaching several hundred of km^2. This is confirmed by the strong increase in SLA observed in HR-bathy. The water levels from the tide gauge at Bonanza (not shown here) confirmed this increase at that period. Navarro et al. (2012) analyzed this event in terms of temporal variability of some hydrological variables in the estuary (they

expanded the analysis to March 2010). One of the stations was located in the estuary mouth recording routinely temperature, conductivity, dissolved oxygen, fluorescence and turbidity. The turbidimeter measured maximum values of about 8000 FNU (Formazin Nephelometric Unit) in that period. Salinity dropped to almost 0 confirming the freshwater nature of the plume in the estuary mouth.

The track coverage is not always optimal in the study area due to the lack of altimeter measurements during the episodes of heavy river discharges. As mentioned before, the best situation in terms of number and distribution of tracks was between January 2000 and September 2008 when the GFO data were available. In other periods it might be possible that the effects in the sea level due to heavy discharges are not observed in the daily maps of SLA just because of the scarcity of altimeter measurements in the area at specific time periods. This is evident in the event of December 1996 (Table 1). During about the second half of the month, the river estuary was in extreme conditions with a fluvially-dominated regime (400 $m^3/s < Qd > 3000$ m^3/s). Even though, the 24th of December the daily mean river discharge was 3670 m^3/s, making this event exceptional (Díez-Minguito et al., 2012). Under these conditions, one might expect a huge discharge of freshwater into the neighboring continental shelf and hence a clear and distinctive positive signal in the HR-bathy daily maps of SLA. The tide gauge confirmed an elevation of the mean daily water level of about 40 cm (not shown here) between 16th and 24th of December. The correlation coefficient between daily river discharge and water level in that period was 0.83 (95% confidence level). Fig. 8 shows the HR-bathy daily maps of SLA from 16th to 31st of December. The river plume was not observed in any of the days shown. The track coverage during that period consisted of only one T/P track (#035) crossing the area twice (19th and 29th of December according to the temporal resolution of this satellite) in the southwestern corner of the selected area and one ERS-2 track (#917) in the northwest (27th of December). Thus, the adjacent continental shelf to the estuary mouth was not covered by any altimeter passage and consequently the optimal interpolation used to generate the gridded maps was not capable to reproduce the expected increase of the sea level in the area.

5. SUMMARY AND CONCLUSIONS

Sixteen years (1994-2009) of sea level variability in the eastern continental shelf of the Gulf of Cadiz, adjacent to the Guadalquivir River estuary mouth, have been analyzed. We have focused on heavy events of freshwater discharges from the estuary and its influence on sea level at the adjacent shelf, ranging at temporal scales comprised between daily to seasonal. Furthermore, the ability of high-resolution daily gridded maps of sea level anomaly generated from the constellation of radar altimeters available at that period capturing these events has been investigated in detail. From the results obtained in this work we outline the following conclusions:

In years with periods of heavy river discharges the monthly means estimated in a yearly basis deviates from the average of the monthly means obtained along the whole time period. From the 9 years of strong discharges, 1996, 1998, 2001 and 2004 showed uncorrelated monthly means with the average of the monthly means. Only 2000 and 2003 presented significant correlations. The lack of in-situ data in some years of heavy discharges precluded this comparison. The remaining years analyzed (no heavy discharges) showed significant and high correlations. We conclude that the sea level in the adjacent shelf of the estuary mouth is highly influenced by sporadic but strong river discharges.

The use of a bathymetry constraint in the methodology developed to generate HR gridded maps of SLA, improves the characterization of mesoscale signals in the coastal strip adjacent to the river estuary. This has been demonstrated analyzing the spatio-temporal distribution of the SLA after two events of heavy river discharges of freshwater from the Guadalquivir River (March 2001 and December 2009). HR-bathy showed a more realistic elevation of the sea level in the vicinity of the estuary mouth in agreement with in-situ observations. The comparison against alternative remotely-sensed source (optical images) of information also confirms the extent of the freshwater plume in the adjacent shelf observed in the sea level maps.

The spatio-temporal distribution of the tracks covered by the satellite altimeter constellation is critical for the mapping capabilities of the HR maps to recover useful information. Any study area has to be covered by the maximum number of tracks in the space and temporal domains in order to get a more realistic characterization of the mesoscale signals.

ACKNOWLEDGMENTS

This work has been partially supported by the ALCOVA Project (CTM2012-37839) funded by the Spanish Ministerio de Economía y Competitividad and FEDER. The low resolution maps of Sea Level Anomaly and along-track data were obtained from AVISO. Special thanks to Dr. Gabriel Navarro (ICMAN-CSIC) for his help on downloading and processing the MODIS-Terra RGB images from AERONET.

REFERENCES

Aviso (2014): SSALTO/DUACS User Handbook: (M)SLA and (M)ADT Near-Real Time and Delayed Time Products, CLS-DOS-NT-06-034 - Issue 4.1.

Birol, F., M. Cancet, and C. Estournel (2010): Aspects of the seasonal variability of the Northern Current (NW Mediterranean Sea) observed by altimetry, *J. Mar. Syst*., 81, p. 297–311. doi:10.1016/j.jmarsys.2010.01.005.

Bouffard J., L. Renault, S. Ruiz, A. Pascual, C. Dufau, and J. Tintoré (2012): Sub-surface small scale eddy dynamics from multi-sensor observations and modelling, *Prog. in Oceanog.*, vol. 106. p.62-79.

Bouffard J., S. Vignudelli, P. Cipollini, and Y. Ménard (2008b): Exploiting the potential of an improved multi-mission altimetric dataset over the coastal ocean. *Geophys. Res. Lett.*, 35, L10601, doi:10.1029/2008GL033488.

Bouffard J., S. Vignudelli, M. Hermann, F. Lyard, P. Marsaleix, Y. Ménard, and P. Cipollini (2008a): Comparison of ocean dynamics with a regional circulation model and improved altimetry in the Northwestern Mediterranean. *Journal of Terrestrial, Atmospheric and Oceanic, sciences special issue "Satellite Altimetry over Land and Coastal Zones: Applications and Challenges"*, 19, No 1-2, 117-133, doi: 10.3319/TAO.2008.19.1-2.117(SA).

Bouffard, J., A. Pascual, S. Ruiz, Y. Faugère, and J. Tintoré (2010): Coastal and mesoscale dynamics characterization using altimetry and gliders: A case study in the Balearic Sea, *J. Geophys. Res.*, 115, C10029, doi:10.1029/2009JC006087.

Bouffard, J., F. Nencioli, R. Escudier, A. M. Doglioli, A.A. Petrenko, A. Pascual, P. M. Poulain, and D. Elhmaidi (2014): Lagrangian analysis of satellite-derived currents: Application to the North Western Mediterranean coastal dynamics, *Adv. in Space Res.*, 53, p. 788-801.

Brown, S. (2010): A novel near-land radiometer wet path-delay retrieval algorithm: application to the Jason-2/OSTM Advanced Microwave Radiometer. *Trans. Geoc. Rem. Sens.*, doi: 10.1109/TGRS.2009.2037220.

Caballero, A., L. Ferrer, A. Rubio, G. Charria, B. H. Taylor, and N. Grima (2013): Monitoring of a quasi-stationary eddy in the Bay of Biscay by means of satellite, *in-situ* and model results. *Deep Sea Res. Part II-Topical Studies in Oceanography*, doi: 10.1016/J.DSR2.2013.09.029.

Carrère, L., and F. Lyard (2003): Modeling the barotropic response of the global ocean to atmospheric wind and pressure forcing - comparisons with observations. *Geophys. Res. Lett.* 30, 1275, doi: 10.1029/2002GL016473.

Criado-Aldeanueva, F., J. García-Lafuente, G. Navarro, and J. Ruíz (2009): Seasonal and interannual variability of the surface circulation in the eastern Gulf of Cadiz (SW Iberia). *J. Geophys. Res.* 114, C01011, doi: 10.1029/2008JC005069.

Davis, R. E. (1998), Preliminary results from directly measuring middepth circulation in the tropical and South Pacific, J. Geophys. Res., 103(C11), 24,619–24,639.

Díez-Minguito, M., A. Baquerizo, M. Ortega-Sánchez, G. Navarro, and M. A. Losada (2012): Tide transformation in the Guadalquivir estuary (SW Spain) and process-based zonation. *J. Geophys. Res.* 117, C03019, doi: 10.1029/2011JC007344.

Ducet, N., P.-Y. Le Traon, and G. Reverdin, (2000): Global high resolution mapping of ocean circulation from Topex/Poseidon and ERS-1 and -2. *J. Geophys. Res.*, 105 (C8), 19477-19498.

Dussurget, R., F. Birol, R. Morrow, and P. De Mey (2011): Fine resolution altimetry data for a regional application in the Bay of Biscay, *Mar. Geod.*, 34, 3–4, 447–476, doi: 10.1080/01490419.2011.584835.

Escudier, R., J. Bouffard, A. Pascual, P. M. Poulain, and M. I. Pujol (2013): Improvement of coastal and mesoscale observation from space: Application to the northwestern Mediterranean Sea, *Geophys. Res. Lett.* 40, 2148-2153, doi: 10.1002/grl.50324.

ESEAS-RI, (2006): Assessment of accuracy and operational properties of different tide gauge sensors. WP4. Deliverable D4.1. European Sea-level Service Research & Infraestructure. 34 pp.

Fu, L. L., and A. Cazenave (2001): Satellite Altimetry and Earth Sciences: A handbook of Techniques and Application, Academic Press, International Geophysics Series, Vol. 69, San Diego, USA, 463 pp.

García-Lafuente, J., J. Delgado, F. Criado-Aldeanueva, M. Bruno, J. del Rio, and J. M. Vargas (2006): Water mass circulation on the continental shelf of the Gulf of Cadiz. *Deep Sea Res. Part II-Topical Studies in Oceanography* 53, 1182-1197, doi: 10.1016/J.DSR2.2006.04.011.

Gill, A.E., and P. P. Niller (1973): The theory of the seasonal variability in the ocean. *Deep Sea Res. and Oceanographic Abstracts* 20, 141-177, doi: 10.1016/0011-7471(73)90049-1.

Gómez-Enri, J., A. Aboitiz, B. Tejedor, and P. Villares (2012): Seasonal and interannual variability in the Gulf of Cadiz: Validation of gridded altimeter products. *Est. Coast. and Shelf Sci.* 96, 114-121, doi: 10.1016/J.ECSS.2011.10.013.

González-Ortegón, E., and P. Drake (2012): Effects of freshwater inputs on the lower trophic levels of a temperate estuary: physical, physiological or trophic forcing? *Aq. Sci.* 74, 455-469, doi: 10.1007/S00027-011-0240-5.

González-Ortegón, E., M. D. Subida, J. A. Cuesta, A. M. Arias, C. Fernández-Delgado, and P. Drake (2010): The impact of extreme turbidity events on the nursery function of a temperate European estuary with regulated freshwater inflow. *Est., Coast. and Shelf Sci.* 87, 311-324, doi: 10.1016/J.ECSS.2010.01.013.

Laiz, I., J. Gómez-Enri, B. Tejedor, A. Aboitiz, and P. Villares (2013): Seasonal sea level variations in the gulf of Cadiz continental shelf from in-situ measurements and satellite altimetry. *Cont. Shelf Res.*, 53, 77-88, doi: 10.1016/J.CSR.2012.12.008.

Le Traon, P. Y., and G. Dibarboure (2004): An illustration of the unique contribution of the TOPEX/Poseidon – Jason-1 tandem mission to mesoscale variability studies, *Mar. Geod*., 27, 3–13

Liu, Y., R. H. Weisberg, S. Vignudelli, L. Roblou, and C. R. Merz (2012): Comparison of the X-TRACK altimetry estimated currents with moored ADCP and HF radar observations on the West Florida Shelf. *Adv. Spac. Res.*, 50, 1085-1098, doi: 10.1016/J.ASR.2011.09.012.

Navarro, G., I.E. Huertas, E. Costas, S. Flecha, M. Díez-Minguito, I. Caballero, V. López-Rodas, L. Prieto, and J. Ruiz (2012): Use of a real-time remote monitoring Network (RTRM) to characterize the Guadalquivir estuary (Spain), *Sensors* 12, 1398-1421, doi: 10.3390/S120201398.

Nencioli, F., F. d'Ovidio, A. M. Doglioli, and A. A. Petrenko (2011): Surface coastal circulation patterns by in-situ detection of Lagrangian coherent structures, *Geophys. Res. Lett.*, 38, L17604, doi: 10.1029/2011GL048815.

Pascual, A., Y. Faugère, G. Larnicol, and P. Y. Le Traon (2006): Improved description of the ocean mesoscale variability by combining four satellite altimeters, *Geophys. Res. Lett.*, 33, doi: 200610.1029/2005GL024633.

Pascual, A., M. Marcos, and D. Gomis (2008): Comparing the sea level response to pressure and wind forcing of two barotropic models: Validation with tide gauge and altimetry data, *J. Geophys. Res.*, 113, doi: 10.1029/2007JC004459.

Pascual, A., J. Bouffard, S. Ruiz, B. B. Nardelli, E. Vidal-Vijande, R. Escudier, J. M. Sayol, and A. Orfila (2013): Recent improvements in mesoscale characterization of the western Mediterranean Sea: Synergy between satellite altimetry and other observational approaches, *Scientia Mar.* 77, 19-36. doi:10.3989/scimar.03740.15A

Prieto, L., G. Navarro, S. Rodríguez-Gálvez, I. E. Huertas, J. M. Naranjo, and J. Ruiz (2009): Meteorological and oceanographic forcing on the pelagic ecosystem of the Gulf of Cadiz shelf (SW Iberian Peninsula). *Cont. Shelf Res.*, 29, 2122–2137.

Relvas, P., and E. D. Barton (2002): Mesoscale patterns in the Cape San Vicente (Iberian Peninsula) upwelling region. *J. Geophys. Res.*107 (C10), 3164.

Roblou, L., F. Lyard, M. Le Henaff, and C. Maraldi (2007): X-track, a new processing tool for altimetry in coastal oceans, in: ESA ENVISAT Symposium, Montreux, Switzerland, April 23–27, 2007, ESA SP-636.

Saraceno, M., P. T. Strub, and P. M. Kosro (2008): Estimates of sea surface height and near-surface alongshore coastal currents from combinations of altimeters and tide

gauge, *J. Geophys. Res.*, 113, C11013, doi: 10.1029/2008JC004756.

Smith, W. H. F., and D. T. Sandwell (1997): Global sea floor topography from satellite altimetry and ship depth soundings, *Science*, 277(5334), 1956–1962.

Stevenson, R.E., (1977): Huelva Front and Malaga, Spain, Eddy chain as defined by satellite and oceanographic data. Deutsche *Hydrographische Zeitschrift* 30 (2), 51–53.

Vignudelli S., P. Cipollini, F. Reseghetti, G. Fusco, G. P. Gasparini, and G. M. R. Manzella (2003): Comparison between XBT data and TOPEX/Poseidon satellite altimetry in the Ligurian-Tyrrhenian area. *Ann. Geophys.*, 21(1, Part 1), 123-135.

Vignudelli S., P. Cipollini, L. Roblou, F. Lyard, G. P. Gasparini, G. M. R. Manzella, and M. Astraldi (2005): Improved satellite altimetry in coastal systems: Case study of the Corsica Channel (Mediterranean Sea). *Geophys. Res. Lett.*, 32, L07608, doi:1029/2005GL22602.

Vignudelli, S., A. Kostianoy, P. Cipollini, and J. Benveniste (eds.) (2011): Coastal Altimetry, Springer, 1st Edition, 2011, XII, 566 p. 216 illus., 186 in color. doi: 10.1007/978-3-642-12796-0.

Volkov, D. L., D. L. Larnicol, and J. Dorandeu (2007): Improving the quality of satellite altimetry data over continental shelves. *J. Geophys. Res.*, 112, C06020, doi: 101029/2006JC003765.

FIGURE CAPTIONS

Figure 1. Study area with the location of the tide gauge (red star: Bonanza) and altimeter tracks used for the optimal interpolation analysis. Yellow dot indicates the position of the nearest altimeter grid point to the tide gauge

Figure 2. Daily Guadalquivir River discharge (in m^3/s) from January 1994 to December 2009. The numbers in parenthesis indicate the heavy river discharges shown in Table 1. An overview of the altimetry missions used is also shown.

Figure 3. Average of monthly means of Mean Sea Level (black line), monthly means (MSL) in 1996 (grey line) and in 2007 (dashed black line) (Fig. 3a). The monthly Mean River Discharge (MRD) in 1996 is shown in Fig. 3b.

Figure 4. Daily maps of SLA in a 2-days temporal interval in the study area between 6th and 20th March 2001 using HR-std (Fig. 4a) and HR-bathy (Fig. 4b).

Figure 5. Top: Daily sea level anomaly (DAC corrected) from the tide gauge (black line) and from the closest grid point of HR-bathy (grey line) and HR-std (dashed black line) between 1st and 20th of March 2001. Also included the temporal location of the closest tracks to the Guadalquivir estuary. Bottom: Daily river discharge at the same period. The geographical location of the tracks available in the area for that period (ERS-2, GFO and Topex/Poseidon) are shown in the upper right corner of the bottom panel.

Figure 6. Along-track values of SLA (1 Hz sampling rate) for the constellation of satellites crossing the area between 09th and 15th of March 2001.

Figure 7. Left panel: RGB MODIS Terra images acquired in several dates during December 2009. Right panel: corresponding HR-bathy maps of SLA.

Figure 8. Daily maps of HR-bathy SLA from 16th to 31st December 1996.

FIGURE 1

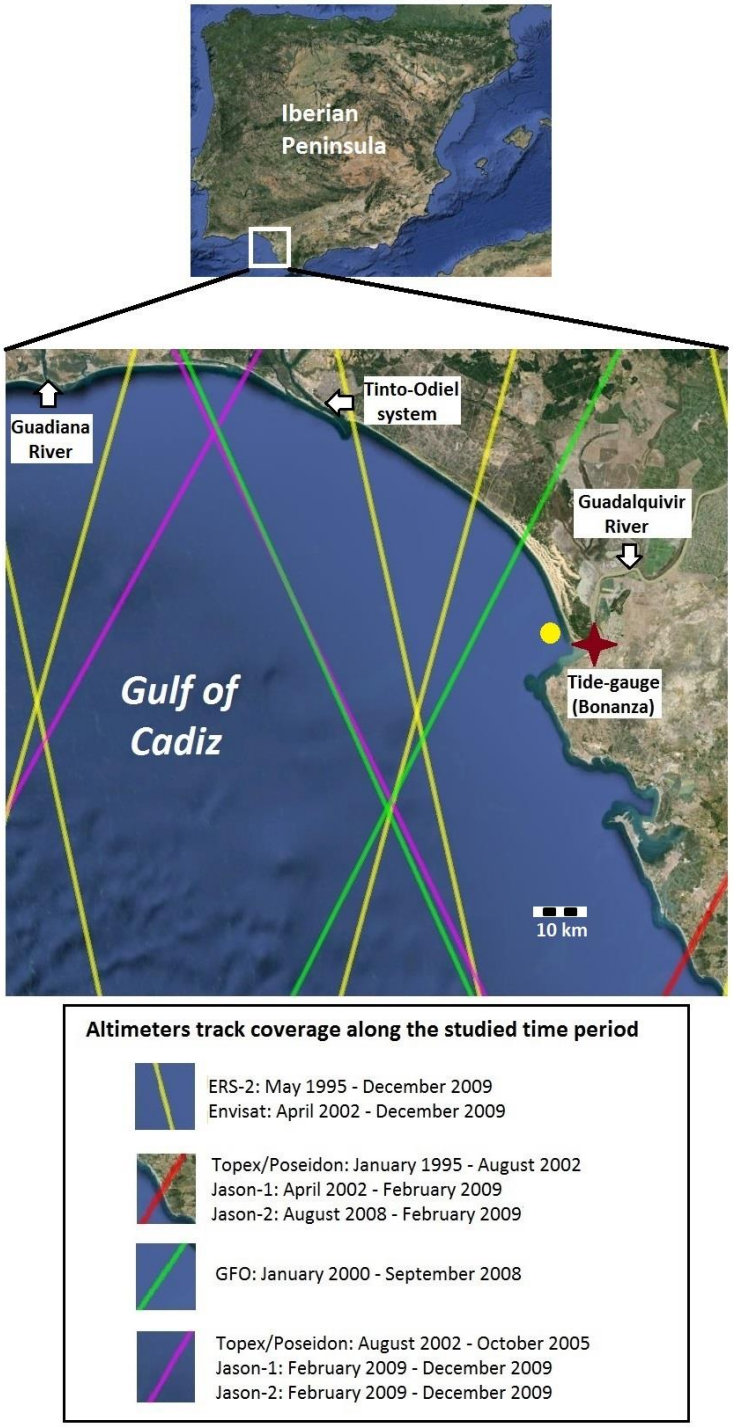

Figure 1. Study area with the location of the tide gauge (red star: Bonanza) and altimeter tracks used for the optimal interpolation analysis. Yellow dot indicates the position of the nearest altimeter grid point to the tide gauge

FIGURE 2

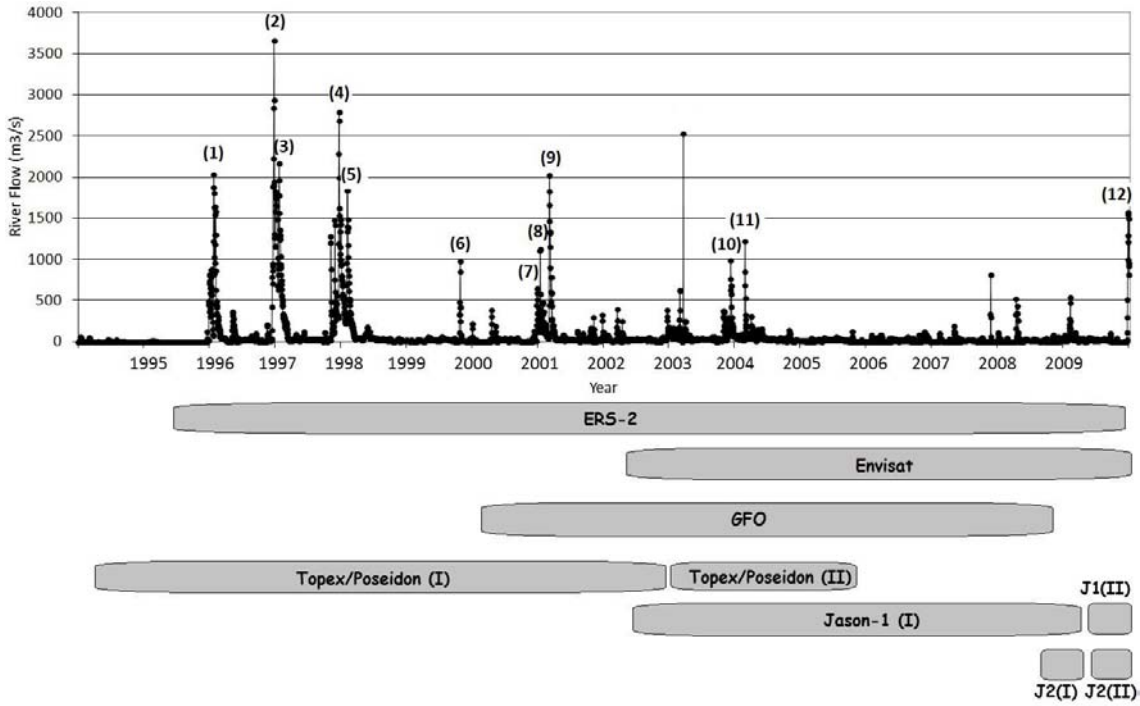

Figure 2. Daily Guadalquivir River discharge (in m^3/s) from January 1994 to December 2009. The numbers in parenthesis indicate the heavy river discharges shown in Table 1. An overview of the altimetry missions used is also shown.

FIGURE 3

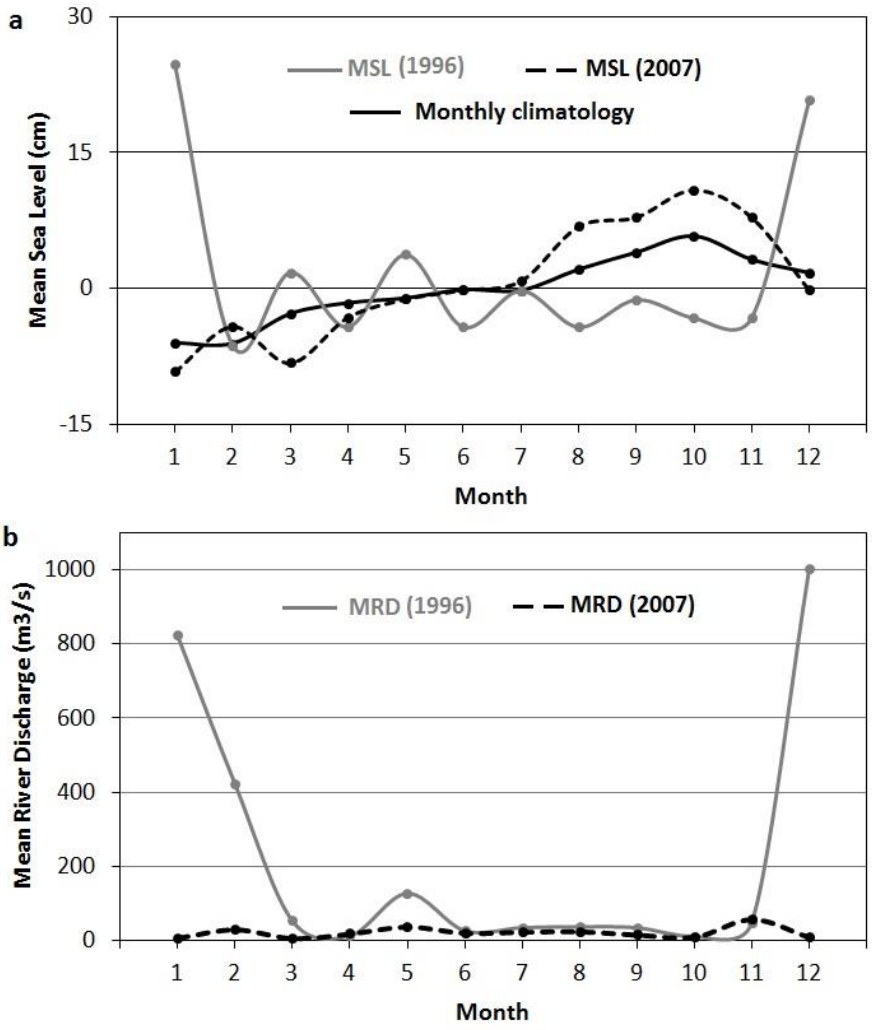

Figure 3. Average of monthly means of Mean Sea Level (black line), monthly means (MSL) in 1996 (grey line) and in 2007 (dashed black line) (Fig. 3a). The monthly Mean River Discharge (MRD) in 1996 is shown in Fig. 3b.

FIGURE 4

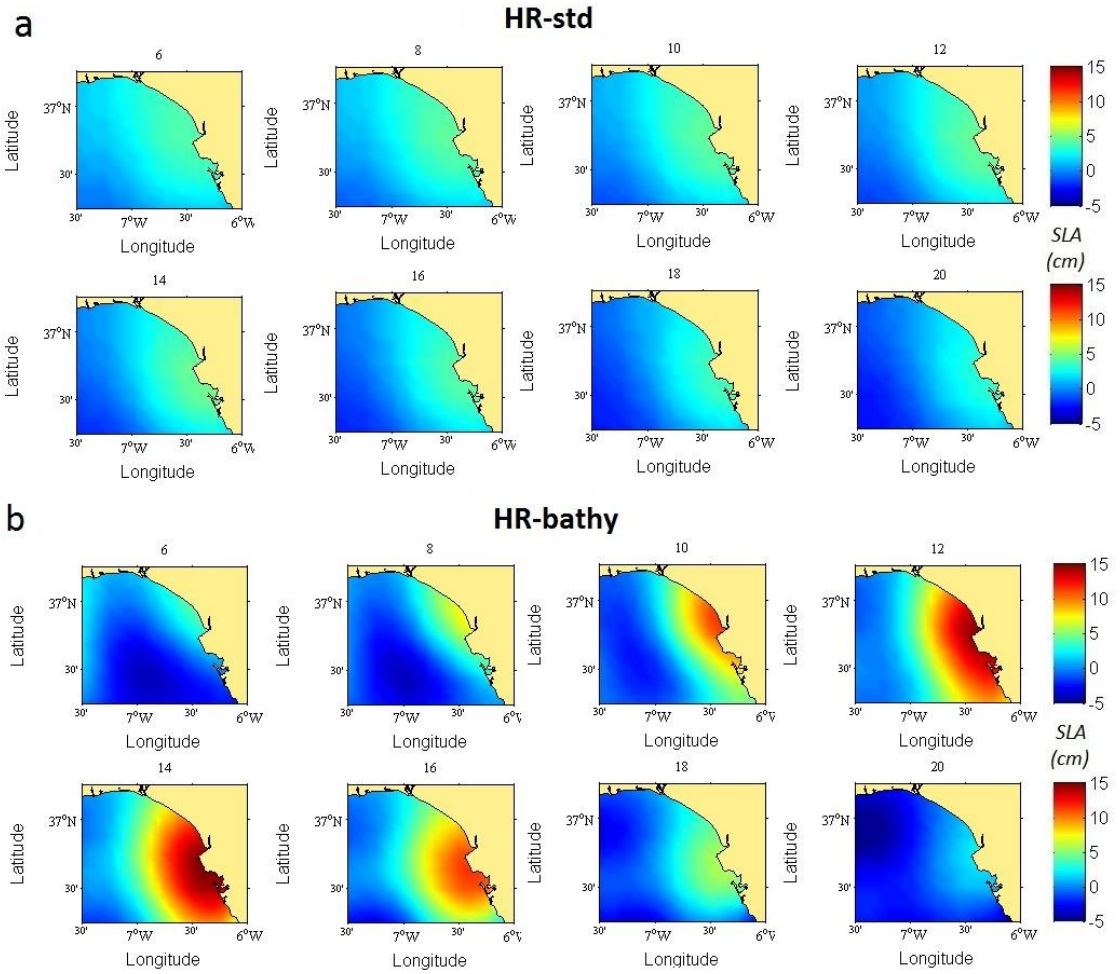

Figure 4. Daily maps of SLA in a 2-days temporal interval in the study area between 6th and 20th March 2001 using HR-std (Fig. 4a) and HR-bathy (Fig. 4b).

FIGURE 5

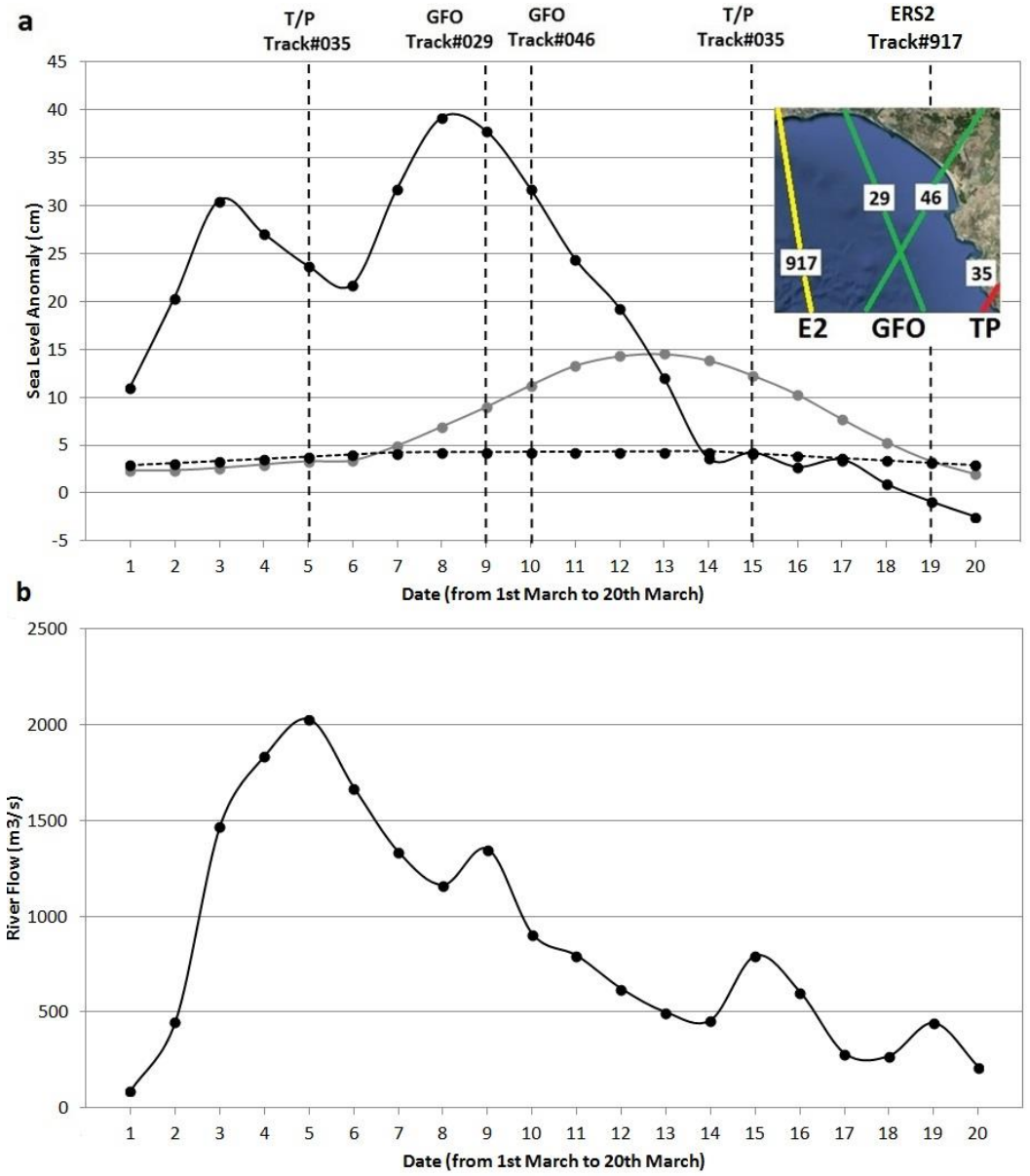

Figure 5. Top: Daily sea level anomaly (DAC corrected) from the tide gauge (black line) and from the closest grid point of HR-bathy (grey line) and HR-std (dashed black line) between 1st and 20th of March 2001. Also included the temporal location of the closest tracks to the Guadalquivir estuary. Bottom: Daily river discharge at the same period. The geographical location of the tracks available in the area for that period (ERS-2, GFO and Topex/Poseidon) are shown in the upper right corner of the bottom panel.

FIGURE 6

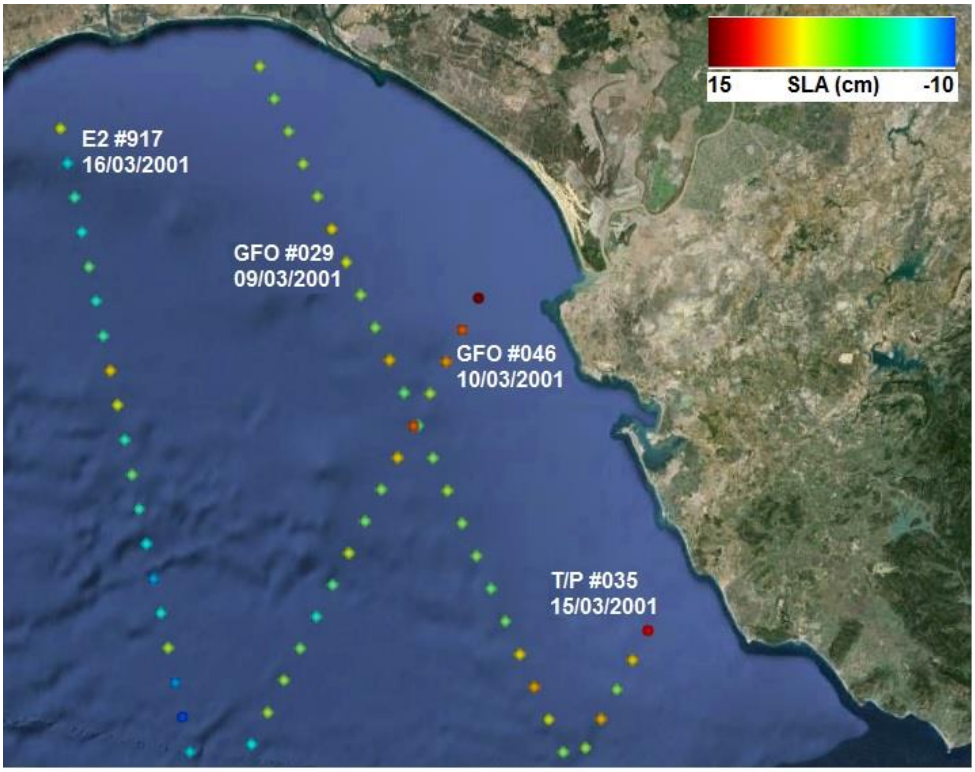

Figure 6. Along-track values of SLA (1 Hz sampling rate) for the constellation of satellites crossing the area between 09th and 15th of March 2001.

FIGURE 7

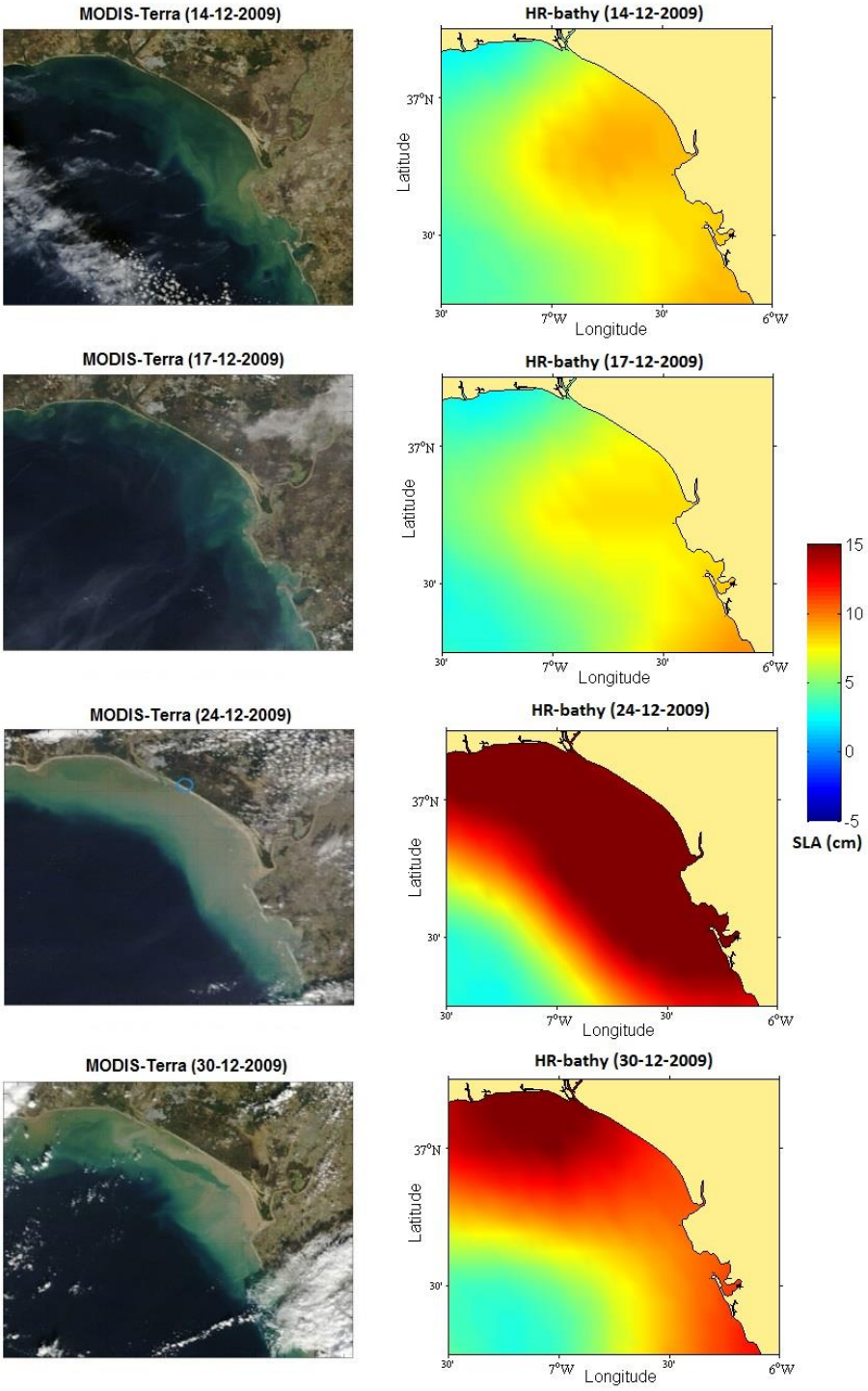

Figure 7. Left panel: RGB MODIS Terra images acquired in several dates during December 2009. Right panel: corresponding HR-bathy maps of SLA.

.

FIGURE 8

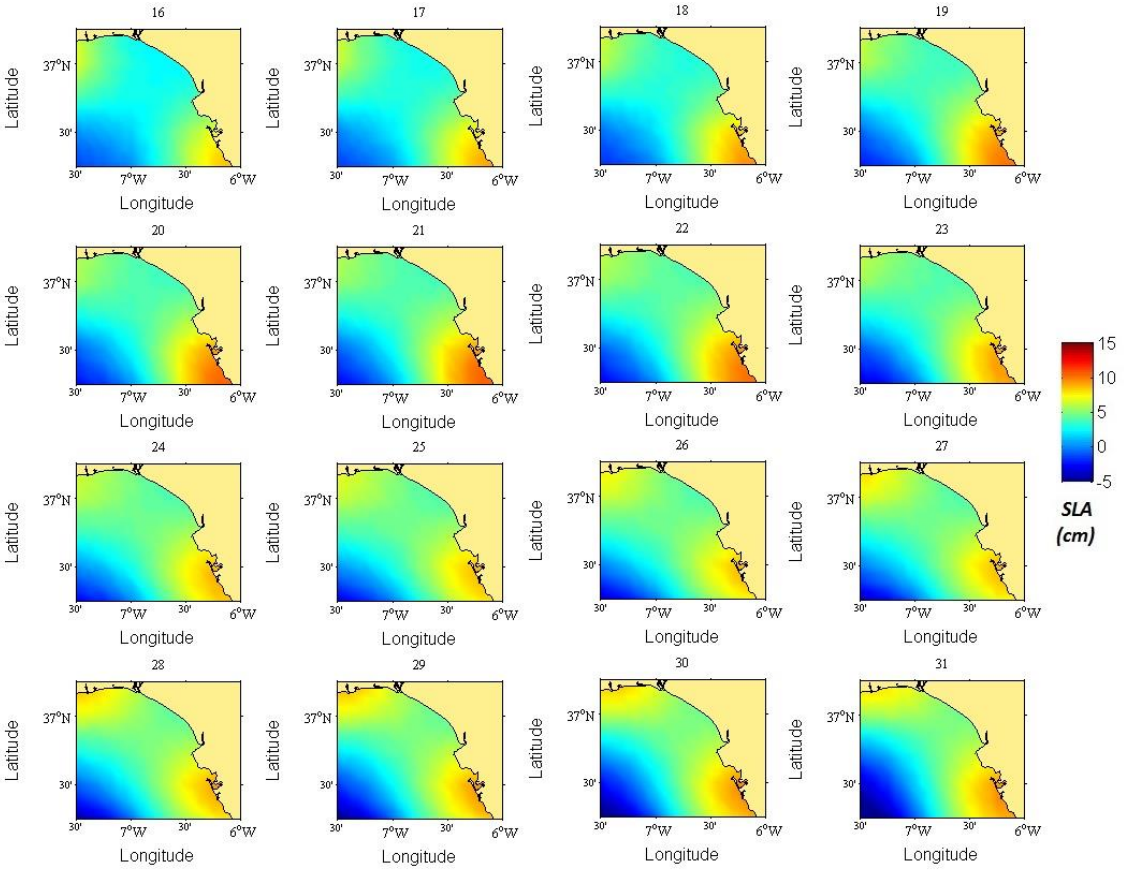

Figure 8. Daily maps of HR-bathy SLA from 16th to 31st December 1996.

TABLE 1

Table 1. Summary of time periods with heavy river discharge, including the number of days with discharges higher than 400 m^3/s during at least three consecutive days, the maximum discharge in each of the periods and the altimeter missions available.

	Months	**Nb. of days**	**Maximum discharge (m^3/s)**	**Altimeter missions available**
1996	January-February (1) December (2)	35 19	2045 3670	ERS-2 / TP(1)
1997	January-February (3) November-December (4)	42 24	2180 2800	ERS-2 / TP(1)
1998	January-February (5)	36	1850	ERS-2 / TP(1)
1999	October (6)	5	985	ERS-2 / TP(1)
2000	December (7)	4	662	ERS-2 / TP(1) GFO
2001	January (8) March (9)	3 15	1137 2028	ERS-2 / TP(1) GFO
2003	December (10)	7	1000	ERS-2 / TP(2) Envisat / GFO / J1(1)
2004	February (11)	4	1235	ERS-2 / TP(2) Envisat / GFO / J1(1)
2009	December (12)	10	1579	ERS-2 / J1(2) / J2(2) / Envisat

(1) Referenced orbit

(2) Interlaced orbit

APPENDIX

A detailed description of the procedure to compute the HR maps of SLA used in this work is given in Escudier et al. (2013). A summary of the main steps is presented here. The procedure basically uses the capabilities of the LR maps and the along-track data to resolve the larger and finer scales, respectively. Firstly, prior to the optimal interpolation, the long-wavelength errors are removed from the along-track data using the mean of the LR maps linearly interpolated to the positions of the along-tracks (step 1). A daily map at a 1/16º x 1/16º regular grid is generated from the LR product by a temporal and spatial linear interpolation. This includes an optimal extrapolation near the coast using the Arhan function (Arhan and Colin de Verdiere, 1985), with a space correlation of 100 km, and a filter at 80 km to remove small scale features (step 2). The HR maps generated are linearly interpolated to the location of the tracks and subtracted to the along-track values (step 3). An optimal interpolation algorithm is then applied to the along-track residuals to generate daily fields of the finer scales (step 4). In this step, a bathymetry constraint can be taken into account in the interpolation process. The constraint is applied by modifying the correlation function and assuming a generalized distance that takes into account the topography (Escudier et al., 2013 and Davis, 1998). The effect of the constraint results in giving more weight to observations that lie on the same bathymetric depth, inhibiting therefore sharp gradients across the coast. The topography used in this study has been extracted from Smith and Sandwell (1997). The fields produced by this interpolation process are called hereinafter Finally (step 5), the smaller scales obtained in step 4 are added to the LR maps (containing the larger scales, step 2) to generate the final product fields (HR-std or HR-bathy if the bathymetry constraint is added).

REFERENCES

Arhan, M., and A. Colin de Verdiere (1985). Dynamics of eddy motions in the eastern North Atlantic. *J. Phys. Oceanogr.* 15 (2), 153–170.

Smith, W. H. F., and D. T. Sandwell (1997): Global sea floor topography from satellite altimetry and ship depth soundings, *Science*, 277(5334), 1956–1962.

Appendix C

Optimal interpolation

C.1 Theory

The algorithm used for the interpolation of altimetry data from along-track to 2D fields is derived from the optimal interpolation method. In this method, we start with a first-guess field (the Background f_B). In this case, the first-guess field is zero. Then we try to correct this background using the observations available f_O. The corrected field is called analysis f_a.

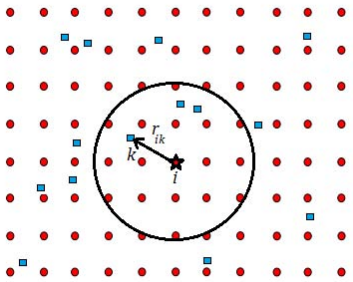

Figure C.1: Schematic view of the problem. In red are the analysis points and in blue are the observations.

$$f_a(r_i) = f_B(r_i) + \sum_{k=1}^{K} W(r_{ik})[f_O(r_k) \quad f_B(r_k)] \qquad \text{(C.1)}$$

r_k is an observation station and r_i an analysis gridpoint. In this algorithm we make some asumptions :

- Background is unbiased $\rightarrow$ we need detrended observation values (that are retrended after)
- Observations are uncorrelated
- Observations are biased with the same bias
- No correlation between background and observation error
- The observation and background error covariance is known (model: Gauss, Arhan...)

Introducing a simpler notation, $A_i = f_a(r_i)$, $O_k = f_O(r_k)$, $B_k = f_B(r_k)$,...

$$A_i = B_i + \sum_{k=1}^{K} W_{ik}[O_k - B_k] \tag{C.2}$$

We substract by the true field (T_i),

$$A_i - T_i = B_i - T_i + \sum_{k=1}^{K} W_{ik}[O_k - B_k] \tag{C.3}$$

We want to have an unbiased analysis. So we apply the expectation operator.

$$\langle A_i - T_i \rangle = \langle B_i - T_i + \sum_{k=1}^{K} W_{ik}[O_k - B_k] \rangle \tag{C.4}$$

Here, $\langle B_i - T_i \rangle = \langle B_k - T_k \rangle = 0$ (Background unbiased) and $\langle O_k - T_k \rangle = C$ with C constant (Observations have the same bias) Thus we obtain,

$$\sum_{k=1}^{K} W_{ik} = 0 \tag{C.5}$$

Squaring both sides of eq. C.3 and applying expectation operator,

$$\begin{aligned} E_A^2 &= \langle (A_i - T_i)^2 \rangle \\ &= \langle (B_i - T_i)^2 \rangle + 2 \sum_{k=1}^{K} W_{ik} \langle (O_k - B_k)(B_i - T_i) \rangle \\ &\quad + \sum_{k=1}^{K} \sum_{l=1}^{K} W_{ik} W_{il} \langle (O_k - B_k)(O_l - B_l) \rangle \end{aligned} \tag{C.6}$$

is the expected analysis error variance that we want to minimize under the constraint $\sum_{k=1}^{K} W_{ik} = 0$ (Eq. C.5). We therefore introduce a Lagrange multiplier λ_i and define the functional :

$$J_i = E_A^2 + \lambda_i (1 - \sum_{k=1}^{K} W_{ik}) \tag{C.7}$$

Differentiating J_i with respect to each of the weights W_{ik}, $1 \leqslant k \leqslant K$, gives

$$\begin{aligned} 0 &= \frac{\partial J_i}{\partial W_{ik}} \\ &= 2 \langle (O_k - B_k)(B_i - T_i) \rangle + 2 \sum_{l=1}^{K} W_{il} \langle (O_k - B_k)(O_l - B_l) \rangle \end{aligned} \tag{C.8}$$

or

$$\sum_{l=1}^{K} W_{il} \langle (O_k - B_k)(O_l - B_l) \rangle + \lambda_i = - \langle (O_k - B_k)(B_i - T_i) \rangle \tag{C.9}$$

The terms $\langle (O_m - T_m)(B_n - T_n) \rangle = 0$ because we assumed that there were no covariance between the background error and the observation error. Giving

$$\sum_{l=1}^{K} W_{il} [\langle (B_k - T_k)(B_l - T_l) \rangle + \langle (O_k - T_k)(O_l - T_l) \rangle] + \lambda_i = \langle (B_k - T_k)(B_i - T_i) \rangle \tag{C.10}$$

Define B_i column vector of length K whose elements are the background error covariance between r_k and r_i. O and B_O are respectively the symetric $K \times K$ observation and background error covariance matrices that only involve observation locations. We obtain then,

$$\begin{vmatrix} B_0 + O & 1 \\ 1 & 0 \end{vmatrix} \begin{vmatrix} W_i \\ \lambda_i \end{vmatrix} = \begin{vmatrix} B_i \\ 1 \end{vmatrix} \tag{C.11}$$

$$(K+1)\times(K+1) \quad (K+1)\times 1 \quad (K+1)\times 1 \tag{C.12}$$

extending it for all i locations of analysis gridpoint,

$$\begin{vmatrix} B_0 + O & 1 \\ 1 & 0 \end{vmatrix} \begin{vmatrix} W \\ \lambda \end{vmatrix} = \begin{vmatrix} B \\ 1 \end{vmatrix} \tag{C.13}$$

$$(K+1)\times(K+1) \quad (K+1)\times N \quad (K+1)\times N \tag{C.14}$$

The corresponding error to the weights W_i found is (From eq. C.6)

$$E_A^2 = E_B^2 - 2W_i^T B_i + W_i^T [B_O + O] W_i \tag{C.15}$$

which gives, with eq. C.11

$$E_A^2 = E_B^2 - W_i^T B_i - \lambda_i \tag{C.16}$$

in matrix form,

$$E_A^2 = E_B^2 - \left| W_i^T \lambda_i \right| \begin{vmatrix} B_i \\ 1 \end{vmatrix} \tag{C.17}$$

C.2 Application

To use the Optimal interpolation, we can therefore :

1. Use a previous guess as backgound field
2. Detrend observations to obtain gaussian-like observation field

3. Use a model to estimate background error covariance (the same as observation error in our case)

4. Apply the formula C.13 to calculate weights

5. Use the calculated weights to obtain the interpolated field (eq. C.2) and the error field (eq. C.17)

There is several models for the background error covariance. The simplest one is a gaussian model :

$$C_{ij} = \langle (B_i - T_i)(B_j - T_j) \rangle = e^{-\frac{|r_i - r_j|^2}{2L^2}} \tag{C.18}$$

But we can use more adequate models such as the one proposed by Arhan and Colin de Verdiere (1985) for AVISO maps :

$$\begin{aligned} C(x,y,t) &= \left[1 + ar + \tfrac{1}{6}(ar)^2 - \tfrac{1}{6}(ar)^3\right] e^{-ar} e^{-(\frac{t}{T})^2} \\ r &= \sqrt{\left(\frac{x - C_{px}t}{L_x}\right)^2 + \left(\frac{y - C_{py}t}{L_y}\right)^2}, \quad a = 3.337 \end{aligned} \tag{C.19}$$

where L_x, L_y are zonal and meridional correlation scales, C_{px},C_{py} are zonal and meridional propagation speed and T is the temporal correlation scale. These two different models are represented in figure C.2. We see that the to have similar correlation function, the correlation scale must be different. For the Arhan function, the correlation scale is the scale where the correlation is null.

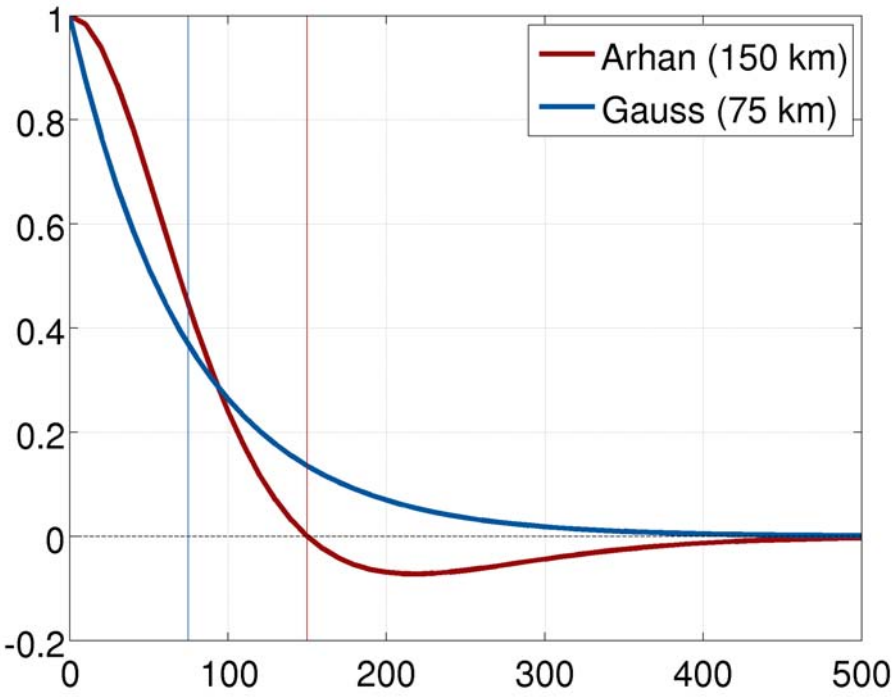

Figure C.2: Different models for the background error covariance.

C.3 Method in two steps

Here is the detailed methodology to obtained the HR maps of SLA. We used the AVISOMED08 fields as first guess.

1. Prior to the optimal interpolation, the along-track data are being processed to remove the long-wavelength errors. The method applied is as following: for each pass of track, the mean over the Mediterranean Sea of the track is compared to the mean of AVISOMED08 linearly interpolated on the same track. The difference between the two is removed from the original along-track data for this pass of track. A regular (in degrees) grid for the area of study (1/16) is generated.

2. Since AVISOMED08 maps are available only weekly and the OI is computed daily, a daily map of AVISOMED08

is created by the temporal linear interpolation of the AVISOMED08 maps. An optimal extrapolation near the coast is calculated with an Arhan function (Arhan and De Verdiere, 1985) with space correlation of 100km for this new AVISO map. It is also filtered at 80km to remove small scale features.

3. Observations (along-track data) in the domain in space (domain + 0.5) and time ($T_0 - 1.5T < t < T_0 + 1.5T$ with T_0 the date of the analyzed map and T the time scale applied)

4. AVISO gridded map values interpolated (linearly) to the location of the tracks are subtracted to the along-track values.

5. The optimal interpolation algorithm is applied to the residuals :

   - The mean of the observations is removed.
   - We apply the OI with the following correlation scheme:

     $$C(r = a - b, t) = e^{-r^2} e^{-\frac{t^2}{T^2}} \qquad \text{(C.20)}$$

     with the following values for the parameters : $T = 5days$, $L = 40km$, $\Phi = 0.7$. The observed noise is estimated to be around 3cm.
   - The error of the OI is computed.
   - The mean is added again.

6. The field computed from residuals is added to the daily field created from AVISO gridded maps.

Acronyms

ADCP

Acoustic Doppler Current Profiler. 21

AVISO

Archiving, Validation and Interpretation of Satellite Oceanographic. 64, 124, 136

AW

Atlantic Water. 13, 15, 69, 82–84

CCG

Central Cyclonic Gyre. 69

CHE11

Modified eddy detection method from Chelton et al. (2011). 116, 120, 123, 125, 134, 136, 139, 147, 149, 154, 156

COADS

Comprehensive Ocean-Atmosphere Data Set. 51

CTD

Conductivity Temperature Depth. 20–22

EAG

Eastern Alboran Gyre. 13, 67, 69

ECMWF

European Centre for Medium-Range Weather Forecasts. 48

EKE

Eddy Kinetic Energy. 3, 4, 92–94, 97, 111, 126

EN4

ENACT-ENSEMBLE version 4. 65, 77, 78, 80, 81, 84

EOF

Empirical Orthogonal Functions. 69, 72

HAL13

Eddy detection method from (Halo et al., 2013). 124, 125, 134, 136–139, 154, 156, 157, 161, 163, 165

HR

High Resolution. 114, 134, 169

KE

Kinetic Energy. 3, 45, 52, 92

LIW

Levantine Intermediate Water. 15, 16, 83, 84

MDT

Mean Dynamic Topography. 14, 25, 65, 67, 71

MLD

Mixed Layer Depth. 4, 85, 87

NEN10

Eddy detection method from Nencioli et al. (2010). 121, 134, 136, 137, 139, 152, 154, 156, 157, 161, 163, 165

OI

Optimal Interpolation. 27, 64, 65, 100, 124

ROMS

Regional Ocean Modeling System. 36, 38, 41, 43, 52

SLA

Sea Level Anomaly. 25, 26, 63–65, 69, 71, 72, 91, 97, 115, 116, 120, 121, 123, 124

SSH

Sea Surface Height. 24–26, 36, 38, 48, 64, 65, 67, 68, 71, 92, 100, 115, 116, 121, 123, 124, 163

SSS

Sea Surface Salinity. 73, 75

SST

Sea Surface Temperature. 16, 17, 20, 21, 24, 50, 65, 73, 75

WAG

Western Alboran Gyre. 13, 17, 67, 69

WIW

Western Intermediate Water. 15, 16, 22, 83, 84

WMDW

Western Mediterranean Deep Water. 15, 85

WMed

Western Mediterranean Sea. 5, 6, 11, 13–18, 25, 27–31, 35, 36, 46, 52, 67, 77, 82, 83, 85, 97, 100, 111, 114, 120, 124, 126, 147–151, 156, 157, 163, 168, 173, 174